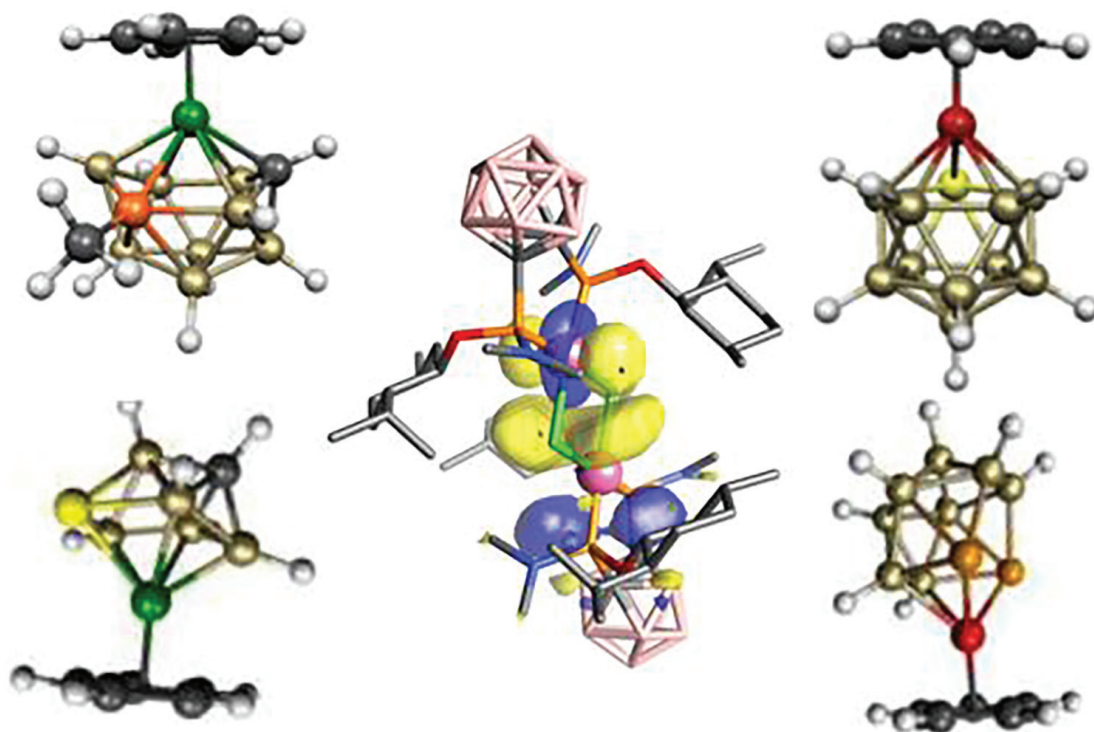




STUDIA UNIVERSITATIS
BABEŞ-BOLYAI



CHEMIA

3/2016
Tom I

**STUDIA
UNIVERSITATIS BABEȘ-BOLYAI
CHEMIA**

**3/2016
Tom I**

EDITORIAL BOARD OF STUDIA UNIVERSITATIS BABEȘ-BOLYAI CHEMIA

ONORARY EDITOR:

IONEL HAIDUC - Member of the Romanian Academy

EDITOR-IN-CHIEF:

LUMINIȚA SILAGHI-DUMITRESCU

EXECUTIVE EDITOR:

CASTELIA CRISTEA

EDITORIAL BOARD:

PAUL ȘERBAN AGACHI, Babeș-Bolyai University, Cluj-Napoca, Romania

LIVAIN BREAU, UQAM University of Quebec, Montreal, Canada

HANS JOACHIM BREUNIG, Institute of Inorganic and Physical Chemistry,
University of Bremen, Bremen, Germany

MIRCEA DIUDEA, Babeș-Bolyai University, Cluj-Napoca, Romania

JEAN ESCUDIE, HFA, Paul Sabatier University, Toulouse, France

ION GROSU, Babeș-Bolyai University, Cluj-Napoca, Romania

EVAMARIE HEY-HAWKINS, University of Leipzig, Leipzig, Germany

FLORIN DAN IRIMIE, Babeș-Bolyai University, Cluj-Napoca, Romania

FERENC KILAR, University of Pecs, Pecs, Hungary

BRUCE KING, University of Georgia, Athens, Georgia, USA

ANTONIO LAGUNA, Department of Inorganic Chemistry, ICMA, University of
Zaragoza, Zaragoza, Spain

JURGEN LIEBSCHER, Humboldt University, Berlin, Germany

KIERAN MOLLOY, University of Bath, Bath, UK

IONEL CĂȚĂLIN POPESCU, Babeș-Bolyai University, Cluj-Napoca, Romania

CRISTIAN SILVESTRU, Babeș-Bolyai University, Cluj-Napoca, Romania

<http://chem.ubbcluj.ro/~studiachemia/>; studiachemia@chem.ubbcluj.ro

http://www.studia.ubbcluj.ro/serii/chemia/index_en.html

YEAR
MONTH
ISSUE

Volume 61 (LXI) 2016
SEPTEMBER
3, TOM I

S T U D I A
UNIVERSITATIS BABEȘ-BOLYAI
CHEMIA
3
TOM I

*Dedicated to Professor Luminița Silaghi-Dumitrescu
on the Occasion of Her 65th Anniversary*

STUDIA UBB EDITORIAL OFFICE: B.P. Hasdeu no. 51, 400371 Cluj-Napoca, Romania,
Phone + 40 264 405352

CUPRINS – CONTENT – SOMMAIRE – INHALT

IONEL HAIDUC, Professor Luminița Silaghi-Dumitrescu at her 65 th anniversary	7
IONEL HAIDUC, Dithioarsinates Revisited. A Mini-Review.....	9
BIANCA DANCIU, ROXANA POPA, ALEXANDRA POP, VALENTIN ZAHARIA, CRISTIAN SILVESTRU, ANCA SILVESTRU, New Diorganochalcogen Compounds based on the 2-(Me ₂ NCH ₂)C ₆ H ₄ Group.....	19
ROBERT BRUCE KING, The Quest for Bridging Trifluorophosphine Ligands in Transition Metal Complexes.....	29
MENYHÁRT B. SÁROSI, EVAMARIE HEY-HAWKINS, Rhodium(I) Complexes of Bisphosphonitocarbaborane(12)S: a Computational Study	39

RADU SILAGHI-DUMITRESCU, DANIELA CIOLOBOC, Comparative Computational Characterization of Ferric Cytochrome P450 and Superoxide Reductase Binding to Cyanide	45
CHRISTA S. BARKSCHAT, AND THOMAS J.J. MÜLLER, Synthesis and Electronic Properties of 3-Aryl 10 <i>h</i> -Phenothiazines	55
BALAZS BREM, EMESE GAL, LUIZA GĂINĂ, TAMAS LOVASZ, EVA-ANDREA MOLNAR, DAN PORUMB, CASTELIA CRISTEA, Novel 1,9-Diacyl-5-(Phenothiazinyl)Dipyrrromethane Dialkyltin Complexes	73
LAVINIA BUTA, RALUCA SEPTELEAN, NOEMI DEAK, ALEXANDRA POP, GABRIELA NEMES, New Stannepine Derivatives. Synthesis and Characterisation.....	81
ALEXANDRU LUPAN, AMR A. A. ATTIA, R. BRUCE KING, The Effect of Electron-Rich Heteroatoms in Metallaborane Clusters.....	91
BIANCA MOLDOVAN, BRIGITTA IASKO, LUMINIȚA DAVID, Antioxidant Activity and Total Phenolic Content of Some Commercial Fruit-Flavoured Yogurts.....	101
NATALIA MIKLÁŠOVÁ, ROMAN MIKLÁŠ, PIROSKA VIRAG, CORINA BIANCA TATOMIR, CRISTINA SZALONTAI, DIANA CENARIU, FERDINAND DEVÍNSKY, EVA FISCHER-FODOR, Cytotoxic Activity of Palladium (II) Complexes of (1 <i>e</i> ,6 <i>e</i>)-1,7-Bis(4-(Dimethylamino) Phenyl)Hepta-1,6-Diene-3,5-Dione Against Human Colon Carcinoma	109
MIHAELA SABOU, ADRIANA GROZAV, LIA MONICA JUNIE, MIRELA FLONTA, VALENTIN ZAHARIA, CASTELIA CRISTEA, Thiazole Derivatives with Antifungal Activity Against <i>Candida</i> Species	117
JULIETA DANIELA CHELARU, MARIA GAVRILOAE, LIANA MARIA MURESAN, Electrochemical Investigation of the Inhibiting Effect Exerted by the Sulfuric Acid Diamide on Bronze Corrosion	125
ÁRPÁD FERENC SZŐKE, GRAZIELLA LIANA TURDEAN, GABRIEL KATONA, LIANA MARIA MURESAN, Electrochemical Determination of Dopamine with Graphene-Modified Glassy Carbon Electrodes	135
SZABOLCS FOGARASI, FLORICA IMRE-LUCACI, ADINA GHIRIȘAN, BARBU RADU HORAȚIU MIȘCA, ÁRPÁD IMRE-LUCACI, Removal of Lead from Industrial Wastewater by Electrocoagulation Using Sacrificial Aluminium Electrodes.....	145
ANA-DOMNICA MĂRINCEAN, SORIN-AUREL DORNEANU, PETRU ILEA, Hydrogen Peroxide Electrosynthesis and Detection in Sulphate Media.....	155
CARMEN MÂNZATU, CORNELIA MAJDIK, BOLDIZSÁR NAGY, The Use of Chemically Activated Fir Cone Carbon in the Removal of Pb ²⁺ Contaminated Aqueous Solutions	167

ANA-MARIA SĂCARĂ, CERASELLA INDOLEAN, LIANA MARIA MUREȘAN, Adsorption, Echilibrium and Kinetic Study of Malachite Green Removal from Aqueous Solutions Using Fir (<i>Abies Nordmanniana</i>) Cones Biomass.....	183
GHISLAIN ARNAUD MOUTHE ANOMBOGO, ANDRADA MĂICĂNEANU, JEAN BAPTISTE BIKE MBAH, CHRISDEL CHANCELICE NDJEUMI, LIVIU COSMIN COTEȚ, RICHARD KAMGA, Physico-Chemical Properties and Crystal Violet Adsorption Performances of H ₃ PO ₄ - Modified Mango Seeds Kernel	195
ANETTA VAIDA, VASILE-MIRCEA CRISTEA, Development of the Sour Water Plant Dynamic Simulator for Improving Design and Operation.....	215
SIMION DRĂGAN, Calculation of the Effective Mass Transfer Area in Turbulent Contact Absorber	227
LILIANA BIZO, MARIA GOREA, GABRIEL KATONA, Influence of MgO/SiO ₂ Ratio and Additives on Bionanoforsterite Powders Characteristics.....	239
THOMAS DIPPONG, CRISTINA MIHALI, FIRUTA GOGA, GHEORGHE ARDELEAN, Mathematical Modeling of the Variation in Water Quality Along the Network of Water Supply of Satu Mare Municipality, Romania	251
FIRUTA GOGA, ROXANA DUDRIC, LILIANA BIZO, ALEXANDRA AVRAM, THOMAS DIPPONG, GABRIEL KATONA, GHEORGHE BORODI, ANDREEA ANTON, Influence of the Thermal Treatment on the Colour of RO·Al ₂ O ₃ (R=Co, Ni) Type Spinel Pigments Prepared by a Modified Sol – Gel Method	263
ANCUTA DANISTEAN, MARIA GOREA, ALEXANDRA AVRAM, SORIN RAPUNTEAN, GHEORGHE TOMOAI, AURORA MOCANU, CORINA GARBO, OSSY HOROVITZ, MARIA TOMOAI-COTISEL, Antimicrobial Activity of Ceramic Disks Loaded with Silver Ions and Nitroxoline.....	275

Studia Universitatis Babes-Bolyai Chemia has been selected for coverage in Thomson Reuters products and custom information services. Beginning with V. 53 (1) 2008, this publication is indexed and abstracted in the following:

- Science Citation Index Expanded (also known as SciSearch®)
- Chemistry Citation Index®
- Journal Citation Reports/Science Edition

This issue of our journal is dedicated to Professor Luminița Silaghi-Dumitrescu at her 65th anniversary.



Professor Luminița Silaghi-Dumitrescu

Professor Luminița Silaghi-Dumitrescu was born on March 9th, 1951 in Brasov, where she got the primary and secondary education. In 1970 she became an undergraduate student in chemistry, at Babes-Bolyai University in Cluj-Napoca, where she graduated with a MSc degree in 1974. In 1983 she obtained the PhD in chemistry with a thesis on “Metallic and Organometallic Dithioarsinates” (supervisor Professor Ionel Haiduc), a work which contributed significantly to the field.

After a short period of appointment in the industry (1975-1978) she became a researcher in the Institute of Chemical Research in Cluj-Napoca, where she was active between 1978-1986. After this period she joined the staff of the Chemistry Faculty at Babes-Bolyai University and became a lecturer in chemistry (1986-1994), associate professor (1994-1999) and full professor (1999-to date). She acted as dean of the Chemistry Faculty (2002-2007) and vice-rector of Babes-Bolyai University (2008-2012).

During her tenure she was teaching courses in Organic chemistry, Organometallic chemistry, Organometallic reagents in organic synthesis and Organometallic reagents in heterocyclic chemistry. An important activity of her was (and continues to be) the supervising of graduate students, which produced

very interesting and original research contributions. In addition to her communication and teaching skills she demonstrated a remarkable ability to supervise research activities and to perform successfully in administrative duties.

A very important part of the professional life of Mrs. Luminița Silaghi-Dumitrescu was devoted to research. Her research interests started during the preparation of her PhD thesis and her expertise now includes Organometallic chemistry (Groups 13-15 elements and transition metals); Chemistry of the coordination compounds (synthesis and structural characterization); Organometallic reagents in organic synthesis (organo-lithium, -magnesium, -titanium and -boron derivatives); Synthesis of novel organometallic compounds as precursors for semiconductors; Synthesis of building blocks for smart polymers (heteroalkenes, heteroallenes of heavier Group 14 and 15 elements). Her contributions were awarded with the „Costin D. Nenitzescu Prize” of the Romanian Academy (1997) and the „Nenitzescu-Criegee Lectureship Prize” of German Chemical Society jointly with the Romanian Academy (2011)..

Her research was supported by numerous national grants (e.g. on Metallomics; Green chemistry; Microwave assisted organic and organometallic synthesis; Organometallic precursors for hybrid electronic devices, etc) and participation in international programs, such as TEMPUS Project “Reforms and Upgraded Chemistry - Undergraduate Studies in Macedonia” (2008-2009) as Romanian co-coordinator; DAAD Programme Stability Pact - “Academic Reconstruction of South Eastern Europe”; “International Master and Postgraduate Programme in Materials Science and Catalysis”, Romanian co-coordinator (2006-2016); MC and WG member COST Action CM 802 - European Phosphorus Sciences Network - PhoSciNet (2009-2012); MC and WG member COST Action CM 1302 – Smart Inorganic Polymers (SIPs) (2013-2017); Grant EC COST (individual) (1993 - 1994), Université Paul Sabatier Toulouse, France; and Royal Society of Chemistry Grant (1998). Her collaboration with Professor Eva Marie Hey-Hawkins of the University of Leipzig, Germany, should be mentioned as a particular success story of mutual interest, which resulted in a considerable number of remarkable joint publications. The contributions of Mrs. Luminița Silaghi-Dumitrescu to the ditioarsinate chemistry remained until today of primordial importance, but her research interests were extended from arsenic chemistry to other areas, with important contributions, published in major high impact chemistry journals. (visit ResearcherID: B-5307-2015)

Currently, Professor Luminița Silaghi-Dumitrescu is continuing with competence and talent her scientific life and she is at the summit of a splendid career, promising more important contributions to the science of chemistry.

The editorial board of *Studia Universitatis Babeș-Bolyai-Chemia* is expressing the best wishes to her for a good health and many years of successful activity.

ONORARY EDITOR

IONEL HAIDUC - Member of the Romanian Academy

*Dedicated to Professor Luminița Silaghi-Dumitrescu
on the occasion of her 65th anniversary*

DITHIOARSINATES REVISITED. A MINI-REVIEW

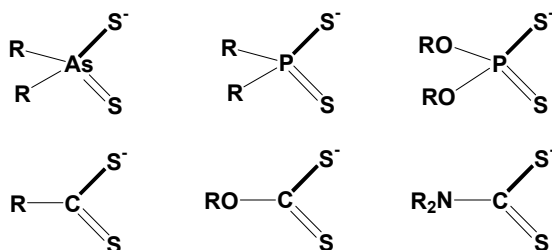
IONEL HAIDUC^{a,*}

ABSTRACT. The dithioarsinato ligands display a variety of coordination patterns in inorganic and organometallic compounds. Their structures and transformations are reviewed.

Keywords: dithioarsinate, 1,1-dithiolato ligands, self-assembly, organometallic, coordination.

1. INTRODUCTION

Dithioarsinates are members of a large family of anionic ligands, 1,1-dithiolates, which also includes dithiophosphinates, dithiophosphates, dithiocarboxylates, dithiocarbonates (xanthates) and dithiocarbamates (Scheme 1)[1]. Among these the dithioarsinates and dithiocarboxylates are less studied.



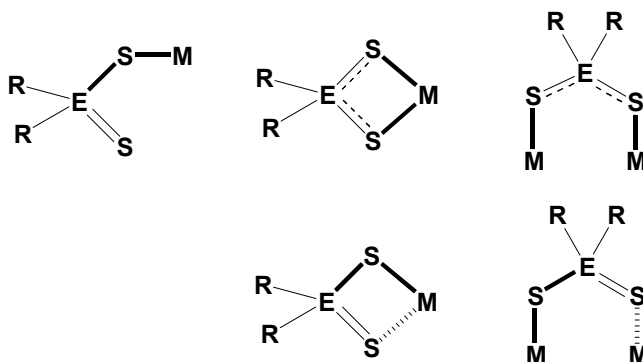
Scheme 1

^a Babeș-Bolyai University, Faculty of Chemistry and Chemical Engineering, 11 Arany Janos str., RO-400028, Cluj-Napoca, Romania

* Corresponding author: ihaiduc@chem.ubbcluj.ro

The 1,1-dithiolates are versatile ligands and display a variety of coordination patterns: monodentate, symmetric or unsymmetric bidentate chelating and bridging (Scheme 2, E = P or As). Our interest for this type of ligands was mainly stimulated by their ability to participate in the formation of inorganic (carbon-free) chelate rings [2].

The history of dithioarsinate chemistry has known three periods. After the preparation of the first metal dithioarsinates in the 19th century [3], the field lay dormant until the 70-thies of the 20th century, when the first X-ray structure determinations were performed. After a new period of some silence, the interest for the field was revitalized recently in particular due to the work of a group in Patras, Greece.



Scheme 2

2. TRANSITION METAL COMPLEXES

A series of dithioarsinates of chromium, manganese, cobalt, nickel, copper, zinc and indium was prepared from sodium dimethyldithioarsinate, $\text{Na}[\text{Me}_2\text{AsS}_2]$ and metal halides or by bubbling H_2S in a methanolic hydrochloric solution of the corresponding dimethylarsinates, $\text{M}[\text{Me}_2\text{AsO}_2]_n$, and the compounds were characterized by spectroscopic methods [4].

The transition metal dithioarsinates reported so far include dimethyldithioarsinates $\text{M}(\text{Me}_2\text{AsS}_2)_n$ with $\text{M} = \text{Cr}(\text{III})$, $n = 3$; $\text{M} = \text{Mn}(\text{II})$ [5a], $\text{Co}(\text{II})$ [5a, b], $\text{Cu}(\text{II})$ [5a,b,c] diphenyldithioarsinates $\text{M}(\text{S}_2\text{AsPh}_2)_n$, with $\text{M} = \text{Cr}(\text{III})$, and $\text{V}(\text{III})$, $n = 3$, $\text{Co}(\text{II})$, $\text{Ni}(\text{II})$, $n = 2$; and $\text{M} = \text{In}(\text{III})$ [4c] and a dibenzylidithioarsinate $\text{Co}[\text{S}_2\text{As}(\text{CH}_2\text{Ph})_2]_2$ [6].

Oxovanadium $\text{VO}(\text{Me}_2\text{AsS}_2)_2$ and oxomolybdenum $\text{MoO}(\text{Me}_2\text{AsMe}_2)_3$ were also investigated in the same period [7].

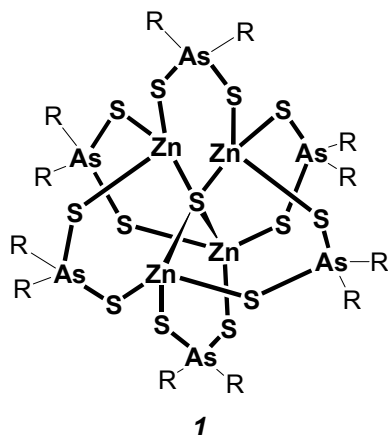
In a structural investigation the chromium complex $\text{Cr}(\text{Me}_2\text{AsS}_2)_3$ was found to display a distorted octahedral coordination geometry [8].

The complex $(\text{Me}_2\text{AsS}_2)_2\text{Pd}$ was prepared from sodium salt $\text{Na}[\text{Me}_2\text{AsS}_2] \cdot 2\text{H}_2\text{O}$, and $\text{Pd}(\text{OAc})_2$. The later also cleaves the disulfide $\text{Me}_2\text{As}(\text{S})\text{--S--AsMe}_2$ to form the complex $(\text{Me}_2\text{AsS}_2)_2\text{Pd}$, but this reacts further to form other $\text{Me}_2\text{As}(\text{S})$ compounds [9].

The copper(I) compound was obtained from $\text{Na}[\text{Me}_2\text{AsS}_2] \cdot 2\text{H}_2\text{O}$ with $\text{CuCl}_2 \cdot 2\text{H}_2\text{O}$ and $\text{Cu}(\text{OAc})_2 \cdot \text{H}_2\text{O}$ and was also formed in the reaction of $\text{Me}_2\text{As}(\text{S})\text{--S--AsMe}_2$, with $\text{Cu}(\text{AcO})_2 \cdot \text{H}_2\text{O}$, the compound $\text{Me}_2\text{As}(\text{S})\text{OAs}(\text{S})\text{Me}_2$ being also observed as by-product [10].

Of the post-transition metals of zinc and cadmium: form dimethyldithioarsinato complexes $\text{M}(\text{Me}_2\text{AsS}_2)_2$ [5a, b].

A spectacular compound is the tetrahedral oxo-centered inverse coordination complex $[(\mu_4\text{--S})\text{Zn}_4(\mu_2\text{--Me}_2\text{AsS}_2)_6]$ (**1**) in which the central sulfur atom is surrounded by four zinc atoms, bridged by six $[\text{Me}_2\text{AsS}_2]$ linkers. The structure was established by X-ray diffraction and a cadmium analogue was obtained [12]. The compound was prepared from $\text{Me}_2\text{As}(\text{S})\text{--S--AsMe}_2$ and $\text{Zn}(\text{ClO}_4)_2 \cdot 6\text{H}_2\text{O}$ and $\text{Cd}(\text{NO}_3)_2 \cdot 4\text{H}_2\text{O}$ in ethanol.



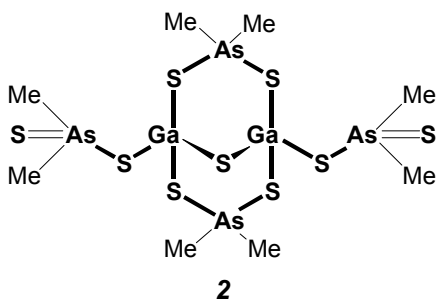
3. MAIN GROUP DERIVATIVES

The alkali metal dithioarsinates, $\text{M}[\text{R}_2\text{AsS}_2]$ ($\text{M} = \text{Na}$, $\text{R} = \text{Me}$ [11]; $\text{M} = \text{K}$, $\text{R} = \text{Ph}$, [4c], CH_2Ph [6]) are conveniently prepared from arsenic acids or their salts, $\text{M}[\text{R}_2\text{AsO}_2]$ by treatment with hydrogen sulfide. Two alkali metal dimethyldithioarsinates, namely the sodium salt $\text{Na}[\text{Me}_2\text{AsS}_2] \cdot 2\text{H}_2\text{O}$ [9] and the potassium salt $\text{K}[\text{Me}_2\text{AsS}_2] \cdot 2\text{H}_2\text{O}$, forming infinite bidimensional sheets, were structurally characterized by X-ray diffraction. [13].

Tris(dimethyldithioarsinato) complexes of Group 13 metals, $M(\text{Me}_2\text{AsS}_2)_3$ ($M = \text{Al, Ga, In, Tl}$) were recently prepared and characterized. [4c, 5b, 11, 14].

The indium(III) derivatives, $\text{In}(\text{S}_2\text{AsR}_2)_3$ ($R = \text{Me, Ph}$), studied by X-ray diffraction are monomeric distorted octahedral, and contain the dithioarsinates as isobidentate ligands [15]. The reaction of $\text{Na}[\text{Me}_2\text{AsS}_2] \cdot 2\text{H}_2\text{O}$ with $\text{Tl}(\text{OAc})_3$ gave $\text{Me}_2\text{AsS}_2\text{Tl}$ and $\text{Me}_2\text{As}(\text{S})\text{OAs}(\text{S})\text{Me}_2$ as by-product [10].

An interesting compound, $[(\text{Me}_2\text{AsS}_2)_2\text{Ga}]_2\text{S} \cdot 0.75\text{H}_2\text{O}$ (**2**), was formed in the hydrolysis (!) of $\text{Ga}(\text{Me}_2\text{AsS}_2)_3$. An X-ray diffraction analysis demonstrated its unique structure containing two monodentate and two bridging dithioarsinato ligands [16].



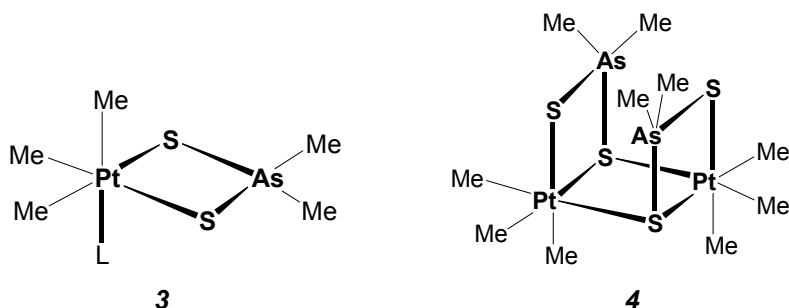
A number of dimethyl- and diphenyldithioarsinates of Main Group metals [$\text{Sn}(\text{IV})$, $\text{Pb}(\text{II})$, $\text{As}(\text{III})$, $\text{Sb}(\text{III})$, $\text{Bi}(\text{III})$] were synthesized [17]. The tris(dimethyldithioarsinato) complexes of group 15 metals, $M(\text{S}_2\text{AsMe}_2)_3$ ($M = \text{Sb, Bi}$) can be prepared by the reaction of $\text{Na}[\text{Me}_2\text{AsS}_2] \cdot 2\text{H}_2\text{O}$ with antimony trichloride and bismuth nitrate pentahydrate, respectively, but the reaction with AsCl_3 gave only $\text{Me}_2\text{As}(\text{S})\text{-S-AsMe}_2$ as isolable product [18].

The crystal structure determination of bismuth dimethyldithioarsinate, $\text{Bi}(\text{S}_2\text{AsMe}_2)_3$ has found in the solid state that the compound is a dimeric supermolecule formed through $\text{Bi} \cdots \text{S}$ secondary bonds. [19]

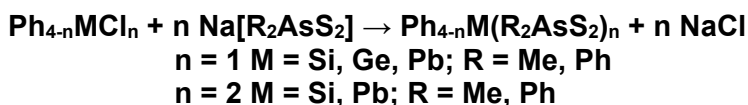
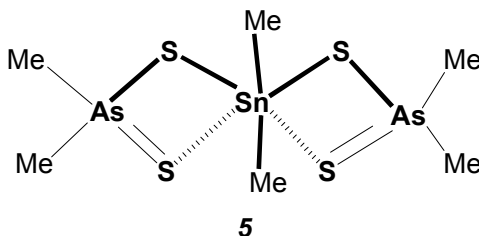
4. ORGANOMETALLIC DERIVATIVES

Very few organometallic dithioarsinato derivatives of transition metals have been reported; most known examples are dealing with main group metal compounds.

A rhenium(I) carbonyl complex $[\text{Re}(\text{CO})_3(\text{Me}_2\text{AsS}_2)\text{py}]$ has been described [20] and several trimethylplatinum compounds, including $[\text{PtMe}_3(\text{Me}_2\text{AsS}_2)\text{L}]$ (**3**), with $\text{L} = \text{py}$ or phosphines PMe_3 , PPh_3 , PMePh_2 , and a binuclear complex $[(\text{PtMe}_3)_2(\text{Me}_2\text{AsS}_2)_2]$ (**4**) have been reported with an X-ray diffraction study of the later [21].



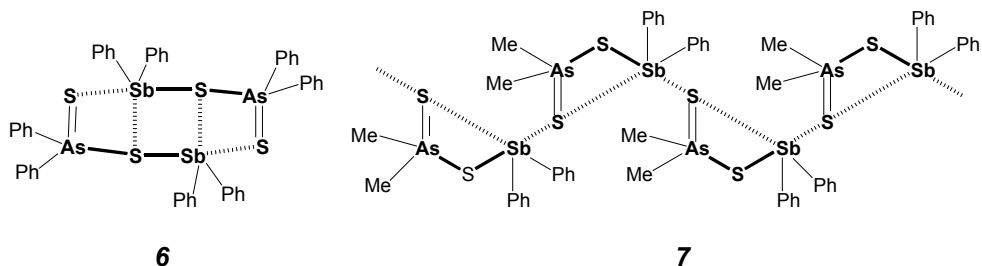
A series of organo-silicon, -germanium, -tin and -lead, derivatives of dimethyl- and diphenyldithioarsinic acids, $\text{Ph}_{4-n}\text{M}(\text{S}_2\text{AsR}_2)_n$ ($\text{M} = \text{Si, Ge, Sn, Pb}$; $n = 1$ and 2 , $\text{R} = \text{Me, Ph}$) were prepared. An X-ray structure analysis of $\text{Me}_2\text{Sn}(\text{S}_2\text{AsMe}_2)_2$ (**5**) established that the dithioarsinato ligand is anisobidentate [22]. On the basis of vibrational spectroscopy it was suggested that $\text{R}_3\text{Pb}(\text{S}_2\text{AsPh}_2)$ and $\text{R}_2\text{Pb}(\text{S}_2\text{AsPh}_2)$, contain Pb-As chelate rings, while in the analogous organosilicon and -germanium derivatives, the dithioarsinato ligand is monodentate.



Phenylantimony(III) dimethyldithioarsinates, $\text{Ph}_n\text{Sb}(\text{S}_2\text{AsMe}_2)_{3-n}$ with $n = 1-2$, have been prepared and the structure of $\text{Ph}_2\text{SbS}_2\text{AsMe}_2$ was determined by X-ray diffraction. The compound is a supramolecular compound, formed by self-assembly of molecular tectons into a chain-like structure with S-AsMe₂-S bridging ligands, displaying short (covalent, 2.655 Å) and long (secondary bonding, 2.830 Å) antimony-sulfur bonds.

Diphenylantimony(III) dithioarsinates, $\text{Ph}_2\text{SbS}_2\text{AsR}_2$ ($\text{R} = \text{Me}$ or Ph), have been synthesised and the structure has been determined for $\text{Ph}_2\text{SbS}_2\text{AsPh}_2$ (**6**). The compound is a dimeric supermolecule formed through Sb...S secondary bonds (3.590 and 3.369 Å) longer than the covalent single

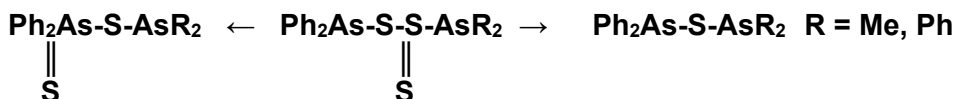
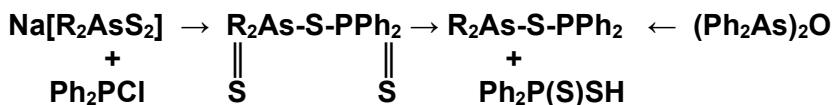
Sb-S bonds (2.486(2) Å. The self-assembly results in the formation of an eight-membered $Sb_2S_4As_2$ ring [23]. An X-ray diffraction analysis showed the $Ph_2SbS_2AsMe_2$ forms a supramolecular chain (**7**) in the crystal *via* bridging dimethyldithioarsinate ligands [17b].



5. VARIOUS REACTIONS INVOLVING DITHIOARSENIC GROUPS

When chlorodiphenylphosphine reacted with sodium dithioarsinates, $Na[R_2AsS_2]$ ($R = Me, Ph$) the products were diorganoarsenic(III) diphenyldithiophosphinates $R_2AsS-P(S)Ph$, instead of the expected diphenylphosphinyl dithioarsinates $Ph_2P-S-As(S)R_2$, as a result of a rearrangement involving migration of sulfur from arsenic(V) to phosphorus(III) proved by infrared and NMR spectroscopic data. An alternative preparation of the phenyl derivative through the direct reaction of $Ph_2P(S)SH$ with $(Ph_2As)_2O$ provides additional proof. The reaction was called “sulfotropic rearrangement” [24].

A similar sulfotropic rearrangement was found for tetraorganodiarsine disulfides, formed in the reaction of chlorodiphenylarsine with sodium dithioarsinates [25]



The oxidation of $(\text{Ph}_2\text{As})_2\text{S}$ with *tert*-butyl hydroperoxide and sulfur in 1:1 and 1:2 molar ratio produces the compounds $\text{Ph}_2\text{As}(\text{S})\text{-S-AsPh}_2$ and $\text{Ph}_2\text{As}(\text{S})\text{-S-As}(\text{S})\text{Ph}_2$, respectively. The dioxidation products are less stable and on recrystallisation an unusual mixed supramolecular adduct $[\text{Ph}_2\text{As}(\text{O})\text{OH}\cdot\text{Ph}_2\text{As}(\text{S})\text{OH}]_2$ self-assembled through hydrogen bonds was isolated [26].

The first oxygen-bridged dithioarsenic(V) compound, $\text{Me}_2\text{As}(\text{S})\text{-O-As}(\text{S})\text{Me}_2$, along with $\text{Me}_2\text{As}(\text{S})\text{-S-As}(\text{O})\text{Me}_2$, was obtained by oxidation of tetramethyldiarsine disulfide $\text{Me}_2\text{As}(\text{S})\text{SAsMe}_2$ with *tert*-butylperoxide. The molecular structure of the oxo-bridged compound was established by single crystal X-ray diffraction. The formation of the oxo-bridged isomer is unexpected and can be rationalized in terms of an oxotropic rearrangement of the sulfur bridged compound. *Ab initio* calculations predict that the oxo-bridged species are more stable than the thio-bridged isomer [27].

The reactions of thioarsinites $\text{R}_2\text{As-SPh}$ ($\text{R} = \text{Me}$ or Ph) with octasulfur in the presence of triethylamine were slow and complex and produced the disulfide $\text{R}_2\text{As}(\text{S})\text{-S-AsR}_2$ mixed with $\text{R}_2\text{As-S-NEt}_3^{(+)}$ and $\text{R}_2\text{As-S}^{(-)}$. The disulfide $\text{Ph}_2\text{As}(\text{S})\text{-S-AsPh}_2$ was not stable and decomposed during work-up to octasulfur and $\text{Ph}_2\text{As-S-AsPh}_2$ which was auto-oxidized to $\text{Ph}_2\text{AsO}_2\text{H}\cdot\text{Ph}_2\text{As}(\text{S})\text{OH}$ [28].

The dimethylarsino dimethyldithioarsinate $\text{Me}_2\text{As}(\text{S})\text{SAsMe}_2$ (also known as "Bunsen's cacodyl disulfide") was prepared from $\text{Me}_2\text{As}(\text{O})\text{OH}$ and hydrogen sulfide or by reaction of dimethylarsine Me_2AsH with excess sulfur. Its molecular structure was established by X-ray diffraction [29, 30].



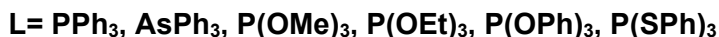
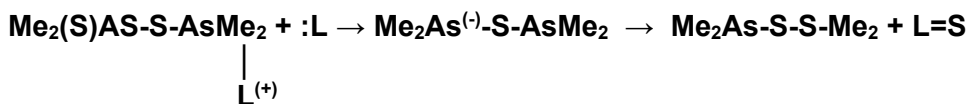
Interesting products were obtained in the reactions of the sulfide $\text{Me}_2\text{As}(\text{S})\text{-S-AsMe}_2$ with various reagents.

The interaction of dimethylarsino dimethyldithioarsinate, $\text{Me}_2(\text{S})\text{As-S-AsMe}_2$, with metal hexacarbonyls under UV irradiation gave complexes of the type $[\text{M}(\text{CO})_5\text{L}]$ ($\text{M} = \text{Cr}$ or W , $\text{L} = \text{Me}_2\text{As-S-AsMe}_2$) and $[\text{MM}'(\text{CO})_{10}\text{L}]$ ($\text{M} = \text{M}' = \text{Cr}$, $\text{L} = \text{Me}_2\text{As-S-AsMe}_2$, and $\text{M} = \text{Cr}$, $\text{M}' = \text{W}$ or $\text{M} = \text{M}' = \text{W}$, $\text{L} = \text{Me}_2\text{As-S-AsMe}_2$). The complex $[\text{Cr}(\text{CO})_5\text{L}]$ decomposes on heating to form $[\text{Cr}(\text{Me}_2\text{As}_2)_3]$ [31].

The reactions of sulfide $\text{Me}_2\text{As}(\text{S})\text{-S-AsMe}_2$ with group 13 halides were studied in detail. With $\text{BF}_3\cdot\text{Et}_2\text{O}$ the product was an equilibrated mixture of $\text{Me}_2\text{As}(\text{S})\text{-S-AsMe}_2$ and $\text{Me}_2\text{As-S-S-AsMe}_2$. While AlCl_3 produced complete isomerisation to $\text{Me}_2\text{As-S-S-AsMe}_2$, the halides GaCl_3 and InCl_3 just formed coordination adducts. With $\text{Tl}(\text{III})$ acetate the unstable complex $(\text{Me}_2\text{AsS}_2)_3\text{Tl}$ formed initially was reduced to the $\text{Tl}(\text{I})$ compound $\text{Me}_2\text{AsS}_2\text{Tl}$ [32].

In the reaction with heavy metal cations in methanol, the disulfide, $\text{Me}_2\text{As(S)-S-AsMe}_2$, produced insoluble salts (complexes) of dimethyldithioarsinic acid, $\text{Me}_2\text{As(S)SH}$, and dimethylarsenium ion, $\text{Me}_2\text{As}^{(+)}$ and finally dimethylarsino sulfenium cation, $\text{Me}_2\text{As-S}^{(+)}$. The reactions of $(\text{Me}_2\text{AsS}_2)_x\text{M}$ with triphenylphosphine and trimethyl phosphite gave $\text{Me}_2\text{As-S-AsMe}_2$ and the metal sulfide [33].

The reactions of the disulfide, $\text{Me}_2\text{As(S)-S-AsMe}_2$ with group 15 Lewis bases was also investigated. Triphenylamine did not react but 4-dimethylaminopyridine and triethylamine isomerised the disulfide to $\text{Me}_2\text{AsSSAsMe}_2$. Triphenylphosphine and P(OR)_3 where (R = Me, Et, Ph) and triphenylarsine desulfurised the disulfide to $\text{Me}_2\text{AsSAsMe}_2$ [34].



With iodine the disulfide $\text{Me}_2\text{As(S)-S-AsMe}_2$ reacted producing an uncommon compound, dimethylarsinosulfenyl iodide, $\text{Me}_2\text{As-S-I}$, containing a rare sulfur-iodine bond [35].

CONCLUSIONS

The chemistry of dithioarsinates is less popular than that of dithiophosphinates, possibly because of fear of toxicity, unpleasant smell of some compounds and non-commercial availability of most starting materials. The dithioarsinates are less robust than the dithiophosphinates and quite often produce unexpected transformations. In fact this makes them attractive due to the serendipity of their chemistry. The popular belief that the arsenic and phosphorus display a similar chemistry is not entirely true and for this reason the investigation of arsenic compounds, including dithioarsinates, but not limited to, deserves attention on its own.

REFERENCES

1. (a) I. Haiduc, *1,1-Dithiolato Ligands*, in "Reference Module in Chemistry, Molecular Sciences and Chemical Engineering" (*on line publication*), Elsevier, Amsterdam **2013**, pag. 1-15, <http://dx.doi.org/10.1016/B978-0-12-409547-2.00884-2>; (b) I. Haiduc: *1,1-Dithiolato ligands and related selenium and tellurium compounds* in vol. "Handbook of Chalcogen Chemistry. New Perspectives in Sulfur, Selenium and Tellurium", Edited by F. Devillanova, RSC Publishing, The Royal Society of Chemistry, London, **2007**, pag. 593-643; (c) I. Haiduc: *1,1-Dithiolato Ligands*, in vol. "Comprehensive Coordination Chemistry II. From Biology to Nanotechnology", J.A. McCleverty, T.J. Meyer, Editors-in-Chief, Volume 1, Fundamentals, Edited by A.B.P. Lever, Elsevier, **2003**, Chapter 1.15, pag. 349-376. (d) I. Haiduc, *Coord. Chem. Revs.* **1997**, *158*, 325.
2. (a) I. Haiduc, I. Silaghi-Dumitrescu, *Coord. Chem. Revs.*, **1986**, *74*, 127. (b) I. Haiduc, *J. Organomet. Chem.*, **2001**, *623*, 29.
3. (a) R. Bunsen, *Liebigs Ann. Chem.*, **1843**, *46*, 1, 21. (b) A. Michaelis, U. Pactor, *Liebigs Ann. Chem.*, **1886**, *233*, 62, 80.
4. (a) A.T Casey, N.S Ham, D.J Mackey, R.L Martin, *Aust. J. Chem.*, **1970**, *23*, 1117. (b) A.T. Casey, D.J. Mackey, R.L. Martin, *Aust. J. Chem.*. **1971**, *24*, 1587. (c) 327 A. Muller, P. Werle, *Chem. Ber.* **1971**, *34*, 3782.
5. (a) A.T. Casey, N.S. Ham, D.J. Mackey, R.L. Martin, *Aust. J. Chem.*, **1970**, *23*, 1117; 325 (b) M. Forster, H. Hertel, W. Kuchen, *Angew. Chem.*, **1970**, *82*, 842; *Angew. Chem.Int. Ed. Engl.*, **1970**, *9*, 811. (c) E.W. Ainscough, A.M. Brodie, G. Leng-Ward, *J. Chem. Soc., Dalton Trans.*, **1974** 2437.
6. A. Müller, P. Werle and P. Christophliemk, *Chem. Ber.*, **1973**, *106*, 3601.
7. (a) B.J. McCormick, J.L. Featherstone, H.J. Stoklosa, J.R. Wasson, *Inorg. Chem.*, **1973**, *12*, 692; (b) Z.R. Baratova, E.V. Semenov, P.M. Solozhenkin, B.S. Pramhananda, *Inorg. Chem.*, **1982**, *21*, 57.
8. L. Silaghi-Dumitrescu, A. Haiduc, F. Cervantes-Lee, K.H. Pannell, *Rev. Roum. Chim.*, **1997**, *42*, 587.
9. P.V. Ioannou, D.G. Vachliotis, V. Nastopoulos, A. J. Tasiopoulos, *Z. Anorg. Allg. Chem.* **2009**, *635*, 2203.
10. P.V. Ioannou, *Main Group Chem.*, **2014**, *13*, 243.
11. M. Forster, H. Hertel and W. Kuchen, *Angew. Chem. Int. Ed. Engl.*, **1970**, *9*, 811.
12. (a) A. Albinati, M. Casarin, C. Maccato, L. Pandolfo, A. Vittadini, *Inorg. Chem.*. **1999**, *38*, 1145. (b) D. Johnstone, J.E. Fergusson, W.T. Robinson, *Bull. Chem. Soc. Japan*, **1972**, *45*, 3721
13. S. Pascu, L. Silaghi-Dumitrescu, A.J. Blake, I. Haiduc, D.B. Sowerby, *Polyhedron* **1998**, *17*, 4115.
14. (a) P.V. Ioannou, D.G. Vachliotis, *Main Group Chem.*, **2012**, *11*, 2012.
15. L. Silaghi-Dumitrescu, I. Silaghi-Dumitrescu, I. Haiduc, R.A. Toscano, V. Garcia-Montalvo, R. Cea-Olivares, *Z. Anorg. Allg. Chem.*, **1999**, *625*, 347.
16. C. Papatriantafyllopoulou, V. Nastopoulos, P.V. Ioannou, *Z. Anorg. Allg. Chem.* **2014**, *640*, 1654.

17. (a) L. Silaghi-Dumitrescu, L.A. Avila-Diaz, I. Haiduc, *Rev. Roum. Chim.*, **1986**, 31, 335. (b) D.B. Sowerby, M.J. Begley, L. Silaghi-Dumitrescu, I. Silaghi-Dumitrescu, I. Haiduc, *J. Organomet. Chem.*, **1994**, 469, 45.
18. P.V. Ioannou, D.G. Vachliotis, *Main Group Chem.*, **2012**, 11, 267.
19. R. Cea-Olivares, K.H. Ebert, L. Silaghi-Dumitrescu, I. Haiduc, *Heteroatom Chem.*, **1997**, 8, 317.
20. E. Lindner, H.M. Ebinger, *J. Organometal. Chem.*, **1974**, 66, 103.
21. E.W. Abel, M.A. Beckett, P.A. Batters, M.B. Hursthouse, *Polyhedron* **1988**, 7, 1855.
22. (a) L. Silaghi-Dumitrescu, I. Haiduc, *J. Organomet. Chem.*, **1983**, 259, 65; (b) I. Haiduc, L. Silaghi-Dumitrescu, *J. Organomet. Chem.*, **1982**, 225, 225; (c) L. Silaghi-Dumitrescu, I. Haiduc, J. Weiss, *J. Organomet. Chem.*, **1984**, 263, 159.
23. C. Silvestru, L. Silaghi-Dumitrescu, I. Haiduc, M.J. Begley, M. Nunn, D.B. Sowerby, *J. Chem. Soc. Dalton Trans.*, **1986**, 1031.
24. L. Silaghi-Dumitrescu, I. Haiduc, *J. Organomet. Chem.* **1983**, 252, 295.
25. L. Silaghi-Dumitrescu, I. Silaghi-Dumitrescu, I. Haiduc, *Rev. Roum. Chim.*, **1989**, 34, 305.
26. L. Silaghi-Dumitrescu, M.N. Gibbons, I. Silaghi-Dumitrescu, J. Zukerman-Schpector, I. Haiduc, D.B. Sowerby, *J. Organomet. Chem.* **1996**, 517, 101.
27. L. Silaghi-Dumitrescu, S. Pascu, A.J. Blake, I. Haiduc, D.B. Sowerby, *J. Organomet. Chem.*, **1997**, 549, 187.
28. T.D. Sideris, G.M. Tsivgoulis, D.G. Vachliotis, P.V. Ioannou, *Main Group Chem.*, **2009**, 8, 163.
29. N. Camerman, J. Trotter, *J. Chem. Soc.*, **1964**, 219.
30. M.W. Fricke, M. Zeller, H. Sun, V.W.-M. Lai, W.R. Cullen, J.A. Shoemaker, M.R. Witkowski, J. T. Creed, *Chem. Res. Toxicol.*, **2005**, 18, 1821.
31. E.W. Ainscough, A.M. Brodie, G. Leng-Ward, *J. Chem. Soc., Dalton Trans.*, **1974**, 2437.
32. P.V. Ioannou, G.M. Tsivgoulis, D.G. Vachliotis, *Main Group Chem.*, **2009**, 8, 151
33. P.V. Ioannou, D.G. Vachliotis, T.D. Sideris, *Z. Anorg. Allg. Chem.*, **2009**, 635, 329.
34. P.V. Ioannou, D.G. Vachliotis, T.D. Sideris, *Z. Anorg. Allg. Chem.*, **2007**, 633, 2077.
35. P.V. Ioannou, D.G. Vachliotis, A. Chrissanthopoulos, *Z. Anorg. Allg. Chem.*, **2015**, 641, 1340.

*Dedicated to Professor Luminița Silaghi-Dumitrescu
on the occasion of her 65th anniversary*

NEW DIORGANOCHALCOGEN COMPOUNDS BASED ON THE 2-(Me₂NCH₂)C₆H₄ GROUP

**BIANCA DANCIU^a, ROXANA POPA^a, ALEXANDRA POP^a,
VALENTIN ZAHARIA^b, CRISTIAN SILVESTRU^a and ANCA SILVESTRU^{a*}**

ABSTRACT. Heteroleptic diorganochalcogen compounds of type R[2-(Me₂NCH₂)C₆H₄]E [R = (phtz)CH₂, E = Se (**1**), S (**2**); R = (4-Cl-phtz)CH₂, E = S (**3**); R = (pz)CH₂CH₂, E = Se (**4**)] were prepared by reacting 2-(Me₂NCH₂)C₆H₄ELi with the appropriate organic halide in a 1:1 molar ratio. The new compounds were investigated in solution by ¹H, ¹³C and ⁷⁷Se NMR where appropriate. For compounds **1** and **4** the crystal and molecular structures were determined by single-crystal X-ray diffraction.

Keywords: *Diorganoselenium compounds, hypercoordination, structure elucidation*

INTRODUCTION

The organoselenium compounds bearing organic groups with possibilities of O→Se or N→Se intramolecular coordination attracted a considerable increased interest during last years due to their improved hydrolytic and thermal stability [1-3]. They are well-known active species in different organic transformations, *i.e.* selective hydrogenation, methoxyseleenylation or selenocyclization [4-7], or as enzyme models and chemotherapeutic reagents [8-10]. A special interest attracted their use as neutral or anionic ligands towards main group or *d* metals, such metal complexes being valuable candidates as single-source precursors for metal selenides [11].

^a *Universitatea Babeș-Bolyai, Facultatea de Chimie și Inginerie Chimică, Str. M. Kogălniceanu, Nr. 1, RO-400084 Cluj-Napoca, Romania*

^b *Facultatea de Farmacie, Universitatea de Medicina și Farmacie Iuliu Hațieganu, RO-400012, Cluj-Napoca, Romania*

* *Corresponding author: ancas@chem.ubbcluj.ro*

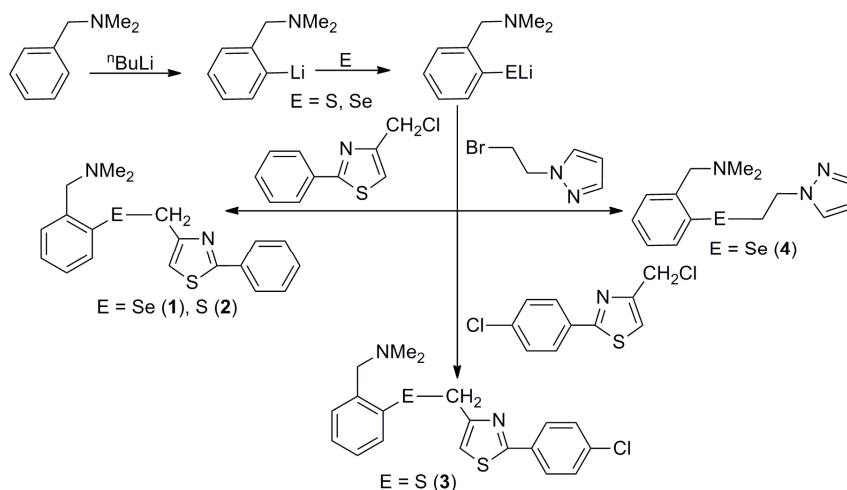
On the other hand, pyrazole or thiazole based compounds proved to have a significant importance in medicinal chemistry, as anti-inflammatory, antibacterial or antitumor agents [12-16].

During last years our studies were focused on organoselenium compounds of type Ar_2Se_2 , ArSeX ($\text{X} = \text{Cl}, \text{Br}, \text{I}$) or ArSeL ($\text{L} =$ organophosphorus ligand) bearing organic groups (Ar) with one or two pendant arms, *i.e.* $2\text{-(R}_2\text{NCH}_2\text{)C}_6\text{H}_4$ and $2,6\text{-(R}_2\text{NCH}_2\text{)}_2\text{C}_6\text{H}_3$ ($\text{R} = \text{Me}, \text{Et}, \text{Pr}^i$, $\text{R}_2 = (\text{CH}_2\text{CH}_2)_2\text{O}, (\text{CH}_2\text{CH}_2)_2\text{NMe}$ [17-20], as well as their metal complexes [21,22]. Recently we reported about the compounds $[2\text{-(R}_2\text{NCH}_2\text{)C}_6\text{H}_4][(\text{3,5-dmpz})\text{CH}_2\text{CH}_2]\text{Se}$, [$\text{R} = \text{Me}, \text{Et}$, $\text{dmpz} =$ dimethylpyrazole] and their behavior towards gold, silver and palladium [23]. As a continuation of our studies we report here about the synthesis and structural characterization of the new diorganoselenium compounds $[2\text{-(Me}_2\text{NCH}_2\text{)C}_6\text{H}_4][(\text{pz})\text{CH}_2\text{CH}_2]\text{Se}$ ($\text{pz} =$ pyrazole) and $[2\text{-(Me}_2\text{NCH}_2\text{)C}_6\text{H}_4][(\text{phtz})\text{CH}_2]\text{Se}$ ($\text{phtz} =$ phenylthiazole), as well as the related sulfur containing compounds $[2\text{-(Me}_2\text{NCH}_2\text{)C}_6\text{H}_4][(\text{phtz})\text{CH}_2]\text{S}$ and $[2\text{-(Me}_2\text{NCH}_2\text{)C}_6\text{H}_4][(\text{4-Cl-phtz})\text{CH}_2]\text{S}$.

RESULTS AND DISCUSSION

Synthesis and spectroscopy

Several diorganochalcogen compounds containing the $2\text{-(Me}_2\text{NCH}_2\text{)C}_6\text{H}_4$ group with potential for $\text{N} \rightarrow \text{E}$ intramolecular interactions were prepared by reacting the lithiated derivative $\text{LiEC}_6\text{H}_4\text{CH}_2\text{NMe}_2$ ($\text{E} = \text{S}, \text{Se}$) with the appropriate organic halide in a 1:1 molar ratio, as depicted in Scheme 1.



Scheme 1

The new compounds were isolated as solid species, soluble in common organic solvents. They were characterized by solution multinuclear NMR (¹H, ¹³C and ⁷⁷Se where appropriate).

The ¹H and ¹³C NMR spectra show the expected resonances for the organic groups. The resonances corresponding to the aromatic protons in all compounds appear as multiplets, due to the proton – proton couplings. The protons in the CH₂ and the NMe₂ groups in the pendant arm of the 2-(Me₂NCH₂)C₆H₄ ligands appear as singlet, thus giving no information about a possible N→E interaction in solution.

The ⁷⁷Se NMR spectra of compounds **1** and **4** present singlet resonances at δ values of 315.28 and 241.1 ppm, respectively.

Single-crystal X-ray diffraction studies

For compounds **1** and **4** the molecular structures were determined by single-crystal X-ray diffraction. The two compounds have similar molecular structures. The Ortep-like diagrams with the atom numbering schemes for compounds **1** and **4** are given in Figures 1 and 2, respectively, while important interatomic distances and angles are given in Table 1.

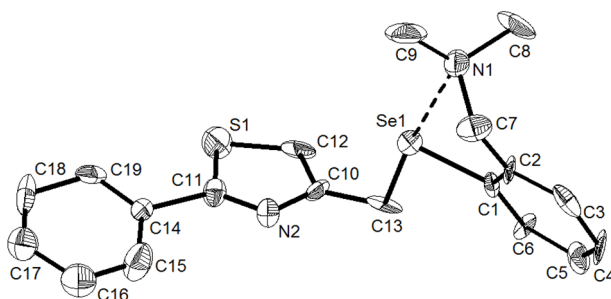


Figure 1. Ortep-like diagram with 30% probability ellipsoids of *R*_{N1}-**1**. Hydrogen atoms are omitted for clarity.

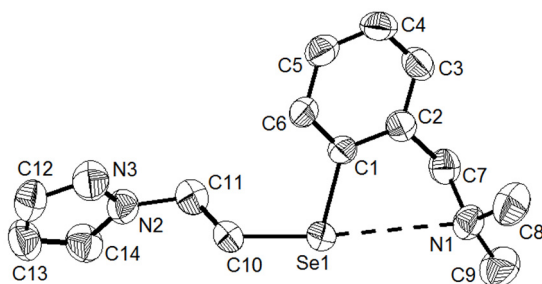


Figure 2. Ortep-like diagram with 50% probability ellipsoids of *R*_{N1}-**4**. Hydrogen atoms are omitted for clarity.

In both compounds a T-shaped coordination geometry is realized around selenium. The 2-(Me₂NCH₂)C₆H₄ group acts as a C,N chelating ligand, while the thiazole group in **1** and the pyrazole group in **4** are not involved in any interaction with selenium.

Table 1. Important interatomic distances (Å) and angles (deg.) in **1** and **4**

1		4	
C1–Se1	1.926(3)	C1–Se1	1.923(3)
C13–Se1	1.983(3)	C10–Se1	1.957(4)
N1–Se1	2.836(3)	N1–Se1	3.093(3)
C1–Se1–C13	99.59(14)	C1–Se1–C10	101.7(2)
N1–Se1–C13	173.15(12)	N1–Se1–C10	172.99(1)
N1–Se1–C1	73.75(11)	C1–Se1–N1	72.05(9)

The N→Se intramolecular interaction is longer in compound **4** than in **1**, but much shorter than the sum of the van der Waals radii of the two elements ($\Sigma r_{vdW}(N,Se)$ 3.54 Å [24]). The five-membered SeC₃N rings are not planar, but folded along the imaginary axes Se1⋯C7. Moreover, the N→Se intramolecular interaction induces planar chirality and, as a consequence, the respective compounds crystallize as 1:1 mixtures of *R* and *S* isomers.

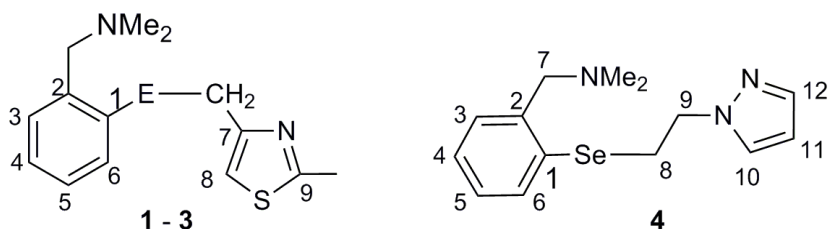
CONCLUSIONS

Our studies revealed a C,N bidentate behavior of the 2-(Me₂NCH₂)C₆H₄ group in compounds **1** and **4** in solid state. The room temperature NMR spectra suggest either the absence of the N→E (E = S, Se) intramolecular interaction in solution, or a dynamic behavior involving de-coordination, inversion at nitrogen and re-coordination to chalcogen, too fast to be observed at the NMR time scale.

EXPERIMENTAL SECTION

Starting materials, *i.e.* 2-(Me₂NCH₂)C₆H₄ELi [25], pzCH₂CH₂Br [26], (phtz)CH₂Cl and (4-Cl-phtz)CH₂Cl [27] were prepared according to literature procedures. ⁿBuLi and other starting chemicals were commercially available. All manipulations involving air sensitive compounds were carried out under argon, using Schlenk techniques. Solvents were dried and distilled prior to use. Elemental analyses were performed on a Flash EA 1112 machine. Melting points have been determined with an ELECTROTHERMAL 9200 apparatus and they are not corrected. Multinuclear NMR spectra (¹H, ¹³C and ⁷⁷Se) were

recorded on a BRUKER 400 instrument operating at 400.1, 100.6 and 76.3 MHz, respectively, using CDCl₃ solutions. The chemical shifts are reported in δ units (ppm) relative to the residual peak of the deuterated solvent (ref. CHCl₃: ¹H 7.26, ¹³C 77.0 ppm) and Me₂Se, respectively. The ¹H and ¹³C chemical shifts were assigned based on 2D experiments (COSY, HSQC and HMBC) using standard BRUKER XWIN-NMR pulse sequences and they are given according to the numbering in Scheme 2. The NMR spectra were processed using the MestReC and MestReNova software [28].



Scheme 2.

Preparation of *N,N*-dimethyl-1-(2(((2-phenylthiazol-4-yl)methyl)selenyl)phenyl)metanamine (1)

Selenium powder (0.347 g, 4.4 mmol) was added to a solution of 2-Me₂NCH₂C₆H₄Li (0.62 g, 4.4 mmol) in THF (30 mL) at room temperature and stirring was continued for 2 hours. To the as obtained lithium organoselenolate a solution of 4-(chloromethyl)-2-phenylthiazol (0.92 g, 4.4 mmol) in THF (20 ml) was added dropwise and the reaction mixture was stirred over night. Then the solvent was removed under reduced pressure and the remained solid was treated with toluene. The precipitated LiCl was filtered off and toluene was removed under reduced pressure, when the title compound resulted as a colourless powder. Yield 1.3 g (76%) M.p. 91°C. Anal. Calc. for C₁₉H₂₀N₂SSe (M = 387.40) C 58.91, H 5.20, N 7.23%. Found: C 58.83, H 5.22, N 7.31%. ¹H NMR: δ 2.21 (s, 6H, NCH₃); 3.46 (s, 2H, NCH₂); 4.26 (s, 2H, SeCH₂); 6.98 (s, 1H, H₈); 7.18 – 7.27 (m, 3H, C₆H₄); 7.43 (m, 3H, C₆H₅-meta+para); 7.62 (m, 1H, C₆H₄); 7.89 – 7.97 (m, 2H, C₆H₅-ortho); ¹³C NMR: δ 26.05 (s, SeCH₂, ¹J_{SeC} 17.2 Hz), 44.77 (s, NCH₃), 64.47 (s, NCH₂), 115.06 (C₈), 126.16 (C₆H₄), 126.57 (C₆H₅-ortho), 127.77 (C₆H₄), 128.89 (C₆H₅-meta), 129.62 (C₆H₄), 129.96 (C₆H₅-para), 131.63 (C₆H₄), 133.66 (C₈), 134.00 (C₁), 140.41 (C₂), 154.88 (C₇), 167.88 (C₆H₅-ipso). ⁷⁷Se NMR: δ 315.28s

Preparation of *N,N*-dimethyl-1-(2-(((2-phenylthiazol-4-yl)methyl)thio)phenyl) metanamine (2)

Sulfur powder (0.138 g, 4.3 mmol) was added to a solution of 2-Me₂NCH₂C₆H₄Li (0.61 g, 4.3 mmol) in THF (30 mL) at room temperature and stirring was continued for 2 hours. To the as obtained lithium organothiolate a solution of 4(-chlorometyl)-2-phenylthiazol (0.90 g, 4.3 mmol) in THF (20 ml) was added dropwise and the reaction mixture was stirred over night. Then the solvent was removed under reduced pressure and the remained oil was treated with toluene. The precipitated LiCl was filtered off, and toluene was removed under reduced pressure, when the title compound resulted as an orange powder. Yield 1.34 g (92%) M.p. 95°C. Anal. Calc. for C₁₉H₂₀N₂S₂ (M = 340.51) C 67.02, H 5.92, N 8.23%. Found: C 67.22, H 6.07, N 8.34%. ¹H NMR: δ 2.26 (s, 6H, NCH₃); 3.51 (s, 2H, NCH₂); 4.31 (s, 2H, SCH₂); 7.01 (s, 1H, H₈); 7.11 – 7.22 (m, 2H, C₆H₄); 7.21 (d, 1H, C₆H₄, ³J_{HH} 7.3 Hz); 7.39 (d, 1H, C₆H₄, ³J_{HH} 7.5 Hz); 7.40 – 7.48 (m, 3H, C₆H₅-meta+para); 7.92 – 7.94 (m, 2H, C₆H₅-ortho); ¹³C NMR: δ 34.29 (SCH₂), 45.34 (NCH₃), 62.02 (NCH₂), 115.76 (C₈), 125.94 (C₆H₄), 126.56 (C₆H₅-ortho), 127.65 (C₆H₄), 128.94 (C₆H₅-meta), 129.29 (C₆H₄), 129.99 (C₆H₅-para), 130.06 (C₆H₄), 133.54 (C₈), 136.30 (C₁), 138.95 (C₂), 153.80 (C₇), 168.17 (C₆H₅-ipso).

Preparation of 1-(2-(((2-(4-chlorophenyl)thiazol-4-yl)methyl)thio)phenyl)-*N,N*-dimethylmethanamine (3)

To a solution of 2-Me₂NCH₂C₆H₄SLi (0.63 g, 3.6 mmol) in THF (30 mL) was added a solution of 4(-chlorometyl)-2-(4-chlorophenyl)thiazol (0.88 g, 3.6 mmol) in THF (20 ml). and the reaction mixture was stirred over night. Then the solvent was removed under reduced pressure and the remained orange oil was treated with toluene. The precipitated LiCl was filtered off, and toluene was removed under reduced pressure. The remained orange oil was treated with n-hexane, when the title compound precipitated as an orange powder. Yield 1.31 g (97%) M.p. 80°C. Anal. Calc. for C₁₉H₁₉ClN₂S₂ (M = 374.95) C 60.86, H 5.11, N 7.47%. Found: C 60.73, H 5.21, N 7.51%. ¹H NMR: δ 2.20 (s, 6H, NCH₃); 3.47 (s, 2H, NCH₂); 4.37 (s, 2H, SCH₂); 6.56 (s, 1H, H₈); 7.18 – 7.24 (m, 2H, C₆H₄); 7.31 – 7.35 (m, 2H, C₆H₄); 7.43 (d, 2H, C₆H₅-meta, ³J_{HH} 7.9 Hz); 8.12 (d, 2H, C₆H₅-ortho, ³J_{HH} 8.1 Hz); ¹³C NMR: δ 30.36 (SCH₂), 45.19 (NCH₃), 62.58 (NCH₂), 109.68 (C₈), 127.30 (C₆H₄), 127.93 (C₆H₄), 128.04 (4-ClC₆H₄-ortho), 128.90 (4-ClC₆H₄-meta), 129.75 (C₆H₄), 129.97 (C₆H₄), 130.56 (4-ClC₆H₄-para), 131.54 (C₈), 134.66 (C₁), 135.61 (C₂), 157.04 (C₇), 166.11 (4-ClC₆H₄-ipso).

Preparation of 1-(2-((2-(1H-pyrazol-1-yl)ethyl)selenyl)phenyl)-N,N-dimethyl-methanamine (4)

Selenium powder (0.68 g, 8.5 mmol) was added to a solution of 2-Me₂NCH₂C₆H₄Li (1.20 g, 8.5 mmol) in THF (25 mL) and the reaction mixture was stirred under argon for 3 hours. Then a solution of 1-(2-bromoethyl)pyrazol (1.49 g, 8.5 mmol) in THF (10 mL) was added dropwise and the reaction mixture was stirred over night. Then the solvent was removed under reduced pressure and the remained solid was treated with toluene. The precipitated LiCl was filtered off, and toluene was removed under reduced pressure. The remained solid was washed with n-hexane and the title compound resulted as a yellow solid. Yield: 2.38 g (91%) M.p. 45°C. Anal. Calc. for C₁₄H₁₉N₃Se (M = 308.28) C 54.54, H 6.21, N 13.63%. Found: C 54.22, H 6.51, N 13.78%. ¹H NMR: δ 2.23 (s, 6H, NCH₃), 3.31 (t, 2H, H₈, ³J_{HH} 7.33 Hz), 3.48 (s, 2H, H₇), 4.40 (t, 2H, H₉, ³J_{HH} 7.44 Hz), 6.24 (s, 1H, H₁₁), 7.21 (m, 2H, C₆H₄), 7.28 (d, 1H, C₆H₄, ³J_{HH} 7.14 Hz), 7.38 (s, 1H, H₁₂), 7.48 (d, 1H, C₆H₄, ³J_{HH} 7.27 Hz), 7.55 (s, 1H, H₁₀). ¹³C NMR: δ 26.04 (C₅), 44.86 (NCH₃), 52.15 (C₇), 64.66 (C₄), 105.47 (C₁₁), 126.31 (C₆H₄), 128.12 (C₆H₄), 129.32 (C₆H₄), 130.11 (C₁₀), 130.81 (C₁₂), 132.31 (C₆H₄), 139.79 (C₆H₄), 140.63 (C₆H₄). ⁷⁷Se NMR: δ 241.1s, broad.

X-ray Crystallographic Studies

X-ray quality crystals of compounds **1** and **4** resulted by slow diffusion from a mixture of CDCl₃ and n-hexane (1/4, v/v). The crystals were attached with paraton/N oil to cryoloops. Data collection and processing were carried on a Bruker SMART APEX CCD system, using graphite-monochromated Mo K α radiation. Details of the crystal structure determination and refinement are given in Table 2.

Table 2. Crystallographic data for compounds **1** and **4**.

	1	4
Empirical formula	C ₁₉ H ₂₀ N ₂ SSe	C ₁₄ H ₁₉ N ₃ Se
Formula weight	387.39	308.28
Temperature, K	297(2)	297(2)
Wavelength, Å	0.71073	0.71073
Crystal system	Triclinic	monoclinic
Space group	P -1	P2(1)/n
Crystal size, mm	0.40 x 0.33 x 0.30	0.40 x 0.32 x 0.28
Unit cell dimensions		
a, Å	6.101(4)	11.797(3)
b, Å	11.062(7)	5.3923(15)
c, Å	14.045(8)	23.848(7)

	1	4
α , °	79.694(10)	90.00
β , °	86.408(9)	103.299(5)
γ , °	81.020(9)	90.00
V , Å ³	920.6(9)	1476.4(7)
Z , Calculated density	2, 1.397 mg/m ³	4, 1.387 mg/m ³
$F(000)$	396	632
Refinement method	Full-matrix least-squares on F^2	
Θ Range for data collection, deg.	1.475 to 24.999	1.75 to 25.00
Reflections collected	8572	13300
Independent reflections [R_{int}]	3202 $R(int) = 0.0447$	2599, $R(int) = 0.0432$
Data/restraints/parameters	3202 / 0 / 208	2599 / 0 / 165
Goodness-of-fit on F^2	1.022	1.056
Final R indices [$I > 2\sigma(I)$]	$R1 = 0.0407$, $wR2 = 0.0864$	$R1 = 0.0445$, $wR2 = 0.1061$
R indices (all data)	$R1 = 0.0531$, $wR2 = 0.0907$	$R1 = 0.0543$, $wR2 = 0.1102$
Largest diff. peak and hole, (e Å ⁻³)	0.502 and -0.303	0.846 and -0.560

The structure was refined with anisotropic thermal parameters. The hydrogen atoms were refined with a riding model and a mutual isotropic thermal parameter. The software package SHELX-97 was used for structure solving and refinement [29]. The drawings were created with the DIAMOND program [30].

ACKNOWLEDGMENTS

Financial support from the Ministry of Education and Research of Romania (Research Project No. PN-II-ID-PCE-2011-3-0659) is greatly appreciated. Roxana Popa is grateful for financial support from the Babes-Bolyai University in form of a grant offered by the College for Advanced Performance Studies.

SUPPLEMENTARY DATA

CCDC 1477916 and 1477915 contain the supplementary crystallographic data for **1** and **4**, respectively. These data can be obtained free of charge via <http://www.ccdc.cam.ac.uk/conts/retrieving.html>, or from the Cambridge Crystallographic Data Centre, 12 Union Road, Cambridge CB2 1EZ, UK; fax: +44 1223 336 033; or e-mail: deposit@ccdc.cam.ac.uk.

REFERENCES

1. G. Mugesh and H.B. Singh, *Chem. Soc. Rev.*, **2000**, 29, 347.
2. T. Wirth (Ed.), *Organoselenium Chemistry: Modern Developments in Organic Synthesis, Topics in Current Chemistry*, vol. 208, Springer, Berlin, **2000**.
3. T. Chivers, *A Guide to Chalcogen-Nitrogen Chemistry*, World Scientific Publishing, Singapore, **2005**.
4. A.J. Mukherjee, S.S. Zade, H.B. Singh, R.B. Sunoj, *Chem. Rev.*, **2010**, 110, 4357.
5. M. Iwaoka, S. Tomoda, *J. Chem. Soc., Chem. Commun.*, **1992**, 1165.
6. L. Uehlin, G. Fragale, T. Wirth, *Chem. Eur. J.*, **2002**, 8, 1125.
7. T. Schewe, *Gen. Pharmacol.*, **1995**, 26, 1153.
8. B.K. Sarma, G. Mugesh, *Chem. Eur. J.*, **2008**, 14, 10603.
9. K.P. Bhabak, G. Mugesh, *Chem. Asian J.*, **2009**, 4, 974.
10. K.P. Bhabak, G. Mugesh, *Chem. Eur. J.*, **2007**, 13, 4594.
11. B. Krebs, G. Henkel, *Chem. Rev.*, **2004**, 104, 801.
12. T.M. Potewar, S. A. Ingale, K. V. Srinivasan, *Tetrahedron*, **2007**, 63, 11066.
13. K.J. Wilson, C.R. Illig, N. Subasinghe, J.B. Hoffman, M.J. Rudolph, R. Soll, C. Molloy, R. Bone, D. Green, T. Randall, M. Zhang, F.A. Lewandowski, Z. Zhou, C. Sharp, D. Maguire, B. Grasberger, R.L. Desjarlais, O.J. Spurlino, *Bioorg. Med. Chem. Lett.*, **2001**, 11, 915.
14. O. Oniga, C. Moldovan, S. Oniga, B.G. Tipericiu, A. Pirnau, P. Verite, O. Crisan, I. Ionut, *Farmacia*, **2010**, 58, 825.
15. M.J. Graneto, R.G. Kurumbail, M.L. Vazquez, Huey-Sheng Shieh, J.L. Pawlitz, J.M. Williams, W.C. Stallings, L. Geng, A.S. Naraian, F.J. Koszyk, M.A. Stealey, X.D. Xu, R.M. Weier, G.J. Hanson, R.J. Mourey, R.P. Compton, S.J. Mnich, G.D. Anderson, J.B. Monahan, R. Devraj, *J. Med. Chem.*, **2007**, 50, 5712.
16. P.E. Almeida da Silva, D.F. Ramosa, H.G. Bonacorso, A.I. de la Iglesia, M.R. Oliveira, T. Coelho, J. Navarini, H.R. Morbidoni, N. Zanatta, M.A.P. Martins, *Int. J. Antimicrob. Agents*, **2008**, 32, 139.
17. A. Pöllnitz, V. Lippolis, M. Arca, A. Silvestru, *J. Organomet. Chem.*, **2011**, 696, 2837.
18. A. Pop, A. Silvestru, E.J. Juárez-Pérez, M. Arca, V. Lippolis, C. Silvestru, *Dalton Trans.*, **2014**, 43 (5), 2221
19. E. Duhamel, A. Pöllnitz, A. Stegarescu, A. Silvestru, *Z. Anorg. Allg. Chem.* **2011**, 637, 1355
20. M. Kulcsar, A. Beleaga, C. Silvestru, A. Nicolescu, C. Deleanu, C. Todasca, A. Silvestru, *Dalton Trans.*, **2007**, 2187.
21. A. Pop, L. Wang, V. Dorcet, T. Roisnel, J.-F. Carpentier, A. Silvestru, Y. Sarazin, *Dalton Trans.*, **2014**, 43, 16459.
22. A. Pöllnitz, A. Rotar, A. Silvestru, C. Silvestru, M. Kulcsar, *J. Organomet. Chem.*, **2010**, 695, 2486.
23. A. Pop, D. Rosca, R. Mitea, A. Silvestru, *Inorg. Chim. Acta*, **2013**, 405, 235.

24. J. Emsley, *Die Elemente*, Walter de Gruyter, Berlin, **1994**.
25. A. Meller, H. Hoppe, W. Meringele, A. Haase, M. Noltemeyer, *Organometallics*, **1998**, *17*, 123.
26. L.D. Field, B.A. Messerle, K.Q. Vuong, P. Turner, T. Failes, *Organometallics*, **2007**, *26*, 2058.
27. M. Palage, D. Matinca, M. Horn, I. Simiti., *Studia, Univ. Babes-Bolyai, Chemia*, **1997**, *XLII (1-2)*, 51-59.
28. MestReC and MestReNova, Mestrelab Research S.L., A Coruña 15706, Santiago de Compostela.
29. G.M. Sheldrick, *Acta Crystallogr. Sect. A*, **2008**, *64*, 112.
30. DIAMOND – Visual Crystal Structure Information System, CRYSTAL IMPACT, Postfach 1251, 53002 Bonn, Germany, **2001**.

*Dedicated to Professor Luminița Silaghi-Dumitrescu
on the occasion of her 65th anniversary*

THE QUEST FOR BRIDGING TRIFLUOROPHOSPHINE LIGANDS IN TRANSITION METAL COMPLEXES

ROBERT BRUCE KING^{1*}

ABSTRACT. Trifluorophosphine is a strong back-bonding ligand like the ubiquitous carbonyl ligand. In fact mononuclear zerovalent trifluorophosphine complexes such as $M(\text{PF}_3)_6$ ($M = \text{Cr}, \text{Mo}, \text{W}$), $M(\text{PF}_3)_5$ ($M = \text{Fe}, \text{Ru}$), and $M(\text{PF}_3)_4$ ($M = \text{Ni}, \text{Pt}$) are even more stable than their well-known carbonyl analogues. However, metal complexes with bridging trifluorophosphine ligands are virtually unknown. We review theoretical studies on the $\text{Co}_2(\text{PF}_3)_8$, $\text{Fe}_2(\text{PF}_3)_9$, and $\text{Cp}_2\text{Fe}_2(\text{PF}_3)_n$ ($\text{Cp} = \eta^5\text{-C}_5\text{H}_5$; $n = 4, 3$) systems analogous to the well-known metal carbonyls $\text{Co}_2(\text{CO})_8(\mu\text{-CO})_2$, $\text{Fe}_2(\text{CO})_9(\mu\text{-CO})_3$, $\text{Cp}_2\text{Fe}_2(\text{CO})_2(\mu\text{-CO})_2$, and $\text{Cp}_2\text{Fe}_2(\mu\text{-CO})_3$ containing two or three bridging CO groups. In most cases structures having features other than bridging PF_3 groups are energetically preferred.

Keywords: *Trifluorophosphine, iron, cobalt, density functional theory*

INTRODUCTION

The use of carbon monoxide as a ligand to stabilize low transition metal oxidation states dates back to the discovery of nickel tetracarbonyl in 1890 as a volatile liquid containing formally zerovalent nickel [1]. Other transition metals were subsequently found to form similar zerovalent binary metal carbonyls as exemplified by $\text{Cr}(\text{CO})_6$, $\text{Mn}_2(\text{CO})_{10}$, $\text{Fe}(\text{CO})_5$, and $\text{Co}_2(\text{CO})_8$. A key to the stabilization of formally zerovalent transition metal derivatives is the removal of electron density from the metal atom by $d\pi \rightarrow \pi\pi^*$ back-donation from filled metal d orbitals into empty CO π^* antibonding orbitals.

¹ *Department of Chemistry, University of Georgia, Athens, Georgia 30602, USA.*

* *Corresponding author: rbking@chem.uga.edu*

The unusual properties of the CO ligand in stabilizing low oxidation states stimulated the search for other ligands with similar properties. In this connection Wilkinson and Irvine [2] in 1951 discovered the binary zerovalent nickel trifluorophosphine complex $\text{Ni}(\text{PF}_3)_4$, as a volatile liquid considerably more stable than $\text{Ni}(\text{CO})_4$. Subsequent work led to the extensive development of metal trifluorophosphine chemistry, particularly in the laboratories of Kruck et al. Thus reactions of phosphorus trifluoride under pressure with various transition metal derivatives led to a variety of metal very stable trifluorophosphine complexes [3, 4, 5, 6, 7, 8, 9, 10, 11, 12]. The strong back-bonding of the trifluorophosphine ligand in metal trifluorophosphine complexes can be related to the the electron withdrawing properties of its three highly electronegative fluorine atoms [13, 14, 15, 16, 17, 18, 19, 20, 21, 22]. Thus PF_3 ligands, like CO ligands, stabilize low formal oxidation states so that zerovalent metal derivatives, such as $\text{Cr}(\text{PF}_3)_6$, $\text{Fe}(\text{PF}_3)_5$, and $\text{Ni}(\text{PF}_3)_4$, are essentially stable towards air oxidation. In addition, their volatility is comparable to the analogous metal carbonyls despite their considerably higher molecular weights. In addition several binary zerovalent metal trifluorophosphine complexes without currently known stable homoleptic metal carbonyl counterparts are known including $\text{M}_2(\text{PF}_3)_8$ ($\text{M} = \text{Rh}, \text{Ir}$) [23], $\text{Pt}(\text{PF}_3)_4$ [24, 25, 26] and $\text{Pt}_4(\text{PF}_3)_8$ [27]. This suggests that PF_3 is even better than CO in stabilizing low transition metal oxidation states. In addition to the strong back-donation of PF_3 ligands, the greater steric protection of the central metal atom by multiple PF_3 ligands relative to that by multiple CO ligands may enhance the stability of some zerovalent metal trifluorophosphine complexes.

These observations on the higher stability of metal trifluorophosphine complexes relative to corresponding metal carbonyls suggested originally that metal trifluorophosphine chemistry might evolve into a more extensive area of inorganic chemistry than even metal carbonyl chemistry. However, as metal trifluorophosphine chemistry continued to develop, metal trifluorophosphine complexes with bridging PF_3 groups analogous to well-known metal carbonyls with bridging carbonyl groups (Figure 1) such as $\text{Co}_2(\text{CO})_8$ { = $\text{Co}_2(\text{CO})_6(\mu\text{-CO})_2$ } [28, 29, 30, 31] and $\text{Fe}_2(\text{CO})_9$ { = $\text{Fe}_2(\text{CO})_6(\mu\text{-CO})_3$ } [32, 33] remained unknown even though metal trifluorophosphine complexes with terminal PF_3 groups are generally more stable than their carbonyl counterparts.

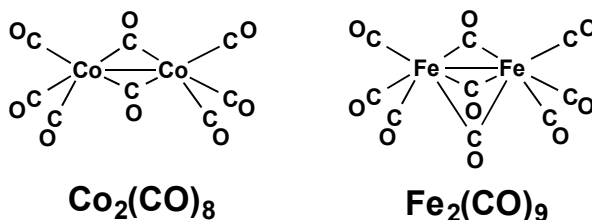


Figure 1. The bridged structures of $\text{Co}_2(\text{CO})_8$ and $\text{Fe}_2(\text{CO})_9$.

The cyclopentadienyliron carbonyl $\text{Cp}_2\text{Fe}_2(\text{CO})_4$ is another example of a common metal carbonyl derivative containing two bridging CO groups. In fact, *cis* and *trans* isomers of $\text{Cp}_2\text{Fe}_2(\text{CO})_2(\mu\text{-CO})_2$ can be isolated separately and structurally characterized by X-ray crystallography (Figure 2) [34, 35, 36]. The doubly bridged Fe–Fe bonding distances in these structures are ~ 2.54 Å corresponding to formal single bonds. Again the analogous $\text{Cp}_2\text{Fe}_2(\text{PF}_3)_2(\mu\text{-PF}_3)_2$ with two bridging PF_3 groups remains unknown even though related CpFe species with terminal PF_3 groups such as $\text{CpFe}(\text{PF}_3)_2\text{H}$ have been synthesized [37]. Another stable binuclear cyclopentadienyliron carbonyl is the triply bridged $\text{Cp}_2\text{Fe}_2(\mu\text{-CO})_3$, which can be synthesized by photolysis of $\text{Cp}_2\text{Fe}_2(\text{CO})_2(\mu\text{-CO})_2$ at low temperatures. This species is of interest in being a stable organometallic triplet state molecule [38, 39, 40, 41]. Thus, the Fe=Fe formal double bond of length 2.265 Å in $\text{Cp}_2\text{Fe}_2(\mu\text{-CO})_3$ has two orthogonal single-electron orthogonal π “half-bond” components analogous to the O=O double bond in ordinary dioxygen thereby accounting for the triplet spin state of this molecule. An analogous $\text{Cp}_2\text{Fe}_2(\text{PF}_3)_3$ has not been synthesized.

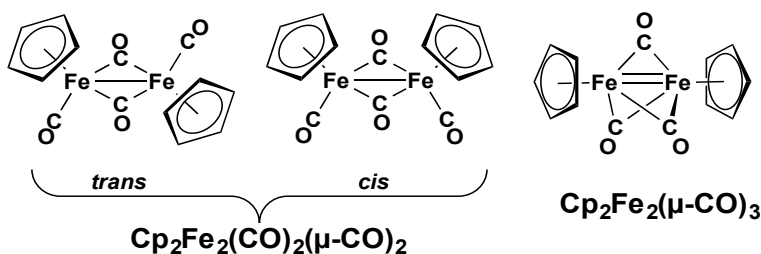


Figure 2. The *trans* and *cis* isomers of the doubly bridged $\text{Cp}_2\text{Fe}_2(\text{CO})_2(\mu\text{-CO})_2$ [$= \text{Cp}_2\text{Fe}_2(\text{CO})_4$] and the triply bridged $\text{Cp}_2\text{Fe}_2(\mu\text{-CO})_3$ structure.

In order to gain some insight into the reasons for the lack of binuclear transition metal complexes having bridging PF_3 groups, we undertook a density functional theory study of trifluorophosphine analogues of binuclear metal carbonyls with bridging CO groups. We review here the highlights of our studies on the $\text{Co}_2(\text{PF}_3)_8$ [42], $\text{Fe}_2(\text{PF}_3)_9$ [43], and $\text{Cp}_2\text{Fe}_2(\text{PF}_3)_n$ ($n = 4, 3$) [44] systems analogous to $\text{Co}_2(\text{CO})_8$, $\text{Fe}_2(\text{CO})_9$, and $\text{Cp}_2\text{Fe}_2(\text{CO})_n$, respectively. Further details are provided in the individual cited articles.

RESULTS AND DISCUSSION

Optimization of $\text{Co}_2(\text{PF}_3)_8$ led only to the unbridged structure having a predicted Co–Co distance of ~ 2.77 Å (Figure 3). This Co–Co distance is somewhat longer than the experimental Co–Co distance of ~ 2.70 Å in an

analogous unbridged $(\text{OC})_4\text{Co}-\text{Co}(\text{CO})_4$ isomer stabilized in a C_{60} matrix [45]. The lengthening of the unbridged $\text{Co}-\text{Co}$ bond upon substituting all of the CO groups with PF_3 groups may be a consequence of the greater steric bulk of PF_3 , thereby forcing the cobalt atoms to remain at a longer distance from each other. The doubly bridged $\text{Co}_2(\text{CO})_6(\mu\text{-CO})_2$ isomer has a shorter $\text{Co}-\text{Co}$ distance of ~ 2.53 Å owing to a bond-shortening effect of the two bridging CO groups [46, 47, 48]. The bridged $\text{Co}_2(\text{CO})_6(\mu\text{-CO})_2$ and unbridged $\text{Co}_2(\text{CO})_8$ isomers are shown to be in equilibrium in solution [49, 50, 51, 52, 53] and are calculated by density functional theory to have similar energies.

A bridging PF_3 group is a feature of the only $\text{Co}_2(\text{PF}_3)_9$ structure found in the density functional theory study (Figure 3). This structure may be regarded as a substitution product of PF_5 in which the two axial fluorine atoms have been replaced by $-\text{Co}(\text{PF}_3)_4$ units, i. e., one-half of the optimized $\text{Co}_2(\text{PF}_3)_8$ structure. However, $\text{Co}_2(\text{PF}_3)_9$ appears to be disfavored thermochemically with respect to exothermic PF_3 loss by ~ 10 kcal/mol to give $\text{Co}_2(\text{PF}_3)_8$. Thus $\text{Co}_2(\text{PF}_3)_9$ is not likely to be a viable species. A high-energy $\text{Co}_2(\text{PF}_3)_7$ structure is also found with a bridging PF_3 group between two $\text{Co}(\text{PF}_3)_3$ units without a $\text{Co}-\text{Co}$ bond. However, this $\text{Co}_2(\text{PF}_3)_6(\mu\text{-PF}_3)$ structure lies ~ 60 kcal/mol in energy above the lowest energy $\text{Co}_2(\text{PF}_3)_7$ structure and thus does not appear to be a viable species.

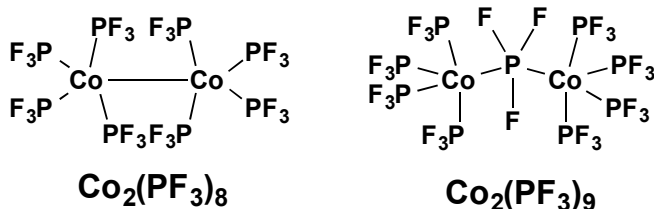


Figure 3. Structures of $\text{Co}_2(\text{PF}_3)_n$ ($n = 8, 9$).

The experimental $\text{Fe}_2(\text{CO})_9$ structure is the triply bridged isomer $\text{Fe}_2(\text{CO})_6(\mu\text{-CO})_3$ [54, 55]. However, a singly bridged $\text{Fe}_2(\text{CO})_8(\mu\text{-CO})$ isomer is of comparable energy. An analogous singly bridged $\text{Os}_2(\text{CO})_8(\mu\text{-CO})$ structure is the experimental $\text{Os}_2(\text{CO})_9$ structure. The lowest energy $\text{Fe}_2(\text{PF}_3)_9$ structure by ~ 28 kcal/mol (Figure 4) is related to the lowest-energy $\text{Co}_2(\text{PF}_3)_9$ structure (Figure 3) by migration of a fluorine atom from the bridging phosphorus atom to an iron atom leaving a bridging PF_2 group rather than a bridging PF_3 group. Formation of the $\text{Fe}_2(\text{PF}_3)_8(\text{F})(\mu\text{-PF}_2)$ structure for $\text{Fe}_2(\text{PF}_3)_9$ can also be interpreted as insertion of an iron atom into a $\text{P}-\text{F}$ bond of an initially bridging PF_3 ligand. The driving force for the splitting of the neutral PF_3 ligand into the anionic PF_2 and F ligands can relate to the reducing power of zerovalent iron.

Similar bridging PF_2 groups are found in the binuclear derivatives $\text{M}_2(\text{PF}_3)_6(\mu\text{-PF}_2)_2$ ($\text{M} = \text{Fe}, \text{Co}$ [56]). These observations suggest that bridging PF_2 groups are more favorable than bridging PF_3 groups.

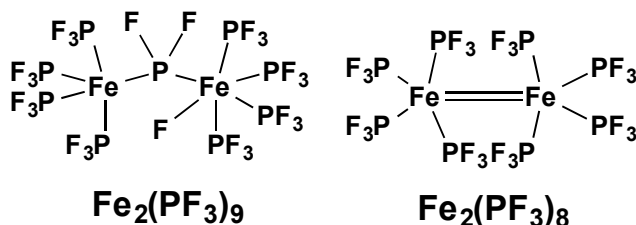


Figure 4. Lowest energy structures of $\text{Fe}_2(\text{PF}_3)_n$ ($n = 8, 9$)

The dissociation energy of $\text{Fe}_2(\text{PF}_3)_9$ to give $\text{Fe}_2(\text{PF}_3)_8 + \text{PF}_3$ is ~ 13 kcal/mol, which is significantly lower than CO dissociation from the stable binary metal carbonyls. Thus the experimental CO dissociation energies of $\text{Cr}(\text{CO})_6$, $\text{Fe}(\text{CO})_5$, and $\text{Ni}(\text{CO})_4$ are 37, 41, and 27 kcal/mol, respectively [57]. More significantly, dissociation of $\text{Fe}_2(\text{PF}_3)_9$ into the mononuclear fragments $\text{Fe}(\text{PF}_3)_5 + \text{Fe}(\text{PF}_3)_4$ is essentially thermoneutral within ~ 1 kcal/mol suggesting that $\text{Fe}_2(\text{PF}_3)_9$ is not a viable species. However, the dissociation of $\text{Fe}_2(\text{PF}_3)_8$ into two $\text{Fe}(\text{PF}_3)_4$ fragments is clearly endothermic at ~ 25 kcal/mol. The optimized $\text{Fe}_2(\text{PF}_3)_8$ structure consists of two $\text{Fe}(\text{PF}_3)_4$ units linked solely by an $\text{Fe}=\text{Fe}$ bond of length ~ 2.51 Å. This $\text{Fe}=\text{Fe}$ distance is ~ 0.26 Å shorter than the $\text{Co}-\text{Co}$ single bond in the likewise unbridged $\text{Co}_2(\text{PF}_3)_8$ structure (Figure 3). This supports the formulation of the $\text{Fe}=\text{Fe}$ bond in $\text{Fe}_2(\text{PF}_3)_8$ as the formal double bond needed to give each iron atom the favored 18-electron configuration. The carbonyl $\text{Fe}_2(\text{CO})_8$ analogous to $\text{Fe}_2(\text{PF}_3)_8$ has been detected spectroscopically in low-temperature matrices but is not viable not under normal conditions [58, 59, 60].

A density functional theory study on the $\text{Cp}_2\text{Fe}_2(\text{CO})_4$ system shows the *cis* and *trans* isomers of the doubly bridged $\text{Cp}_2\text{Fe}_2(\text{CO})_2(\mu\text{-CO})_2$ structure (Figure 2) to be the lowest energy structures consistent with the fact that both stereoisomers have been isolated and characterized structurally by X-ray crystallography. However, an unbridged $\text{Cp}_2\text{Fe}_2(\text{CO})_4$ isomer was also found lying ~ 6 kcal/mol in energy above the doubly bridged $\text{Cp}_2\text{Fe}_2(\text{CO})_2(\mu\text{-CO})_2$ isomers. The predicted $\text{Fe}-\text{Fe}$ distance of ~ 2.73 Å in the unbridged $\text{Cp}_2\text{Fe}_2(\text{CO})_4$ isomer is ~ 0.2 Å longer than that in the doubly bridged $\text{Cp}_2\text{Fe}_2(\text{CO})_2(\mu\text{-CO})_2$ isomer. A density functional theory study on the $\text{Cp}_2\text{Fe}_2(\text{PF}_3)_4$ system using methods similar to those used earlier for the $\text{Cp}_2\text{Fe}_2(\text{CO})_4$ system led to only unbridged *cis* and *trans* structures with no

evidence for any low-energy $\text{Cp}_2\text{Fe}_2(\text{PF}_3)_4$ structures with bridging PF_3 groups. The less sterically hindered *trans*- $\text{Cp}_2\text{Fe}_2(\text{PF}_3)_4$ structure was found to lie ~ 5 kcal/mol in energy below its *cis* stereoisomer. The predicted Fe–Fe distances of ~ 2.98 Å and ~ 3.01 Å for *trans*- and *cis*- $\text{Cp}_2\text{Fe}_2(\text{PF}_3)_4$, respectively, are nearly 0.3 Å longer than that for the unbridged $\text{Cp}_2\text{Fe}_2(\text{CO})_4$ isomer. This presumably is an effect of the greater bulk of the $\text{CpFe}(\text{PF}_3)_2$ halves of the $\text{Cp}_2\text{Fe}_2(\text{PF}_3)_4$ molecule as compared with the $\text{CpFe}(\text{CO})_2$ halves of the unbridged $\text{Cp}_2\text{Fe}_2(\text{CO})_4$ molecule.

A density functional theory study on the $\text{Cp}_2\text{Fe}_2(\text{PF}_3)_3$ system also showed the only structures within ~ 11 kcal/mol of the lowest energy structure to be unbridged triplet and quintet spin state structures with two terminal PF_3 groups on one iron atom and a third terminal PF_3 group on the other iron atom. This is in stark contrast to the experimentally known triply bridged $\text{Cp}_2\text{Fe}_2(\mu\text{-CO})_3$ structure of the carbonyl analogue. The Fe=Fe distances in these unbridged $\text{Cp}_2\text{Fe}_2(\text{PF}_3)_3$ structures range from ~ 2.44 Å for a quintet spin state structure to 2.7 to 2.8 Å for the triplet spin state structures. All of these Fe=Fe distances are significantly less than the ~ 3.0 Å Fe–Fe single bond distances in the unbridged $\text{Cp}_2\text{Fe}_2(\text{PF}_3)_4$ structures thereby suggesting formal double bonds of various types.

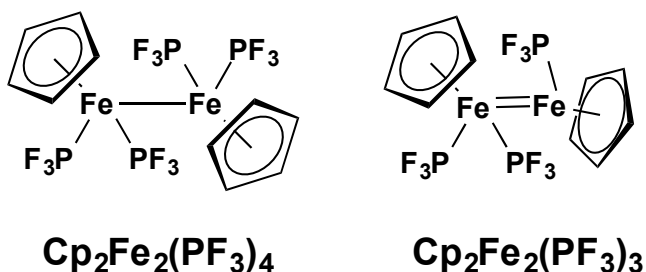


Figure 5. The lowest energy $\text{Cp}_2\text{Fe}_2(\text{PF}_3)_n$ ($n = 4, 3$) structures.

The pentacarbonyl $\text{Cp}_2\text{Fe}_2(\text{CO})_5$ is not known and presumed not to be viable. Application of the 18-electron rule and assuming the nearly universal terminal pentahapto coordination of the Cp ligands require the absence of an iron-iron bond in $\text{Cp}_2\text{Fe}_2(\text{CO})_5$. This means that a bridging CO group is the only way to hold the two iron atoms together in $\text{Cp}_2\text{Fe}_2(\text{CO})_5$. However, the trifluorophosphine analogue $\text{Cp}_2\text{Fe}_2(\text{PF}_3)_5$ appears to be viable since loss of PF_3 to give $\text{Cp}_2\text{Fe}_2(\text{PF}_3)_4$ is endothermic at ~ 23 kcal/mol. Furthermore, a $\text{Cp}_2\text{Fe}_2(\text{PF}_3)_4(\mu\text{-PF}_3)$ structure with a bridging PF_3 group lies within ~ 8 kcal/mol of the lowest energy $\text{Cp}_2\text{Fe}_2(\text{PF}_3)_5$ isomer (Figure 6). However, the lowest energy $\text{Cp}_2\text{Fe}_2(\text{PF}_3)_5$ structure has a bridging $\mu\text{-PF}_2$ group and a terminal PF_4 group, i. e., $\text{Cp}_2\text{Fe}_2(\text{PF}_3)_3(\text{PF}_4)(\mu\text{-PF}_2)$ in which a

fluorine atom has migrated from the bridging PF₃ group to a terminal PF₃ group. The predicted exothermicity of this process indicates that bridging PF₂ groups with four-coordinate phosphorus atoms are more favorable than bridging PF₃ groups with five-coordinate phosphorus atoms. The terminal PF₄ group bonded to the iron atom is related to phosphorus pentafluoride by replacing one of the P–F bonds with a P–Fe bond. It is a net donor of one electron to the iron atom so both iron atoms in the Cp₂Fe₂(PF₃)₃(PF₄)(μ-PF₂) structure have the favored 18-electron configuration.

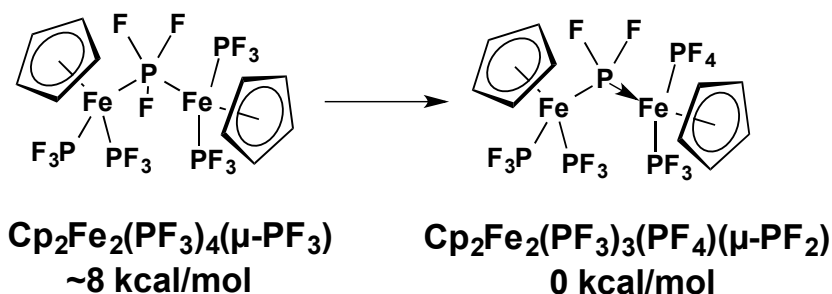


Figure 6. The exothermic conversion of Cp₂Fe₂(PF₃)₄(μ-PF₃) to Cp₂Fe₂(PF₃)₃(PF₄)(μ-PF₂) involving fluorine migration from a bridging PF₃ group to a terminal PF₃ group.

CONCLUSIONS

Density functional theory studies on the Co₂(PF₃)₈, Fe₂(PF₃)₉, and Cp₂Fe₂(PF₃)_{*n*} (Cp = η⁵-C₅H₅; *n* = 4, 3) systems confirm the experimentally observed reluctance for the strong back-bonding PF₃ ligand to form binuclear metal complexes containing bridging PF₃ groups despite the fact that their carbonyl analogues contain two or three CO groups bridging a central metal-metal bond. Thus for Co₂(PF₃)₈ and Cp₂Fe₂(PF₃)_{*n*} (*n* = 4, 3) all of the low-energy structures are unbridged structures with the two parts held together only by metal-metal bonds. The lowest energy Fe₂(PF₃)₉ structure by a substantial margin is of the type Fe₂(PF₃)₈(F)(μ-PF₂) where one of the iron atoms has inserted into a P–F bond of one of the PF₃ ligands.

Bridging PF₃ groups without a central metal-metal bond are found in low-energy structures of the ligand-rich species Co₂(PF₃)₉ and Cp₂Fe₂(PF₃)₅. However, Co₂(PF₃)₉ is not likely to be a viable species since loss of one PF₃ ligand to give Co₂(PF₃)₈ is an exothermic process by ~10 kcal/mol. Furthermore the PF₃-bridged Cp₂Fe₂(PF₃)₄(μ-PF₃) is disfavored relative to migration of fluorine from the bridging PF₃ group to a terminal PF₃ group to give Cp₂Fe₂(PF₃)₃(PF₄)(μ-PF₂).

The reluctance of PF_3 to bridge two metal atoms compared with CO can be related to the coordination number of the donor atom. Thus terminal and bridging CO groups have dicoordinate and tricoordinate carbon atoms, respectively (Figure 7). Similarly, terminal and bridging PF_3 groups have tetracoordinate and pentacoordinate phosphorus atoms, respectively. Thus the phosphorus atom in a bridging PF_3 group has energetically less favorable hypervalent coordination, necessarily involving high-energy d orbitals or multicenter three-center four-electron bonding. In fact, the $\text{Co}_2(\text{PF}_3)_8(\mu\text{-PF}_3)$ and $\text{Cp}_2\text{Fe}_2(\text{PF}_3)_4(\mu\text{-PF}_3)$ having bridging PF_3 groups without metal-metal bonds may be regarded as substitution products of phosphorus pentafluoride, PF_5 .

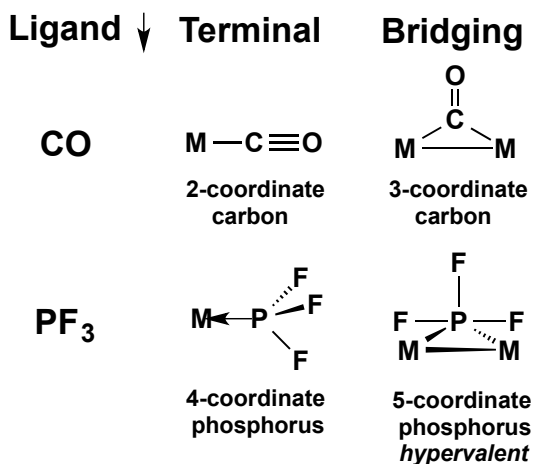


Figure 7. Comparison of terminal and bridging CO and PF_3 ligands showing the hypervalent nature of a bridging PF_3 group.

ACKNOWLEDGMENTS

I would like to dedicate this manuscript to Prof. Dr. Luminița Silaghi-Dumitrescu in recognition of her major contributions to Romanian chemistry as well as to many aspects of the research, teaching, and administration at Babeș-Bolyai University during her long career there. In addition her research activities in diverse areas of inorganic, organic, organometallic, and coordination chemistry have had considerable impact beyond the borders of Romania. On a more personal note, my wife (Jane) and I remember with pleasure both her visits to the University of Georgia (USA) as well as adventurous and interesting road trips with her in various parts of southeastern Europe previously unfamiliar to us. The latter include visits to Macedonia (Skopje and Lake Ohrid in 2011), Bulgaria (Sofia and Varna in 2013), and northern Greece (Delphi and Meteora in 2006).

REFERENCES

1. L. Mond, C. Langer, F. Quincke, *J. Chem. Soc.* **1890**, 57, 749.
2. J.W. Irvine, G. Wilkinson, *Science*, **1951**, 113, 742.
3. J.C. Green, D.I. King, J.H.D. Eland, *Chem. Comm.*, **1970**, 17, 1121.
4. I.H. Hillier, V.R. Saunders, M.J. Ware, P.J. Bassett, D.R. Lloyd, N. Lynaugh, *Chem. Comm.*, **1970**, 20, 1316.
5. P.J. Bassett, B.R. Higginson, D.R. Lloyd, N. Lynaugh, P.J. Roberts, *J. Chem. Soc. Dalton Trans.* **1974**, 21, 2316.
6. J. Müller, K. Fenderl, B. Mertschenk, *Chem. Ber.*, **1971**, 104, 700.
7. R.A. Head, J.F. Nixon, G.J. Sharp, R.J. Clark, *J. Chem. Soc. Dalton*, **1975**, 20, 2054.
8. J.F. Nixon, E.A. Seddon, R.J. Suffolk, M.J. Taylor, J.C. Green, R.J. Clark, *J. Chem. Soc. Dalton Trans.* **1986**, 4, 765.
9. J.-M. Savariault, A. Serafini, M. Pellissier, P. Cassoux, *Theor. Chim. Acta*, **1976**, 42, 155.
10. M. Braga, *Inorg. Chem.*, **1985**, 24, 2702.
11. M. Braga, *J. Mol Struct. Theochem*, **1992**, 253, 167.
12. G. Frenking, K. Wichmann, N. Fröhlich, J. Grobe, W. Golla, D. Le Van, B. Krebs, M. Läge, M. *Organometallics*, **2002**, 21, 2921.
13. J.C. Green, D.I. King, J.H.D. Eland, *Chem. Comm.* **1970**, 1121.
14. Hiller, I.H.; Saunders, V.R.; Ware, M.J.; Bassett, P.J.; Lloyd, D.R.; Lynaugh, N. *Chem. Comm.* **1970**, 1316.
15. Bassett, P.J.; Higginson, B.R.; Lloyd, D.R.; Lynaugh, N.; Roberts, P.J. *J. Chem. Soc. Dalton* **1974**, 2316.
16. Müller, J.; Fenderl, K.; Mertschenk, B. *Chem. Ber.* **1971**, 104, 700.
17. Head, R.A.; Nixon, J.F.; Sharp, G.J.; Clark, R. J. *J. Chem. Soc. Dalton* **1975**, 2054.
18. Nixon, J.F.; Seddon, E.A.; Suffolk, R.J.; Taylor, M.J.; Green, J.C.; Clark, R. J. *J. Chem. Soc. Dalton* **1986**, 765.
19. Savariault, J.-M.; Serafini, A.; Pellissier, M.; Cassoux, P. *Theor. Chim. Acta* **1976**, 42, 155.
20. Braga, M. *Inorg. Chem.* **1985**, 24, 2702.
21. Braga, M. *J. Mol Struct.* **1992**, 85, 167.
22. Frenking, G.; Wichmann, K.; Fröhlich, N.; Grobe, J.; Golla, W.; Le Van, D.; Krebs, B.; Läge, M. *Organometallics* **2002**, 21, 2921.
23. Bennett, M.A.; Johnson, R.N.; Turney, T.W. *Inorg. Chem.* **1976**, 15, 2938.
24. Kruck, T.; Baur, K. *Angew. Chem.* **1965**, 77, 505.
25. Kruck, T.; Baur, K.Z. *anorg. allgem. Chem.* **1969**, 364, 192.
26. Drews, T.; Rusch, D.; Seidel, S.; Willemsen, S.; Seppelt, K. *Chem. Eur. J.* **2008**, 14, 4280.
27. Hammill, C.L.; Clark, R.J.; Ross, C.W.; Marshall, A.G.; Schmutz, J. *Inorg. Chem.* **1997**, 26, 5973.
28. Sumner, G.G.; Klug, H.P.; Alexander, L.E. *Acta Cryst.* **1964**, 17, 732.
29. Leung, P.C.; Coppens, P. *Acta Cryst.* **1983**, B39, 535.

30. Braga, D.; Grepioni, F.; Sabatino, P.; Gavezzotti, A. *J. Chem. Soc. Dalton Trans.* **1992**, 1185.
31. Wei, C.H.; Dahl, L.F. *J. Am. Chem. Soc.*, **88**, 1821 (1966).
32. Powell, H.M.; Ewens, R.V.G. *J. Chem. Soc.* **1939**, 286.
33. Cotton, F.A.; Troup, J.M. *J. Chem. Soc. Dalton* **1974**, 800.
34. Mills, O. S. *Acta Cryst.* **1958**, *11*, 620.
35. Bryan, R.F.; Greene, P.T. *J. Chem. Soc. A* **1970**, 3068.
36. Mitschler, A.; Rees, B.; Lehmann, M.S. *J. Am. Chem. Soc.* **1978**, *100*, 3390.
37. Kruck, T., Knoll, L. *Chem. Ber.* **1972**, *105*, 3783.
38. Caspar, J.V.; Meyer, T.J. *J. Am. Chem. Soc.* **1980**, *102*, 7794.
39. Hooker, R.H.; Mahmoud, K.A.; Rest, A. *J. Chem. Commun.* **1983**, 1022.
40. Hepp, A.F.; Blaha, J.P.; Lewis, C.; Wrighton, M.S. *Organometallics* **1984**, *3*, 174.
41. Blaha, J.P.; Bursten, B.E.; Dewan, J.C.; Frankel, R.B.; Randolph, C.L.; Wilson, B.A.; Wrighton, M. S. *J. Am. Chem. Soc.* **1985**, *1076*, 4561.
42. Yang, H.-q.; Li, Q.-s.; Xie, Y.; King, R.B.; Schaefer, H.F. *Mol. Phys.* **2010**, *108*, 2477.
43. Zou, R.; Li, Q.-s.; Xie, Y.; King, R.B.; Schaefer, H.F. *Chem. Eur. J.* **2008**, *14*, 11149.
44. S. Gong, Q. Luo, Q.-s. Li, Y. Xie, R.B. King, H.F. Schaefer, *New J. Chem.*, **2015**, *39*, 3708.
45. T.Y. Garcia, J.C. Fettinger, M.M. Olmstead, A.L. Balch, *Chem. Comm.*, **2009** 7143.
46. G.G. Sumner, H.P. Klug, L.E. Alexander, *Acta Cryst.*, **1964**, *17* 732.
47. P.C. Leung, P. Coppens *Acta Cryst.*, B **1983**, *39*, 535.
48. D. Braga, F. Grepioni, P. Sabatino, A. Gavezzotti, *J. Chem. Soc. Dalton Trans.* **1992**, 1185.
49. K. Noack, *Spectrochim. Acta*, **1963**, *19*, 1925.
50. K. Noack, *Helv. Chim. Acta*, **1964**, *47*, 1064.
51. K. Noack, *Helv. Chim. Acta*, **1964**, *47*, 1554.
52. G. Bor, *Spectrochim. Acta*, **1963**, *14*, 1209.
53. G. Bor, *Spectrochim. Acta*, **1963**, *14*, 2065.
54. Powell, H.M.; Ewens, R.V.G. *J. Chem. Soc.* **1939**, 286.
55. Cotton, F.A.; Troup, J.M. *J. Chem. Soc. Dalton* **1974**, 800.
56. Kruck, T.; Lang, W. *Angew. Chem. Int. Ed.* **1967**, *6*, 454.
57. L.S. Sunderlin, D. Wang, and R.R. Squires, *J. Am. Chem. Soc.* **1993**, *115*, 12060.
58. Poliakoff, M.; Turner, J.J. *J. Chem. Soc. A*, **1971**, 2403.
59. Fletcher, S.C.; Poliakoff, M.; Turner J. J. *Inorg. Chem.* **1986**, *25*, 3597.
60. Fedrigo, S.; Haslett, T.L.; Moskovits, M. *J. Am. Chem. Soc.* **1996**, *118*, 5083.

*Dedicated to Professor Luminița Silaghi-Dumitrescu
on the occasion of her 65th anniversary*

RHODIUM(I) COMPLEXES OF BISPHOSPHONITOCARBABORANE(12)S: A COMPUTATIONAL STUDY

MENYHÁRT B. SÁROSI^{a*}, EVAMARIE HEY-HAWKINS^{a*}

ABSTRACT. Density functional calculations indicate that, the steric and packing factors seem to play a much more significant role than the electronic effects in influencing the bending of the rhodium(I) complexes of bisphosphonitocarbaborane(12)s.

Keywords: *Rhodium(I) Complexes, Bisphosphonitocarbaborane(12)s, Density Functional Theory, Natural Bond Orbital Analysis*

INTRODUCTION

The rhodium(I) complexes **1–5** (Scheme 1) with various bisphosphonitocarbaborane(12) ligands are chloro-bridged dimers in which the Rh₂Cl₂ four-membered ring is either in a butterfly conformation (**1–4**) or planar (**5**) [1]. Density functional calculations were carried out to elucidate which factors determine the conformational preferences in these complexes.

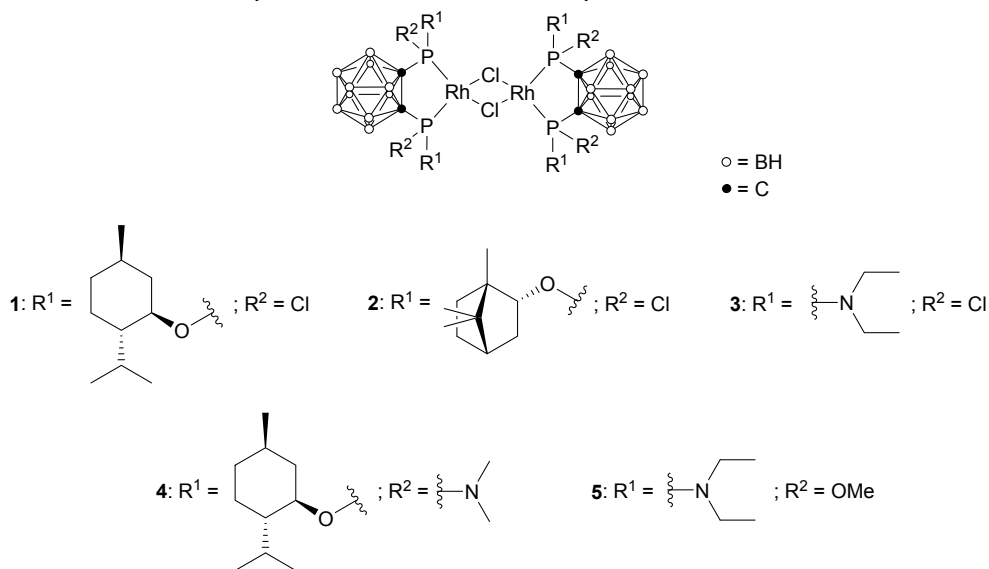
RESULTS AND DISCUSSION

Bis(phosphanes) are versatile ligands for late transition metals, which can be used in homogeneous catalysis. Due to the tunability of the steric and electronic properties, a range of different ligands has been employed over the last few decades. 1,2-Dicarbaborane(12) [*ortho*-carbaborane(12)] is

^a *Universität Leipzig, Institut für Anorganische Chemie, Johannisallee 29, 04103 Leipzig, Germany.*

* *Corresponding authors: hey@uni-leipzig.de; menyhart.sarosi@uni-leipzig.de*

of interest as a C_2 -symmetric backbone for phosphanes. Tertiary phosphane derivatives were first obtained in 1963 by dilithiation of *ortho*-carbaborane(12) and subsequent reaction with chlorodiphenylphosphane [2]. Since then several derivatives with organophosphorus substituents have been prepared and their reactivity and coordination chemistry have been investigated. Several of these compounds have been applied in homogeneous catalysis [3]. Specifically, the corresponding rhodium complexes are of interest in homogeneous catalysis. We have, therefore, prepared several rhodium(I) bisphosponitocarbaborane(12) complexes (**1–5**) (Scheme 1) which were shown by X-ray crystallography to be chloro-bridged dimers in which the Rh_2Cl_2 four-membered ring is either in a butterfly conformation (**1–4**) or planar (**5**) [1]. We here report the results of density functional calculations which allowed elucidating the factors determining the conformational preferences in these complexes.



Scheme 1. Chloro-bridged rhodium(I) bisphosponitocarbaborane(12) complexes **1–5** [1].

A driving force for bending of such binuclear square-planar complexes of d^8 transition metal appears to be the donor–acceptor interactions between the d_z^2 electrons and empty p_z orbitals of the two metal atoms [4,5]. However, only for large degrees of bending is the $M \cdots M$ interaction attractive enough to make the molecule more stable in its bent form with $\theta < 140^\circ$. The fold angle θ is defined as the dihedral angle between the coordination planes of the two metal centers ($M-X-X-M$: $M = Ni, Pd, Pt, Rh, Ir$; $X = Cl, Br, I$). Steric factors can also have a major influence on the fold angle θ , as shown by an energy difference of $10 \text{ kJ} \cdot \text{mol}^{-1}$ between a planar and folded modification

of $[\{\text{Rh}(\mu\text{-Cl})(\text{H}_2\text{PCH}_2\text{PH}_2)\}_2]$ [6]. However, steric effects seem to be important in preventing bending only for bulky terminal ligands [7]. Furthermore, packing effects in the crystal may also be considered to play an important role in the degree of folding of the molecules [4,6].

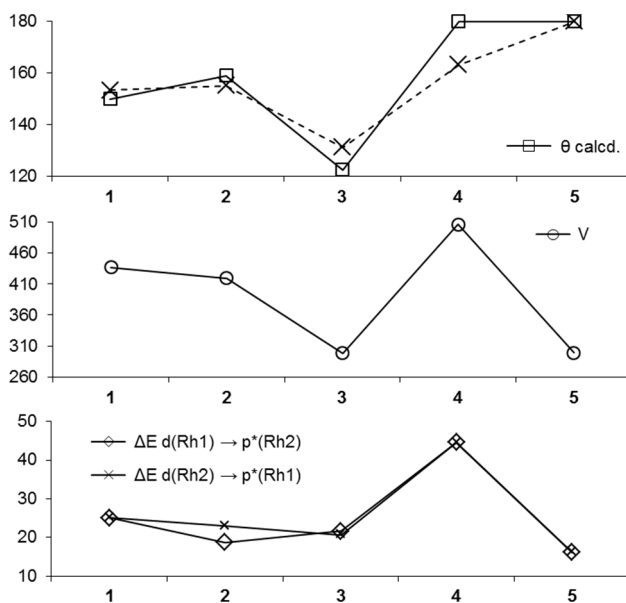


Figure 1. Optimized and experimental Rh–Cl–Cl–Rh fold angles θ (top, [°]), ligand volumes (middle, V , [cm³.mol⁻¹]) and second-order energy lowering values (bottom, ΔE , [kJ.mol⁻¹]) for rhodium complexes 1–5.

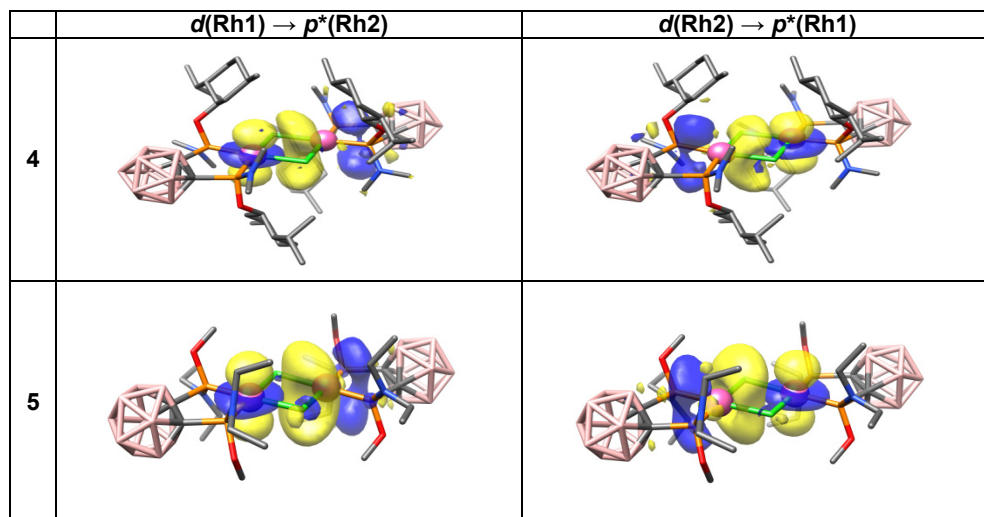
The optimized fold angles θ in complexes 1–4 correlate well with the calculated ligand volumes (Figure 1), indicating the significant influence of the steric factors on the bending of these complexes. The almost equal second-order energy lowering ($\Delta E^{(2)}$) values, in contrast with the decreasing fold angles θ in 1, 2 and 3, clearly indicate that the influence of $d \rightarrow p^*$ interactions on the level of bending is insignificant when compared with the effects of the steric factors. Complex 4 is perhaps the best example where steric and packing effects override electronic ones. Even though the crystal structure of 4 presents a bent Rh_2Cl_2 central unit, θ relaxes to 180° after optimization. On the other hand, the fold angle θ is unchanged or insignificantly altered after optimizing the structures of 1, 2 and 3. Thus, the bending observed in the crystal structure of 4 is only due to packing effects in the crystal and not caused by electronic effects. Furthermore, the bending in the optimized structure of 4 is sterically prohibited by the bulky ligands, in spite of the associated significant $d \rightarrow p^*$ interactions with the highest of all the $\Delta E^{(2)}$ values presented in Figure 1.

Finally, complex **5** stands out from the group with a planar Rh_2Cl_2 central unit in both the X-ray [1] and the optimized structure associated with a small ligand volume. The small ligand should allow the bending of **5**. However, the associated $d \rightarrow p^*$ interaction energies seems to be too weak to cause bending in **5**.

The values discussed above are summarized in Table 1. All in all, the steric and crystal packing effects seem to play a much more significant role than the electronic effects in influencing the bending of the rhodium complexes of the present study. This tendency of the bulky ligands to prevent bending is in good agreement with findings from previous studies [7].

Table 1. Optimized geometries and natural bond orbitals (NBO) involved in the $d \rightarrow p^*$ donor–acceptor interactions identified in **1–5**. Rh: pink, Cl: green, P: orange, O: red, N: blue, C: gray, B: tan. Hydrogen atoms are not shown.

	$d(\text{Rh1}) \rightarrow p^*(\text{Rh2})$	$d(\text{Rh2}) \rightarrow p^*(\text{Rh1})$
1		
2		
3		



CONCLUSIONS

Density functional calculations indicate that steric factors and packing seem to play a much more significant role than electronic effects in influencing the bending of the rhodium complexes **1–5**.

EXPERIMENTAL SECTION

The geometries of complexes **1–5** were optimized using the M06-L density functional [8] of the Gaussian 09 program package [9]. The calculations were performed using the LANL2TZ(f) basis set for Rh, the LANL08d basis set for P and Cl [10], along with the effective core potential of Hay and Wadt [11], obtained from the EMSL Basis Set Library [12]. For the remaining atoms, the D95V(d) basis set was used [13]. The existing $d \rightarrow p^*$ donor–acceptor interactions were identified with Natural Bond Orbital (NBO) analysis [14]. Additionally, the volume of one bisphosphonito-carbaborane(12) ligand in each rhodium complex was also calculated. Images of the optimized structures and of the NBOs were rendered with the UCSF Chimera program package [15].

ACKNOWLEDGMENTS

The study was carried out using the computational resource at the Faculty of Chemistry and Chemical Engineering, Babeş-Bolyai University (M.B.S.).

REFERENCES

1. E. Hey-Hawkins and co-workers, manuscript in preparation.
2. R.P. Alexander, H. Schroeder, *Inorg. Chem.*, **1963**, 2, 1107.
3. S. Bauer, E. Hey-Hawkins, in: *Boron Science, New Technologies and Applications*, chapter 22, ed. N. S. Hosmane, ISBN 978-1-4398266-3-8, CRC Press: Boca Raton, FL, USA, **2012**, 529.
4. R.H. Summerville, R. Hoffmann, *J. Am. Chem. Soc.*, **1976**, 98, 7240.
5. G. Aullón, P. Alemany, S. Alvarez, *Inorg. Chem.*, **1996**, 35, 5061.
6. P. Hofmann, C. Meier, W. Hiller, M. Heckel, J. Riede, M.U. Schmidt, *J. Organomet. Chem.*, **1995**, 490, 51.
7. G. Aullón, G. Ujaque, A. Lledós, S. Alvarez, P. Alemany, *Inorg. Chem.*, **1998**, 37, 804.
8. a) Y. Zhao, D.G. Truhlar, *J. Chem. Phys.*, **2006**, 125, 194101; b) Y. Zhao, D.G. Truhlar, *Acc. Chem. Res.*, **2008**, 41, 157.
9. M.J. Frisch, G.W. Trucks, H.B. Schlegel, G.E. Scuseria, M.A. Robb, J.R. Cheeseman, G. Scalmani, V. Barone, B. Mennucci, G. A. Petersson, H. Nakatsuji, M. Caricato, X. Li, H.P. Hratchian, A.F. Izmaylov, J. Bloino, G. Zheng, J.L. Sonnenberg, M. Hada, M. Ehara, K. Toyota, R. Fukuda, J. Hasegawa, M. Ishida, T. Nakajima, Y. Honda, O. Kitao, H. Nakai, T. Vreven, J. Montgomery, J.A., J.E. Peralta, F. Ogliaro, M. Bearpark, J.J. Heyd, E. Brothers, K.N. Kudin, V.N. Staroverov, R. Kobayashi, J. Normand, K. Raghavachari, A. Rendell, J.C. Burant, S.S. Iyengar, J. Tomasi, M. Cossi, N. Rega, J.M. Millam, M. Klene, J.E. Knox, J.B. Cross, V. Bakken, C. Adamo, J. Jaramillo, R. Gomperts, R.E. Stratmann, O. Yazyev, A.J. Austin, R. Cammi, C. Pomelli, J.W. Ochterski, R.L. Martin, K. Morokuma, V.G. Zakrzewski, G.A. Voth, P. Salvador, J.J. Dannenberg, S. Dapprich, A.D. Daniels, O. Farkas, J.B. Foresman, J.V. Ortiz, J. Cioslowski, D.J. Fox, *Gaussian 09, Revision A.02*, Gaussian, Inc., Wallingford CT, **2009**.
10. a) A.W. Ehlers, M. Bohme, S. Dapprich, A. Gobbi, A. Hollwarth, V. Jonas, K.F. Kohler, R. Stegmann, A. Veldkamp, G. Frenking, *Chem. Phys. Lett.*, **1993**, 208, 111; b) C.E. Check, T.O. Faust, J.M. Bailey, B.J. Wright, T.M. Gilbert, L.S. Sunderlin, *J. Phys. Chem. A*, **2001**, 105, 8111; c) L.E. Roy, P.J. Hay, R.L. Martin, *J. Chem. Theory Comput.*, **2008**, 4, 1029.
11. a) P.J. Hay, W.R. Wadt, *J. Chem. Phys.*, **1985**, 82, 270; b) P. J. Hay, W. R. Wadt, *J. Chem. Phys.*, **1985**, 82, 284; c) P.J. Hay, W.R. Wadt, *J. Chem. Phys.*, **1985**, 82, 299.
12. a) D. Feller, *J. Comput. Chem.*, **1996**, 17, 1571; b) K.L. Schuchardt, B.T. Didier, T. Elsethagen, L. Sun, V. Gurumoorthi, J. Chase, J. Li, T.L. Windus, *J. Chem. Inf. Model.*, **2007**, 47, 1045.
13. T.H. Dunning Jr., P.J. Hay, in *Modern Theoretical Chemistry*, H.F. Schaefer III, Ed., Plenum, New York, **1976**, Vol. 3, p. 1-28.
14. A.E. Reed, L.A. Curtiss, F. Weinhold, *Chem. Rev.*, **1988**, 88, 899.
15. E.F. Pettersen, T.D. Goddard, C.C. Huang, G.S. Couch, D.M. Greenblatt, E.C. Meng, T.E. Ferrin, *J. Comput. Chem.*, **2004**, 25, 1605.

*Dedicated to Professor Luminița Silaghi-Dumitrescu
on the occasion of her 65th anniversary*

COMPARATIVE COMPUTATIONAL CHARACTERIZATION OF FERRIC CYTOCHROME P450 AND SUPEROXIDE REDUCTASE BINDING TO CYANIDE

RADU SILAGHI-DUMITRESCU,^{a*} DANIELA CIOLOBOC^a

ABSTRACT. The active sites of the enzymes superoxide reductase (SOR) and cytochrome P450 feature square pyramidal FeN₄S centers, with a thiolate in axial position trans to the substrate binding site but with differing equatorial nitrogenous ligands. The respective catalytic cycles also share a common intermediate – a ferric-(hydro)peroxo species. The detailed catalytic mechanisms are still a matter of debate for both enzymes, as some of their key catalytic intermediates have very short lifetimes. Inhibitors such as cyanide were therefore often employed to probe active sites of these enzymes and identify important structural features controlling reactivity; among these studies, ENDOR spectral data on ferric-cyanide complexes were previously reported. Here, density functional calculations are employed in order to more accurately correlate the experimental data with electronic structure elements. The data are shown to be in good agreement with experiment and also provide new insight.

Keywords: *cytochrome P450, superoxide reductase, DFT, ENDOR*

INTRODUCTION

Superoxide reductases[1,2] and cytochromes P450[3] share a common motif at their active sites: a ferrous center with FeN₄S coordination, where a thiolate sulfur occupies an axial position, trans to the substrate binding site (cf. Figure 1). The four nitrogen atoms belong to a porphyrin in P450 and to four equatorial histidine side-chains in SOR.

^a *Department of Chemistry, Babes-Bolyai University, 11 Arany Janos str, Cluj-Napoca, Romania*

* *Corresponding author rsilaghi@chem.ubbcluj.ro*

Figure 1 illustrates the proposed catalytic cycles of SOR[4-11] and P450.[3] Two apparently orthogonal functions have been proposed for the thiolate ligand in P450 and SOR ferric-peroxo catalytic intermediates, under a framework known as “the push effect”[12]. Thus, at the ferric-hydroperoxo level, the thiolate is assumed to facilitate O-O bond cleavage in P450[3, 13], while in SOR the same thiolate would favour Fe-O bond cleavage[14, 15].

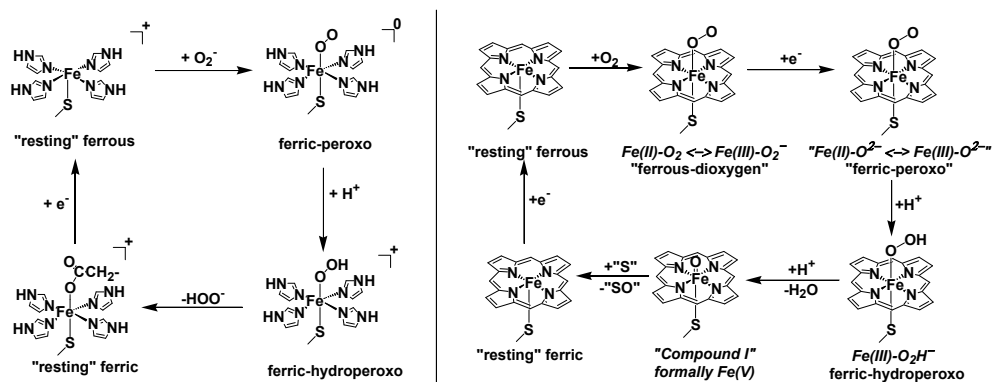


Figure 1. Proposed catalytic cycles of SOR (left) and P450 (right). For P450, “S” is a generic organic substrate that undergoes oxygen atom insertion to yield “SO”.

It was previously reported[9,10] that the trans (“push”) effect of the thiolate in heme-(hydro)peroxo adducts appears to be small at the geometric level. Thus, thiolate-ligated “ferric-peroxo” and ferric-hydroperoxo complexes featured Fe-O and O-O bond lengths very similar to those where the thiolate was replaced by imidazole, imidazolate, or phenoxide[9,10]. Slightly longer Fe-O and O-O bonds were noted in thiolate compared to non-thiolate models, possibly indicating an electronic basis for the proposed[14,15] apparently orthogonal facets of the “push effect”: Fe-O bond cleavage and O-O bond cleavage. On the other hand, the energetics of the “ferrous-dioxygen” - “ferric-peroxo” - ferric-hydroperoxo sequence were clearly different with thiolate compared to imidazole[9,10]. As expected based on simple charge arguments, the thiolate-ligated “ferric-peroxo” adduct had a much higher proton affinity than its imidazole-ligated counterpart. Along the same lines, reduction of “ferrous-dioxygen” to “ferric-peroxo” was harder to accomplish in thiolate models than in imidazole models[9,10]. The latter feature, which we described as “thiolate obstruction”, appears to also be active in nitric oxide reduction by another heme-thiolate active enzyme, P450nor, and its physiological utility as a “control switch” has been pointed out[9, 10].

A comparison of SOR and P450 from the point of view of their cyanide adducts, employing ENDOR spectroscopy to probe spin density distribution within these two enzymes, has recently been reported, concluding strong similarities between SOR and P450[16,17]. While DFT calculations were employed in order to examine electronic structures[16,18], detailed calculations on ENDOR parameters have to our knowledge not been reported to date on the SOR and P450 cyanide adducts. Such data are reported here, further delineating differences between the two enzymes, and also addressing the issue of heterogeneity in cyanide binding geometry.

RESULTS AND DISCUSSION

DFT-optimized geometries (cf. Figure 2 and Table 1) are in good agreement with previous results on other low-spin Fe(III) adducts of SOR[18] and hemes[19-21]; for the latter, a general agreement with experiment was previously noted[21].

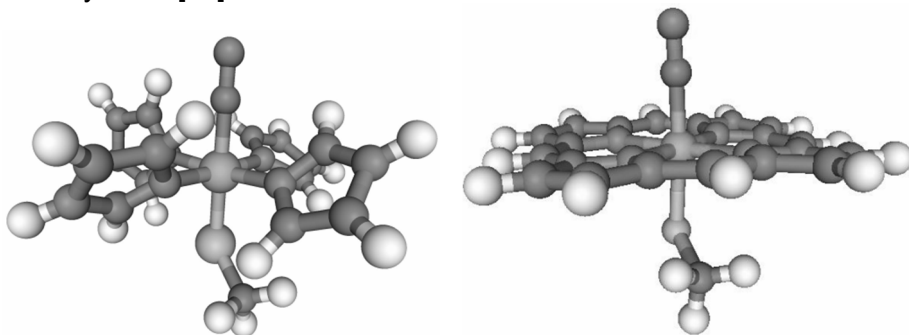


Figure 2. DFT-optimized $S=1/2$ Fe(III)-CN SOR and P450 models (following protocol described in [18,20,22]).

Essentially identical Fe-C-N moieties were obtained for models P450 (Figure 2), SOR (Figure 2), and for a truncated version of the Figure 2 SOR model, where the imidazole ligands were replaced with ammonia (SORr). SORr was further used in order to explore the conformational space. Despite previous proposals for a distinctly bent Fe-C-N unit in SOR, and despite the fact that the crystal structure of a P450 Fe(III)-cyanide adduct indeed shows a bent Fe-C-N moiety (pdb code 1N2N[23]), no local minimum for a bent Fe-C-N moiety could be located in any of the models examined here. When starting the geometry optimization from Fe-C-N angles ranging between 125° and 155° , the Fe-C-N moiety converged back to linearity.

However, modifying the Fe-C-N angle to 166°, 156°, 146° and 136°, with all other parameters unchanged, resulted in energy increases of 0.6, 1.9, 4.0, and 6.9 kcal/mol, respectively; a 5.5-kcal/mol energy difference was obtained after allowing the rest of the molecule to relax in response to the 136°-angle constraint. Also, it is unlikely that the bent local minima are actually differences in iron-imidazole(histidine) torsion angles. These very small energy differences suggest that within the respective protein active sites, factors as simple as even one strong hydrogen bond may in principle induce bending of the Fe-C-N moiety; steric constraints are also a likely cause of bending, at least in P450. Last but not least, it may be noted that the above-discussed data are an indication of a shallow potential surface around the Fe-C-N angle, and do not preclude the existence of local minima with a bent Fe-C-N moiety (or the identification thereof with a different functional or different numerical settings for convergence) – as long as any such minimum would be separated from the global minimum by extremely small barriers and would hence present negligible experimental relevance for the protein in its native environments.

The Fe-S bond in the SOR model is 0.1-0.2 Å shorter than measured by EXAFS for the resting ferrous and ferric states of SOR[24]. This difference is consistent with the high-spin character of the resting states compared to low-spin for the cyanide adducts. However, our previously calculated Fe-S bond length for the ferrous resting SOR was also 0.1-Å shorter than measured by EXAFS[18]. In principle, the SOR protein may impose an Fe-S bond longer than the intrinsic equilibrium distance, which, as shown by calculated Fe(III)-OO(H) distances[18] and as elaborated based on spectroscopy[24] and model compounds, would be beneficial (but not necessarily required[18]) for the SOR catalytic cycle. Tables 2 and 3 show that elongation of the Fe-S bond in the SOR Fe(III)-CN model by 0.2 Å (with a negligible energy cost, not shown), would affect –SCH₃ carbon and hydrogen spin densities and couplings to a small but detectable extent; the effect on the cyanide ligand appears to be very small but may in principle be detectable by virtue of a slightly altered isotropic coupling of the CN carbon atom (cf. Table 3).

Table 1. Key distances (Å) and angles for DFT-optimized SOR and P450 Fe(III)-CN models.

Model	Fe-S	Fe-CN	C-N	Fe-N ^c	Fe-C-N	S-Fe-C	H-C-S-Fe
SOR	2.24	1.94	1.18	2.04	179°	174°	-166°, 76°, -46°
SORr ^a	2.21	1.94	1.18	2.06	176°	177°	168°, 49°, -75°
SORrN ^b	2.14 ^b	1.87	1.18	2.06	179°	179°	-
P450	2.28	1.96	1.18	2.01	179°	175°	174°

^aequatorial imidazoles replaced with ammonia. ^baxial thiolate replaced with NH₃; column 2 lists the axial Fe-NH₃ distance. ^caverage of four equatorial Fe-N bonds.

Table 2. DFT-derived charges and spin densities (the latter are shown in parentheses).

Model	Fe	S	C ^{methyl}	H ^{methyl}	C ^{CN}	N ^{CN}
SOR	0.98 (0.77)	-0.21 (0.25)	-0.52 (-0.01)	0.18, 0.15, 0.19 (-0.000, 0.011, 0.008)	0.02 (-0.04)	-0.52 (0.05)
SORL ^a	0.99 (0.79)	-0.25 (0.23)	-0.52 (-0.01)	0.18, 0.15, 0.16 (-0.000, 0.010, 0.007)	0.03 (-0.04)	-0.52 (0.05)
SORr	0.83 (0.81)	-0.23 (0.21)	-0.53 (-0.01)	0.14, 0.21, 0.16 (-0.000, 0.010, 0.007)	-0.07 (-0.04)	-0.44 (0.06)
SORr bent	0.80 (0.82)	-0.22 (0.20)	-0.53 (-0.04)	0.14, 0.21, 0.17 (-0.001, 0.010, 0.006)	-0.13 (-0.04)	-0.35 (0.05)
P450	0.92 (0.87)	-0.18 (0.23)	-0.50 (-0.01)	0.1, 0.15, 0.15 (-0.001, 0.009, 0.008)	0.13 (-0.04)	-0.58 (0.05)
P450tw	0.92 (0.86)	-0.18 (0.24)	-0.50 (-0.01)	0.13, 0.11, 0.16 (0.011, 0.003, 0.002)	0.13 (-0.05)	-0.58 (0.04)

^aFe-S bond elongated by 0.2 Å compared to SOR while leaving all other geometrical parameters unchanged. The energy difference between SOR and SOR(long) was 2.8 kcal/mol.

For SOR, two of the methyl-thiolate protons are predicted to exhibit couplings that would make them readily detectable (cf. Table 3). These large couplings are due to isotropic components (15-26 MHz, cf. Table 3) and are one order of magnitude larger than those of other protons in the model (as exemplified by the third proton within the methyl-thiolate ligand). Correspondingly, the two strongly-coupled protons feature spin densities one order of magnitude higher than the third proton in the methyl-thiolate ligand (cf. Table 2). The origin of these increased spin densities is readily seen in hyperconjugation between the π electrons of the Fe-S bond and the C-H bonds of the Cys β carbon. This hyperconjugation, although not explicitly discussed in each case, is indeed seen in all heme-thiolate and SOR adducts examined to date, including catalytically relevant ferrous-dioxygen, ferric(hydro)peroxo, Compound I, or Fe-NO adducts[5,18,20,21,25]. Because of the sterical steric constraints imposed by the imidazole ligand sitting above the Cys- β -carbon in SOR, rotation around the S-CH₃ bond in the SOR model (or in the actual protein) is impossible, and the S---CH hyperconjugation is maximized for the two protons placed \sim symmetrically outside of the Fe-S-C β plane; the third proton (corresponding in fact to the Cys C α carbon atom of SOR) is \sim in the Fe-S-C β plane.

In the P450tw model, where the H-C-S-Fe dihedral was twisted to 25° compared to the value of \sim 0° in the global minimum, the isotropic Fermi contributions for the methyl protons, at 3 and 7 MHz respectively, are still distinctly above the values calculated for the other protons, and thus these protons might be observable by ENDOR. By contrast, in a P450 S=1/2

Fe(III)-OOH model with a similar H-C-S-Fe dihedral, the methyl protons have calculated Fermi contributions below 1 MHz, i.e., indistinguishable from other protons in the model and therefore unlikely to be observed experimentally by ENDOR[22].

Table3. Isotropic Fermi contact couplings (shown in italics) and anisotropic spin dipole couplings for SOR and P450 cyanide adduct models (in MHz for H and in Gauss for ^{13}C and ^{15}N).

Model	C^{methyl}	H^{methyl}	C^{CN}	N^{CN}
SOR	<i>-2.106</i> -0.282, 0.001, 0.282	<i>-0.437</i> -1.705, -1.435, 3.140 <i>26.723</i> 2.016, -1.357, 3.373 <i>16.692</i> -2.230, -1.178, 3.408	<i>-6.475</i> -1.065, -0.551, 1.616	<i>0.342</i> -0.670, -0.590, 1.259
SORL	<i>-1.664</i> -0.292, 0.003, 0.292	<i>-0.921</i> -1.540, -1.311, 2.851 <i>24.550</i> -1.895, -1.180, 3.075 <i>15.221</i> -2.098, -0.968, 3.067	<i>-6.891</i> -1.051, -0.525, 1.576	<i>0.367</i> -0.692, -0.590, 1.282
SORr	<i>-2.066</i> -0.243, 0.039, 0.204	<i>-0.730</i> -1.617, -1.352, 2.970 <i>13.372</i> -2.191, -1.260, 3.451 <i>23.109</i> -1.944, -1.426, 3.370	<i>-6.574</i> -1.184, -0.580, 1.763	<i>0.395</i> -0.804, -0.702, 1.506
SORr Bent	<i>-2.145</i> -0.229, 0.020, 0.209	<i>-0.939</i> -1.616, -1.313, 3.369 <i>12.623</i> -0.772, -0.445, 1.218 <i>22.422</i> -1.900, -1.469, 3.369	<i>-6.528</i> -1.242, -0.538, 1.781	<i>0.348</i> -0.918, -0.537, 1.455
P450 (global minimum)	<i>-2.038</i> -0.298, 0.071, 0.227	<i>-1.545</i> -1.602, -1.454, 3.056 <i>20.916</i> -2.300, -1.335, 3.635 <i>18.344</i> -2.483, -1.366, 3.848	<i>-7.844</i> -1.007, -0.557, 1.564	<i>0.332</i> -0.673, -0.550, 1.223
P450tw ^a	<i>-2.066</i> -0.277, 0.101, 0.176	<i>25.176^b</i> -1.959, -1.607, 3.566 <i>7.642</i> -1.778, -1.515, 3.293 <i>3.752</i> -2.488, -1.522, 4.009	<i>-7.536</i> -0.997, -0.569, 1.566	<i>0.329</i> -0.647, -0.536, 1.183

^aP450 model with H-C-S-Fe dihedral placed at 25°. ^bthis proton does not exist in the actual P450 protein, where it is replaced by the cysteine Ca.

The isotropic Fermi contact couplings computed in Table 3 are in good agreement with experiment insofar as showing a detectable shift for the cyanide carbon atom, albeit smaller than measured experimentally (~ 7 MHz here, compared to 20-30 MHz in experiment)[16,17]. On the other hand, the anisotropic coupling constants range between 0.5 and 1.8, i.e. close to the experimental values[16,17]. However, our DFT-derived anisotropic constants appear to be affected to $\sim 10\%$ of their value when bending the Fe-C-N angle, whereas variations as high as 40% were proposed to arise from such bending, in order to interpret the fact that three different signals arising from iron-bound cyanide were observed experimentally by ENDOR[17].

Results obtained during molecular dynamics simulations illustrate the high mobility of the cyanide adduct. Figure 3 displays the evolution in time of the Fe-C-N angle over a course of 500 femtoseconds. The angle fluctuates very rapidly between the equilibrium point computed at 0 Kelvin (180°) and the lowest value (158°). These fluctuations may also engender fluctuations on electronic structure and, implicitly, modification of the anisotropic constants. On the other hand the high mobility of the cyanide adduct emphasizes the fact that multiple conformers are accessible which may impact on the ENDOR parameters; the frozen matrix and very low temperatures employed for these measurements may in principle help trap apparent local minima.

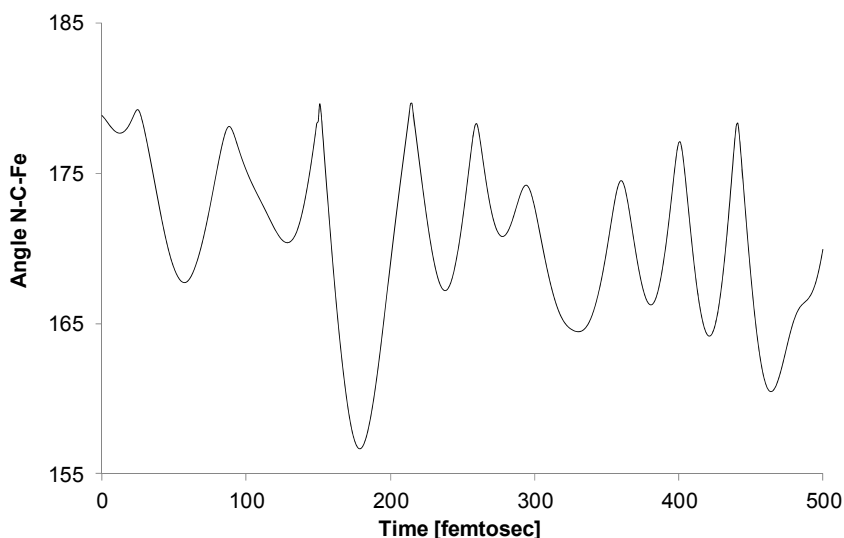


Figure 3. The Fe-C-N angle variation over a course of 500 femtoseconds.

The Fe-C bond length (data not shown) oscillates with an amplitude of 0.12 Å between 1.98 Å and 1.86 Å – a range also likely to have ENDOR-detectable effects on the electronic structures. Overall, this reveals that beyond the quasi-linear energy minimum of the ferric-cyanide adduct in SOR, the entire conformational space, with rotation around the Fe-C bond and bending of the Fe-C-N angle down to $\sim 155^\circ$, is very much accessible, so that any influence from the second coordination sphere or beyond (e.g., the “distal” aminoacids E47 and K48, or indeed further from these) may easily lock the adduct into a distinct local minimum. The dynamics calculations also confirm a tendency of the Fe-C-N to gravitate around 170° , i.e. slightly but distinctly different from true linearity.

CONCLUSIONS

To conclude, computation of ENDOR-related parameters with DFT methods has allowed for a useful comparison between SOR and P450 active sites while also maintaining good agreement and even allowing for reinterpretation of some of the experimental data. The dynamics data reveal a relatively mobile Fe-C-N angle in SOR, with an average value distinctly below 180° in agreement with spectroscopic experimental data, even though the equilibrium geometry (and unique energy minimum) is precisely at 180° .

EXPERIMENTAL SECTION

Unless otherwise specified, geometries were optimized without any constraints with the BP86 functional, which uses the gradient-corrected exchange functional proposed by Becke (1988)[26], the correlation functional by Perdew (1986)[27], and the DN** numerical basis set (comparable in size to 6-31G**), as implemented in Spartan[28]. For the SCF calculations, a fine grid was used, and the convergence criteria were set to 10^{-6} (for the root-mean square of electron density) and 10^{-8} (energy), respectively. For geometry optimization, convergence criteria were set to 0.001 au (maximum gradient criterion) and 0.0003 (maximum displacement criterion). This methodology was previously shown to yield reasonable results on P450 and SOR models, as well as on related bioinorganic centers.[7,21,29-36] Hyperfine couplings, Mulliken charges and spin densities were obtained from UBP86/6-31G** energy calculations at geometries shown in Table 1, using the Gaussian98[37] software package. Molecular dynamics (MD) simulations were performed on the SOR model using the extended Lagrangian approach with the ADMP (Atom Centered Density Matrix Propagation) model using the Gaussian09 software package and the same functional and basis sets as for the energy profiles.

ACKNOWLEDGEMENTS

Funding from the Romanian Ministry for Education and Research (PCE 480/2012) is gratefully acknowledged. Prof. Donald M. Kurtz, Jr. (University of Texas at San Antonio) is thanked for helpful discussions.

REFERENCES

1. F.J. Jenney, M. Verhagen, X. Cui, M. Adams, *Science*, **1999**, 286, 306-308
2. D.M.J. Kurtz, E. Coulter, *J. Biol. Inorg. Chem.*, **2002**, 6., 653-658.
3. M. Sono, M. P. Roach, E.D. Coulter, J.H. Dawson, *Chem. Rev.*, **1996**, 96, 2841-2887.
4. E. Coulter, J. Emerson, D.J. Kurtz, D. Cabelli, *J. Am. Chem. Soc.*, **2000**, 122, 11555-11556.
5. R. Silaghi-Dumitrescu, I. Silaghi-Dumitrescu, E.D. Coulter, J.P. Emerson, D.M. Kurtz, Jr., *J. Inorg. Biochem.*, **2001**, 86, 432.
6. D.M. Kurtz, Jr., J.P. Emerson, R. Silaghi-Dumitrescu, I. Kung, A. Das, L. Ljungdahl, *J. Inorg. Biochem.*, **2003**, 96, 69.
7. R. Silaghi-Dumitrescu, I. Silaghi-Dumitrescu, E. D. Coulter, D. M. Kurtz, Jr., *Inorg Chem*, **2003**, 42, 446-56.
8. D.M. Kurtz, W.N. Lanzilotta, R. Silaghi-Dumitrescu, *Abstr. Pap. Amer. Chem. Soc.*, **2004**, 227, U1431-U1432.
9. R. Silaghi-Dumitrescu, *Rev. Roum. Chim.*, **2008**, 53, 1149-1156.
10. R. Silaghi-Dumitrescu, *Chem. Pap.*, **2011**, 65, 559-565.
11. A.A.A.A. Attia, D. Cioloboc, A. Lupan, R. Silaghi-Dumitrescu, *J. Biol. Inorg. Chem.*, **2013**, 18, 95-101.
12. J.H. Dawson, R.H. Holm, R.H. Trudell, G. Barth, R.E. Linder, E. Nunnernberg, C. Djerassi, S.C. Tang, *J. Am. Chem. Soc.*, **1976**, 98, 3707.
13. F. Ogliaro, S. deVisser, S. Shaik, *J. Inorg. Biochem.*, **2002**, 91, 554-567.
14. M.D. Clay, C.A. Cosper, F.E. Jenney, M.W. Adams, M.K. Johnson, *Proc. Natl. Acad. Sci. USA*, **2003**, 100, 3796-3801.
15. J.A. Kovacs, *Chem. Rev.*, **2004**, 104, 825-848.
16. T.C. Yang, R.L. McNaughton, M.D. Clay, F.E. Jenney, Jr., R. Krishnan, D.M. Kurtz, Jr., M.W. Adams, M.K. Johnson, B.M. Hoffman, *J. Am. Chem. Soc.*, **2006**, 128, 16566-78.
17. M.D. Clay, T.C. Yang, F.E. Jenney, Jr., I.Y. Kung, C.A. Cosper, R. Krishnan, D.M. Kurtz, Jr., M.W. Adams, B.M. Hoffman, M.K. Johnson, *Biochemistry*, **2006**, 45, 427-38.
18. R. Silaghi-Dumitrescu, I. Silaghi-Dumitrescu, E.D. Coulter, D.M. Kurtz, Jr., *Inorg. Chem.*, **2003**, 42, 446-456.
19. P. Rydberg, E. Sigfridsson, U. Ryde, *J. Biol. Inorg. Chem.*, **2004**, 9, 203-223.

20. R. Silaghi-Dumitrescu, *J. Biol. Inorg. Chem.*, **2004**, 9, 471-476.
21. R. Silaghi-Dumitrescu, I. Silaghi-Dumitrescu, *Rev. Roum. Chim.*, **2004**, 3-4, 257-268.
22. R. Silaghi-Dumitrescu, C.E. Cooper, *Dalton Trans.*, **2005**, 3477-3482.
23. R. Fedorov, D.K. Ghosh, I. Schlichting, *Arch. Biochem. Biophys.*, **2003**, 409, 25-31.
24. M.D. Clay, F.J. Jenney, P. Hagedoorn, G. George, M. Adams, M.K. Johnson, *J. Am. Chem. Soc.*, **2002**, 124, 788-805.
25. R. Silaghi-Dumitrescu, *Eur. J. Inorg. Chem.*, **2003**, 1048-1052.
26. A.D. Becke, *Phys. Rev.*, **1988**, 3098-3100.
27. J.P. Perdew, *Phys. Rev.*, **1986**, B33, 8822-8824.
28. S. Spartan, *Spartan 5.0, Wavefunction, Inc., 18401 Von Karman Avenue Suite 370, Irvine, CA 92612 U.S.A.*
29. R. Silaghi-Dumitrescu, *Inorg. Chem.*, **2004**, 43, 3715-3718.
30. R. Silaghi-Dumitrescu, *J. Biol. Inorg. Chem.*, **2004**, 9, 471-476.
31. R. Silaghi-Dumitrescu, *Arch. Biochem. Biophys.*, **2004**, 424, 137-140.
32. R. Silaghi-Dumitrescu, I. Silaghi-Dumitrescu, *J. Inorg. Biochem.*, **2006**, 100, 161-6.
33. R. Silaghi-Dumitrescu, B.J. Reeder, P. Nicholls, C.E. Cooper, M.T. Wilson, *Biochem. J.*, **2007**, 403, 391-395.
34. R. Silaghi-Dumitrescu, *Eur. J. Inorg. Chem.*, **2008**, 5404-5407.
35. A. Mot, Z. Kis, D.A. Svistunenko, G. Damian, R. Silaghi-Dumitrescu, S.V. Makarov, *Dalton Trans.*, **2010**, 39, 1464-6.
36. R. Silaghi-Dumitrescu, S.V. Makarov, *Eur. J. Inorg. Chem.*, **2010**, 1129-1132.
37. *Gaussian 98 (Revision A.1)*, M.J. Frisch, G.W. Trucks, H.B. Schlegel, G.E. Scuseria, M.A. Robb, J.R. Cheeseman, V.G. Zakrzewski, J.A. Montgomery, R.E. Stratmann, J.C. Burant, S. Dapprich, J.M. Millam, A.D. Daniels, K.N. Kudin, M.C. Strain, O. Farkas, J. Tomasi, V. Barone, M. Cossi, R. Cammi, B. Mennucci, C. Pomelli, C. Adamo, S. Clifford, J. Ochterski, G.A. Petersson, P.Y. Ayala, Q. Cui, K. Morokuma, D.K. Malick, A.D. Rabuck, K. Raghavachari, J.B. Foresman, J. Cioslowski, J.V. Ortiz, B.B. Stefanov, G. Liu, A. Liashenko, P. Piskorz, I. Komaromi, R. Gomperts, R.L. Martin, D.J. Fox, T. Keith, M.A. Al-Laham, C.Y. Peng, A. Nanayakkara, C. Gonzalez, M. Challacombe, P.M.W. Gill, B.G. Johnson, W. Chen, M.W. Wong, J.L. Andres, M. Head-Gordon, E.S. Replogle and J.A. Pople, *Gaussian, Inc., Pittsburgh PA*, 1998.

*Dedicated to Professor Luminița Silaghi-Dumitrescu
on the occasion of her 65th anniversary*

SYNTHESIS AND ELECTRONIC PROPERTIES OF 3-ARYL 10H-PHENOTHIAZINES

CHRISTA S. BARKSCHAT^a, and THOMAS J. J. MÜLLER^{a,b}

ABSTRACT. 3-Bromo 10H-phenothiazines, even the 10H-unsubstituted derivative, can be efficiently coupled with several boronic acids to give 3-aryl 10H-phenothiazines with good to excellent yields. Selected electronic properties (UV/Vis spectroscopy, cyclic voltammetry, DFT calculations) are discussed and correlations of the Hammett-Taft substituent parameters are established for rationalizing the transmission of the remote electronic substituent effects.

Keywords: *Cross-coupling – DFT calculations – Heterocycles – Substituent Effects – UV/Vis Spectroscopy*

INTRODUCTION

The Suzuki cross-coupling [1] is the most practical and most versatile catalytic arylation methodology and has found widespread application in biaryl formation ranging from natural product synthesis over medicinal chemistry to electronic materials. A major advantage over other Pd-catalyzed cross-coupling reactions is definitely the uneventful handling of boronic acids and boronates as robust organometallics that even do not require anhydrous reaction conditions. As a consequence, Suzuki arylations have efficiently been used for the synthesis of electroactive materials.

^a *Organisch-Chemisches Institut, Ruprecht-Karls-Universität Heidelberg, Im Neuenheimer Feld 270, D-69120 Heidelberg, Germany*

^b *New address: Institut für Organische Chemie und Makromolekulare Chemie, Heinrich-Heine-Universität Düsseldorf, Universitätsstrasse 1, D-40225 Düsseldorf, Germany*

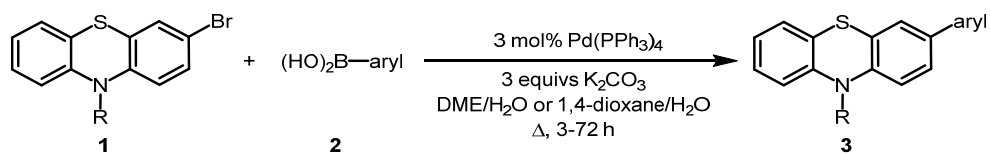
* *Corresponding author: ThomasJJ.Mueller@hhu.de*

Phenothiazine, a heteroaromatic S,N-tricycle, and its derivatives have been intensively studied at the Faculty of Chemistry and Chemical Engineering at Babeş-Bolyai University in Cluj-Napoca, as witnessed by numerous publications [2]. Most interestingly, phenothiazines display low oxidation potentials, forming stable deeply colored radical cations with perfect Nernstian reversibility [3-6]. Since 2000 we have been systematically exploring the synthetic and physical organic chemistry of oligophenothiazines in linear [7] and cyclic [8] topologies. Besides the inherent electro- and photochromicity of phenothiazine conjugates [9], we became particularly interested in luminescence characteristics of π -conjugated expanded derivatives [10,11] and the peculiar behavior of (oligo)phenothiazines as potent donors in donor-acceptor conjugates, even enabling photo-induced electron transfer [12-16]. As a consequence hole transport in OLED [17], mesoporous organo silica hybrid materials [18], and chromophores in dye-sensitized solar cells can also be devised on the basis of oligophenothiazines [19-21]. Particularly interesting for nanotechnology are native (oligo)phenothiazines displaying a pronounced ability to form self-assembled monolayers on gold surfaces [22-24] as well as on zinc and iron oxide surfaces [25].

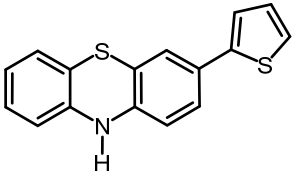
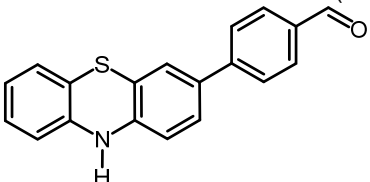
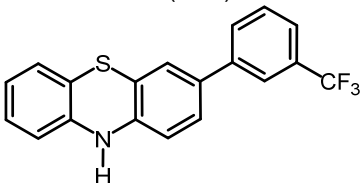
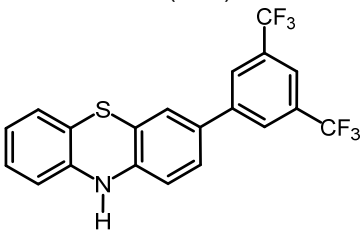
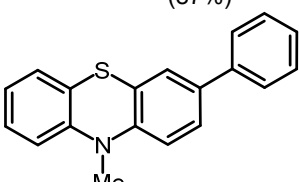
Employing Suzuki coupling as a key reaction to establish oligophenothiazines and derivatives by biaryl formation we devised borolated phenothiazines as versatile building blocks [26] that were successfully transformed in various functional 3-(hetero)arylated and 3,7-di(hetero)arylated phenothiazines [27]. Amazingly, while Suzuki coupling with N-substituted derivatives is wide spread and established the use of 3-bromo 10*H*-phenothiazine without *N*-substituent has remained unexplored. Here, we report a series of Suzuki coupling of 3-bromo 10*H*-phenothiazines with several boronic acids and selected electronic properties are discussed on the basis of UV/Vis spectroscopy, cyclic voltammetry, and DFT calculations.

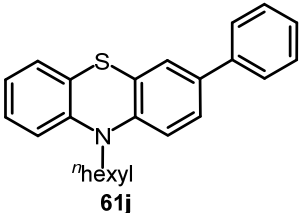
RESULTS AND DISCUSSION

Most conveniently, we could employ standard Suzuki conditions, developed and applied in several studies [7,26], for reacting three different 3-bromo 10*H*-phenothiazines **1**, i. e. the unsubstituted derivative **1a**, the methyl (**1b**), and the *n*-hexyl derivative **1c**, with equimolar amounts of various aryl boronic acids **2** in the presence of Pd(PPh₃)₄ as a catalyst and potassium carbonate as a base in boiling aqueous DME or 1,4-dioxane. The resulting 3-aryl 10*H*-phenothiazines **3** were obtained as slightly colored microcrystalline solids (**3a-i**) or as a pale yellow oil (**3j**) in 56-97% yield (Scheme 1, Table1).

SYNTHESIS AND ELECTRONIC PROPERTIES OF 3-ARYL 10*H*-PHENOTHIAZINES**Scheme 1****Table 1.** Experimental details of the synthesis of 3-aryl 10*H*-phenothiazines **3**.

Entry	3-bromo-10 <i>H</i> -phenothiazine 1	aryl boronic acid 2	Time <i>t</i>	3-aryl 10 <i>H</i> -phenothiazines 3 (yield) ^a
1	R = H (1a) [28]	aryl = 2,6(MeO) ₂ C ₆ H ₃ (2d)	12 h	<p>61d 3a (78%)</p>
2	1a	aryl = <i>p</i> - ^t BuC ₆ H ₄ (2b)	48 h	<p>61b 3b (80%)</p>
3	1a	aryl = <i>m</i> -H ₂ NC ₆ H ₄ (2e)	45 h	<p>61e 3c (78%)</p>
4	1a	aryl = Ph (2a)	16 h	<p>61a 3d (67%)</p>

Entry	3-bromo-10 <i>H</i> -phenothiazine 1	aryl boronic acid 2	Time <i>t</i>	3-aryl 10 <i>H</i> -phenothiazines 3 (yield) ^a
5	1a	aryl = 2-thienyl (2h)	22 h	 61h
6	1a	aryl = OHCC ₆ H ₄ (2c)	72 h	 61c
				3e (68%)
				3f
7	1a	aryl = <i>m</i> -F ₃ CC ₆ H ₄ (2f)	25 h	 61f
				(80%)
				3g
8	1a	aryl = 3,5-(F ₃ C) ₂ C ₆ H ₃ (2g)	12 h	 61g
				(97%)
				3h
9	R = Me (1b) [29]	2a	3 h	 61i
				(87%)
				3i (83%)

Entry	3-bromo-10H-phenothiazine 1	aryl boronic acid 2	Time <i>t</i>	3-aryl 10H-phenothiazines 3 (yield) ^a
10 ^b	R = ⁿ hexyl (1c) [30]	2a	25 h	 61j 3j (56%)

^aIsolated yield after chromatography on silica gel. ^bThe reaction was conducted in a degassed mixture of 1,4-dioxane (8 mL) and water (4 mL).

The structural assignments are in excellent agreement with the ¹H and ¹³C NMR resonances for phenothiazine typical NMR spectra [31]. Although the slightly colored appearance of the solids indicated a propensity to facile air oxidation, no special precautions had to be taken for preparing the NMR spectra samples. Most characteristically, the proton resonances of the NH-signals of the compounds **3a-h**, recorded in d⁶-DMSO, appear as distinct singlets between δ 8.6-8.8. The resonances of the methyl (**3i**) and methylene protons (**3j**) that are directly adjacent to the electronegative 10-nitrogen core appear in the spectra recorded in CDCl₃ as a singlet at δ 3.38 or as a triplet at δ 3.95, respectively. Likewise in the IR spectra of compounds **3a-h** the bands between 3300 and 3400 cm⁻¹ can be unambiguously assigned to the distinct NH stretch vibrations [32], which are absent in the spectra of compounds **3i** and **3j**. For the latter CH stretch vibrations are clearly observed between 2900 and 3000 cm⁻¹. For all derivatives **3** the base peak in the mass spectra is the molecule peak, indicating the peculiar stability of phenothiazinyl radical cations. The most characteristic fragmentation pattern is the α -cleavage of the methyl or hexyl substituent adjacent to the nitrogen atom in the spectra of phenothiazines **3i** and **3j**.

Selected electronic properties of the 3-aryl 10H-phenothiazines **3** were determined by recording UV/Vis spectra and cyclic voltammograms (Table 2). For comparison the same data were measured for phenothiazine (**4**), 10-methyl 10H-phenothiazine (**5**), and 10-*n*-hexyl 10H-phenothiazine (**6**).

In the UV/Vis spectra all phenothiazines **3** display two distinct absorption bands, an intense band between 254 and 287 nm and a variable weaker longer wavelength absorption that varies with the aryl substitution pattern between 318 and 402 nm. As a consequence of the electron withdrawing substituent effect at the remote *p*-position on the 3-aryl moiety this latter absorption band obviously arises from pronounced charge transfer characteristics. This finding and interpretation is in good agreement with the electronic properties

of a series of 3-(hetero)aryl substituted 10-*n*-hexyl 10*H*-phenothiazines [27c]. Comparison of two consanguineous series reveals the electronic effect of *N*-substitution. The longest wavelength absorption in the UV/Vis spectra of phenothiazine (**4**), 10-methyl 10*H*-phenothiazine (**5**), and 10-*n*-hexyl 10*H*-phenothiazine (**6**) appears at 320, 310, and 311 nm, respectively. The same trend is found for 3-phenyl derivatives where the NH derivative **3d** displays the most redshifted maximum at 335 nm, for the hexyl derivative **3j** this band is found at 322 nm and for the methyl derivative **3i** the maximum appears at 318 nm. Assuming a charge transfer character of this band with phenyl being a weak acceptor moiety, the NH derivative **3d** with represents the most pronounced donor character followed by the hexyl derivative **3j** and the methylated compound **3i**. While the correlation between methyl and hexyl substitution is logical, the NH effect is counterintuitive at first sight. However, considering the pseudoequatorial orientation of the small H atom in the butterfly conformation of phenothiazine an efficient overlap of the nitrogen lone pair with the annelated benzo cores can be assumed [33]. Alkyl substituents must adopt pseudoaxial orientations due to steric interactions. Hence, the overlap of the nitrogen lone pair with the π -systems is considerably diminished.

Table 2. Selected UV/Vis spectroscopic and electrochemical data of 3-aryl 10*H*-phenothiazines **3** and reference phenothiazines **4-6** and selected Hammett-Taft substituent parameters $\sigma_{p/m}$, σ_R , and σ_{R^+} (UV/Vis spectra recorded in DMSO; cyclic voltammetry recorded in 0.1 M dichloromethane solution of NBu₄PF₆ as an electrolyte, Pt working electrode and Pt counter electrode vs Ag/AgCl reference electrode, ferrocene as internal standard ($E_{1/2}^{0/+1} = 450$ mV) [34], scan rate $\nu = 100$ mV/s, $T = 20$ °C).

3-aryl 10 <i>H</i> -phenothiazines 3	Absorption λ_{max} [nm]	$E_{1/2}^{0/+1}$ [mV]	$E_{1/2}^{+1/+2}$ [mV]	$E_{1/2}^{0/-1}$ [mV]	$\sigma_{p/m}$	σ_R	σ_{R^+}
3a	262, 322	542	1170	-	-	-	-
3b	270, 333	587	1185	-	-0.20 ^a	-0.16 ^a	-0.26 ^a
3c	265, 329	589	784 (irr)	-	-0.16 ^b	-0.18 ^b	-0.16 ^b
3d	268, 335	611	1153	-	0.00 ^c	0.00 ^c	0.00 ^c
3e	265sh, 287, 346	-	-	-	-	-	-
3f	284, 402	671	1267	-1802 (irr)	0.42 ^d	0.23 ^d	0.72 ^d
3g	265, 328 ^e	-	-	-	-	-	-
3h	271, 340, 372	-	-	-	-	-	-
3i	265, 318 ^e	741	-	-	-	-	-
3j	268, 322	701	-	-	-	-	-

3-aryl 10H-phenothiazines 3	Absorption λ_{max} [nm]	$E_{1/2}^{0/+1}$ [mV]	$E_{1/2}^{+1/+2}$ [mV]	$E_{1/2}^{0/-1}$ [mV]	$\sigma_{p/m}$	σ_R	σ_{R^+}
4	254, 320 ^f [34]	624	-	-	-	-	-
5	254, 310 ^e	764	-	-	-	-	-
6	256, 311	728	-	-	-	-	-

^aSubstituent parameter *p*-Bu. ^bSubstituent parameter *m*-NH₂. ^cSubstituent parameter H.

^dSubstituent parameter *p*-CHO. ^eRecorded in CHCl₃. ^fRecorded in acetonitrile.

This assignment is additionally supported by the first reversible oxidation potentials $E_{1/2}^{0/+1}$, which are also lowest for the NH derivatives **3d** (611 mV) and **4** (624 mV) in both consanguineous series. Likewise the potentials of the hexyl derivatives appear anodically shifted at 701 (**3j**) and 728 mV (**6**), and for the methyl substitution in compounds **3i** and **5** the oxidation is shifted most anodically to 741 and 764 mV, respectively. All this underlines the peculiar and very electron rich character of NH phenothiazine substituents as potent donors.

For scrutinizing the remote electronic substituent effect on the oxidation of the phenothiazinyl core we recorded redox potentials of another consanguineous series of derivatives (**3b-d**, and **3f**) bearing substituents in *p*- and *m*-positions of the phenyl ring. For these substituents suitable Hammett σ -parameters are available, however, out of curiosity we also were interested to determine the effect of the 2,6-dimethoxy substitution (**3a**) on the first oxidation potential. Indeed the lowest oxidation potential is found for the 2,6-dimethoxy derivative **3a**. From ESR measurements of the radical cation of 1,3-dimethoxy benzene it is known that the methoxy substituents can considerably accommodate spin density [36]. Although twofold *ortho*-methoxy substitution causes a torsional angle of 52° in a related biphenyl [37], an efficient stabilization of the phenothiazinyl radical cation by the remote substituents can be assumed. Besides first oxidations at potentials between 542 and 671 mV with Nernstian behavior (Figure 1) the derivatives **3a-d**, and **3f** also display second oxidations, which are also reversible in arrange between 1170 and 1267 mV, with exception of the *m*-aniline derivative **3c**. In that case the second oxidation occurs, due to the similarity of the ionization potentials of phenothiazine (7.02 eV) and aniline (7.55 eV) [38], at considerable lower potential, also causing irreversible consecutive reactions of the dication, such as dimerization or deprotonation [39]. The appearance of a reduction wave for compound **3f** at a cathodic potential of -1802 mV can be assigned to the irreversible reduction in the phenothiazinyl expanded benzaldehyde. This reduction is considerably

anodically shifted in comparison to benzaldehyde ($E_{red} = -2581$ mV, measured in a 0.1 M solution of NBu_4ClO_4 as an electrolyte in sulfolane vs. Ag/AgClO_4 at a scan rate $\nu = 167$ mV/s, $T = 50$ °C) [40], presumably to due to the extended conjugation of the π -system.

For further elucidating the remote substituent effect the first oxidation potentials $E_{1/2}^{0/+1}$ of the four derivatives **3b-d**, and **3f** of the consanguineous series bearing *p*- and *m*-phenyl substituents were subjected to Hammett-Taft correlation analyses with the parameters $\sigma_{p/m}$, σ_R , and σ_{R^+} [41]. The obtained correlations gave for $\sigma_{p/m}$: $E_{1/2}^{0/+1} = 138.16 \sigma_{p/m} + 612.43$ [mV] ($R^2 = 0.9981$); for σ_R : $E_{1/2}^{0/+1} = 203.8 \sigma_R + 620.1$ [mV] ($R^2 = 0.9717$); and for σ_{R^+} : $E_{1/2}^{0/+1} = 88.117 \sigma_{R^+} + 607.89$ [mV]; ($R^2 = 0.992$). This indicates that the remote electronic effect is transmitted by both resonance and inductive effects, however, with a dominance imposed by the stabilization of positive charges as a consequence of the generation of radical cations.

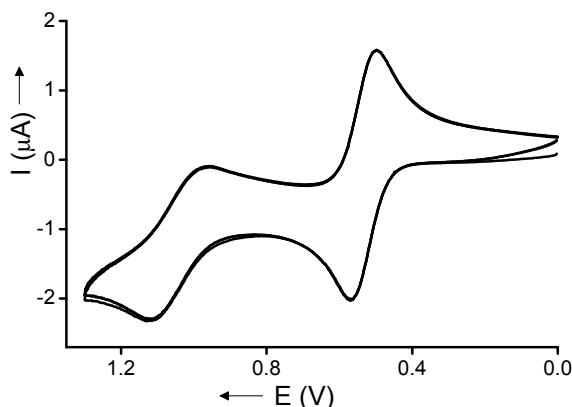


Figure 1. Cyclic voltammogram of compound **3d** (recorded in 0.1 M dichloromethane solution of NBu_4PF_6 as an electrolyte, Pt working electrode and Pt counter electrode vs Ag/AgCl reference electrode, ferrocene as internal standard, scan rate $\nu = 100$ mV/s, $T = 20$ °C).

Additional insight in the electronic structure of 3-aryl substituted 10*H*-phenothiazines was obtained by quantum chemical calculations for the four representative structures **3b-d**, and **3f** on the DFT level of theory (B3LYP 6–31 G^*) [42]. The HOMO energies of the geometry optimized structures were considered for correlation studies, both with $\sigma_{p/m}$, σ_R , and σ_{R^+} [41], and the experimentally obtained first oxidation potentials $E_{1/2}^{0/+1}$ of the corresponding compounds **3b-d**, and **3f** (Table 3).

Table 3. Computed HOMO energies (B3LYP 6–31 G*), first oxidation potentials $E_{1/2}^{0/+1}$, and selected Hammett-Taft substituent parameters $\sigma_{p/m}$, σ_R , and σ_{R^+} of structures **3b-d**, and **3f**.

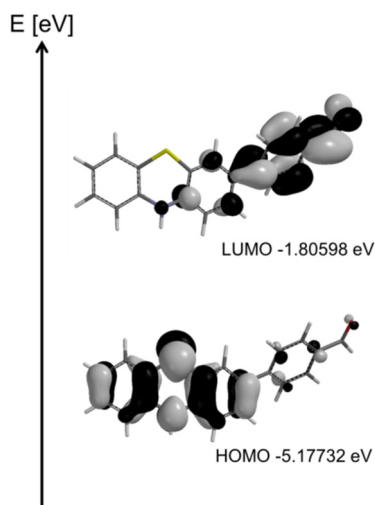
Structure	$\sigma_{p/m}$	σ_R	σ_{R^+}	$E_{1/2}^{0/+1}$ [mV]	E_{HOMO} [eV]
3b	-0.20 ^a	-0.16 ^a	-0.26 ^a	587	-4.925
3c	-0.16 ^b	-0.18 ^b	-0.16 ^b	589	-4.890
3d	0.00 ^c	0.00 ^c	0.00 ^c	611	-4.969
3f	0.42 ^d	0.23 ^d	0.72 ^d	671	-5.177

^aSubstituent parameter *p*-Bu. ^bSubstituent parameter *m*-NH₂. ^cSubstituent parameter H. ^dSubstituent parameter *p*-CHO.

The correlations of the Hammett-Taft substituent parameters $\sigma_{p/m}$, σ_R , and σ_{R^+} with the calculated HOMO energies are reasonable with R^2 between 0.953 and 0.966, as already established with the first oxidation potentials $E_{1/2}^{0/+1}$. The correlation between the HOMO energies and the first oxidation potentials $E_{1/2}^{0/+1}$ fits even better ($R^2 = 0.98$). Therefore, it should be possible to predict the oxidation potentials of congeners of compounds **3** by employing the calculated HOMO energies in the following equation:

$$E_{1/2}^{0/+1} = -301.73 E_{HOMO} - 891.23 \text{ [mV]} \quad (R^2 = 0.98),$$

where E_{HOMO} is given in [eV].

**Figure 2.** Frontier molecular orbitals, HOMO (bottom) and LUMO (top) of structure **3f**.

A closer inspection of the Kohn-Sham frontier molecular orbitals indicates that the longest-wavelength electronic absorption bands that can be assigned to arise from states with considerable HOMO to LUMO transitions that possess significant charge-transfer character. In particular, for the formyl substituted derivative **3f** this charge-transfer character becomes apparent, where the HOMO displays phenothiazine-centered coefficient density and the LUMO coefficients are predominantly localized in the formylphenyl moiety (Figure 2).

CONCLUSIONS

In summary we could show that the Suzuki coupling of 3-bromo 10*H*-phenothiazines, in particular with the 10-unsubstituted derivative, with several boronic acids proceeds very efficiently and can be employed for the rapid access of various 3-(hetero)aryl 10*H*-phenothiazines. Extensive UV/Vis spectroscopic measurements and cyclic voltammetry as well as DFT calculations have revealed that the electronic properties of these derivatives can be correlated with Hammett-Taft parameters indicating a significant contribution of resonance in transmitting the electronic substituent from the remote substituent position by virtue on the effect of the first oxidation potential. For further exploitation of the insights in the electronic structure extracted from DFT calculations, especially with 10-unsubstituted phenothiazines as donors, underline a considerable charge-transfer character from the phenothiazine to most favorably an electron acceptor at the remote substituent position. This is particularly interesting for devising novel types of light-harvesting dyes for organic photovoltaics. Further studies in these directions are currently underway.

EXPERIMENTAL SECTION

All reactions were carried out in flame-dried Schlenk flasks under nitrogen. Reagents and catalyst were purchased as reagent grade and were used without further purification. Solvents were dried and distilled by standard procedures [43]. 3-Bromo 10*H*-phenothiazines **1** were prepared according published procedures [28-30]. Column chromatography: silica gel 60, mesh 70–230. TLC: silica gel plates. Melting points: uncorrected values. ¹H and ¹³C NMR spectra: d₆-DMSO, d₆-acetone, or CDCl₃ (locked to Me₄Si). The assignments of quaternary C, CH, CH₂ and CH₃ were made with the aid of DEPT spectra. Elemental analyses were carried out in the Microanalytical Laboratories of the Organisch-Chemisches Institut, Ruprecht-Karls-Universität, Heidelberg, Germany.

Electrochemistry: Cyclic voltammetry experiments (EG & G potentiostatic instrumentation) were performed under argon in dry and degassed CH₂Cl₂ at room temperature and at scan rates of 100, 250, 500, and 1000 mVs⁻¹. The electrolyte was Bu₄NPF₆ (0.025 M). The working electrode was a 1 mm platinum disk, the counter-electrode was a platinum wire, and the reference electrode was an Ag/AgCl electrode. The potentials were corrected to the internal standard of Fc/Fc⁺ in CH₂Cl₂ ($E_{1/2}^{0/+1} = 450$ mV) [34].

General procedure (GP) for the synthesis of 3-aryl 10H-phenothiazines 3

In a 50 mL Schlenk flask with a magnetic stir bar 3-bromo-10H-phenothiazine **1** (1.0 equiv), aryl boronic acid **2** (1.1 equiv), Pd(PPh₃)₄ (40 mg, 0.03 mmol), K₂CO₃ (159 mg, 1.15 mmol), DME (10 mL), and water (5 mL) were placed and degassed with nitrogen for 5 min (for experimental details see Table 4). The light brown suspension was heated to reflux under nitrogen for the time indicated. After cooling to room temp the reaction mixture was extracted with dichloromethane (2 x 50 mL) and the combined organic layers with water (2 x 50 mL). The combined organic layers were dried (anhydrous MgSO₄), the solvents were removed in vacuo and the residue was purified by flash chromatography on silica gel (ether/pentane) to give the 3-aryl phenothiazines **3**.

Table 4. Experimental details of the synthesis of 3-aryl 10H-phenothiazines **3**.

Entry	3-bromo-10H-phenothiazine 1	aryl boronic acid 2	3-aryl 10H-phenothiazines 3 (yield)
1 ^a	349 mg (1.25 mmol) of 1a	254 mg (1.40 mmol) of 2,6-dimethoxyphenyl boronic acid (2a)	330 mg (78%) of 3a
2 ^b	224 mg (0.80 mmol) of 1a	157 mg (0.88 mmol) of 4- <i>tert</i> -butylphenyl boronic acid (2b)	214 mg (80%) of 3b
3 ^c	305 mg (1.10 mmol) of 1a	193 mg (1.21 mmol) of 3-aminophenyl boronic acid (2c)	249 mg (78%) of 3c
4 ^d	321 mg (1.15 mmol) of 1a	155 mg (1.27 mmol) of phenyl boronic acid (2d)	213 mg (67%) of 3d
5 ^e	327 mg (1.17 mmol) of 1a	160 mg (1.30 mmol) of 2-thienyl boronic acid (2e)	226 mg (68%) of 3e
6 ^f	270 mg (0.97 mmol) of 1a	160 mg (1.06 mmol) of 4-formylphenyl boronic acid (2f)	239 mg (80%) of 3f
7 ^g	311 mg (1.12 mmol) of 1a	234 mg (1.23 mmol) of 3-(trifluoromethyl) phenyl boronic acid (2g)	373 mg (97%) of 3g
8 ^a	151 mg (0.54 mmol) of 1a	154 mg (0.59 mmol) of 3,5-bis(trifluoromethyl) phenyl boronic acid (2h)	194 mg (87%) of 3h

Entry	3-bromo-10 <i>H</i> -phenothiazine 1	aryl boronic acid 2	3-aryl 10 <i>H</i> -phenothiazines 3 (yield)
9 ^h	292 mg (1.00 mmol) of 3-bromo-10-methyl-10 <i>H</i> -phenothiazin (1b)	134 mg (1.10 mmol) of phenyl boronic acid (2d)	240 mg (83%) of 3i
10 ^{g,i}	362 mg (1.00 mmol) of 3-brom-10-hexyl-10 <i>H</i> -phenothiazin (1c)	121 mg (1.00 mmol) of phenyl boronic acid (2d)	201 mg (56%) of 3j

^aReaction time of 12 h. ^bReaction time of 48 h. ^cReaction time of 45 h. ^dReaction time of 16 h.

^eReaction time of 22 h. ^fReaction time of 72 h. ^gReaction time of 25 h. ^hReaction time of 3 h.

ⁱThe reaction was conducted in a degassed mixture of 1,4-dioxane (8 mL) and water (4 mL).

3-(2,6-Dimethoxyphenyl)-10*H*-phenothiazine (**3a**)

According to the GP and after chromatography on silica gel (ether/pentane 1:2) 330 mg (78%) of compound **3a** were obtained as a rose powder, R_f (diethyl ether/pentane 1:2) = 0.30, Mp 204-205 °C.

¹H NMR (d_6 -DMSO, 300 MHz), δ 3.64 (s, 6 H), 6.66-6.83 (m, 7 H), 6.90 (m_c, 1 H), 6.98 (m_c, 1 H), 7.23 (t, J = 8.4 Hz, 1 H), 8.59 (s, 1 H). ¹³C NMR (d_6 -DMSO, 75 MHz), δ 55.8 (CH₃), 104.5 (CH), 113.9 (CH), 114.6 (CH), 115.5 (C_{quat}), 116.6 (C_{quat}), 117.9 (C_{quat}), 121.8 (CH), 126.4 (CH), 127.6 (CH), 127.7 (C_{quat}), 128.4 (CH), 128.8 (CH), 130.2 (CH), 140.7 (C_{quat}), 142.4 (C_{quat}), 157.3 (C_{quat}). MS (EI⁺, 70 eV) m/z (%): 336 (21), 335 (M⁺, 100), 289 (14). IR (KBr), $\tilde{\nu}$ [cm⁻¹]: 3381 (m), 3000 (w), 2935 (w), 2834 (w), 2182 (w), 1891 (w), 1579 (s), 1504 (w), 1469 (vs), 1428 (s), 1377 (w), 1303 (s), 1265 (m), 1246 (vs), 1171 (w), 1107 (vs), 1033 (w), 1024 (w), 886 (w), 819 (w), 789 (w), 745 (m). UV/VIS (DMSO), λ_{max} [nm] (ϵ): 262 (38400), 322 (6400). Anal. calcd. for C₂₀H₁₇NO₂S (335.4): C 71.62, H 5.11, N 4.18, S 9.56; Found: C 71.57, H 5.39, N 4.02, S 9.13.

3-(4-*tert*-Butylphenyl)-10*H*-phenothiazine (**3b**)

According to the GP and after chromatography on silica gel (ether/pentane 1:1) 214 mg (80 %) of compound **3b** were obtained as a rose powder, R_f (diethyl ether) = 0.90, Mp 253-255 °C.

¹H NMR (d_6 -DMSO, 300 MHz), δ 1.27 (s, 12 H), 6.67-6.77 (m, 3 H), 6.90-7.00 (m, 2 H), 7.17 (d, J = 1.8 Hz, 1 H), 7.26 (dd, J = 1.8 Hz, J = 8.3 Hz, 1 H), 7.39 (d, J = 8.4 Hz, 2 H), 7.46 (d, J = 8.4 Hz, 2 H), 8.66 (s, 1 H). ¹³C NMR (d_6 -DMSO, 75 MHz), δ 31.2 (CH₃), 34.3 (C_{quat}), 114.6 (CH), 114.8 (CH), 116.3 (C_{quat}), 117.1 (C_{quat}), 121.9 (CH), 124.0 (CH), 125.5 (CH), 125.7 (CH), 125.8 (CH), 126.4 (CH), 127.7 (CH), 133.8 (C_{quat}), 136.5 (C_{quat}), 141.3 (C_{quat}), 141.9 (C_{quat}), 149.3 (C_{quat}). MS (EI⁺, 70 eV) m/z (%): 332 (24), 331 (M⁺, 100), 317 (13), 316 (52), 301 (27). IR (KBr), $\tilde{\nu}$ [cm⁻¹]: 3372 (m, br), 2961 (m), 1605 (w), 1577 (w), 1460 (m, sh), 1471 (vs), 1431 (w), 1307 (m), 1269 (w), 1125 (w),

1034 (w), 813 (s), 744 (s). – UV/VIS (DMSO), λ_{max} [nm] (ϵ): 270 (36600), 333 (8400). HRMS calcd. for C₂₂H₂₁NS: 331.1394; Found: C: 331.1423.

3-(10H-Phenothiazin-3-yl)phenylamine (3c)

According to the GP and after chromatography on silica gel (ether/pentane 1:1) 249 mg (78%) of compound **3c** were obtained as a greenish brown powder, R_f (diethyl ether) = 0.46, Mp 193-194 °C.

¹H NMR (d₆-DMSO, 300 MHz), δ 5.06 (s, 2 H), 6.49 (mc, 1 H), 6.65-6.76 (m, 5 H), 6.90-7.07 (m, 4 H), 7.18 (dd, $J = 1.8$ Hz, $J = 8.3$ Hz, 1 H), 8.64 (s, 1 H). ¹³C NMR (d₆-DMSO, 75 MHz), δ 111.4 (CH), 112.8 (CH), 113.7 (CH), 114.6 (CH), 114.7 (CH), 116.3 (C_{quat}), 116.9 (C_{quat}), 121.9 (CH), 124.0 (CH), 125.7 (CH), 126.4 (CH), 127.7 (CH), 129.4 (CH), 134.8 (C_{quat}), 139.9 (C_{quat}), 141.2 (C_{quat}), 141.9 (C_{quat}), 149.2 (C_{quat}). MS (EI+, 70 eV) m/z (%): 291 (19), 290 (M⁺, 100), 289 (25), 258 (10). IR (KBr), $\tilde{\nu}$ [cm⁻¹]: 3362 (vs), 3049 (m), 1602 (vs), 1576 (vs), 1471 (vs), 1424 (vs), 1379 (w), 1305 (vs), 1253 (w), 1224 (m), 1169 (w), 1155 (w), 1125 (w), 1078 (w), 1033 (w), 994 (w), 864 (m), 820 (s), 783 (vs), 746 (vs), 688 (s), 656 (m). UV/VIS (DMSO), λ_{max} [nm] (ϵ): 265 (41800), 329 (10700). Anal. calcd. for C₁₈H₁₄N₂S (290.4): C 74.45, H 4.86, N 9.65, S 11.04; Found: C 74.18, H 4.81, N 9.49, S 10.78.

3-Phenyl-10H-phenothiazine (3d)

According to the GP and after chromatography on silica gel (ether/pentane 1:25) 213 mg (67 %) of compound **3d** were obtained as a rose powder, R_f (diethyl ether) = 0.75, Mp 217-218 °C.

¹H NMR (d₆-DMSO, 300 MHz), δ 6.67-6.77 (m, 3 H), 6.91-6.99 (m, 2 H), 7.20 (d, $J = 1.8$ Hz, 1 H), 7.27-7.31 (m, 2 H), 7.38 (t, $J = 7.3$ Hz, 2 H), 7.55 (d, $J = 7.4$ Hz, 2 H), 8.68 (s, 1 H). ¹³C NMR (d₆-DMSO, 75 MHz), δ 114.6 (CH), 114.9 (CH), 116.3 (C_{quat}), 117.2 (C_{quat}), 122.0 (CH), 124.3 (CH), 125.8 (CH), 126.0 (CH), 126.4 (CH), 126.9 (CH), 127.7 (CH), 128.9 (CH), 133.8 (C_{quat}), 139.3 (C_{quat}), 141.5 (C_{quat}), 141.8 (C_{quat}). MS (EI+, 70 eV) m/z (%): 276 (20), 275 (M⁺, 100), 274 (25). IR (KBr), $\tilde{\nu}$ [cm⁻¹]: 3362 (vs), 3055 (w), 1881 (w), 1601 (m), 1576 (m), 1487 (s), 1469 (vs), 1424 (m), 1382 (w), 1305 (m), 1273 (w), 1155 (w), 1125 (w), 1078 (w), 1032 (w), 884 (w), 819 (s), 758 (vs), 749 (vs), 689 (s). UV/VIS (DMSO), λ_{max} [nm] (ϵ): 268 (35800), 335 (8000). HRMS calcd. for C₁₈H₁₃NS (275.3): 275.0768; Found: 275.0776.

3-Thiophen-2-yl-10H-phenothiazine (3e)

According to the GP and after chromatography on silica gel (ether/pentane 1:4) 226 mg (68%) of compound **3e** were obtained as golden brown crystals that were sensitive to oxidation in solution, R_f (diethyl ether/pentane 1:4) = 0.24, Mp 220-222 °C.

^1H NMR (d_6 -DMSO, 300 MHz), δ 6.66-6.77 (m, 3 H), 6.90-7.06 (m, 3 H), 7.18 (d, $J = 1.8$ Hz, 1 H), 7.24 (dd, $J = 1.8$ Hz, $J = 8.1$ Hz, 1 H), 7.32 (m_c , 1 H), 7.40 (m_c , 1 H), 8.71 (s, 1 H). ^{13}C NMR (d_6 -DMSO, 75 MHz), δ 114.6 (CH), 114.8 (CH), 116.0 (C_{quat}), 117.3 (C_{quat}), 122.1 (CH), 122.4 (CH), 123.0 (CH), 124.5 (CH), 125.1 (CH), 126.4 (CH), 127.8 (CH), 127.85 (C_{quat}), 128.5 (CH), 141.4 (C_{quat}), 141.6 (C_{quat}), 142.9 (C_{quat}). MS (EI+, 70 eV) m/z (%): 282 (20), 281 (M^+ , 100), 280 (17), 249 (24), 248 (14), 236 (14), 204 (11). IR (KBr), $\tilde{\nu}$ [cm^{-1}]: 3362 (vs), 3070 (w), 1603 (w), 1576 (m), 1532 (w), 1471 (vs), 1428 (s), 1389 (w), 1298 (s), 1259 (w), 1211 (w), 1153 (w), 1125 (w), 1076 (w), 1033 (w), 930 (w), 879 (w), 811 (vs), 751 (vs), 693 (s). UV/VIS (DMSO), λ_{max} [nm] (ϵ): 265 (19000, sh), 287 (21900), 346 (8700). HRMS calcd. for $\text{C}_{16}\text{H}_{11}\text{NS}_2$: 281.0332; Found: 281.0349.

4-(10H-Phenothiazin-3-yl)-benzaldehyde (3f)

According to the GP and after chromatography on silica gel (ether/pentane 1:2) 239 mg (80%) of compound **3f** were obtained as an intense yellow powder, R_f (diethyl ether/pentane 1 : 2) = 0.10, Mp 202 °C.

^1H NMR (d_6 -DMSO, 300 MHz), δ 6.67-6.78 (m, 3 H), 6.91-6.99 (m, 2 H), 7.33 (d, $J = 1.7$ Hz, 1 H), 7.40 (dd, $J = 1.8$ Hz, $J = 8.3$ Hz, 1 H), 7.80 (d, $J = 8.3$ Hz, 2 H), 7.90 (d, $J = 8.3$ Hz, 2 H), 8.80 (s, 1 H), 9.98 (s, 1 H). ^{13}C NMR (d_6 -DMSO, 75 MHz), δ 114.7 (CH), 114.9 (CH), 116.1 (C_{quat}), 117.4 (C_{quat}), 122.2 (CH), 124.7 (CH), 126.2 (CH), 126.4 (CH), 126.6 (CH), 127.8 (CH), 130.3 (CH), 132.1 (C_{quat}), 134.6 (C_{quat}), 141.3 (C_{quat}), 142.5 (C_{quat}), 144.9 (C_{quat}), 192.6 (CH). MS (EI+, 70 eV) m/z (%): 304 (17), 303 (M^+ , 100), 274 (22), 273 (15), 241 (19). IR (KBr), $\tilde{\nu}$ [cm^{-1}]: 3435 (s, br), 2924 (w), 2852 (w), 1691 (s), 1598 (vs), 1575 (s), 1521 (w), 1491 (m), 1471 (vs), 1435 (w), 1387 (w), 1308 (s), 1272 (m), 1218 (m), 1175 (s), 1079 (w), 1033 (w), 836 (m), 811 (s), 750 (s). UV/VIS (DMSO), λ_{max} [nm] (ϵ): 284 (24700), 402 (11400). Anal. calcd. for $\text{C}_{19}\text{H}_{13}\text{NOS}$ (303.4): C 75.22, H 4.32, N 4.62, S 10.57; Found: C 75.29, H 4.37, N 4.53, S 10.28.

3-(3-Trifluoromethylphenyl)-10H-phenothiazine (3g)

According to the GP and after chromatography on silica gel (ether/pentane 1:2) 373 mg (97%) of compound **3g** were obtained as a light yellow powder, R_f (diethyl ether/pentane 1:2) = 0.30, Mp 217 °C

^1H NMR (d_6 -DMSO, 300 MHz), δ 6.67-6.77 (m, 3 H), 6.90-7.01 (m, 2 H), 7.32-7.39 (m, 2 H), 7.57-7.62 (m, 2 H), 7.87 (m_c , 2 H), 8.74 (s, 1 H). ^{13}C NMR (d_6 -DMSO, 75 MHz), δ 114.7 (CH), 114.9 (CH), 116.2 (C_{quat}), 117.4 (C_{quat}), 122.1 (CH), 122.2 (m_c , CH), 123.4 (m_c , CH), 124.6 (CH), 126.2 (m_c , C_{quat}), 126.3 (CH), 126.4 (CH), 127.8 (CH), 129.8 (CH), 129.9 (d, $J = 28$ Hz,

C_{quat} , 130.0 (CH), 132.0 (C_{quat}), 140.3 (C_{quat}), 141.5 (C_{quat}), 142.2 (C_{quat}). MS (EI+, 70 eV) m/z (%): 344 (22), 343 (M^+ , 100), 342 (16), 311 (17). IR (KBr), $\tilde{\nu}$ [cm^{-1}]: 3435 (m, br), 3363 (s), 2928 (w), 1602 (w), 1577 (w), 1479 (s), 1448 (m), 1422 (m), 1382 (w), 1335 (vs), 1303 (w), 1293 (w), 1263 (w), 1174 (vs), 1111 (s), 1074 (m), 1043 (m), 877 (w), 798 (s), 756 (s), 694 (m). UV/VIS ($CHCl_3$), λ_{max} [nm] (ϵ): 265 (34000), 328 (6800). Anal. calcd. for $C_{19}H_{12}F_3NS$ (343.4): C 66.46, H 3.52, N 4.08; Found: C 66.46, H 3.26, N 4.03.

3-(3,5-Bis-trifluoromethylphenyl)-10H-phenothiazine (3h)

According to the GP and after chromatography on silica gel (ether/pentane 1:2) 194 mg (87%) of compound **3h** were obtained as a light green powder, R_f (diethyl ether/pentane 1:2) = 0.34, Mp 199 °C

1H NMR (d_6 -DMSO, 300 MHz), δ 6.67 (d, J = 7.7 Hz, 1 H), 6.73-6.77 (m, 2 H), 6.92 (m_c , 1 H), 6.98 (m_c , 1 H), 7.48-7.51 (m, 2 H), 7.94 (s, 1 H), 8.22 (s, 2 H), 8.81 (s, 1 H). ^{13}C NMR (d_6 -DMSO, 75 MHz), δ 114.7 (CH), 114.8 (CH), 116.2 (C_{quat}), 117.6 (C_{quat}), 120.0 (m_c , CH), 123.5 (d, J = 271 Hz, C_{quat}), 122.3 (CH), 125.0 (CH), 126.3 (m_c , CH), 126.4 (CH), 126.8 (CH), 127.8 (CH), 130.3 (C_{quat}), 130.9 (quat, J = 32 Hz, CH), 141.3 (C_{quat}), 141.8 (C_{quat}), 142.8 (C_{quat}). MS (EI+, 70 eV) m/z (%): 412 (22), 411 (M^+ , 100), 410 (13), 379 (16). IR (KBr), $\tilde{\nu}$ [cm^{-1}]: 3435 (s, br), 2927 (w), 1605 (w), 1578 (w), 1478 (m), 1465 (m), 1377 (s), 1280 (vs), 1184 (m), 1130 (s), 1067 (w), 899 (w), 881 (w), 749 (w), 682 (w). UV/VIS (DMSO), λ_{max} [nm] (ϵ): 271 (27300), 340 (7100), 372 (7000). Anal. calcd. for $C_{20}H_{11}F_6NS$ (411.3): C 58.40, H 2.70, N 3.40; Found: C 58.55, H 2.39, N 3.36.

10-Methyl-3-phenyl-10H-phenothiazine (3i)

According to the GP and after concentration of the extraction solvents 240 mg (83%) of compound **3i** were obtained as colorless crystals, Mp 126-127 °C.

1H NMR ($CDCl_3$, 300 MHz), δ 3.38 (s, 3 H), 6.83 (m_c , 2 H), 6.93 (m_c , 1 H), 7.15 (d, J = 7.5 Hz, 2 H), 7.19-7.31 (m, 1 H), 7.37-7.42 (m, 4 H), 7.52 (d, J = 7.3 Hz, 2 H). ^{13}C NMR ($CDCl_3$, 75 MHz), δ 35.3 (CH_3), 114.1 (CH), 114.2 (CH), 122.5 (CH), 123.1 (C_{quat}), 123.8 (C_{quat}), 125.6 (CH), 126.1 (CH), 126.5 (CH), 126.9 (CH), 127.2 (CH), 127.5 (CH), 128.8 (CH), 135.6 (C_{quat}), 140.0 (C_{quat}), 145.1 (C_{quat}), 145.6 (C_{quat}). MS (EI+, 70 eV) m/z (%): 290 (20), 289 (M^+ , 100), 275 (13), 274 (59), 144 (15). IR (KBr), $\tilde{\nu}$ [cm^{-1}]: 3436 (m, br), 1629 (w, br), 1602 (w), 1577 (w), 1464 (vs), 1335 (m), 1260 (m), 1142 (w), 1042 (w), 873 (w), 810 (w), 762 (m), 750 (m), 697 (w). UV/VIS ($CHCl_3$), λ_{max} [nm] (ϵ): 265 (31200), 318 (7200). Anal. calcd. for $C_{19}H_{15}NS$ (289.4): C 78.86, H 5.22, N 4.84, S 11.08; Found: C 78.50, H 5.24, N 4.81, S 11.03.

10-Hexyl-3-phenyl-10H-phenothiazine (3j)

According to the GP and after chromatography on silica gel (pentane) 201 mg (56%) of compound **3j** were obtained as a light yellow oil, R_f (pentane) = 0.31.

^1H NMR (d_6 -acetone, 300 MHz), δ 0.84 (m_c , 3 H), 1.28 (m_c , 4 H), 1.45 (m_c , 2 H), 1.79 (m_c , 2 H), 3.95 (t, $J = 7.0$ Hz, 2 H), 6.93 (m_c , 1 H), 7.00-7.08 (m, 2 H), 7.13-7.22 (m, 2 H), 7.29 (m_c , 1 H), 7.38-7.48 (m, 4 H), 7.59 (m_c , 2 H). ^{13}C NMR (d_6 -acetone, 75 MHz), δ 14.2 (CH_3), 23.2 (CH_2), 27.1 (CH_2), 27.5 (CH_2), 32.1 (CH_2), 47.8 (CH_2), 116.6 (CH), 116.8 (CH), 123.3 (CH), 125.1 (C_{quat}), 126.0 (C_{quat}), 126.1 (CH), 126.7 (CH), 127.1 (CH), 127.8 (CH), 128.0 (CH), 128.3 (CH), 129.6 (CH), 136.1 (C_{quat}), 140.6 (C_{quat}), 145.5 (C_{quat}), 146.0 (C_{quat}). MS (EI+, 70 eV) m/z (%): 360 (30), 359 (M^+ , 100), 288 (35), 275 (19), 274 (79), 256 (13). IR (Film), $\tilde{\nu}$ [cm^{-1}]: 2954 (s), 2927 (s), 2855 (m), 1599 (m), 1576 (m), 1508 (w), 1483 (m), 1462 (vs), 1443 (m), 1395 (w), 1332 (m), 1293 (w), 1250 (s), 1133 (w), 1105 (w), 818 (m), 761 (vs), 747 (s), 697 (s). UV/VIS (CH_2Cl_2), λ_{max} [nm] (ϵ): 236 (20400), 268 (37300), 322 (8100). Anal. calcd. for $\text{C}_{24}\text{H}_{25}\text{NS}$ (359.5): C 80.17, H 7.01, N 3.89, S 8.92; Found: C 80.40, H 7.07, N 4.07, S 8.86.

ACKNOWLEDGMENTS

The authors cordially acknowledge the financial support of the Deutsche Forschungsgemeinschaft (SFB 486, project B6) and the Fonds der Chemischen Industrie.

REFERENCES

1. a) A. Suzuki, *Acc. Chem. Res.* **1982**, *15*, 178-184. b) T. Watanabe, N. Miyaura, A. Suzuki, *Synlett* **1992**, 207-210. c) T. Oh-e, N. Miyaura, A. Suzuki, *J. Org. Chem.* **1993**, *58*, 2201-2208. d) A. Suzuki, *Pure Appl. Chem.* **1994**, *66*, 213-222. e) N. Miyaura, A. Suzuki, *Chem. Rev.* **1995**, *95*, 2457-2383. f) A. Suzuki, *J. Organomet. Chem.* **1999**, *576*, 147-168. g) A.D. Schlüter, *J. Polym. Sci.: Part A: Polym. Chem.* **2001**, *39*, 1533-1556. h) S. Kotha, K. Lahiri, D. Kashinath, *Tetrahedron* **2002**, *58*, 9633-9695.
2. a) A. Bende, I. Grosu, I. Turcu, *J. Phys. Chem. A* **2010**, *114*, 12479-12489. b) E. Gal, C. Cristea, L. Silaghi-Dumitrescu, T. Lovasz, A. Csampai, *Tetrahedron* **2010**, *66*, 9938-9944. c) L. Gaina, C. Cristea, C. Moldovan, D. Porumb, E. Surducianu, C. Deleanu, A. Mahamoud, J. Barbe, I. A. Silberg, *Int. J. Mol. Sci.* **2007**, *8*, 70-80. d) I. A. Silberg, G. Cormos, D. C. Oniciu In *Adv. Heterocycl. Chem.*, A. R. Katritzky, ed., **2006**, *90*, 205-237. e) D. Dicu, L. Muresan, I. C. Popescu, C. Cristea, I. A. Silberg, P. Brouant, *Electrochim. Acta* **2000**, *45*, 3951-3957. f) I. A. Silberg, C. Cristea, *Heterocycl. Commun.* **1996**, *2*, 117-124.

3. K. Okada, T. Imakura, M. Oda, H. Murai, M. Baumgarten, *J. Am. Chem. Soc.* **1996**, *118*, 3047-3048.
4. R. Duesing, G. Tapolski, T.J. Meyer, *J. Am. Chem. Soc.* **1990**, *112*, 5378-5379.
5. W.E. Jones, P. Chen, T.J. Meyer, *J. Am. Chem. Soc.* **1992**, *114*, 387-388.
6. J. Daub, R. Engl, J. Kurzawa, S.E. Miller, S. Schneider, A. Stockmann, M.R. Wasielewski, *J. Phys. Chem. A* **2001**, *105*, 5655-5665.
7. M. Sailer, A.W. Franz, T.J.J. Müller, *Chem. Eur. J.* **2008**, *14*, 2602-2614.
8. K. Memminger, T. Oeser, T.J.J. Müller, *Org. Lett.* **2008**, *10*, 2797-2800.
9. G. Zhou, N. Pschirer, J.C. Schöneboom, F. Eickemeyer, M. Baumgarten, K. Müllen, *Chem. Mater.* **2008**, *20*, 1808-1815.
10. M. Hauck, M. Stolte, J. Schönhaber, H.-G. Kuball, T.J.J. Müller, *Chem. Eur. J.* **2011**, *17*, 9984-9998.
11. M. Hauck, J. Schönhaber, A.J. Zuccherro, K.I. Hardcastle, T.J.J. Müller, U.H. F. Bunz, *J. Org. Chem.* **2007**, *72*, 6714-6725.
12. N. Bucci, T.J.J. Müller, *Tetrahedron Lett.* **2006**, *47*, 8329-8332.
13. N. Bucci, T.J.J. Müller, *Tetrahedron Lett.* **2006**, *47*, 8323-8327.
14. S. Bay, T. Villnow, G. Ryseck, V. Rai-Constapel, P. Gilch, T.J.J. Müller, *ChemPlusChem* **2013**, *78*, 137-141.
15. S. Bay, G. Makhloufi, C. Janiak, T.J.J. Müller, *Beilstein J. Org. Chem.* **2014**, *10*, 1006-1016.
16. S. Bay, T.J.J. Müller, *Z. Naturforsch.* **2014**, *69b*, 541-553.
17. T.J.J. Müller, A. W. Franz, C. S. Barkschat (née Krämer), M. Sailer, K. Meerholz, D. Müller, A. Colsmann, U. Lemmer, *Macromol. Symp.* **2010**, *287*, 1-7.
18. Z. Zhou, A. W. Franz, M. Hartmann, A. Seifert, T.J.J. Müller, W. R. Thiel, *Chem. Mater.* **2008**, *20*, 4986-4992.
19. T. Meyer, D. Ogermann, A. Pankrath, K. Kleinermanns, T.J.J. Müller, *J. Org. Chem.* **2012**, *77*, 3704-3715.
20. H. Tian, X. Yang, R. Chen, Y. Pan, L. Li, A. Hagfeldt, L. Sun, *Chem. Commun.* **2007**, 3741-3743.
21. S. S. Park, Y. S. Won, Y. C. Choi, J. H. Kim, *Energy Fuels* **2009**, *23*, 3732-3736.
22. C. Lambert, V. Kriegisch, *Langmuir* **2006**, *22*, 8807-8812.
23. C. S. Barkschat, S. Stoycheva, M. Himmelhaus, T.J.J. Müller, *Chem. Mater.* **2010**, *22*, 52-63.
24. A. W. Franz, S. Stoycheva, M. Himmelhaus, T.J.J. Müller, *Beilstein J. Org. Chem.* **2010**, *6*, No 72. doi:10.3762/bjoc.6.72.
25. J. Rechmann, A. Sarfraz, A. C. Götzinger, E. Dirksen, T.J.J. Müller, A. Erbe, *Langmuir* **2015**, *31*, 7306-7316.
26. For synthesis of phenothiazinyl boronic acid derivatives, see e. g. a) C. S. Krämer, T.J. Zimmermann, M. Sailer, T.J.J. Müller, *Synthesis* **2002**, 1163-1170. b) A.W. Franz, T.J.J. Müller, *Synthesis* **2008**, 1121-1125.
27. For representative phenothiazine functionalization with phenothiazinyl boronates, see e. g. a) C.S. Krämer, K. Zeitler, T.J.J. Müller, *Tetrahedron Lett.* **2001**, *42*, 8619-8624. b) M. Sailer, F. Rominger, T.J.J. Müller, *J. Organomet. Chem.* **2006**, *691*, 299-308. c) M. Sailer, M. Nonnenmacher, T. Oeser, T.J.J. Müller, *Eur. J. Org. Chem.* **2006**, 423-435. d) M. Hauck, R. Turdean, K. Memminger, J. Schönhaber, F. Rominger, T.J.J. Müller, *J. Org. Chem.* **2010**, *75*, 8591-8603.
28. J. Cymerman-Craig, W.P. Rogers, G.P. Warwick, *Austr. J. Chem.* **1955**, *8*, 252-257.

29. S. Ebdrup, *Austr. J. Chem. Soc., Perkin Trans. 1* **1998**, 1147-1150.
30. Y.S. Kang, P. Baglioni, H.J.D. McManus, L. Kevan, *J. Phys. Chem.* **1991**, *95*, 7944-7947.
31. N.S. Angerman, S.S. Danyluk, *Org. Magn. Res.* **1972**, *4*, 895-906.
32. M.A. Palafox, M. Gil, J.L. Nunez, G. Tardajos, *Int. J. Quant. Chem.* **2002**, *89*, 147-171.
33. E. Wagner, S. Filipek, M.K. Kalinowski, *Monatsh. Chem.* **1988**, *119*, 929-932.
34. P. Zanello, in: *Ferrocenes* (Eds.: A. Togni, T. Hayashi), VCH, Weinheim, New York, Basel, Cambridge, Tokyo, **1995**, pp 317-430.
35. T.J. Kemp, P. Moore, G.R. Quick, *J. Chem. Soc. Perkin Trans. II* **1980**, 291-295.
36. W.T. Dixon, D. Murphy, *J. Chem. Soc. Perkin Trans. II* **1976**, 1823-1828.
37. J.A. Elix, K.L. Gaul, D.C.R. Hockless, J.H. Wardlaw, *Aust. J. Chem.* **1995**, *48*, 1049-1053.
38. J.E. Bloor, B.R. Gilson, R.J. Haas, C.L. Zirkle, *J. Med. Chem.* **1970**, *13*, 922-925.
39. M. Jonsson, D.D.M. Wayner, J. Lusztyk, *J. Phys. Chem.* **1996**, *100*, 17539-17543.
40. N.R. Armstrong, R.K. Quinn, N. E. Vanderborgh, *Anal. Chem.* **1974**, *46*, 1759-1764.
41. C. Hansch, A. Leo, R.W. Taft, *Chem. Rev.* **1991**, *91*, 165-195.
42. Application of B3LYP 6-31 G* density functionals as implemented in SPARTAN '08 V 1.2.0, Wavefunction Inc., Irvine, **2008**.
43. H.G.O. Becker, W. Berger, G. Domschke, E. Fanghänel, J. Faust, M. Fischer, F. Gentz, K. Gewalt, R. Gluch, R. Mayer, K. Müller, D. Pavel, H. Schmidt, K. Schollberg, K. Schwetlick, E. Seiler, G. Zeppenfeld, *Organikum*, 20th ed., Johann Ambrosius Barth, Heidelberg, Leipzig, **1996**.

*Dedicated to Professor Luminița Silaghi-Dumitrescu
on the occasion of her 65th anniversary*

NOVEL 1,9-DIACYL-5- (PHENOTHIAZINYL)DIPYRRROMETHANE DIALKYL TIN COMPLEXES

BALAZS BREM^{a*}, EMESE GAL^a, LUIZA GĂINĂ^a, TAMAS LOVASZ^a,
EVA-ANDREA MOLNAR^a, DAN PORUMB^a and CASTELIA CRISTEA^a

ABSTRACT New 1,9-diacyl-5-(phenothiazinyl)dipyrromethane (aphdpm) obtained by diacylation of 5-phenothiazinyl-dipyrromethane were subjected to complexation reactions with dimethyl- and di-*n*-butyltin(IV) dichloride which afforded complexes of the type [Me₂Sn(aphdpm)] and [(*n*-Bu)₂Sn(aphdpm)] respectively [where aphdpm: 1,9-diformyl-5-(phenothiazinyl)dipyrromethane and 1,9-dibenzoyl-5-(phenothiazinyl) dipyrromethane]. Plausible structures of the new tin(IV) complexes were proposed based on spectroscopic FT-IR, ¹H-, ¹³C-, ¹¹⁹Sn-NMR and mass spectrometry studies.

Keywords: *Dipyrromethane, Phenothiazine, Tin complexes*

INTRODUCTION

Dipyrromethanes bearing acyl groups at the α positions of the pyrrole units are key precursors to porphyrins with diverse substituents in the *meso* positions and thus the synthetic procedures gained additional importance. Taking benefit from the electron rich nature of the pyrrole units, substitution was readily achieved in the presence of mild electrophiles. Thus, Vilsmeier formylation [1] and benzoylation procedures were applied in the preparation of acyl-dipyrromethanes [2] producing both mono- and diacylated dipyrromethanes

^a Babeş-Bolyai University, Faculty of Chemistry and Chemical Engineering 11 Arany Janos str.,
RO-400028, Cluj-Napoca, Romania

* Corresponding author: brembalazs@gmail.com

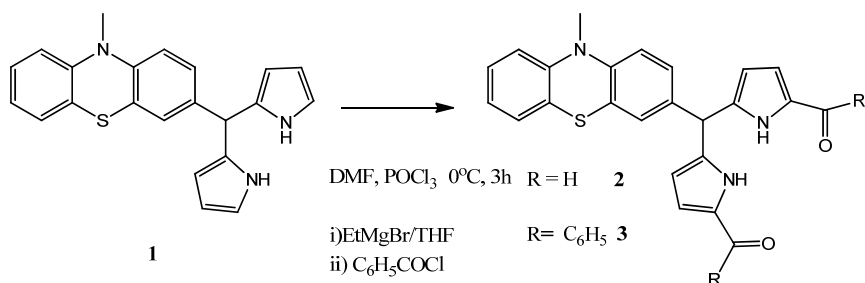
with high regioselectivity for the α positions of the pyrrole rings. The treatment of a dipyrromethane with ethylmagnesium bromide in THF followed by the reaction of the pyrrolate intermediate with acid chloride also generated a mixture of mono- and diacylated dipyrromethane [3]. Optimization of the reaction conditions (reagents ratio, solvent, temperature) afforded increased ratio of diacylated : monoacylated derivatives (5:1) [4].

The properties of the dipyrromethanes can be conveniently modulated by the presence of various structural motifs in the *meso* position (methylene bridge) and/or by introducing different substituents in the α positions of the pyrrole units. The current interest on organotin(IV) complexes lays on a wide range of applications [5] such as catalysts, biocides [6] or antitumor agents [7]. 1,9-Diacyldipyrromethane-tin complexes were reported to be formed selectively from a crude acylation mixture upon treatment with dibutyltin dichloride [8].

Dipyrromethane derivatives functionalized in the *meso* position with phenothiazine units were first reported by our research group [9] and in this work we focus on their chemical characterization by describing the acylation and tin complexation of 1,9-diacyl-phenothiazinyl-dipyrromethanes ligands. Taking into consideration the biological activity potential of the individual heterocyclic units embedded in their structure, we consider the new phenothiazine functionalized dipyrromethane derivatives as stimulating structures for applications in biological systems.

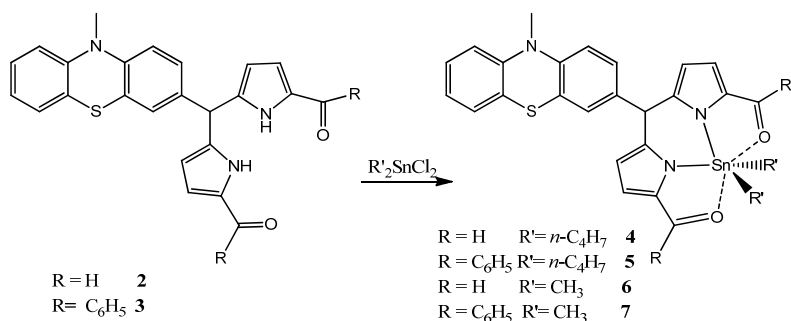
RESULTS AND DISCUSSION

The reactivity of the starting phenothiazinyl-dipyrromethanes **1** is governed by the presence of two types of electron rich heteroaromatic units susceptible of readily undergoing electrophilic substitution under the influence of mild electrophiles. Careful selection of the reaction conditions was required for increasing the regioselectivity. The synthesis of 1,9-diformyl-phenothiazinyl-dipyrromethane **2** and 1,9-dibenzoyl-phenothiazinyl-dipyrromethane **3** are presented in Scheme 1. Vilsmeier formylation performed at 0°C offered a high regioselectivity towards the α positions of the pyrrole units generating diformyl derivative **2** in 65% yields. 1,9-dibenzoyl-phenothiazinyl-dipyrromethane **3** was prepared in 45% yields by a two steps procedure which implied the treatment of the starting phenothiazinyl-dipyrromethane with ethylmagnesium bromide, followed by the reaction of dipyrromethane analog of the "pyrrole Grignard reagent," with benzoyl chloride.

**Scheme 1**

The FT-IR analysis of the acylation products **2** and **3** displayed the absorption band corresponding to the stretching vibration of the carbonyl bonds situated at 1650 cm^{-1} .

The reaction of diacyl derivatives **2**, **3** with dibutyltin dichloride and dimethyltin dichloride respectively, afforded the corresponding tin complexes **2SnBu₂** **4**, **3SnBu₂** **5**, **2SnMe₂** **6** and **3SnMe₂** **7** (scheme 2) which were isolated by passage through a silica pad followed by precipitation from methanol.

**Scheme 2**

The structural assignments of the complexes were based on FT-IR, ^1H -, ^{13}C - and ^{119}Sn -NMR spectroscopy and high resolution mass spectrometry studies. The molecular weight of each complex **4-7** was determined from the HRMS(APCI+) spectrum which displayed the molecular ion in high abundance. In the IR domain the main spectral changes included the disappearance of the IR stretching vibrations of the N-H bonds of the ligands and the shifting of the characteristic stretching vibration of the carbonyl bonds towards lower wavenumber values. Deeper structural assignments of dialkyltin complexes **4-7** were achieved based on 2D-NMR homonuclear correlation

(H-H COSY) and heteronuclear (HMQC) experiments. Upon complexation, the protons attached to the pyrrole units appeared more shielded (chemical shift values with additional 0.3–0.2 ppm), but only a negligible effect of the environment was recorded for the protons of the phenothiazine unit situated in the *meso* position. The alkyl groups connected to the tin atom gave two sets of signals in both ^1H - and ^{13}C -NMR spectra according to their *syn* or *anti* spatial position with respect to the *meso*-substituent.

For each complex **4-7** the decoupled ^{119}Sn -NMR spectrum displayed a signal situated in the range from -219 ppm to -272 ppm. An upfield shift of the chemical shift value was observed as a result of a structural change of the alkyl substituent from dibutyl to dimethyl group, as well as in the case of a change of the acyl group from benzoyl to formyl group (figure 1). The undecoupled ^{119}Sn -NMR spectra revealed multiplet signals with splitting patterns mainly governed by the vicinal heteronuclear coupling constants ^{119}Sn - ^1H of about 80 Hz.

A correlation between the range of the chemical shift values recorded in the ^{119}Sn -NMR spectra of different coordination butyltin complexes with the coordination numbers of the central tin atom was previously described, offering the possibility to assign the coordination geometry around the central tin atom [10]. Based on the evidence that six-coordinate compounds are producing chemical shifts values ranging from -210 to -400 ppm, we assumed an octahedral coordination geometry for each of the complexes **4-7**.

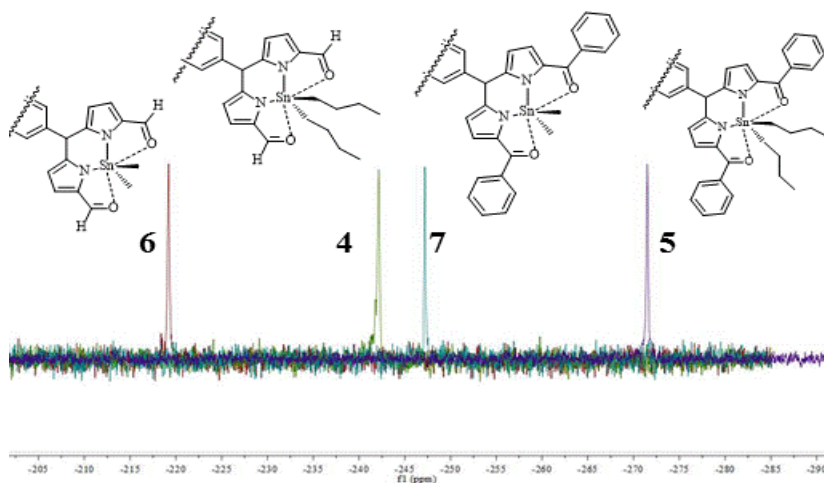


Figure 1. 149 MHz ^{119}Sn -NMR spectra of 1,9-diacyl-5-(phenothiazinyl)-dipyrromethane dialkyltin complexes

CONCLUSIONS

Synthetic procedures for the preparation of novel 1,9-diacyl-phenothiazinyl-dipyrromethane derivatives based on Vilsmeier formylation and acylation with benzoyl chloride respectively, were described.

New [diacyl-5-(phenothiazine-3-yl)dipyrromethane]-dialkyltin complexes were obtained and their structure was confirmed by high resolution spectroscopic techniques (FT-IR, ^1H -, ^{13}C -, ^{119}Sn -NMR spectroscopy and HRMS). An octahedral coordination geometry of the central tin atom was sustained by literature data regarding the plausible correlation between the ^{119}Sn -NMR chemical shifts and the coordination geometry of butyltin complexes.

EXPERIMENTAL SECTION

All chemicals used were of reagent grade. The melting points were determined in capillaries with an Electrothermal 9100 instrument. HRMS spectra were recorded on a Thermo LTQ *Orbitrap XL* with ESI+ ionization mode. NMR spectra were recorded in solution at room temperature on a 400 and 600 MHz Bruker Avance instrument. Chemical shifts are expressed in terms of δ (ppm) relative to standard tetramethylsilane (TMS). FT-IR spectra were recorded in KBr pellet using a Bruker Vector 22 instrument.

5-(phenothiazinyl)dipyrromethane: **1** was prepared according to our previously reported procedure [9].

Synthesis of 5,5'-((10-methyl-10*H*-phenothiazin-3-yl)methylene)bis(1*H*-pyrrole-2-carbaldehyde) (2). DMF (10 mL) was treated with POCl_3 (1 mL, 10.2 mmol) at 0°C under argon, and the resulting solution was stirred for 10 min (Vilsmeier reagent). A solution of **1** (1.00 g, 2.8 mmol) in DMF (15 mL) at 0°C under argon was treated with the freshly prepared Vilsmeier reagent, and the resulting solution was allowed to stir for 1.5 h at 0°C . Saturated aqueous sodium acetate solution (100 mL) was added, and the ice bath was removed. The mixture was then stirred for 4 h and allowed to warm to room temperature. The mixture was extracted with ethyl acetate. The collected organic phase was washed with brine, dried with MgSO_4 , and filtered. The filtrate was concentrated to dryness under reduced pressure. The crude product was purified by column chromatography (using silica gel and DCM/MeOH ratio 20/1 as eluent), the product is a brown-yellow solid, 65% yield, m.p. $192\text{--}194^\circ\text{C}$ (decomp.); MS (ESI+): 414 [$\text{M}+\text{H}^+$], 396; ^1H -NMR (400MHz, CDCl_3): δ ppm: 3.35 (s, 3H, N- CH_3 -), 5.47 (s, 1H, H_5), 6.04 (m, 2H, $\text{H}_{3,7}$), 6.74 (d, 1H, $\text{H}_{1'}$, $^3\text{J}=8.8\text{Hz}$), 6.81-6.83 (m, 3H, H_9 , $\text{H}_{2,8}$), 6.94 (t, 1H, H_7 , $^3\text{J}=7.3\text{Hz}$), 7.02-7.05 (m, 2H, $\text{H}_{4,2}$), 7.12 (d, 1H, H_6 , $^3\text{J}=7.3\text{Hz}$), 7.18 (t, 1H, H_8 , $^3\text{J}=7.3\text{Hz}$), 9.18 (s, 2H, $\text{H}_{1a,9a}$), 10.52 (brs, 2H, $\text{H}_{10,11}$); ^{13}C -NMR (100 MHz, CDCl_3):

δ ppm = 35.3 (CH, C_a), 43.4 (CH, C₅), 111.4 (CH, C_{3,7}), 114.1 (CH, C₉), 114.2 (CH, C₁), 122.2 (CH, C_{2,8}), 122.6 (CH, C₇), 122.9 (Cq, C_{4a}), 124 (Cq, C_{5a}), 126.9 (CH, C₄), 127.2 (CH, C₂), 127.4 (CH, C₆), 127.5 (CH, C₈), 132.6 (Cq, C_{3,6}), 133.3 (Cq, C₃), 141.3 (Cq, C_{1,9}), 145.3 (Cq, C_{9a}), 145.5 (Cq, C_{10a}), 178.9 (Cq, C_{1a,9a}); IR (KBr): $\bar{\nu}$ (cm⁻¹): 3243, 2970, 2815, 1650, 1488, 1352, 1287, 1254, 1111, 786, 747, 669.

(5,5'-((10-methyl-10H-phenothiazin-3-yl)methylene)bis(1H-pyrrole-5,2-diy))bis(phenylmethanone) (3). A solution of EtMgBr (35 mL, 35 mmol, 1.0M solution in THF) was added slowly to a water cooled flask containing a solution of 5-(phenothiazinyl)dipyrromethane (2.5 g, 7 mmol) in toluene (200 mL) under argon. An exothermic reaction with gas evolution was observed. The resulting mixture was stirred at room temperature for 30 min. A solution of benzoyl chloride (4.07 mL, 35 mmol) in toluene (25 mL) was added over 10 min, and the resulting solution was further stirred for 10 min. The reaction mixture was poured into saturated aqueous NH₄Cl (200 mL) and ethyl acetate (150 mL). The organic layer was washed with water and brine, dried MgSO₄, and filtered. The filtrate was concentrated to dryness under reduced pressure. The crude product was purified by column chromatography (using silica gel and DCM/MeOH ratio 40/1 as eluent) and afforded the product as a brown solid in 48% yield, m.p. 114 °C (decomp.); MS (ESI+): 566 [M+H⁺], 457, 390, 274; ¹H-NMR (400MHz, CDCl₃): δ ppm: 3.37 (s, 3H, H_a), 5.63 (s, 1H, H₅), 6.01 (m, 2H, H_{3,7}), 6.56 (m, 2H, H_{2,8}), 6.77 (d, 1H, H₁, ³J = 8.3 Hz), 6.84 (d, 1H, H₉, ³J = 8.1 Hz), 6.95 (t, 1H, H₇, ³J = 7.5 Hz), 7.12 (d, 1H, H₆, ³J = 7 Hz), 7.19 (t, 1H, H₈, ³J = 7 Hz), 7.27-7.30 (m, 1H, H_{2,4}), 7.38-7.42 (m, 4H, H_c), 7.49-7.52 (m, 2H, H_d), 7.79 (d, 4H, H_b, ³J = 7.3 Hz), 11.68 (brs, 2H, H_{10,11}); ¹³C-NMR (100 MHz, CDCl₃): δ ppm: 35.3 (CH, C_a), 44 (CH, C₅), 111.1 (CH, C_{3,7}), 114 (CH, C₉), 114.2 (CH, C₁), 120.9 (CH, C_{2,8}), 122.5 (CH, C₇), 123.2 (Cq, C_{4a}), 124 (Cq, C_{5a}), 127.2 (CH, C₄), 127.4 (CH, C₂), 127.5 (CH, C₆), 127.7 (CH, C₈), 128 (CH, C_c), 129 (CH, C_d), 129.6 (CH, C_b), 131 (Cq, C_a), 131.6 (Cq, C_{4,6}), 138.2 (Cq, C₃), 141.01 (Cq, C_{1a,9a}), 145.1 (Cq, C_{9a}), 145.7 (Cq, C_{10a}), 184.5 (Cq, C_{1a,9a}); IR (KBr): $\bar{\nu}$ (cm⁻¹): 3433, 3262, 2957, 2871, 1596, 1567, 1463, 1401, 1332, 1289, 1237, 928, 774, 728, 696;

General procedure for Tin Complexation of 1,9-diacyl-dipyrro-methanes.

A crude sample of phenothiazinyl-1,9-diacyl-dipyrromethane (**2**, **3**) (2 mmol) was treated with TEA (6 mmol) and R₂SnCl₂ (2 mmol) in DCM (4 mL) at room temperature and left to stand overnight. The mixture was filtered over a short pad of silica eluted with DCM. The eluent was concentrated to dryness. The residue was dissolved in a minimum amount of diethyl ether, and then methanol was added, yielding a precipitate, which upon filtration afforded a colorless/rose solid (65-80%).

5,5-dibutyl-10-(10-methyl-10H-phenothiazin-3-yl)-5,10-dihydrodipyrrolo [1,2-c:2',1'-f][1,3,2]diazastannine-3,7-dicarbaldehyde (4). Column chromatography (DCM), MeOH precipitation, afforded the product as a white solid in 78% yields, m.p. 97-99 °C (decomp.); MS (ESI+): 646 [M+H⁺]; ¹H-NMR (600MHz, CDCl₃): δ ppm = 0.75

(t, 3H, H_δ, ³J= 7.32 Hz), 0.83 (t, 3H, H_δ, ³J= 7.32 Hz), 1.14-1.18 (m, 2H, H_γ), 1.28-1.34 (m, 4H, H_{γβ}), 1.45-1.48 (m, 4H, H_{β,α}), 1.62-1.66 (m, 2H, H_α), 3.35 (s, 3H, H_a), 5.46 (s, 1H, H₁₀), 6.18 (d, 2H, H_{1,9}, ³J= 3.8 Hz), 6.73 (d, 1H, H₁, ³J= 8.3 Hz), 6.80 (d, 1H, H₉, ³J= 8 Hz), 6.91 (d, 1H, H₄, ⁴J= 2 Hz), 6.93 (td, 1H, H₇, ⁴J= 0.8 Hz, ³J= 7.5 Hz), 6.96 (dd, 1H, H₂, ⁴J= 1.3 Hz, ³J= 8.3 Hz), 7.08 (d, 2H, H_{2,8}, ³J= 3.8 Hz), 7.12 (dd, 1H, H₆, ⁴J= 1.3 Hz, ³J= 7.6 Hz), 7.17 (td, 1H, H₈, ⁴J= 1.3 Hz, ³J= 8.2 Hz), 9.18 (s, 2H, H_{1,9}); ¹³C-NMR (125 MHz, CDCl₃): δppm= 13.4 (CH, C_δ), 13.6 (CH, C_δ), 23.9 (CH, C_α), 24.4 (CH, C_γ), 26 (CH, C_γ), 26.4 (CH, C_α), 27 (CH, C_β), 27.2 (CH, C_β), 35.2 (CH, C_a), 44.2 (CH, C₁₀), 114.03 (CH, C₉), 114.08 (CH, C₁), 115.4 (CH, C_{1,9}), 122.5 (CH, C₇), 123 (Cq, C_{4a}), 123.8 (Cq, C_{5a}), 123.9 (CH, C_{2,8}), 126.5 (CH, C₄), 126.9 (CH, C₆), 127.1 (CH, C₂), 127.5 (CH, C₈), 137.93 (Cq, C_{9a,10a}), 137.98 (Cq, C₃), 144.6 (Cq, C_{9a}), 145.6 (Cq, C_{10a}), 151.9 (Cq, C_{3,7}), 178.6 (Cq, C_{1a,9a}); ¹¹⁹Sn-NMR (149 MHz, CDCl₃): δppm= - 242.16.

5,5-dimethyl-10-(10-methyl-10H-phenothiazin-3-yl)-5,10-dihydrodipyrrolo [1,2-c:2',1'-f][1,3,2]diazastannine-3,7-dicarbaldehyde (5). Column chromatography (DCM), MeOH precipitation, afforded the product as a cream white solid in 80% yields, m.p. 164-167 °C (decomp.); MS (ESI+): 562 [M+H⁺], 469, 299; ¹H-NMR (400MHz, CDCl₃): δppm= 0.79 (s, 3H, H_α), 1.01 (s, 3H, H_α), 3.33 (s, 3H, H_a), 5.48 (s, 1H, H₁₀), 6.2 (d, 2H, H_{1,9}, ³J= 3.8 Hz), 6.72 (d, 1H, H₁, ³J= 8.25 Hz), 6.79 (d, 1H, H₉, ³J= 8.1 Hz), 6.91-6.94 (m, 3H, H_{7,4,2}), 7.07 (d, 2H, H_{2,8}, ³J= 3.8 Hz), 7.12 (dd, 1H, H₆, ⁴J= 1.5 Hz, ³J= 7.6 Hz), 7.17 (td, 1H, H₈, ⁴J= 1.5 Hz, ³J= 8.1 Hz), 9.14 (s, 2H, H_{1a,9a}); ¹³C-NMR (100 MHz, CDCl₃): δppm= 3.66 (CH, C_α), 4.64 (CH, C_α), 35.2 (CH, C_a), 44.2 (CH, C₁₀), 114 (CH, C₉), 114.2 (CH, C₁), 115.2 (CH, C_{1,9}), 122.5 (CH, C₇), 122.9 (Cq, C_{4a}), 123.9 (Cq, C_{5a}), 124 (CH, C_{2,8}), 126.3 (CH, C₄), 126.6 (CH, C₆), 127.1 (CH, C₂), 127.5 (CH, C₈), 137.5 (Cq, C_{9a,10a}), 137.9 (Cq, C₃), 144.6 (Cq, C_{9a}), 145.6 (Cq, C_{10a}), 151.7 (Cq, C_{3,7}), 178.4 (Cq, C_{1a,9a}); ¹¹⁹Sn-NMR (149 MHz, CDCl₃): δppm= -219.24; IR (KBr): $\bar{\nu}$ (cm⁻¹) = 2962, 2851, 1592, 1499, 1305, 1062, 788, 747, 755;

5,5-dibutyl-10-(10-methyl-10H-phenothiazin-3-yl)-5,10-dihydrodipyrrolo [1,2-c:2',1'-f][1,3,2]diazastannine-3,7-diyl)-bis(phenylmethanone) (6). Column chromatography (DCM), MeOH precipitation, afforded the product as a pink solid in 65% yields, m.p. 86-87 °C (decomp.); HRMS (APCI +): Calcd. for C₄₄H₄₄SnN₃O₂S [M+H⁺] 798.2154, Found 798.2171; ¹H-NMR (400MHz, CDCl₃): δppm= 0.71 (t, 3H, H_δ, ³J= 7.32 Hz), 0.79 (t, 3H, H_δ, ³J= 7.32 Hz), 1.10-1.19 (m, 2H, H_γ), 1.27-1.39 (m, 4H, H_{γβ}), 1.47-1.55 (m, 4H, H_{β,α}), 1.73-1.77 (m, 2H, H_α), 3.34 (s, 3H, H_a), 5.52 (s, 1H, H₁₀), 6.22 (d, 2H, H_{1,9}, ³J= 3.8 Hz), 6.74 (d, 1H, H₁, ³J= 8.3 Hz), 6.79 (d, 1H, H₉, ³J= 8 Hz), 6.91 (t, 1H, H₇, ³J= 7.5 Hz), 7.01 (d, 1H, H₄, ⁴J= 2 Hz), 7.03 (dd, 1H, H₂, ⁴J= 2 Hz, ³J= 7.3 Hz), 7.09-7.17 (m, 4H, H_{2,8,6,8}), 7.48- 7.52 (m, 4H, H_c), 7.55-7.58 (m, 2H, H_d), 7.91 (d, 4H, H_b); ¹³C-NMR (100 MHz, CDCl₃): δppm= 13.6 (CH, C_δ), 13.7 (CH, C_δ), 24 (CH, C_α), 24.8 (CH, C_γ), 25.9 (CH, C_γ), 26.4 (CH, C_α), 27.2 (CH, C_β), 27.3 (CH, C_β), 35.2 (CH, C_a), 44.7 (CH, C₁₀), 114 (CH, C₉), 114.06 (CH, C₁), 115.3 (CH, C_{1,9}), 122.4 (CH, C₇), 123.2 (Cq, C_{4a}), 123.7 (Cq, C_{5a}), 124.1 (CH, C_{2,8}), 126.6 (CH, C₄), 127 (CH, C₆), 127.1

(CH, C₂), 127.4 (CH, C₈), 128.4 (CH, C_c), 129 (CH, C_b), 131.6 (CH, C_d), 135.8 (C_q, C_a), 137.7 (C_q, C_{9a,10a}), 137.5 (C_q, C₃), 144.5 (C_q, C_{9a}), 145.7 (C_q, C_{10a}), 151.6 (C_q, C_{3,7}), 184.6 (C_q, C_{1a,9a}); ¹¹⁹Sn-NMR (149 MHz, CDCl₃): δppm= -271.50 ppm; IR (KBr): $\bar{\nu}$ (cm⁻¹)= 2955, 2851, 1538, 1463, 1382, 1333, 1258, 1064, 887, 727, 697, 623.

(5,5-dimethyl-10-(10-methyl-10H-phenothiazin-3-yl)-5,10-dihydrodipyrrolo [1,2-c:2',1'-f][1,3,2]diazastannine-3,7-diyl)-bis(phenylmethanone) (7). Column chromatography (DCM), MeOH precipitation, afforded the product as a rose-white solid in 67% yields, m.p. 160-163 °C (decomp.); MS (ESI+): 714.1 [M+H⁺]; ¹H-NMR (400MHz, CDCl₃): δppm= 0.83 (s, 3H, H_α'), 1.11 (s, 3H, H_α), 3.34 (s, 3H, H_a), 5.55 (s, 1H, H₁₀), 6.26 (d, 2H, H_{1,9}, ³J= 3.8 Hz), 6.74 (d, 1H, H₁, ³J= 8.3 Hz), 6.79 (d, 1H, H₉, ³J= 8 Hz), 6.93 (t, 1H, H₇, ³J= 7.3 Hz), 7.03 (dd, 1H, H₂, ⁴J= 2 Hz, ³J= 8.3 Hz), 7.06 (d, 1H, H₄, ⁴J= 2 Hz), 7.11-7.19 (m, 4H, H_{2,8,8,6}), 7.49-7.53 (m, 4H, H_c), 7.56-7.60 (m, 2H, H_d), 7.92 (d, 4H, H_b, ³J= 8.5 Hz); ¹³C-NMR (100 MHz, CDCl₃): δppm= 4.1 (CH, C_α), 5.1 (CH, C_α'), 35.2 (CH, C_a), 44.6 (CH, C₁₀), 113.9 (CH, C₉), 114.1 (CH, C₁'), 115 (CH, C_{1,9}), 122.4 (CH, C₇), 123 (C_q, C_{4a}'), 123.7 (C_q, C_{5a}'), 124.2 (CH, C_{2,8}), 126.4 (CH, C₄'), 126.6 (CH, C₆'), 127.1 (CH, C₂'), 127.4 (CH, C₈'), 128.3 (CH, C_b'), 129 (CH, C_c'), 131.6 (CH, C_d'), 135.3 (C_q, C_a'), 137.5 (C_q, C_{9a,10a}'), 138.4 (C_q, C₃'), 144.5 (C_q, C_{9a}'), 145.6 (C_q, C_{10a}'), 151.4 (C_q, C_{3,7}'), 184.2 (C_q, C_{1a,9a}'); ¹¹⁹Sn-NMR (149 MHz, CDCl₃): δppm= -247.19; IR (KBr): $\bar{\nu}$ (cm⁻¹) = 2923, 2850, 1530, 1414, 1308, 1017, 850, 750, 677.

REFERENCES

1. K.E. Borbas, H.L. Kee, D. Holten, J.S. Lindsey, *Org. Biomol. Chem.*, **2008**, 6, 187.
2. W.S. Cho, H.J. Kim, B.J. Littler, M.A. Miller, C.H. Lee, J.S. Lindsey, *J. Org. Chem.* **1999**, 64, 7890.
3. C-H. Lee, F. Li, K. Iwamoto, J. Dadok, A.A. Bothner-By, J.S. Lindsey, *Tetrahedron* **1995**, 51, 11645.
4. P.D. Rao, S. Dhanalekshmi, B.J. Littler, J.S. Lindsey, *J. Org. Chem.*, **2000**, 65, 7323.
5. M. Nath, P.K. Saini, *Dalton Trans.*, **2011**, 40, 7077.
6. S.R. Collinson, D.E. Fenton, *Coord. Chem. Rev.*, **1996**, 148, 19.
7. L. Pelleerito, L. Nagy, *Coord. Chem. Rev.*, **2002**, 224, 111.
8. S-I. Tamaru, L. Yu, W.J. Youngblood, K. Muthukumaran, M. Taniguchi, J.S. Lindsey, *J. Org. Chem.*, **2004**, 69, 765.
9. B. Brem, E. Gal, L. Gaina, C. Cristea, L. Silaghi-Dumitrescu, *Rev. Roum. Chim.*, **2014**, 59(11-12), 949.
10. J. Holeček, M. Nádvorník, K. Handlíř, A. Lyčka, *J. Organomet. Chem.*, **1986**, 315 (3), 299.

*Dedicated to Professor Luminița Silaghi-Dumitrescu
on the occasion of her 65th anniversary*

NEW STANNEPINE DERIVATIVES. SYNTHESIS AND CHARACTERISATION

LAVINIA BUTA^a, RALUCA SEPTELEAN^a, NOEMI DEAK^a,
ALEXANDRA POP^a, GABRIELA NEMES^{a*}

ABSTRACT. A new diphenylstannepinic derivative has been synthesized and completely characterized in solution and in solid state (multinuclear NMR spectroscopy, HRMS, X-ray diffraction). As a result of the reaction of the diphenylstannepinic derivative with bromine, a brominated product was evidenced by NMR spectroscopy.

Keywords: *diphenylstannepine, dibromostilbene, dihalostannepine*

INTRODUCTION

The synthesis and characterization of low coordinated compounds containing heavy elements of group 14 remain in actuality [1-4] and represent a permanent interest for our research group [5-7] which is focused on the field of heterophosphapropenes [8,9] and heterophosphaallenes [10] as potential precursors in the production of materials with controlled properties. The chemistry of low coordinated silicon and germanium compounds containing a phosphalkenyl group is well studied; however, in the case of tin, only a scarce number of phosphastannapropenes have been reported to date [9]. Furthermore, phosphastannaallenes were not reported until now, due to the difficulty in stabilizing the $>Sn=C<$ moiety. The quest for finding the suitable geometric and steric parameters in order to stabilize these systems is a real

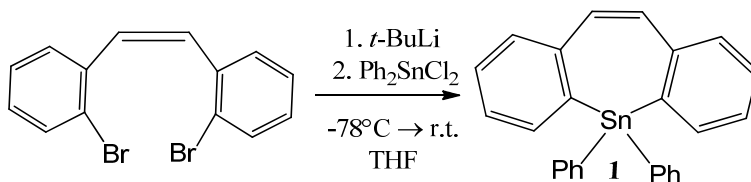
^a Babeş-Bolyai University, Faculty of Chemistry and Chemical Engineering, 11 Arany Janos str.,
RO-400028, Cluj-Napoca, Romania,

* Corresponding author: sgabi@chem.ubbcluj.ro

challenge in the synthesis of phosphastannaallenes. To stabilize the $-P=C-Sn<$ and $-P=C=Sn<$ fragments, we propose a stannepine type compound based on a tin containing heterocycle, similar with other already reported species [11]. The synthesis of previous phosphastannapropenes in which the tin atom was included in a stannepine ring has been performed via a chlorination of the dimethyl stannepine [9,12]. However, the synthesis of dichlorostannepine starting from its dimethyl analogue is not very convenient; therefore we tried to find a more efficient alternative way for obtaining dihalostannepine derivatives. This paper presents the synthesis and structural characterization of a new diphenylstannepine derivative and some preliminary results regarding the bromination reaction of this compound.

RESULTS AND DISCUSSION

The synthesis of the new diphenylstannepine **1** was realized starting from 1,1'-dibromostilbene, which was allowed to react with diphenyltin dichloride, via a lithiated intermediate, according to the procedure described in literature for the dimethyl analogue [11,12]. The synthetic route to compound **1** is described in Scheme 1.



Scheme 1

Diphenylstannepine **1** was investigated in solution by multinuclear NMR spectroscopy and MS spectrometry. The ^{119}Sn NMR spectrum of compound **1** shows one signal situated at -134.48 ppm, while the dimethylstannepine analog exhibits a specific signal at -76.0 ppm, as shown in the ^{119}Sn NMR spectrum. The ^1H NMR spectrum highlights all the specific resonances of the protons in the chemical shift range expected for this derivative. For example, the signal of the protons situated in the $\text{CH}=\text{CH}$ bridge appears as a singlet at the chemical shift of 6.87 ppm (see experimental part). ^{13}C NMR spectra analysis has led to an accurate attribution of all the signals, in the expected field, for all the carbons atoms. The ^{13}C NMR spectrum is shown in Figure 1.

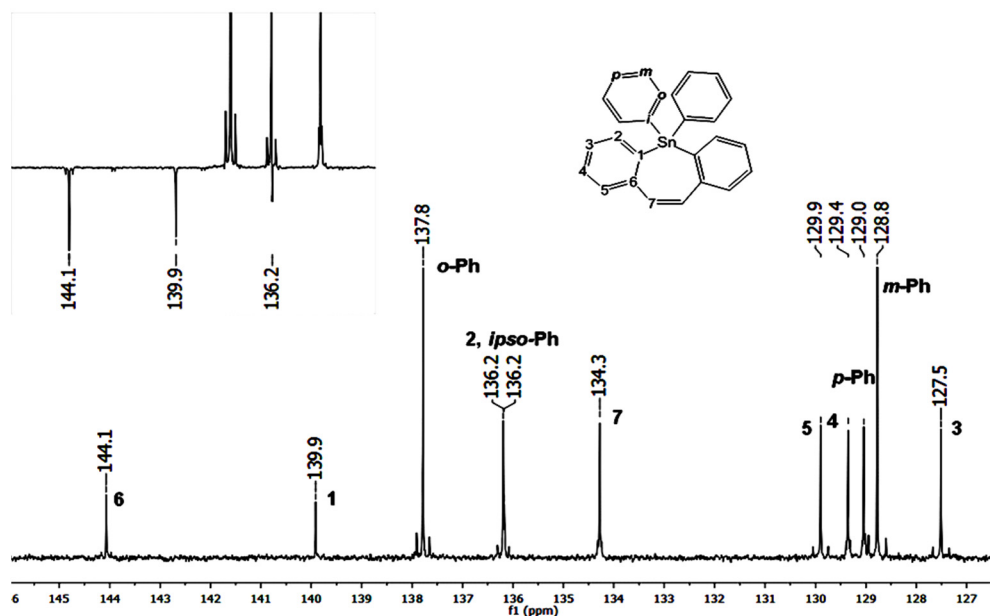


Figure 1. ^{13}C NMR spectrum for the diphenylstannepine **1**.

The assignment of all NMR signals was challenging, since all the resonances appear in a tight area of chemical shifts. Actually, the correct assignment of all signals (in carbon and proton NMR spectrum) was possible using various 2D-NMR experiments (COSY, HSQC, HMBC,) at two working frequencies (400.13 and 600.13 MHz for ^1H and 100.61 MHz for ^{13}C , respectively). Two of the most relevant bidimensional NMR spectra (HSQC and HMBC) used for the assignment of the carbon and hydrogen atoms are presented in Figure 2.

From the HSQC experiments (Figure 2a), the assignment of carbon atoms, such as the CH=CH bridge was possible; for this fragment a strong correlation can be seen between the corresponding hydrogen and carbon atoms, respectively the peaks at 6.86 ppm (^1H) and 134.3 ppm (^{13}C) in Figure 2. In the HMBC spectra, the same hydrogen atom (namely the protons of the CH=CH fragment situated at 6.86 ppm and highlighted in red on Figure 2) exhibits strong correlations with three other carbon atoms from the stannepinic ring. The identification of all signals from the hydrogen and carbon atoms from compound **1** was possible by corroboration of all the NMR analysis results.

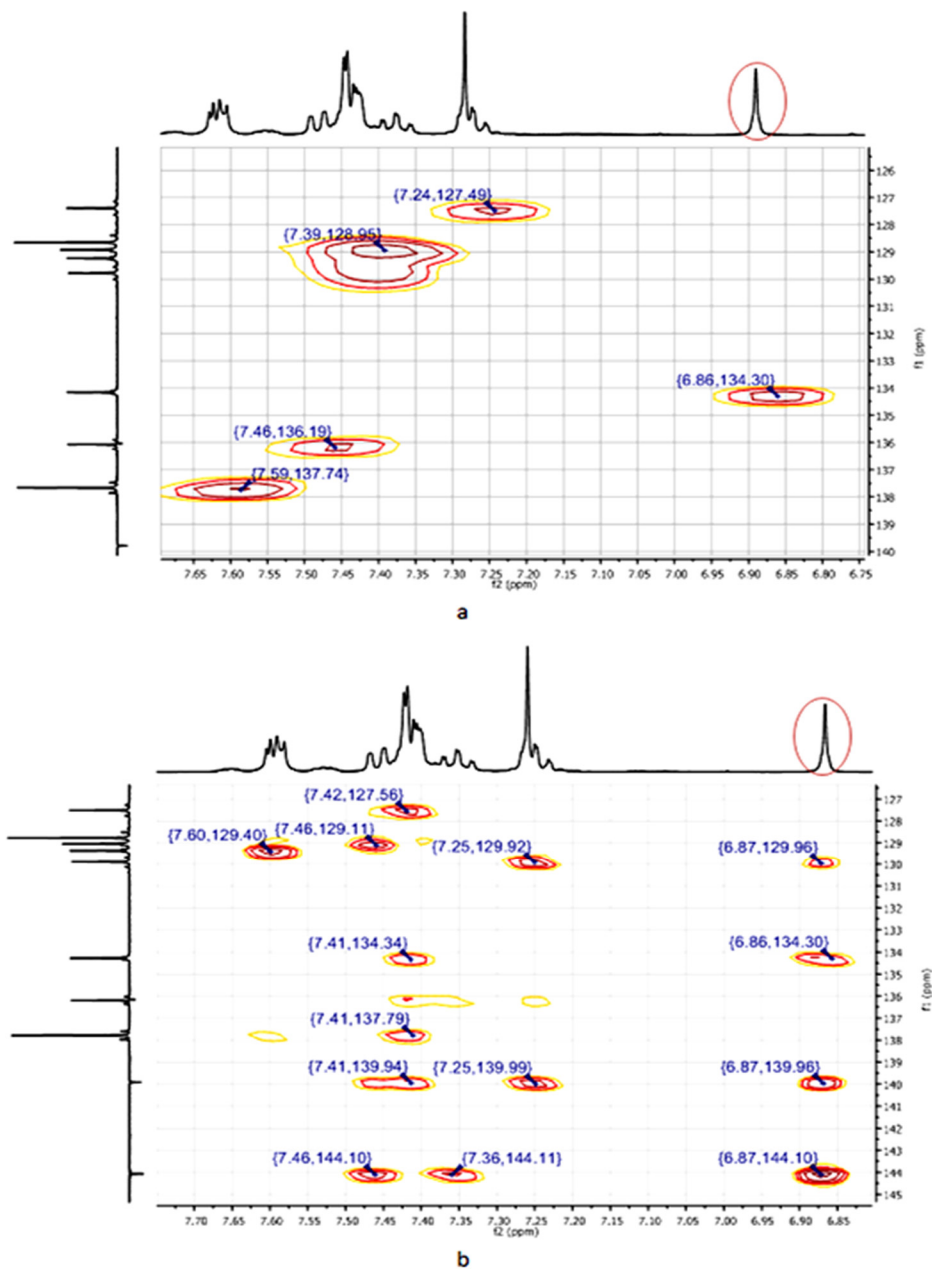


Figure 2. Details of the HSQC (a) and HMBC (b) NMR spectra of the diphenylstannepine 1.

The molecular structure of compound **1** was determined in solid state by single crystal X-Ray diffraction. The compound crystallizes in a triclinic system in the P1 space group with 2 molecules per unit cell. The crystal and refinement data are summarized in Table 1, (see experimental part). The tin atom has a tetrahedral environment, with the C(13)–Sn(1)–C(21) angle of $100.98(1)^\circ$ and the C(1)–Sn(1)–C(7) angle of $108.59(1)^\circ$ respectively (Figure 3). The value of the dihedral angle between the two planes, each containing an aromatic stannepinic phenyl ring is 66.15° in **1**, slightly more open than in the dichlorostannepine analogue (62.06°) [12].

The main geometrical parameters of **1** (bond lengths and bond angles) are shown in Table 2. Comparing the geometrical parameters of diphenylstannepine **1** with the dichloro analogue it is noticed that the Sn–C_(stannepine) bond length has similar values (2.12 Å in **1** and 2.11 Å in dichlorostannepine) while the C_(stannepine)–Sn–C_(stannepine) angle ranges from 100.98° in **1** to 108.55° in the dichlorostannepine [12].

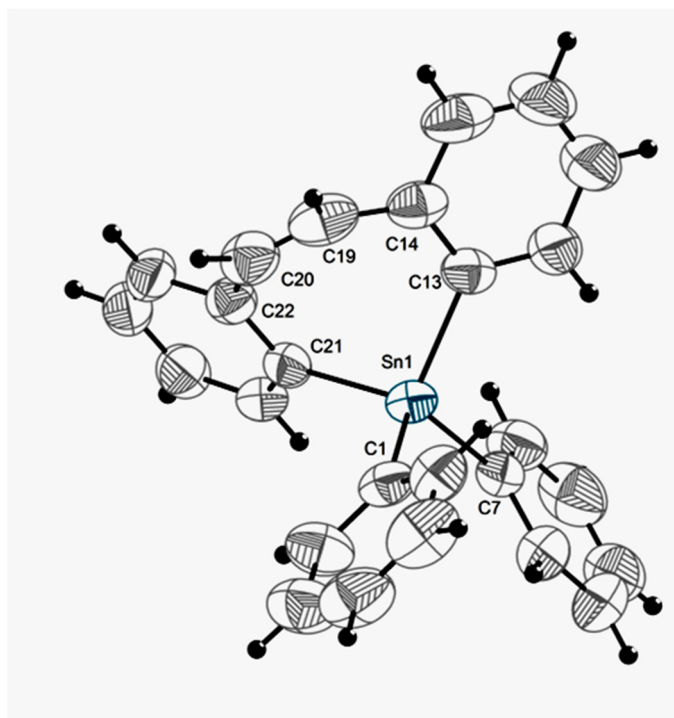
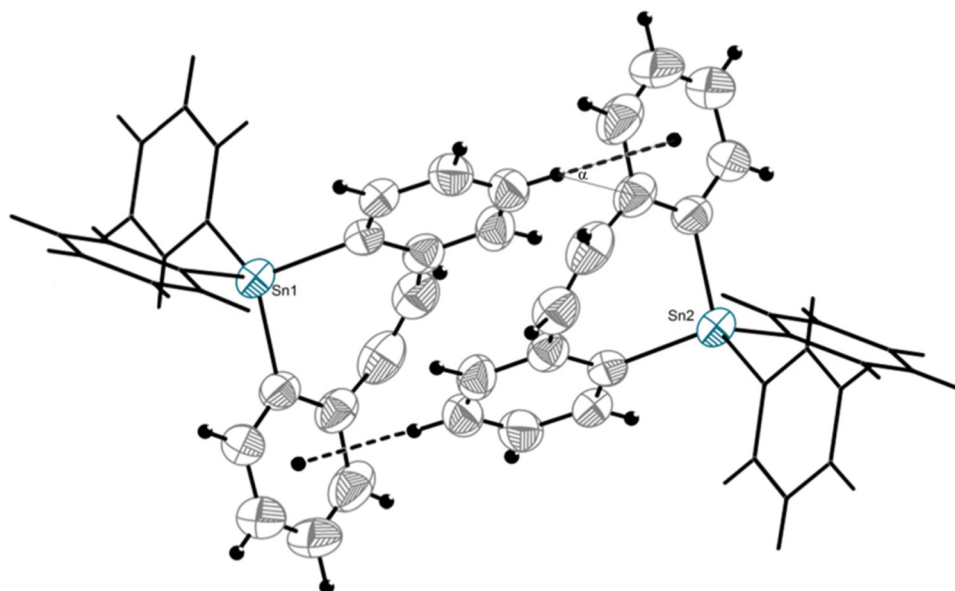


Figure 3. Molecular structure of diphenylstannepine **1** in solid state. The atoms are drawn with 50% probability ellipsoids

Table 2. Relevant interatomic distances (Å) and angles (°) for compound **1**.

Distances (Å)		Angles (°)	
Sn(1) - C(1)	2.1385(3)	C(1) - Sn(1) - C(7)	108.59(1)
Sn(1) - C(7)	2.1319(3)	C(1) - Sn(1) - C(13)	115.45(1)
Sn(1) - C(13)	2.1259(3)	C(1) - Sn(1) - C(21)	111.37(1)
Sn(1) - C(21)	2.1232(3)	C(7) - Sn(1) - C(13)	108.59(1)
C(13) - C(14)	1.3910(2)	C(7) - Sn(1) - C(21)	111.74(1)
C(14) - C(19)	1.4750(2)	C(13) - Sn(1) - C(21)	100.98(1)
C(19) - C(20)	1.3395(2)		
C(20) - C(22)	1.4770(2)		
C(21) - C(22)	1.3921(2)		

An association between two molecules of **1** was revealed in the crystal packing, formed through C–H \cdots π contacts as shown in Figure 4. The C–H \cdots π distance (2.78 Å) and corresponding C–H \cdots π α plane angle (29°) are appropriate for such intermolecular interaction and in agreement with the literature data (2.60 - 2.86 Å for sp^2 -C–H \cdots π distance and the α angle $<30^\circ$). [13, 14, 15]

**Figure 4.** Association in the crystal packing of diphenylstannepine **1**.

Concerning the reactivity of diphenylstannepine **1**, a reaction with bromine in the presence of iron (as a catalyst) [16] was performed. This reaction led to a mixture of compounds, among them a brominated derivative was identified by NMR spectroscopy. ^{119}Sn NMR spectra showed a resonance at -53.26 ppm, at a value of the chemical shift expected for such compounds (when compared to -12.49 for the dichlorinated analogue [12]).

CONCLUSIONS

Two novel stannepine derivatives were evidenced. Diphenylstannepine derivative **1** was completely characterized in solution, by multinuclear NMR spectroscopy experiments, and in the solid state, by a single-crystal X-ray diffraction study. A new brominated stannepine product was evidenced by a preliminary NMR study. The complete characterization of this compound is still in progress since its separation from the reaction mixture could not be achieved yet.

EXPERIMENTAL SECTION

All manipulations were performed under a dry and oxygen free atmosphere (argon) using standard Schlenk techniques. THF was freshly distilled upon Na/benzophenone. 2-bromobenzyl bromide, Ph_3P and 2-bromobenzylaldehyde were purchased from Alfa Aesar, *t*-BuOK, *t*-BuLi, Ph_2SnCl_2 from SIGMA-ALDRICH and used as supplied. Z-2,2'-dibromostilbene was prepared according to the literature procedure [17].

NMR spectra were recorded in CDCl_3 on a Bruker Avance 400 MHz spectrometer at the following frequencies: 400.13 (reference TMS) for ^1H ; 100.61 MHz (reference TMS) for ^{13}C ; 149.21 MHz (reference SnMe_4) for ^{119}Sn and Bruker Avance 600 MHz spectrometer at the following frequencies: 600.13 (reference TMS) for ^1H ; 125.61 MHz (reference TMS) for ^{13}C . The general notation of the hydrogen and carbon atoms used for assignment of the NMR resonances of compound **1** is shown in Figure 1.

Crystallographic data for the structural analysis were collected at room temperature on a Bruker-SMART APEX instrument by using graphite-monochromated Mo-K α radiation ($\lambda = 0.71073 \text{ \AA}$). The crystals were attached with paraton/N oil to cryoloops and the data were collected at room temperature (294 K) (Table 1). The structures were refined with anisotropic thermal parameters. The hydrogen atoms were refined with a riding model and a mutual isotropic thermal parameter. For structure solving and refinement the

software package SHELX-97 was used [18]. The drawings were created with the Diamond program [19]. The Crystallographic data for the structural determinations have been deposited in the Cambridge Crystallographic Data Base (CCDC 1465305).

Table 1. Crystal Data and Structure Refinement for **1**.

Empirical formula	C ₂₆ H ₂₀ Sn	Absorption coefficient (mm ⁻¹)	1.230
Formula weight	451.11	F(000)	452
Temperature (K)	294(2)	Crystal size, mm	0.330 x 0.280 x 0.260
Wavelength (Å)	0.71073	θ range for data collection (°)	1.835 to 25.000
Crystal system	Triclinic	Reflections collected	9058
Space group	<i>P</i> - 1	Independent reflections	3517 [R(int) = 0.0461]
Unit cell dimensions		Refinement method	Full-matrix least-squares on F ²
<i>a</i> (Å)	9.3401(13)	Data/restraints/parameters	3517 / 0 / 244
<i>b</i> (Å)	10.3276(15)	Goodness-of-fit on F ²	0.981
<i>c</i> (Å)	11.3543(16)	Final R indices [I > 2σ(I)]	R1 = 0.0405, wR2 = 0.0830
α (°)	80.999(2)	R indices (all data)	R1 = 0.0561, wR2 = 0.0909
β (°)	80.119(2)	Largest diff. peak and hole, eÅ ⁻³	0.684 and -0.327
γ (°)	77.272(2)		
Volume (Å ³)	1044.4(3)	Calculated density (g/cm ³)	1.434
Z	2		

Synthesis of (Z)-5,5-diphenyl-5H-dibenzo[b,f]stannepine (1)

A solution of *t*-BuLi (9.18 ml, 15.6 mmol, 1.7 M in pentane, 10% excess) was added dropwise to (Z)-2,2'-dibromostilbene (2.4 g, 7.1 mmol) dissolved in 170 ml THF at -78°C. After 2h at this temperature, a solution of diphenyltin dichloride (2.54 g, 7.4 mmol) in 20 ml THF was added dropwise and the reaction mixture was allowed to warm up to room temperature overnight. The resulting solution was quenched with 100 ml of a water:diethylether mixture (1:1). After separation of the phases, the aqueous layer was washed with diethyl ether (2 x 25 ml) and the combined organic layers were washed with brine and dried over Na₂SO₄. All volatile compounds were removed under reduced pressure. Recrystallization from diethyl ether yielded **1** as colorless crystals (1.5 g, 47%).

¹H NMR, 400.13 MHz (CDCl₃) ppm: 6.87 (2H, s, CH=CH bridge), 7.22-7.27 (2H, m, *H*-3), 7.35 (2H, dt, ³J_{H-H} = 7.3, ⁴J_{H-H} = 1.4 Hz *H*-*para*-Ph), 7.42-7.44 (8H, m, *H*-4,5, *H*-*meta*-Ph), 7.46 (2H, ³J_{H-H} = 7.3, ⁴J_{H-H} = 1.0 Hz, dd, *H*-2), 7.59 (4H, m, ³J_{H-Sn} = 50.0 Hz, *H*-*orto*-Ph).

^{13}C NMR, 100.61 MHz (CDCl_3) ppm: 127.5 (C-3, $^3J_{\text{C-Sn}} = 49.1$ Hz), 128.8 ($^3J_{\text{C-Sn}} = 51.5$ Hz, C-meta-Ph), 129.0 ($^4J_{\text{C-Sn}} = 9.8$ Hz, C-4), 129.3 ($^4J_{\text{C-Sn}} = 11.3$ Hz, C-para-Ph), 129.9 ($^3J_{\text{C-Sn}} = 45.7$ Hz, C-5), 134.3 ($^3J_{\text{C-Sn}} = 12.0$ Hz, CH=CH), 136.1 ($^1J_{\text{C-Sn}} = 526.6$ and 551.2 Hz, ipso-C Ph), 136.2 ($^2J_{\text{C-Sn}} = 34.1$ Hz, C-2), 137.8 ($^2J_{\text{C-Sn}} = 37.9$ Hz, C-orto-Ph), 139.9 ($^1J_{\text{C-Sn}} = 499.1$ and 477.8 Hz, C-1), 144.1 ($^2J_{\text{C-Sn}} = 28.5$ Hz, C-6).

^{119}Sn NMR, 149.21 MHz (CDCl_3), ppm: -134.48

HRMS [APCI] (m/z): 453.0691 [M^+](calcd. for $\text{C}_{26}\text{H}_{21}\text{Sn} = 453.0665$); 375.0215 [$\text{M}^+ - \text{Phenyl}$] (calcd. for $\text{C}_{20}\text{H}_{15}\text{Sn} = 375.0196$).

REFERENCES

1. P.P. Power, *Chemical Reviews*, **1999**, *99*, 3463.
2. B.E. Eichler, D.R. Power, R. West, *Organometallics*, **1998**, *17*(11), 2147.
3. J. Escudie, H. Ranaivonjatovo, L. Rigon, *Chemical Reviews*, **2000**, *100*, 3639.
4. V.Y. Lee, A. Seckiguchi, *Organometallics compounds of low coordinated Si, Ge, Sn and Pb*, **2010**, John Wiley & Sons Ltd, West Sussex, U.K, ISBN: 978-0-470-72543-6.
5. J. Escudie, G. Nemes, *Comptes Rendus de Chimie*, **2010**, *13*, 954.
6. T.G. Kocsor, D. Matioszek, G. Nemes, A. Castel, Annie, J. Escudie, P.M. Petrar, N. Saffon-Merceron, I. Haiduc, *Inorganic Chemistry*, **2012**, *51*, 7782.
7. T.G. Kocsor, G. Nemes, N. Saffon, S. Mallet-Ladeira, D. Mandec, A.Castel, J. Escudie, *Dalton Transactions*, **2014**, *43*, 2718.
8. R. Septelean, G. Nemes, J. Escudie, I. Silaghi-Dumitrescu, H. Ranaivonjatovo, P. Petrar, H. Gornitzka, L. Silaghi-Dumitrescu, N. Saffon, *European Journal of Inorganic Chemistry*, **2009**, *5*, 628.
9. P.M. Petrar, R. Septelean, N. Deak, H. Gornitzka, G. Nemes, *Journal of Organometallic Chemistry*, **2015**, *787*, 14.
10. T.G. Kocsor, N. Deak, D. Ghereg, G. Nemes, J. Escudié, H. Gornitzka, S. Ladeira, A. Castel, *Journal of Organometallic Chemistry*, **2014**, *755*, 1204.
11. A. Caruso, A.M. Siegler, J.D. Tovar, *Angewandte Chemie International Edition*, **2010**, *49*, 4213.
12. R. Septelean, G. Nemes, P.M. Petrar, *Revue Roumaine de Chimie*, **2014**, *59* (11-12), 997.
13. S.S. Batsanov, *Inorganic Materials*, **2001**, *9*, 871.
14. E.R.T. Tiekink, J. Zukerman-Schpector, *The Importance of Pi-Interactions in Crystal Engineering*, **2012**, John Wiley & Sons Ltd, The Atrium, Southern Gate, Chichester, West Sussex, PO19 8SQ, U. K. ISBN 978-0-470-68827-4.

15. E. Gagnon, A. Rochefort, V. Metivaud, J. D. Wuest, *Organic Letters*, **2010**, *12*, 380.
16. D. Dakternieks, K. Jurkschat, R. Tozer, *Organometallics*, **1996**, 1467.
17. A. Terfort, H. Brunner, *Journal of the Chemical Society, Perkin Transaction 1*, **1996**, 1467.
18. G.M. Sheldrick, SHELX-97, Universität Göttingen, Germany, **1997**.
19. DIAMOND – Visual Crystal Structure Information System, CRYSTAL IMPACT: Bonn, Germany, **2001**.

*Dedicated to Professor Luminița Silaghi-Dumitrescu
on the occasion of her 65th anniversary*

THE EFFECT OF ELECTRON-RICH HETEROATOMS IN METALLABORANE CLUSTERS

ALEXANDRU LUPAN^{a*}, AMR A.A. ATTIA^a, R. BRUCE KING^b

ABSTRACT. The experimentally synthesized and structurally characterized metallaborane clusters containing highly electronegative heteroatoms namely (S, P, and Se) were studied by density functional theory in order to provide an insight into the influence of these heteroatoms on the polyhedral framework of metallaboranes.

Keywords: Metallaboranes, Density functional theory, heteroatoms, electronegativity.

INTRODUCTION

The most stable boranes are the deltahedral borane dianions $B_nH_n^{2-}$ which adopt the geometries of the most spherical deltahedra having in general vertices of degrees 4 and 5. Such boranes have $2n + 2$ skeletal electrons, as required by the Wade-Mingos rules [1,2,3,4]. BH vertices can be replaced by isoelectronic CH vertices leading to stable neutral $C_2B_{n-2}H_n$. In 1960s Hawthorne successfully substituted BH vertices in dicarbaboranes with transition metal units such as CpCo (Cp = $\eta^5-C_5H_5$) leading to neutral cobaltadicarbaboranes [5].

Phosphorous and carbon have similar electronegativities owing to their diagonal relationship in the periodic table. However, replacement of a CH vertex by a phosphorus atom in carborane cages leads to the possibility

^a Babeş-Bolyai University, Faculty of Chemistry and Chemical Engineering, Department of Chemistry, 11 Arany Janos str., RO-400028, Cluj-Napoca, Romania

^b The University of Georgia, Department of Chemistry and Center for Computational Quantum Chemistry, 1004 Cedar Street, Athens, GA 30602, USA.

* Corresponding author: alupan@chem.ubbcluj.ro

of new chemistry arising from the basic properties of the phosphorus external lone pair. The first icosahedral diphosphaborane $P_2B_{10}H_{10}$ was initially synthesized in low yield in 1989 [6]. Subsequent improvements in the synthesis of $P_2B_{10}H_{10}$ made it more readily available to synthesize the cobaltadiphosphaborane $CpCoP_2B_9H_9$ [7]. Other work led to the synthesis of various ferradiphosphacarboranes such as $CpFeCP_2B_8H_9$ [8].

One important aspect in the chemistry of the metalladiphosphaboranes is the basicity of the phosphorus lone pairs. A phosphorus vertex is a four skeletal electron donor so that a $CpFeCPB_{n-3}H_{n-2}$ structure has $2n+2$ skeletal electrons and thus exhibits most spherical *closo* deltahedral geometries. The 11-vertex iron complex $CpFeCHP(CH_3)B_8H_8$ has been synthesized [9] in which the iron atom is located in the unique degree 6 vertex while the carbon and phosphorus atoms are located in the only two available degree 4 vertices. Interestingly one of the Fe-B bonds is abnormally long suggesting that a degree 6 vertex is not favored. Related to the ferracarbaphosphaboranes are the isoelectronic ferrathiacarboranes $CpFeCHSB_{n-3}H_{n-3}$. Two examples of such species have been synthesized by Kudinov and coworkers [10], namely the icosahedral 12-vertex $CpFeC(NHMe_3)SB_9H_9$ and the 11-vertex $CpFeC[B(OH)_2]SB_8H_8$.

The 10- and 12-vertex cobaltthiaboranes were first synthesized by Sneddon and co-workers in low yield [11]. A more efficient synthesis of $CpCoSB_{10}H_{10}$ was recently carried out by Welch and co-workers [12]. X-ray crystallography showed an icosahedral structure with adjacent cobalt and sulfur atoms. [12]. The synthesis of $B_9H_9E_2$ ($E = S$ or Se) species having two sulfur or selenium vertex atoms has been reported [13]. Such species appear to have nido structures derived by removal of a vertex from a regular icosahedron to leave a pentagonal face. A similar introduction of a $CpCo$ unit into the diselenaborane $B_9H_9Se_2$ gives a low yield of a novel 12-vertex nido species $CpCoSe_2B_9H_9$ having a bent pentagonal face.[13]

This study aimed at investigating the effect of the electron-rich heteroatoms, namely S, P and Se, on the polyhedral framework of metallaborane clusters by using density functional theory. We review our results in this area.

RESULTS AND DISCUSSION

A. Phosphorus as a "carbon copy" and its heavier congeners

The low energy 8-vertex $CpCoP_2B_5H_5$ structures are based on the most spherical deltahedron namely the D_{2d} bisdisphenoid. The lowest such structure has the cobalt atom located in a degree 5 vertex and the phosphorus

atoms located in non-adjacent degree 4 vertices (figure 1). All of the 9-vertex $\text{CpCoP}_2\text{B}_6\text{H}_6$ structures have central CoP_2B_6 tricapped trigonal prisms. The lowest energy $\text{CpCoP}_2\text{B}_6\text{H}_6$ structure has the phosphorus atoms located in non-adjacent positions with one at a degree 4 vertex and the other located at a degree 5 vertex. The latter is adjacent to the cobalt atom located in the only adjacent degree 5 vertex that is not adjacent to the degree 4 phosphorus atom. [14]

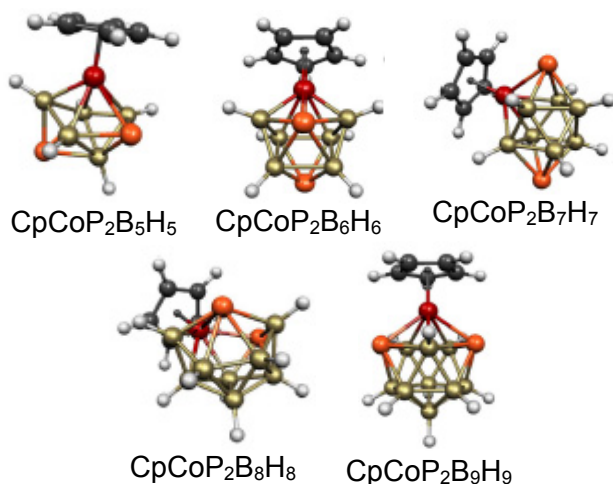


Figure 1. The lowest energy $\text{CpCoP}_2\text{B}_{n-2}\text{H}_{n-2}$ structures.

The geometries of the 10-vertex cobaltadiphospha-boranes $\text{CpCoP}_2\text{B}_7\text{H}_7$ are based on the D_{4d} bicapped square antiprism. The lowest energy such structure is the unique structure having both phosphorus atoms located at degree 4 vertices. The 11-vertex $\text{CpCoP}_2\text{B}_8\text{H}_8$ system is based on the 11-vertex most spherical deltahedron. This C_{2v} deltahedron has a single degree 6 vertex, and consequently two degree 4 vertices. The lower symmetry leads inherently to a more complicated potential energy surface. The lowest energy such structure has a $\text{P}\cdots\text{P}$ edge that is too long for a direct bond thereby leading to a polyhedron with a quadrilateral face including a $\text{P}\cdots\text{P}$ diagonal. The lowest energy 12-vertex $\text{CpCoP}_2\text{B}_9\text{H}_9$ structures are all regular icosahedra. The most stable such structure has two Co-P edges and non-adjacent P atoms. [14]

The lowest energy 8-vertex $\text{CpFeCHP}(\text{CH}_3)\text{B}_5\text{H}_5$ structures are all bisdisphenoids having the iron atoms located mainly in degree 5 vertices with phosphorus and carbon atoms in non-adjacent positions (Figure 2).

The 9-vertex systems are based on the most spherical *closo* tricapped trigonal prism having the iron atom located at a degree 5 vertex. In all such structures the phosphorus atom is adjacent to the iron atom while the carbon atom prefers a degree 4 vertex. The situation is similar for the 10-vertex $\text{CpFeCHP}(\text{CH}_3)\text{B}_7\text{H}_7$ system exhibiting also the geometry of the corresponding most spherical deltahedron, namely the bicapped tetragonal antiprism. Such structures have the carbon and phosphorus atoms located in the only two degree 4 vertices. [15]

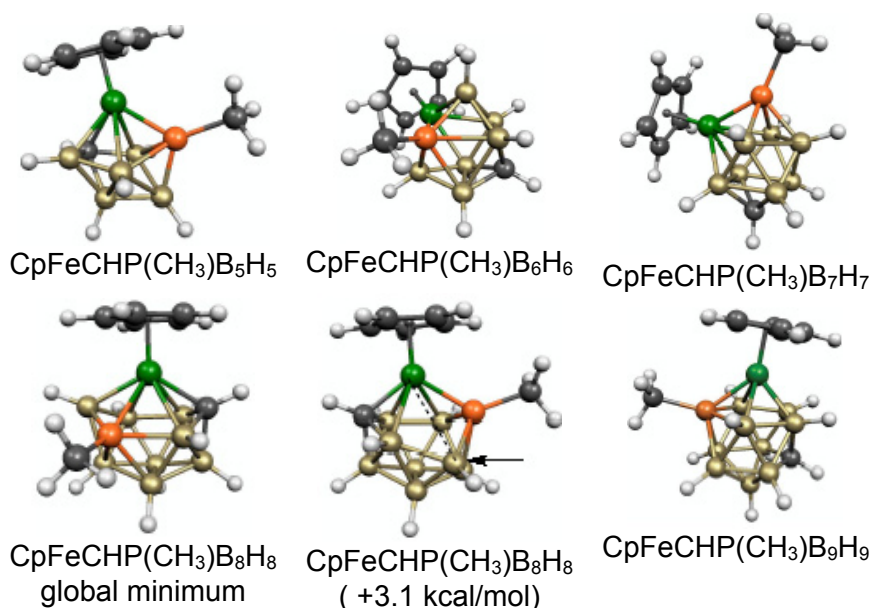


Figure 2. The lowest energy $\text{CpFeCHP}(\text{CH}_3)\text{B}_{n-3}\text{H}_{n-3}$ structures.

The experimental $\text{CpFeCHP}(\text{CH}_3)\text{B}_8\text{H}_8$ structure is not the global minimum but a slightly higher energy structure (+3.1 kcal/mol) having the phosphorus atom located in a degree 4 vertex. Lengthening one of the Fe-B bonds converts the two adjacent deltahedral faces into a single quadrilateral face thus reducing the degree of the iron vertex from 6 to 5. [15]

The 12-vertex structures based on the FeCPB_9 framework clearly favor the regular icosahedron over any other arrangement of the 12 vertex atoms. The most stable such structure has an Fe-P edge with the carbon vertex placed antipodally to the phosphorus vertex. [15]

B. The electron rich sulfur and selenium vertices: a route to more open structures

A sulfur vertex contributes four skeletal electrons so that a $\text{CpCoSB}_{n-2}\text{H}_{n-2}$ system has $2n + 2$ skeletal electrons and thus prefers a *closo* deltahedral bisdisphenoid geometry according to the Wade-Mingos rules. The lowest energy $\text{CpCoSB}_6\text{H}_6$ structure is a bisdisphenoid having the cobalt atom at a degree 5 vertex and the sulfur atom at a non-adjacent degree 4 vertex (Figure 3). The lowest energy 9-vertex cobaltathiaborane structures are tricapped trigonal prisms having the cobalt atom located in a degree 5 vertex and the sulfur atom in the non-adjacent degree 4 vertex. The same location pattern was found for the lowest energy $\text{CpCoSB}_8\text{H}_8$ structure based on the most spherical 10-vertex deltahedron, namely the bicapped tetragonal antiprism. This trend continues for the 11-vertex $\text{CpCoSB}_9\text{H}_9$ family in which the low-energy structures are all isomers of the corresponding *closo* deltahedron. The most stable such structure is the unique isomer having the cobalt atom located in the unique degree 6 vertex and the sulfur atom located in an adjacent degree 4 vertex. [16]

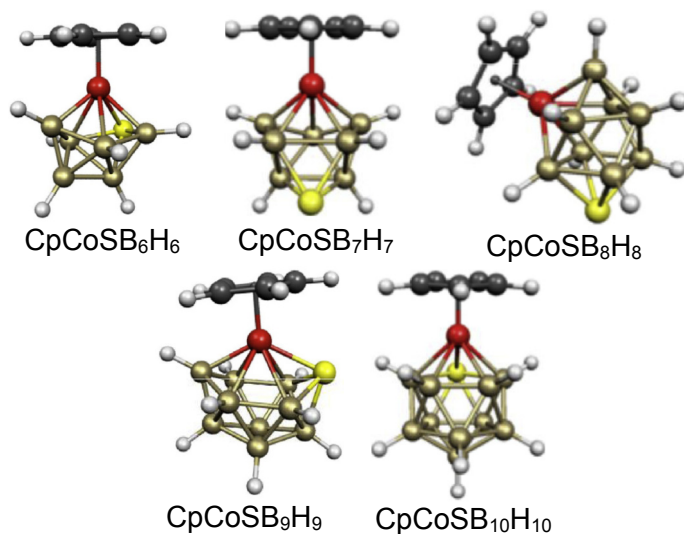


Figure 3. The lowest-energy $\text{CpCoSB}_{n-2}\text{H}_{n-2}$ structures.

For the 12-vertex $\text{CpCoSB}_{10}\text{H}_{10}$ structures, isomers based on the icosahedron have much lower energies than those based on any other possible 12-vertex polyhedra such as the cuboctahedron or anticuboctahedron. The lowest-energy cobaltathiaborane icosahedron has a direct Co-S edge.

The highest energy such structure has the cobalt and sulfur atoms located on at antipodal vertices. [16]

Various ferrathiacarboranes such as $\text{CpFeC}(\text{NHCMe}_3)\text{SB}_9\text{H}_9$ and $\text{CpFeC}[\text{B}(\text{OH})_2]\text{SB}_8\text{H}_8$, have been synthesized and structurally characterized by X-ray crystallography [17]. The ferrathiacarboranes are isoelectronic with the dicobaltadicarbaboranes and the cobaltathiaboranes. The question arises regarding the geometrical preferences of the ferrathiacarboranes $\text{CpFeCHSB}_n\text{H}_n$ as compared with the previously discussed iron phosphacarboranes $\text{CpFeCHP}(\text{CH}_3)\text{B}_{n-3}\text{H}_{n-3}$ and whether two heteroatoms known to exhibit a preference for a lower vertex degree, namely sulfur and carbon in this case, would induce deviations from the deltahedral sphericity.

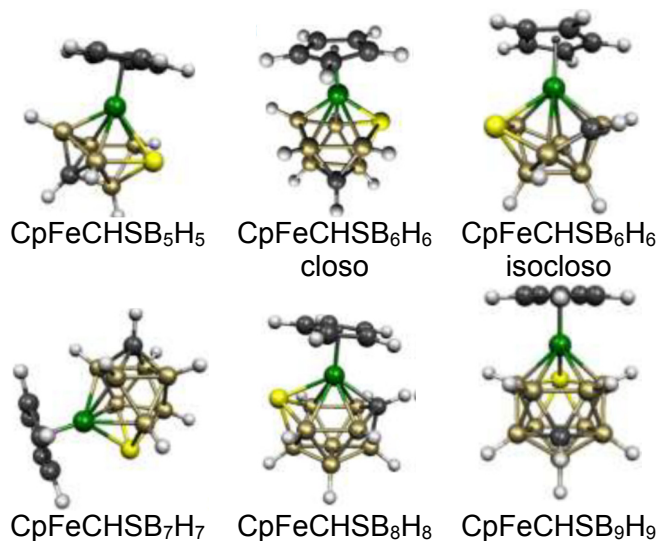


Figure 4. The lowest-lying $\text{CpFeCHSB}_{n-3}\text{H}_{n-3}$ structures.

The lowest energy 8-vertex $\text{CpFeCHSB}_5\text{H}_5$ structures are based on the most spherical deltahedron, namely the bisdisphenoid with the iron atom in a degree 5 vertex directly connected to a degree 4 vertex sulfur atom. The carbon atom is located in the only other degree 4 vertex which is non-adjacent to either iron or sulfur atoms (figure 4). [18] The lowest energy 9-vertex iron thiacarbaborane $\text{CpFeCHSB}_6\text{H}_6$ structure is a *closo* tricapped trigonal prismatic which is very close in energy to an *isocloso* isomer. The low-energy *closo* structure is the unique structure having the iron atom located in a degree 5 vertex and sulfur and carbon atoms located in degree 4 vertices but not with adjacent iron and carbon atoms and with a direct Fe-S bond. The 10-vertex $\text{CpFeCHSB}_7\text{H}_7$ global minimum structure is the most spherical deltahedron having the heteroatoms at degree 4 vertices with the

added preference for iron-sulfur adjacency. The most stable $\text{CpFeCHSB}_8\text{H}_8$ structure is the unique *closo/isocloso* isomer with both heteroatoms located at degree 4 vertices and the iron atom located in the unique degree 6 vertex. [18] This is the experimentally reported polyhedral arrangement for the boronic acid $\text{CpFeC}[\text{B}(\text{OH})_2]\text{SB}_8\text{H}_8$ [17]. The lowest energy 12-vertex structure $\text{CpFeCHSB}_9\text{H}_9$ is reported to be the only isomer having adjacent iron and sulfur atoms as well as non-adjacent and non-antipodal iron and carbon atoms. [18]

While a CH vertex is a donor of 3 skeletal electrons, a group 16 element vertex (S or Se) has an external lone pair thus leaving 4 skeletal electrons for skeletal bonding. Thus a thia- or selenaborane has the $2n + 2$ skeletal electrons necessary for a spherical cage. This can also be predicted for neutral boranes having extra hydrogen atoms. In practice such “extra” hydrogen atoms cannot remain on a closed polyhedron. However removal of a vertex leaves an open face which is suitable for edge-capping extra hydrogens. Such species are called *nido*-boranes. The ability of each sulfur and selenium atom to provide four skeletal electrons provides the possibility of *nido* metallaborane structures without bridging hydrogen atoms. Such species having 11 vertices obtained by removal of a vertex from an icosahedron (and consequently having a pentagonal opened face) have been reported [19].

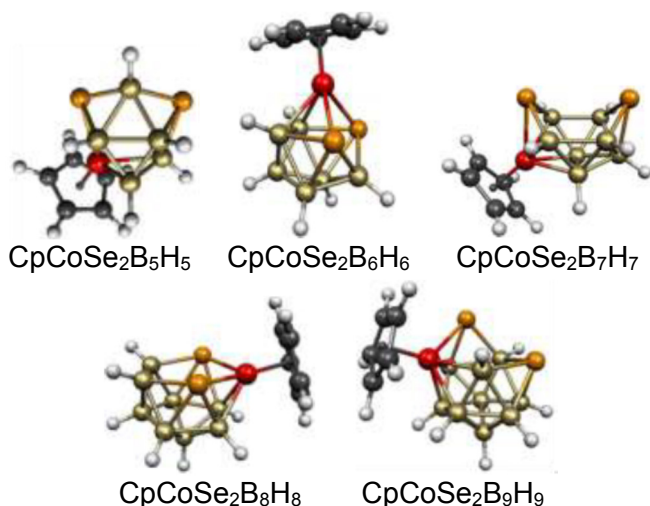


Figure 5. The lowest-lying $\text{CpCoSe}_2\text{B}_{n-3}\text{H}_{n-3}$ structures.

The most stable 8-vertex cobaltaselenaborane $\text{CpCoSe}_2\text{B}_5\text{H}_5$ structure originates from the 9-vertex most spherical deltahedron by the removal of a degree 5 vertex leading to a pentagonal open face providing two degree 3 vertices for the selenium atoms (Figure 5). [20]

The lowest energy 9-vertex $\text{CpCoSe}_2\text{B}_6\text{H}_6$ structures are generated by the removal of a degree 4 vertex from the *closo* 10-vertex most spherical deltahedron, namely the bicapped tetragonal antiprism. This leaves a large tetragonal open face. The 10-vertex $\text{CpCoSe}_2\text{B}_7\text{H}_7$ system is a simple one, derived from the 11-vertex most spherical *closo* deltahedron by removal of the single degree 6 vertex. This decreases the degrees of the two former two degree 4 vertices to just 3 where the two selenium atoms are located. This structure resembles the well-known structure of nido decaborane, $\text{B}_{10}\text{H}_{14}$. The lowest energy $\text{CpCoSe}_2\text{B}_9\text{H}_9$ structure originates from a regular icosahedron by distorting a vertex so that two edges are broken leaving a degree 4 vertex as well as two degree 3 vertices for the selenium atoms. [20]

CONCLUSIONS

Density functional theory results show that the lowest energy $\text{CpCoP}_2\text{B}_{n-3}\text{H}_{n-3}$ ($n = 8$ to 12) structures have the cobalt atom at a degree 5 or 6 vertex and the phosphorus atoms at degree 4 vertices with strong preference of the phosphorus atoms to occupy non-adjacent vertices. The lowest energy structures of the isoelectronic $\text{CpFeCHP}(\text{CH}_3)\text{B}_{n-3}\text{H}_{n-3}$ ($n = 8$ to 12) have adjacent iron and phosphorus atoms and non-adjacent phosphorus and carbon atoms. One of the Fe–B bonds from the degree 6 iron vertex in the 11-vertex $\text{CpFeCHP}(\text{CH}_3)\text{B}_8\text{H}_8$ structure appears to be fragile, readily elongating to ~ 3.1 Å in one of the low-energy structures, consistent with experimental observation on this system. The lowest energy structures for the $\text{CpCoSB}_n\text{H}_n$ ($n = 6$ – 10) systems were found to be the *closo* deltahedra in accord with expectations for these $2n + 2$ Wadean skeletal electron systems. The sulfur atoms in these structures were shown to prefer locations at the lowest degree vertices. Results on the ferrathiocarboranes $\text{CpFeCHSB}_{n-3}\text{H}_{n-3}$ ($n = 8$ – 12) indicate energetic preferences for deltahedral structures having the iron atoms located at degree 5 or 6 vertices, the carbon and sulfur atoms located at degree 4 vertices, and Fe–S edges. The lowest energy $\text{CpCoSe}_2\text{B}_{n-3}\text{H}_{n-3}$ ($n = 8$ – 12) structures have central $\text{CoSe}_2\text{B}_{n-3}$ nido polyhedra derived from *closo* or *isocloso* deltahedron by removal of a vertex. This leads to an “open” non-triangular face having four to six edges. The two selenium vertices in such structures are located on this open face reflecting the general preference of selenium for low-degree vertices.

THEORETICAL METHODS

Full geometry optimizations have been carried out at the M06L/6-311G(d,p) level of theory. The natures of the stationary points after optimization were checked by calculations of the harmonic vibrational frequencies. If significant imaginary frequencies were found, the optimization was continued by following the normal modes corresponding to imaginary frequencies to insure that genuine minima were obtained.

All calculations were performed using the Gaussian 09 package [21] with the default settings for the SCF cycles and geometry optimization, namely the fine grid (75,302) for numerically evaluating the integrals, 10^{-8} hartree for the self-consistent field convergence, maximum force of 0.000450 hartree/bohr, RMS force of 0.000300 hartree/bohr, maximum displacement of 0.001800 bohr, and RMS displacement of 0.001200 bohr.

ACKNOWLEDGMENTS

Funding from the Romanian Ministry of Education and Research, Grant PN-II-RU-TE-2014-4-1197, is gratefully acknowledged.

REFERENCES

1. K. Wade, *Chem. Commun.*, **1971**, 792-793.
2. K. Wade, *Adv. Inorg. Chem. Radiochem.*, **1976**, 18, 1-66.
3. D.M.P. Mingos, *Nature Phys. Sci.*, **1972**, 236, 99-102.
4. D.M.P. Mingos, *Acc. Chem. Res.*, **1984**, 17, 311-319.
5. M.F. Hawthorne, *Acc. Chem. Res.*, **1968**, 1, 281-288.
6. J.L. Little, J.G. Kester, J.C. Huffman, L.J. Todd, *Inorg. Chem.*, **1989**, 28, 1087-1091.
7. R. McLellan, N.M. Boag, K. Dodds, D. Ellis, S.A. Macgregor, D. McKay, S.L. Masters, R. Noble-Eddy, N.P. Platt, D.W.H. Rankini, H.E. Robertson, G.M. Rosair, A.J. Welch, *Dalton Trans.*, **2011**, 40, 7181.
8. M. Bakardjiev, J. Holub, M. J. Carr, J. D. Kennedy, B. Štíbr, *Dalton Trans.*, **2005**, 909.
9. D. Kadlecěk, A.M. Shedlow, S.O. Kang, P. J. Carroll, L.G. Sneddon, *J. Am. Chem. Soc.*, **2003**, 125, 212.
10. D.S. Perekalin, I.V. Glukhov, J. Holub, I. Císařova, B. Štíbr, A.R. Kudinov, *Organometallics*, **2008**, 27, 5273-5278.

- 11 S.O. Kang, P.J. Carroll, L.G. Sneddon, *Inorg. Chem.* **1989**, *28*, 961.
- 12 M.T. Serrate, D. Ellis, G.M. Rosair, A.J. Welch, *J. Organomet. Chem.* **2013**, *747*, 211.
- 13 G.D. Friesen, A. Barriola, P. Daluga, P. Ragatz, J. C. Huffman, L.J. Todd, *Inorg. Chem.* **1980**, *19*, 458-466.
- 14 A.A.A. Attia, A. Lupan, R.B. King, *Polyhedron*, **2015**, *85*, 933-940
- 15 A. A. A. Attia, A. Lupan, R. B. King *RSC Adv.*, **2016**, *6*, 1122-1128
- 16 A. Lupan, R.B. King, *Polyhedron*, **2014**, *78*, 130-134
17. D.S. Perekalin, I.V. Glukhov, J. Holub, I. Císařova, B. Štíbr, A.R. Kudinov, *Organometallics*, **2008**, *27*, 5273–5278.
- 18 A.A.A. Attia, A. Lupan, R.B. King, *Polyhedron*, **2016**, in press
19. G.D. Friesen, A. Barriola, P. Daluga, P. Ragatz, J.C. Huffman,; L.J. Todd, *Inorg. Chem.*, **1980**, *19*, 458-466.
- 20 A.A.A. Attia, A. Lupan, R.B. King, *submitted*.
21. Gaussian 09 (Revision A.02), Gaussian, Inc., Wallingford, CT, 2009.

*Dedicated to Professor Luminița Silaghi-Dumitrescu
on the occasion of her 65th anniversary*

ANTIOXIDANT ACTIVITY AND TOTAL PHENOLIC CONTENT OF SOME COMMERCIAL FRUIT- FLAVOURED YOGURTS

BIANCA MOLDOVAN^a, BRIGITTA IASKO^a, LUMINIȚA DAVID^{a*}

ABSTRACT. There is currently an increasing interest in developing functional foods and in the use of natural food antioxidants as health promoting additives. The purpose of our study was to compare the antioxidant potential and the total phenolic content of 12 commercial available fruit flavoured yogurts from three different producers present on the Romanian dairy market. The free radical scavenging capacity was evaluated using the 2, 2-azino-bis(3-ethylbenzothiazoline)-6-sulphonic acid (ABTS) assay and the total phenolic content (TPC) was determined by Folin-Ciocalteu method. The TPC of the investigated samples varied between 362.3 and 926.7 μg gallic acid equivalents/mL yogurt and the antioxidant activity (AA) was in the range of 197.1 ÷ 653.8 μM Trolox. A positive linear correlation between the antioxidant activity and the total phenolic content ($R^2 = 0.915; 0.912; 0.687$) was established for the yogurt samples.

Keywords: fruit-flavoured yogurt, polyphenols, antioxidant activity

INTRODUCTION

Fermented foods have been consumed since ancient times. Fermentation was used to improve the shelf-life of some foods. The most famous examples of consumed fermented products are bread, cheese and wine [1]. Beside these, yogurt has also an important place, being one of the most popular traditionally consumed fermented foods, firstly consumed in the Middle Asia and nowadays widely spread in the whole world. Yogurt is a basic dairy product, produced by some thermophilic lactic acid generating bacteria such

^a Babeș-Bolyai University, Faculty of Chemistry and Chemical Engineering, 11 Arany Janos Str., RO-400028, Cluj-Napoca, Romania

* Corresponding author: muntean@chem.ubbcluj.ro

as *Streptococcus thermophilus* and *Lactobacillus delbrueckii* spp. *Bulgaricus* during the slow fermentation of milk lactose [2]. Compared to milk, yogurt has increased nutritional properties being a good source of proteins, vitamins (thiamine, riboflavin, niacin, nicotinic acid, folic acid, ascorbic acid), minerals and microelements (calcium, phosphorus, zinc, magnesium) [3]. Yogurt is considered a healthy food being an excellent source of probiotics, energy and calcium. In addition, consumption of yogurt has proved to be beneficial to the immune system, inflammatory diseases, allergies, cancer prevention, reduction of constipation, regulation of blood pressure, weight control, obesity, decrease of cholesterol absorption and many others [4-6]. Moreover, lactose intolerant people can consume yogurt since during fermentation milk lactose is converted to lactic acid [7].

Yogurt is often flavoured or fortified to create value-added products, as yogurt's flavour gained lately an important role on consumers' demand. Flavouring of yogurt can be achieved by addition of synthetic compounds or natural ingredients such as fruit juices or fruit pulp. The enrichment with various plant derived health beneficial ingredients can improve the nutritional properties of fermented dairy food products.

Strawberry is the leading fruit used in Europe for flavouring yogurt [2]. Other fruits, such as peach, apricot, apple, banana, orange, plum, cherries are also widely used to enhance the flavour of yogurt. Apart of giving different tastes to yogurt, these fruit based additives are an important source of active compounds which provide specific health benefits including antioxidant, anti-inflammatory and antimicrobial activities [8, 9]. Despite its nutritional characteristics, yogurt as well as other dairy products are extremely poor in phenolic compounds. Hence, adding fruits reach in phenolics improves the antioxidant activity of yogurt [10].

Antioxidant compounds protect the human organisms from oxidative damages of the free radicals and play an important role in prevention of some degenerative diseases. The most active antioxidants of fruits are polyphenols such as anthocyanins, flavonols, catechins and carotenoids and vitamins. Among these, phenolics have received lately an increased attention, fruits reach in these compounds being intensively used as functional ingredients in the food industry.

Despite the widely consumption of fruit flavoured yogurt and its improved nutritional properties, there are not many studies reporting the antioxidant capacity and phenolic content of these commercial available dairy products [11].

The aim of our study was to assess the antioxidant activity and the total phenolic content of 12 commercial available fruit flavoured yogurt samples. The samples were chosen in order to include fruits with powerful antioxidant capacity such as strawberry, sour cherries, wild berries and apricots and were provided by different producers.

RESULTS AND DISCUSSION

The total phenolic content (TPC) of 12 fruit flavoured yogurts was estimated using the Folin-Ciocalteu reagent. The TPC of the investigated samples varied from one producer to another and among the added fruits (Figure 1). Elevated TPC values were recorded for the wild berry and the sour cherry flavoured yogurts, the highest phenolic content being determined for the sour cherry flavoured yogurt from producer 3 (926.7 μg gallic acid equivalents/mL yogurt) while the lowest value was 362.3 μg gallic acid equivalents/mL for the apricot yogurt from producer 2. The differences in the total phenolic content might be due to the different phenolic profile of the fruits used for flavouring the yogurt as well as to the different fruit content of the investigated yogurts which varied from one producer to another (Table 1).

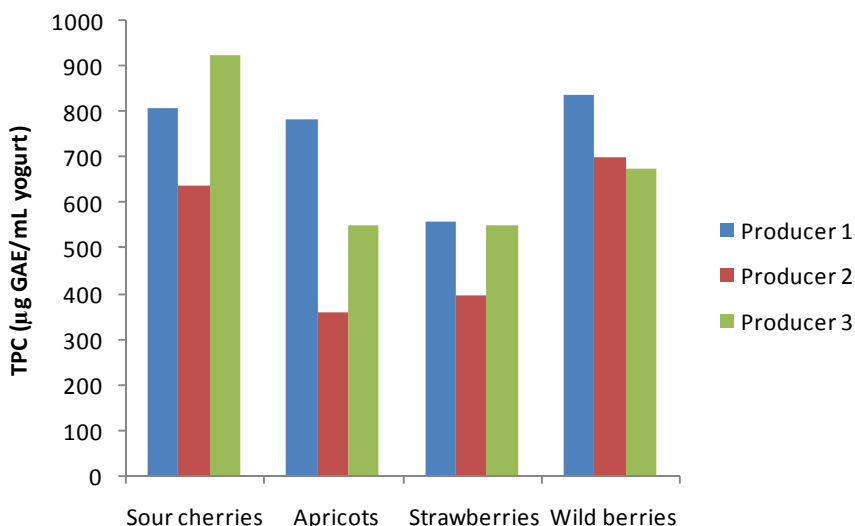


Figure 1. Total phenolic content (μg GAE/mL yogurt) of investigated yogurts

The antioxidant capacity (AA) of the 12 investigated fruit flavoured yogurts was determined using the ABTS radical cation method, based on the free radical scavenging capacity of antioxidant molecules. The total antioxidant capacity of the studied yogurts was assessed using a dose response curve for ABTS^+ as function of stock solutions of Trolox standard (concentration from 50 to 800 μM) and expressed as μM Trolox equivalents. The obtained values of AA for the investigated samples presented a large variation, ranging from 197.1 to 653.8 μM Trolox. The highest levels of the antioxidant capacity were obtained for yogurts from producer 1 (Figure 2).

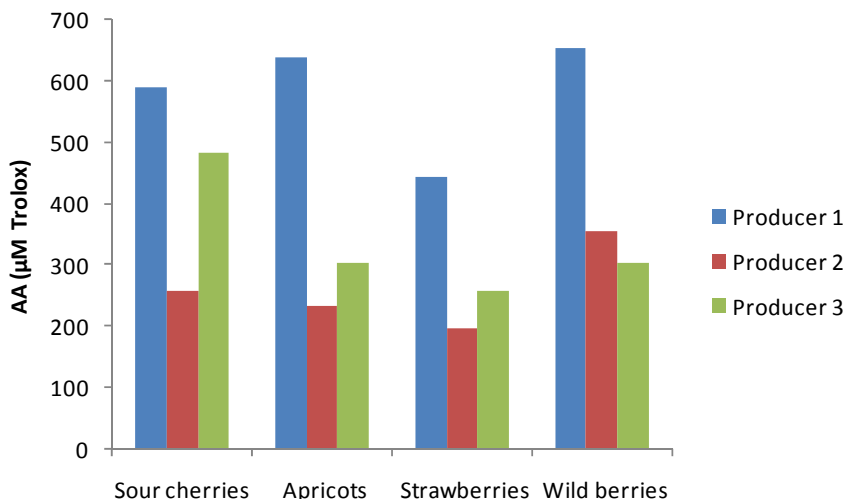


Figure 2. Antioxidant activity ($\mu\text{M Trolox}$) of investigated yogurts

Wild berries flavoured yogurt from producer 1 exhibited the highest radical scavenging capacity comparable to that of apricots flavoured yogurt from the same producer (653.8 and 639.4 $\mu\text{M Trolox}$, respectively). Comparing yogurts with added wild berries from all three producers is notable that yogurts from producers 2 and 3 presented similar antioxidant activities (355.7 and 302.8 $\mu\text{M Trolox}$, respectively) values that are almost half than that of yogurt from producer 1. Generally, the lowest levels of the antioxidant capacity of investigated samples were obtained for the yogurts from producer 2, with wild berries added yogurt as the only exception. Strawberry flavoured yogurts presented the lowest values of antioxidant activity in all the investigated cases.

By comparing the values of antioxidant activities it's important to take into account the free radical scavenging capacity of the contained fruits in the analyzed yogurts. It's well known that wild berries possess a stronger antioxidant activity than cultivated strawberries or apricots [12, 13]. The literature studies on the antioxidant activity of commercial fruit flavoured yogurts are poor and the reported data were obtained by applying different assays such as DPPH scavenging method, β -carotene bleaching inhibition and ferric reducing antioxidant power assay [11]. There are no reported data regarding evaluation of the antioxidant activity of commercial fruit yogurts using the ABTS assay.

A positive linear correlation between the antioxidant capacity and total phenolic content of the investigated yogurts was established (Figure 3).

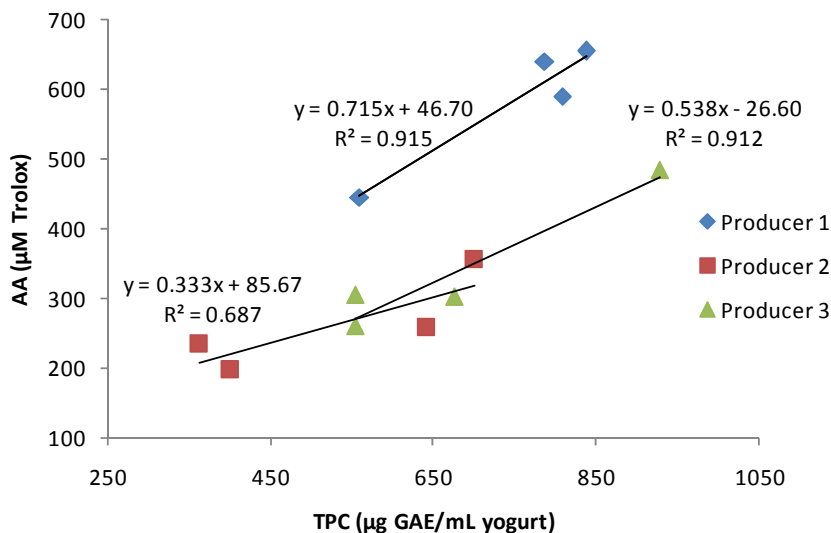


Figure 3. Correlation between total phenolic content and antioxidant activity of investigated yogurts

The high linear correlation coefficients R^2 (0.915 for yogurts of producer 1 and 0.912 for yogurts of producer 3) clearly indicated that the phenolic compounds from the added fruits significantly contributed to the antioxidant capacity of the derived dairy products. The results are consistent with those reported by other research groups [14, 15]. The poor correlation between the two investigated parameters of yogurts from producer 2 ($R^2 = 0.687$) may be explained by the fact that the total phenolic content does not necessarily incorporate all the antioxidants present in the samples. Some antioxidants (such as citric acid) are added in the fermented dairy products of producer 2 as labelled by producer.

CONCLUSIONS

The present study delivers key information on the total phenolic content and antioxidant capacity of some commercial available fruit flavoured yogurts, less investigated until now. Wild berry yogurts showed the highest AA value, while the highest TPC was recorded for sour cherry flavored yogurt. The radical scavenging capacity decreased in the order: wild berry > apricots > sour cherry > strawberry. Addition of fruits to yogurt enhances its nutritional properties due to their high antioxidant content.

EXPERIMENTAL SECTION

Yogurt samples

Twelve fruit flavoured yogurts were purchased from a local market from Cluj-Napoca, Romania. The samples were selected taking into account the addition of fruits with high antioxidant capacity. The composition of the chosen yogurt samples is given in Table 1. All samples were kept refrigerated at 2°C and analyzed at 24 h after purchase.

Table 1. Composition of the investigated yogurts as labeled by producer

Producer	Type of yogurt	Composition
1	Sour cherries	Pasteurized milk, sugar, sour cherry 2%, glucose-fructose syrup, colors (aronia and carrot juice), flavor, milk proteins, corn modified starch, thickener (pectin), lactic ferments
	Apricots	Pasteurized milk, sugar, apricot 2%, colors (carrot and red pepper extracts, β -carotene), flavor, milk proteins, corn modified starch, thickener (pectin), lactic ferments
	Strawberries	Pasteurized milk, sugar, strawberry 2%, glucose-fructose syrup, colors (red beet and carrot juice, β -carotene), flavor, milk proteins, corn modified starch, thickener (pectin), lactic ferments
	Wild berries	Pasteurized milk, sugar, wild berries 2.3% (blackberry, strawberry, raspberry, blueberry, black elderberry), colors (black carrot and red beet concentrated juice, hibiscus), flavor, milk proteins, corn modified starch, thickener (pectin), lactic ferments
2	Sour cherries	Pasteurized milk, sugar, sour cherry 2% (sour cherry pulp, sour cherry concentrated juice, water, modified starch, stabilizer: pectin, acidifying agent: citric acid), color (carrot concentrated juice), milk proteins, lactic ferments
	Apricots	Pasteurized milk, sugar, apricot 2% (apricot pulp, apricot concentrated juice, water, modified starch, flavor, stabilizer: pectin, acidifying agent: citric acid), colors (carrot concentrated juice, β -carotene), milk proteins, lactic ferments
	Strawberries	Pasteurized milk, sugar, strawberry 2% (strawberry pulp, strawberry concentrated puree, water, modified starch, stabilizer: pectin, flavor, acidifying agent: citric acid), colors (carrot concentrated juice, β -carotene), milk proteins, lactic ferments
	Wild berries	Pasteurized milk, sugar, wild berries 2% (black currant, blackberry, raspberry and strawberry concentrated juice, water, modified starch, stabilizer: pectin, flavor, acidifying agent: citric acid), colors (aronia, grapes and carrot concentrated juice), milk proteins, lactic ferments

Producer	Type of yogurt	Composition
3	Sour cherries	Semi-skimmed yogurt, sugar, sour cherry 3.7%, glucose-fructose syrup, color (carrot concentrated juice), flavor
	Apricots	Semi-skimmed yogurt, sugar, apricot 3.7%, glucose-fructose syrup, color (pumpkin and apple concentrate), flavor
	Strawberries	Semi-skimmed yogurt, sugar, strawberry 3.7%, glucose-fructose syrup, color (carrot concentrated juice), flavor
	Wild berries	Semi-skimmed yogurt, sugar, wild berries concentrated juice (raspberry 2.3%, strawberry 1.8%, blackcurrant 0.7%, red currant 0.5%), glucose-fructose syrup, color (carmin), flavor

Chemicals and reagents

All chemicals and reagents were purchased from Merck (Darmstadt, Germany), were of analytical grade and were used without further purification. A TYPDP1500 Water distiller (Techosklo LTD, Držkov, Czech Republic) was used to obtain the distilled water.

Extraction procedure

A volume of 10 mL yogurt was stirred with 10 mL ethanol:water mixture (60:40) at room temperature for 30 minutes. The resulting mixture was centrifuged at 5000 rpm for 15 minutes in a Hettig 1004 EBA 21 centrifuge (Germany). The collected supernatant was stored at 2°C and further used to evaluate the total phenolic content and antioxidant activity of the samples.

Determination of total phenolic content

The TPC was determined by the method of Singleton [16] using the Folin-Ciocalteu reagent.

Yogurt extract (0.3 mL) was mixed with 0.2 N Folin-Ciocalteu reagent (1.5 mL). After 5 min, 1.2 mL of 0.7N Na₂CO₃ solution were added. The mixture was incubated at room temperature for 2 hours and then the absorbance was measured at 765 nm, using an UV-VIS Perkin Elmer Lambda 25 double beam spectrophotometer against a blank sample as reference. Quantitative determinations were performed based on a five points standard calibration curve (10; 25; 50; 75; 100 µg/mL) of gallic acid in 80% methanol. The results were expressed as µg galic acid equivalents (GAE)/mL yogurt.

Determination of antioxidant capacity

The ABTS^{•+} method of Re et al. [17], slightly modified was used to determine the antioxidant activity of the examined yogurts. 360 mg of ABTS were dissolved in 100 mL distilled water. The ABTS radical cation was generated

by mixing ABTS solution (7mM) and of potassium persulfate solution (2.45 mM) in equal volumes. The resulting solution was kept in the dark for 24 h. To 6 mL of diluted ABTS⁺ solution (absorbance around 0.8), 0.1 mL yogurt extract were added. After 15 minutes, the decrease of the absorbance of ABTS⁺ was monitored at 734 nm. A calibration curve of the standard -Trolox (6-hydroxy-2,5,7,8-tetramethylchroman-2-carboxylic acid) (50-800 μM Trolox), was used to determine the antioxidant capacity of the samples. The AA was expressed in μM Trolox equivalents.

REFERENCES

1. J.B. Prajapati, B.M. Nair, The history of fermented foods, in: *Fermented functional foods*, CRC Press, Boca Raton, SUA, **2003**, 1-25.
2. W. Routray, N.H. Mishra, *Comprehensive Reviews in Food Science and Food Safety*, **2011**, 10(4), 208.
3. H.H. Gahruie, M.H. Eskandari, G. Mesbahi, M.A. Hanifpour, *Food Science and Human Wellness*, **2015**, 4, 1.
4. J.W. Anderson, S.E. Gilliland, *Journal of American College of Nutrition*, **1999**, 18, 43.
5. A. Lourens-Hattingh, B.C. Viljoen, *International Dairy Journal*, **2001**, 11, 1.
6. G.D. Miller, J.K. Jarvis, L.D. McBean, *Handbook of Dairy Foods and Nutrition*, CRC Press, Boca Raton, SUA, **2006**.
7. M.E. Sanders, J. Hamilton-Miller, G. Reid, G. Gibson, *Clinical Infectious Diseases*, **2007**, 44, 886.
8. M. Crisan, L. David, B. Moldovan, A. Vulcu, S. Dreve, M. Perde-Schrepler, C. Tatomir, A. G. Filip, P. Bolfa, M. Achim, I. Chiorean, I. Kacso, C. Berghian Grosan, L. Olenic, *Journal of Materials Chemistry B*. **2013**, 1, 3152.
9. A.G. Filip, M.Potara, A. Florea, I. Baldea, D. Olteanu, P. Bolfa, S. Clichici, L. David, B. Moldovan, L. Olenic, S. Astilean, *RSC Advances*, **2015**, 5, 6743.
10. J. O'Connell, P. Fox, *International Dairy Journal*, **2001**, 11, 103.
11. E. Pereira, L. Barros, I. C.F.R. Ferreira, *Antioxidants*, **2013**, 2, 62.
12. J. Scalzo, A. Politi, N. Pellegrini, B. Mezzetti, M. Battino, *Nutrition*, **2005**, 21, 207.
13. B. Moldovan, O. Ghic, L. David, C. Chișbora, *Revista de Chimie-Bucharest*, **2012**, 63, 463.
14. Y. Cai, Q. Luo, M. Sun, H. Corke, *Life Sciences*, **2004**, 74, 2157.
15. K. Tawaha, F.Q. Alali, M. Gharaibeh, M. Mohammad, T. El-Elimat, *Food Chemistry*, **2007**, 104, 1372.
16. V.L. Singleton, R. Orthofer, R.M. Lamuela-Raventos, *Methods in Enzymology*, Academic Press, San Diego, USA, **1999**, 299.
17. R. Re, N. Pellegrini, A. Proteggente, A. Pannala, M. Yango, C. Rice-Evans, *Free radical biology and medicine*, **1999**, 26, 1231.

*Dedicated to Professor Luminița Silaghi-Dumitrescu
on the occasion of her 65th anniversary*

CYTOTOXIC ACTIVITY OF PALLADIUM (II) COMPLEXES OF (1E,6E)-1,7-BIS(4-(DIMETHYLAMINO)PHENYL)HEPTA-1,6- DIENE-3,5-DIONE AGAINST HUMAN COLON CARCINOMA

**NATALIA MIKLÁŠOVÁ^a, ROMAN MIKLÁŠ^a, PIROSKA VIRAG^b, CORINA
BIANCA TATOMIR^b, CRISTINA SZALONTAI^b, DIANA CENARIU^c,
FERDINAND DEVÍNSKY^a, EVA FISCHER-FODOR^{b*}**

ABSTRACT. Two palladium(II) complexes of (1E,6E)-1,7-bis(4-(dimethylamino)phenyl)hepta-1,6-diene-3,5-dione were synthesized and structurally characterized with the aim of testing their cytotoxicity towards human colon tumor cells *in vitro*. Complexes **A** and **B** have the capacity to inhibit the cell growth in HT-29 and DLD-1 cell lines, the activity of **A** being superior as a result of a better accumulation inside the tumor cells.

Keywords: *palladium complexes, curcumin derivative, cytotoxicity, colon cancer, cellular uptake*

INTRODUCTION

The natural extract curcumin exhibits *in vitro* antitumor effect against a variety of cancer cells [1], but this activity is not transposable to clinics due to the low bioavailability of the compound [2], which generates a minor effect on the cancer patients survival [3]. Seeking out for more active prodrugs,

^a *Research Department, Institute of Oncology "Prof.Dr.I.Chiricuta", 34-36 Republicii str., RO-400015, Cluj-Napoca, Romania*

^b *Department of Chemical Theory of Drugs, Faculty of Pharmacy, Comenius University in Bratislava, Kalinčiaková 8, Bratislava 83104, Slovakia*

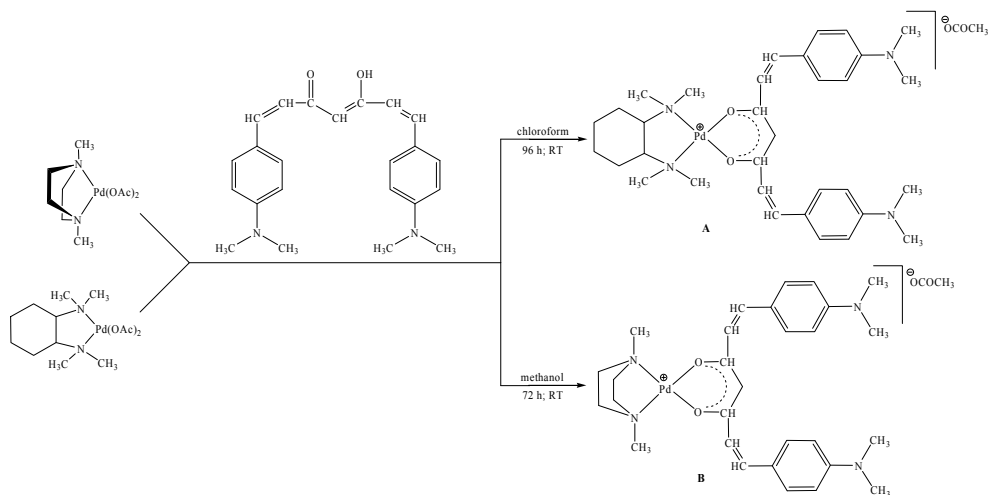
^c *Faculty of Medicine, Iuliu Hatieganu University of Medicine and Pharmacy Cluj Napoca, 8, Babes str, RO-400012, Cluj Napoca, Romania*

* *Corresponding author: fischer.eva@iocn.ro*

synthetic strategies were elaborated to obtain metal complexes of curcumin with enhanced selectivity *in vivo* [4]. We reported previously novel palladium complexes with curcumin derivative ligands having antiproliferative [5] and immunomodulatory effects [6]. The curcumin derivative used in synthesis of palladium complexes tested in this work, 1,7-bis(4-(dimethylamino)phenyl) hepta-1,6-diene-3,5-dione, has been reported and tested for its biological activity against activation of AP-1 family of transcription factors [7]. It was tested for its cytotoxic ability, displaying a comparable or better activity than curcumin in a series of different curcuminoids. Pabon [8] observed a comparable activity of the curcumin derivative, containing dimethylamino moieties, with the pure curcumin when the anti-oxidant activity was investigated by FRAP assay. The aim of the present study was to obtain new metal complexes with enhanced capacity to target the tumor cells; the selected biologic substrates were the human colon cancer cells, a tumor type where curcumin alone was proven to be efficient more in prevention than in cancer cure [3].

RESULTS AND DISCUSSION

The synthesis of curcumin derivative with dimethylamino groups on the aromatic rings follows the pathway described previously in the literature [9]. Palladium complexes with the curcumin like ligand and the precursor palladium complexes used in syntheses (**Scheme 1**) were prepared based on a procedure reported formerly in our papers [5, 6].



Scheme 1. Synthetic pathway for palladium(II) complexes **A** and **B**

Cytotoxicity

The biological tests showed that the (1*E*,6*E*)-1,7-bis(4-(dimethylamino)phenyl)hepta-1,6-diene-3,5-dione ligand has no toxic effect against colon cancer cell lines in the studied concentration range; the attempts to calculate IC₅₀ values resulted ambiguous and unconverged data in a 95% confidence interval. The half inhibitory concentrations (IC₅₀) corresponding to complexes **A** and **B** were calculated using the sigmoidal dose-response curves (**Table 1**);

Table 1. Half inhibitory concentrations IC₅₀ of curcuminoid like ligand and palladium(II) complexes **A** and **B**.

Compound	Cell line	IC ₅₀ value [μM] ± Standard deviation
Complex A	DLD-1	19.17 ± 4.35
	HT-29	5.54 ± 0.37
Complex B	DLD-1	49.65 ± 6.13
	HT-29	68.51 ± 6.56

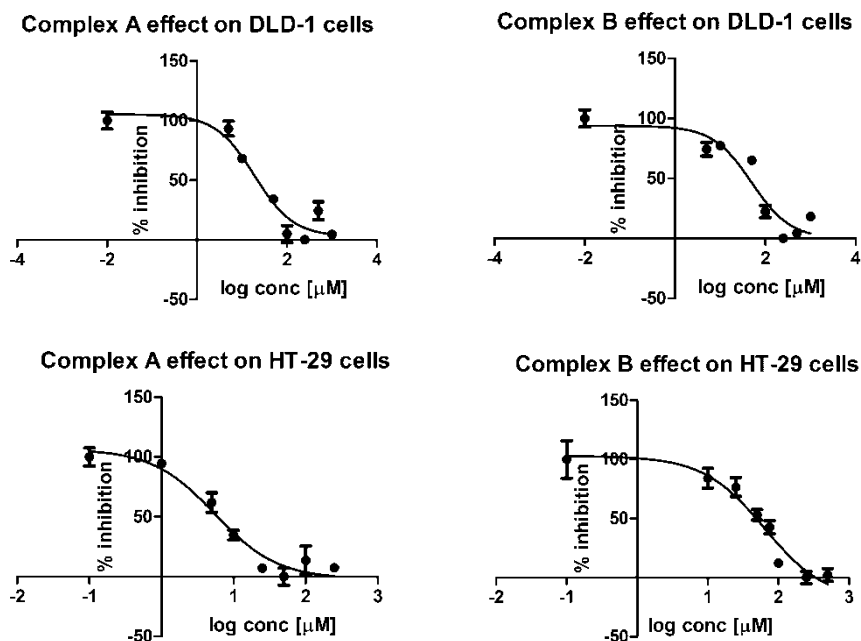


Figure 1. Sigmoidal dose-response curve corresponding to inhibitory activity of complexes **A** and **B** against DLD-1 and HT-29 cells growth.

a lower IC₅₀ value indicates more significant toxicity. The inhibitory effect of complex **A** against tumor cells growth is superior to the effect of complex **B** in both DLD-1 and HT-29 cell lines *in vitro* (**Figure 1**). The IC₅₀ value for compound **A** is markedly decreased in HT-29 cells. The complexes show a superior toxicity when compared with the nearly inactive ligand.

Cellular accumulation

The (1*E*,6*E*)-1,7-bis(4-(dimethylamino)phenyl)hepta-1,6-diene-3,5-dione and its complexes (**A** and **B**) are fluorescent molecules, and their accumulation in the cancer cells can be tracked using fluorescence intensity measurements on treated cells.

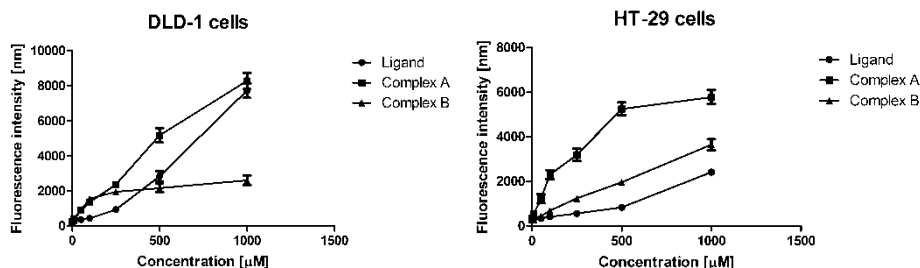


Figure 2. The compounds cellular uptake into DLD-1 cells following 24 hours treatment with the compounds, measured using fluorescence at 620nm emission, 540nm excitation; median values obtained from 6 independent experiments

Table 2. Linear regression data proving the dose-response relationship between the compounds concentration and their cellular accumulation rate within 24 hours treatment of DLD-1 and HT-29 cells; $p < 0.0001$ (the deviation from zero was significant for all compounds)

Best-fit values	Ligand	Complex A	Complex B
DLD-1 cells			
Slope	7.20 ± 0.28	8.163 ± 0.26	2.27 ± 0.24
r^2	0.94	0.96	0.65
F	675.4	998.4	86.32
Deviation from zero	Significant	Significant	Significant
HT-29 cells			
Slope	1.99 ± 0.08	5.89 ± 0.43	3.37 ± 0.11
r^2	0.93	0.81	0.95
F	624.9	186.5	881.0
Deviation from zero	Significant	Significant	Significant

The compounds accumulate in HT-29 and even in the *K-ras* mutant DLD-1 cells after 24 hours of exposure (**Figure 2**) and the cellular uptake in all compounds was dose-related (**Table 2**). Complex **A** displays the biggest accumulation rate in both DLD-1 and HT-29 cells (one-way analysis of variance, Bonferroni post-test, $p < 0.05$). The curcumin like ligand is selective, with good affinity for the DLD-1 line but with lower uptake in the HT-29 cells. The accumulation of complex **B** was better in HT-29 cells at 1mM concentration, and the decrease was very rapid. In DLD-1 cells a plateau was observed above 250 μM , where, despite the dose augmentation, the cells do not take up more complex. Although complex **A** is the most cytotoxic, there is no statistically significant correlation between the intracellular fluorescence and the IC_{50} values of studied compounds (nonparametric Spearman correlation, p value 0.917).

It is known that the DLD-1 and HT-29 tumor cells are sensitive to platinum-based-based drugs [10]. The accumulation of the platinum-based compounds in the colorectal tumor cells is related to the drug transporter molecules belonging to ABC family such ABCB1 and ABCG2 drug efflux pumps [11]. The alteration of ABCB1 and ABCG2 in colon carcinoma cells lead to a decrease of the cytotoxic drugs efficacy [12], including the metal-based drugs such as oxaliplatin.

The most toxic compound, complex **A** was proven to be one with the best accumulation in the cell, in agreement with previous studies which demonstrated a relation between the cellular uptake of Pd(II) complexes and their cytotoxic activity [13].

On the assumption that the favourable *in vitro* effect of complex **A** could be translated to chemotherapy, the compound might be functionalized [14] or encapsulated [15], to obtain a satisfactory *in vivo* activity.

CONCLUSIONS

Despite its capacity to accumulate in tumor cells, the curcuminoid ligand showed no toxicity against colon adenocarcinoma cell lines, IC_{50} values being relatively high, above the highest concentration used in biological tests. Once incorporated inside the cells, the fluorescence of the three compounds was detected at 620 nm emission, with 540 nm excitation. The cellular uptake of the two palladium complexes **A** and **B** exhibit different patterns: complex **A** incorporation was superior to **B** in both cell lines. Complex **A** displays also the most important *in vitro* inhibitory growth capacity against colon carcinoma HT-29 and *K-ras* mutant DLD-1 cells.

EXPERIMENTAL SECTION

All chemicals necessary in the syntheses were of reagent grade and were used as they received.

All synthesized products were structurally characterized by NMR spectra, measured on a Varian Gemini 2000 spectrometer at working frequencies 300 Mz (for $^1\text{H-NMR}$) and 75 Mz (for $^{13}\text{C-NMR}$). Spectra were measured in CDCl_3 , using as internal standard TMS. The infrared spectra were recorded on a Nicolet 6700 FT-IR spectrophotometer, scanning between 400 and 4000 cm^{-1} . UV-Vis spectra were measured with a Genesys 10S UV-Vis spectrophotometer in ethanol at a concentration of 10^{-5} mol/L . Purification of curcumin derivative and complexes **A** and **B** was done by column chromatography performed on silica gel (0.035-0.070 mm 60 Å, Acros). Melting points were determined with a Koffler apparatus without correction.

Syntheses: Complex **A**: 0.38 mmol (0.14 g) of (1*E*,6*E*)-1,7-bis(4-(dimethylamino)phenyl)hepta-1,6-diene-3,5-dione were dissolved in 5 mL of chloroform and to this solution were added dropwise 0.38 mmol (0.15 g) of palladium precursor complex containing *N,N,N',N'*-tetramethylcyclohexane-1,2-diamine dissolved in 3 mL of chloroform. Reaction was left on stirring for 96 h at room temperature, then the mixture was filtered and the solvent evaporated under vacuum. The final product was obtained, after purification *via* silica gel chromatography (CHCl_3 :MeOH, 9:1) as a reddish powder (0.07 g, 26 %). M.p.: $170\text{ }^\circ\text{C}$ (decomposed without melting).

$^1\text{H-NMR}$ (300 Mz, CDCl_3) δ (ppm): 1.24-1.36 (m, 2H); 1.42-1.54 (m, 2H); 1.81 (d, 2H); 1.89 (s, 3H); 2.18 (d, 2H); 2.82 (s, 6H); 2.84 (s, 6H); 3.01 (s, 12H); 3.18 (m, 2H); 5.72 (s, 1H); 6.57 (d, 2H); 6.73 (d, 4H); 7.40 (d, 2H); 7.45 (d, 4H). $^{13}\text{C-NMR}$ (75 MHz, CDCl_3) δ (ppm): 25.02 (1C); 25.28 (2C); 25.56 (2C); 40.32 (4C); 43.56 (2C); 73.18 (4C); 105.34 (1C); 113.17 (4C); 120.79 (2C); 124.35 (2C); 130.90 (4C); 142.04 (2C); 153.43 (2C); 179.61 (2C). IR ν_{max} (cm^{-1}): 3359; 2931; 1727; 1660; 1597; 1508; 1431; 1407; 1342; 1298; 1272; 1165; 1070; 995; 971; 862; 847; 823; 692; 632. UV-Vis λ_{max} (nm): 272; 504.

Complex **B**: (1*E*,6*E*)-1,7-bis(4-(dimethylamino)phenyl)hepta-1,6-diene-3,5-dione (0.67 mmol, 0.24 g) was dissolved in 10 mL of methanol. To this solution was added dropwise the palladium precursor complex containing *N,N'*-dimethylpiperazine (0.67 mmol, 0.23 g) dissolved in 5 mL of dry methanol. Reaction mixture was stirred at room temperature for 72 h. Final product was purified by silica gel chromatography (CHCl_3 :MeOH, 9:1), being isolated as a reddish powder (0.06 g, 14 %). M.p.: $195\text{ }^\circ\text{C}$ (decomposed without melting).

$^1\text{H-NMR}$ (300 Mz, CDCl_3) δ (ppm): 1.89 (s, 3H); 2.59 (s, 6H); 2.72 (d, 4H); 3.00 (s, 12H); 3.84 (d, 4H); 5.74 (s, 1H); 6.57 (d, 2H); 6.71 (d, 4H); 7.44 (dd, 6H). $^{13}\text{C-NMR}$ (75 MHz, CDCl_3) δ (ppm): 24.14 (1C); 40.33 (4C); 46.57 (2C); 59.50 (4C); 105.76 (1C); 113.15 (4C); 120.61 (2C); 124.42 (2C); 130.89 (4C); 142.37 (2C); 153.33 (2C); 179.42 (2C).

IR ν_{\max} (cm⁻¹): 3414; 1592; 1497; 1429; 1409; 1364; 1298; 1232; 1158; 1125; 994; 969; 946; 858; 818; 794; 688; 643. UV-Vis λ_{\max} (nm): 272; 503.

The absorption of complexes **A** and **B** was monitored by UV-vis spectra in an interval of 96 hours, each spectrum being recorded once in 24 hours. No significant changes of characteristic wavelengths were observed, thus the two palladium complexes **A** and **B** are considered stable in ethanolic solution and atmospheric conditions.

Biologic activity: To evaluate the curcumin like ligand and its palladium complexes **A** and **B**, a pair of *in vitro* cultivated human colon adenocarcinoma cell lines from the European Collection of Cell Cultures (Salisbury, UK) was used as biologic system. The cell lines were the human colon adenocarcinoma HT-29 and DLD-1 cells, respectively, epithelial, adherent cells with high proliferation rate. They were cultivated as described earlier [10] using media acquired from Sigma Aldrich (St Louis, USA); at 37 °C in a sterile Unitherm incubator (from Uniequip, Planegg, Germany) with humidified atmosphere and 5% CO₂ content. Cells passage was made at 85-90% confluence, using Trypsin-EDTA solution.

For cytotoxicity test the cells were plated on 96-well microplates (Nunclon delta surface plates from Thermo Fischer Scientific, Waltham, MA, USA) at a concentration of 13×10^3 cell/well in 190 μ l media and they were incubated for 48 hours. At subconfluency they were treated with 10 μ l of ligand or complex. The curcumin derivative and the complexes **A** and **B**, were dissolved in absolute ethanol, to obtain a stock solution of 2 mM. From these stock solutions, it was prepared working solutions through a serial dilution in PBS, from 1000 to 10 μ M for each compound. Dissolved compounds were intensively colored, therefore for every concentration color controls were required, by applying the solution in wells without cells, containing cell culture media only. As reference values, untreated cells were used.

The cytotoxicity of the compounds was measured in triplicate, using the MTT dye (3-(4,5-dimethylthiazol-2-yl)-2,5-diphenyltetrazolium bromide, from Sigma Aldrich), as described earlier [16] the 96-well plates were measured in colorimetry using a Synergy 2.0 microplate reader (from BioTek Company, Winooski, USA) at 570 nm wavelength. Two independent measurements were performed. The absorbance of each well reflected the number of viable cells present.

For cellular uptake, the cells were seeded on 96-well microplates and treated the same as for MTT testing. Six wells were used for every concentration. After 24-hours of incubation with studied compounds, the cell culture media was gently removed; wells were washed twice with PBS and filled with 100 μ l PBS. The plates were measured in fluorescence, at 540 nm excitation and 620 nm emission, using the Synergy 2.0 microplate reader.

The results were analyzed with the Graph Pad Prism 5 software (from GraphPad Software, La Jolla, USA).

ACKNOWLEDGMENTS

This work was supported by the Slovak Research and Development Agency under the contract No. APVV-0516-12, by VEGA 1/0346/16, by the Romanian National Authority for Scientific Research and Innovation, CCCDI – UEFISCDI Grant for Exploratory Research Project PN-II-ID-PCE-2011-3-1057 and PNIII subprogram 3.1 Romanian-South African cooperation grant no. 9BM/2016 AFROMET.

REFERENCES

1. M. Fridlender, Y. Kapulnik, H. Koltai, *Frontiers in Plant Sciences*, **2015**, *6*, 799.
2. M. Kumaravel, P. Sankar, R. Rukkumani. *European Review for Medical and Pharmacological Sciences*, **2012**, *16*, 1900.
3. G. Bar-Sela, R. Epelbaum, M. Schaffer, *Current Medicinal Chemistry*, **2010**, *17*, 190.
4. S. Wanninger, V. Lorenz, A. Subhan, F.T. Edelmann. *Chemical Society Reviews*, **2015**, *44*, 4986.
5. N. Miklasova, E. Fischer-Fodor, R. Miklas, L. Kuckova, J. Kozisek, T. Liptaj, O. Soritau, J. Valentova, F. Devinsky, *Inorganic Chemical Communication*, **2014**, *46*, 229.
6. E. Fischer-Fodor, R. Mikláš, L.T. Krausz, P. Virag, D.C. Moldovan, M. Perde Schrepler, I. Berindan-Neagoe, F. Devínsky, N. Miklášová, *Studia UBB Chemia*, **2015**, *LX*, 93.
7. H. Hatcher, R. Planalp, J. Cho, F.M. Torti, S.V. Torti, *Cellular and Molecular Life Sciences*, **2008**, *65*, 1631.
8. H.J.J. Pabon, *Recueil des Travaux Chimiques des PaysBas*, **1964**, *83*, 379.
9. P.J. Roughley, D.A. Whiting, *Journal of the Chemical Society, Perkin Transactions 1*, **1973**, 2379.
10. S. Cetean, C. Căinap, O. Sorițău, C. Tatomir, P. Virag, A. Hangan, L. Oprean, R. Oprean, *Revista Romana de Medicina de Laborator*, **2015**, *23*, 439.
11. L. Ekblad, J. Kjellström, A. Johnsson, *Anticancer Drugs*, **2010**, *21*, 523.
12. D. Theile, S. Grebhardt, W.E. Haefeli, J. Weiss, *Biochemical Pharmacology*, **2009**, *78*, 1366.
13. F.C. S. de Paula, W. Guerra, I.R. Silva, J.N. Silveira, F.V. Botelho, L.Q. Vieira, E.C. Pereira-Maia, *Chemistry & Biodiversity*, **2008**, *5*, 2124.
14. R. Kotcherlakota, A.K. Barui, S. Prashar, M. Fajardo, D. Briones, A. Rodríguez-Diéguez, C. R. Patra, S. Gómez-Ruiz, *Biomaterials Science*, **2016**, *4*, 448.
15. X. Yang, Z. Li, N. Wang, L. Li, L. Song, T. He, L. Sun, Z. Wang, Q. Wu, N. Luo, C. Yi, C. Gong, *Scientific Reports*, **2015**, *5*, 10322.
16. L. Timko, E. Fischer-Fodor, M. Garajová, M. Mrva, G. Chereches, F. Ondriska, M. Bukovský, M. Lukáč, J. Karlovská, J. Kubincová, F. Devínsky, *European Journal of Medicinal Chemistry*, **2015**, *93*, 263.

*Dedicated to Professor Luminița Silaghi-Dumitrescu
on the occasion of her 65th anniversary*

THIAZOLE DERIVATIVES WITH ANTIFUNGAL ACTIVITY AGAINST *CANDIDA* SPECIES

MIHAELA SABOU^a, ADRIANA GROZAV^{b*}, LIA MONICA JUNIE^a,
MIRELA FLONTA^c, VALENTIN ZAHARIA^b and CASTELIA CRISTEA^d

ABSTRACT. The antifungal activity of a series of thiazole, benzothiazole and benzothiazolyl-phenothiazine derivatives against *Candida albicans* and non-*Candida albicans* species causing invasive candidiasis was investigated using the diffusion method and the broth dilution procedure. Minimal inhibitory concentrations revealed antifungal activity against *C. albicans*, *C. guilliermondii*, *C. krusei* and *C. parapsilosis* strains isolated from clinical materials (blood, urine and peritoneal fluids cultures). The tested hydrazine-thiazole derivatives showed promising antifungal activity against both fluconazole susceptible and resistive *Candida* species, while the benzothiazolyl-phenothiazine derivatives were not effective.

Keywords: *Thiazole, Benzothiazole, Phenothiazine, Candida species.*

INTRODUCTION

Health care associated infections have become a cause of major public concern due to complications inducing morbidity, mortality and increased treatment costs for both immunocompromised as well as non-immunocompromised

^a Faculty of Medicine, "Iuliu Hațieganu" University of Medicine and Pharmacy, RO-400012, Victor Babes 41, Cluj-Napoca, Romania.

^b Faculty of Pharmacy, "Iuliu Hațieganu" University of Medicine and Pharmacy, RO-400012, Victor Babes 41, Cluj-Napoca, Romania.

^c Teaching Hospital of Infectious Diseases, RO-400000, Cluj-Napoca, Romania

^d Babes-Bolyai" University, Faculty of Chemistry and Chemical Engineering, RO-400028, Cluj-Napoca, Romania.

*Corresponding author: adriana.ignat@umfcluj.ro

patients. *Staphylococcus aureus*, *Enterococcus* species, *Escherichia coli*, *Pseudomonas aeruginosa* and *Candida* species are the most common groups of organisms that cause nosocomial infections in both adults and children. [1]. Candidiasis affected a significant number of individuals and the ratio of sepsis episodes of fungal etiology has risen [2]. Health care-associated candidiasis appears globally hierarchized as the third reported cause of invasive nosocomial infection [3,4]. Among *Candida* species, *C. albicans* was historically identified as predominant in causing invasive candidiasis, but more recently several non-*C. albicans* species such as *C. tropicalis*, *C. parapsilosis* complex, *C. glabrata* and *C. krusei* were increasingly incriminated as responsible for invasive infections [5,6]. According to medical statistics, the top four *Candida* species involved in invasive infections were *C. albicans* (58.4%) followed by *C. parapsilosis* complex (19.5%), *C. tropicalis* (9.3%), and *C. glabrata* (8.3%) [7,8]. Minimal immune suppression seemed required to predispose an individual to infections and the high mortality associated to candidemia varied in different geographic areas (e.g. 15%-35% in Europe, up to 46% in USA and up to 54% in Brazil). [9]

In our previously reported studies we tested the antifungal activity of benzothiazol and benzothiazolyl-phenothiazine derivatives against *C. albicans* ATCC 14053 standard strain [10,11]. In this work we extended the screening of antifungal activity of selected hydrazino-thiazole, phenyl-benzothiazole and phenothiazinyl-benzothiazole derivatives against several *Candida* species isolated from clinical materials which were collected from patients with invasive fungal infections health cared in the *Hospital of Infectious Diseases Cluj-Napoca*, Romania.

RESULTS AND DISCUSSION

The chemical structures of the heterocyclic compounds selected for evaluation of antifungal activity against *Candida* spp. are presented in figure 1. The chemical synthesis of hydrazones **1-3** containing different substituents attached to the phenyl and thiazole unit, benzothiazolyl-phenothiazine derivatives **4,5** differentiated by the substitution pattern of the phenothiazine core and 2-phenyl-benzothiazole **6**, were described previously in some of our works [10,11].

The *Candida* strains subjected to this study were responsible for invasive infections in health-care patients with different comorbidities or immunosuppression in critical stages and were isolated from physiological fluids (blood, urine, peritoneal liquid, or bronco-alveolar lavage liquid) and the results are presented in Table 1. The minimal inhibitory concentrations (MIC) were determined according to CLSI standard [12]

THIAZOLE DERIVATIVES WITH ANTIFUNGAL ACTIVITY AGAINST *CANDIDA* SPECIES

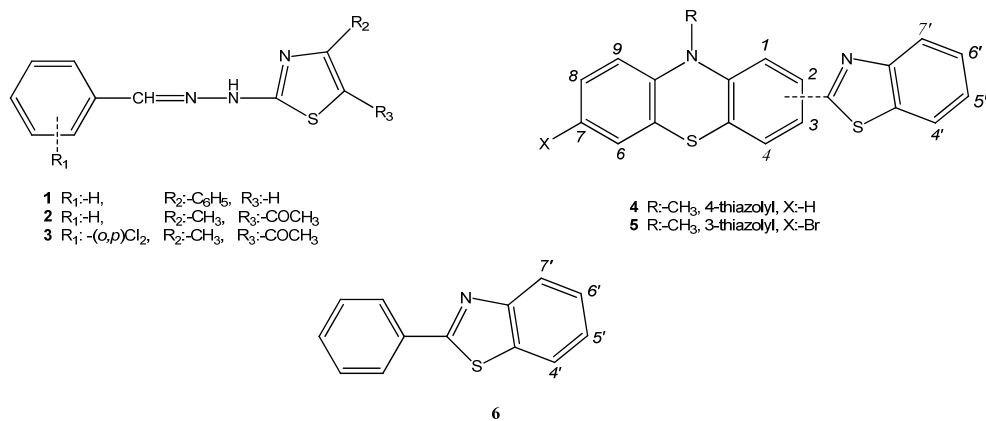


Figure 1. The chemical structures of the tested antifungal agents.

Table 1. Minimal inhibitory concentration (MIC) of different antifungal drugs against isolated *Candida* strains

<i>Candida</i> strain source	MIC (µg/ml)					
	Fluconazole	Voriconazole	Caspofungin	Micafungin	Amph-B	5-FC
<i>C. albicans</i> Blood culture	1 (S)	0.12 (S)	0.25 (S)	0.06 (S)	2 (I)	1 (S)
<i>C. glabrata</i> Blood culture	16 (I)	0.5 (S)	0.83 (S)	0.012 (S)	1 (S)	1 (S)
<i>C. glabrata</i> Br-alv lavage	4 (DDS)	0.12 (S)	0.25 (S)	0.06 (S)	0.5 (S)	1 (S)
<i>C. glabrata</i> Blood culture	4 (DDS)	0.12 (S)	0.25 (S)	0.06 (S)	1 (S)	1 (S)
<i>C. guilliermondii</i> Urine culture	32 (R)	0.12 (S)	0.25 (S)	0.06 (S)	2 (I)	1 (S)
<i>C. krusei</i> Peritoneal fluid	8 (R)	0.12 (S)	0.25 (S)	0.12 (S)	0.5 (S)	8 (I)
<i>C. lusitanae</i> Blood culture	32 (R)	0.008 (S)	0.12 (S)	0.06 (S)	0.5 (S)	256 (R)
<i>C. norvegiensis</i> Urine culture	16 (DDS)	0.25 (S)	0.25 (S)	0.12 (S)	1 (S)	4 (S)
<i>C. parapsilosis</i> Blood culture	1 (S)	0.12 (S)	1 (S)	0.5 (S)	1 (S)	1 (S)
<i>C. parapsilosis</i> Blood culture	1 (S)	0.12 (S)	0.5 (S)	0.5 (S)	0.5 (S)	1 (S)
<i>C. albicans</i> ATCC 10231	1 (S)	0.12 (S)	0.25 (S)	0.06 (S)	0.12 (S)	1 (S)

S=sensible; I=intermediate; R=resistant; DDS=dose-dependent sensibility;
 Amph-B= Amphotericin B; 5-FC= 5-Fluorocytosine

Three of the non-*C.albicans* strains appeared to be resistant to fluconazole, the most largely employed antifungal drug.

The *in vitro* susceptibility of *Candida* species to the synthetic compounds **1-6** was screened using the diffusion method and the results are presented in Table 2.

Table 2. Inhibition zone diameter (mm) resulted by diffusion method using 10 µl solution 2.5 mg/ml of compound **1-6**.

<i>Candida</i> strain source	Inhibition zone diameter (mm)						
	Fluconazole	1	2	3	4	5	6
<i>C. albicans</i> Blood culture	25	6	4	12	8	6	6
<i>C. glabrata</i> Blood culture	4	0	0	0	0	0	7
<i>C. glabrata</i> Br-alv lavage	4	0	4	0	0	0	6
<i>C. glabrata</i> Blood culture	4	0	4	0	0	0	6
<i>C. guilliermondii</i> Urine culture	2	6	4	12	0	0	0
<i>C. krusei</i> Peritoneal fluid	0	6	8	6	0	0	7
<i>C. lusitaniae</i> Blood culture	0	0	0	0	0	0	0
<i>C. norvegiensis</i> Urine culture	6	6	4	4	0	0	0
<i>C. parapsilosis</i> Blood culture	31	6	7	12	0	0	0
<i>C. parapsilosis</i> Blood culture	24	7	7	12	0	0	0
<i>C. albicans</i> ATCC 10231	30	2	2	12	0	0	8

Neither of the tested compounds **1-6**, nor fluconazole were active against *C. lusitaniae*, while in the case of *C. albicans* and *C. parapsilosis* strains all the tested compounds **1-6** showed inhibition zones with considerably smaller diameter in comparison to the antimycotic drug.

Hydrazones **1-3** and phenyl-benzothiazole **6** exhibited a moderate antifungal activity against *C. guilliermondii* and *C. krusei* strains which seemed resistant to fluconazole, while *C. glabrata* strain appeared slightly sensitive to phenyl-benzothiazole **6**.

Benzothiazolyl-phenothiazine derivatives **4, 5** appeared inactive against any of the isolated non-*C. albicans* strains.

Hydrazones **2**, **3** and phenyl-benzothiazole **6** pointed by the diffusion method screening as potential antifungal agents against *C. albicans* and non-*C. albicans* strains: *C. guilliermondii*, *C. krusei* and *C. parapsilosis* were further employed in MIC determination experiments using the broth dilution method. The results thus obtained are summarized in table 3.

Table 3. Minimal inhibitory concentration (MIC) for hydrazones **2**, **3** and phenyl-benzothiazole **6**.

<i>Candida strain</i>	MIC ($\mu\text{g/ml}$)			
	Fluconazole	2	3	6
<i>C. albicans</i> Blood culture	1 (S)	0.16	0.8	64
<i>C. guilliermondii</i> Urine culture	32 (R)	32	0.16	64
<i>C. krusei</i> Peritoneal fluid	8 (R)	0.8	32	1.2
<i>C. parapsilosis</i> Blood culture	1 (S)	0.5 (S)	1 (S)	64
<i>C. parapsilosis</i> Blood culture	1 (S)	0.5 (S)	0.5 (S)	64
<i>C. albicans</i> ATCC 10231	1 (S)	32	1.2	64

S=sensible; R=resistant;

Hydrazones **2**, **3** gave the impression of effective antifungal agents against the two non-*C. albicans* strains resistant to fluconazole: *C. guilliermondii* and *C. krusei* and proved to be even more effective than the commercial antifungal drug against *C. albicans* and *C. parapsilosis* strains isolated from the blood of health-care patients.

Phenyl-benzothiazole **6** appeared effective only against *C. krusei* isolated from peritoneal fluid.

CONCLUSIONS

The antifungal activity of heterocyclic compounds containing the thiazole unit screened *in vitro* pointed out the sensibility of *C. albicans* and non-*C. albicans* strains isolated from clinical materials towards hydrazinothiazole derivatives. Substituted benzothiazole derivatives appeared to be less effective and the presence of the phenothiazine unit did not favour the antifungal activity.

EXPERIMENTAL SECTION

Compounds **1-6** were synthesized according to our previously reported procedures [10,11].

The *Candida* species strains were isolated from clinical materials which were collected from patients with invasive fungal infections health cared in the *Hospital of Infectious Diseases Cluj-Napoca*.

The *Candida* species strains were isolated from blood, urine, peritoneal liquid and bronco-alveolar lavage liquid cultures.

The identification and the susceptibility profile of the isolated *Candida* strains to six different commercial antifungal drugs was determined using the automated systems Vitek 2 YST and AST-SY01.

Antifungal activity tests:

The fungus strains were cultivated on Sabouraud dextrose agar with incubation at $37\pm 2^{\circ}\text{C}$ for 48h in aerobic conditions.

a) The Diffusion method was carried out according to previously reported procedure [11] using a fungus culture which has been adjusted to 0.5 McFarland standard inoculated in Muller Hinton agar plates; 10 μl from 2.5 mg/ml solution of synthetic compounds in DMSO were disposed on sterile paper disks. Standard Fluconazol 25 $\mu\text{g}/\text{disc}$ (Oxoid, England) was employed. After incubation at $37\pm 2^{\circ}\text{C}$ for 72 hours the plates were examined for inhibition zone, which was measured and recorded in mm.

The tests were repeated three times to ensure reliability.

b) Broth dilution procedure was carried out according to the protocols previously described [11]. MIC was determined using microdilution trays using a stock solution 2.5 mg/ml in DMSO and distilled water. Each tray included a growth control well and a sterility (uninoculated) well.

The rights of the patients regarding the confidentiality of personal information were respected in agreement to Helsinki declaration of Ethical Principles for Medical Research Involving Human Subjects

ACKNOWLEDGMENTS

This work was supported by the Swiss Enlargement Contribution in the framework of the Romanian-Swiss Research Program, project number IZERZO-142198/1 (A. Grozav).

This paper was published under the frame of European Social Found, Human Resources Development Operational Programme 2007-2013, project no. POSDRU/159/1.5/S/136893" (A. Grozav).

REFERENCES

1. E.R.M. Sydnor, T.M. Perl, *Clinical Microbiology Reviews* **2011**, *1*, 141.
2. G.S. Martin, D.M. Mannino, S. Eaton, M. Moss, *The New England Journal of Medicine*, **2003**, *348*, 1546.
3. M.A. Pfaller, D.J. Diekema, *Clinical Microbiology Reviews*, **2007**, *20*, 133.
4. N. Azie, D. Neofytos, M. Pfaller, H.U. Meier-Kriesche, S.P. Quan, D. Horn, *Diagnostic Microbiology and Infectious Disease*, **2012**, *73*, 293.
5. M.T. Montagna, G. Caggiano, G. Lovero et al. *Infection*, **2013**, *41*, 645.
6. J.R. Rees, R.W. Pinner, R.A. Hajjeh, M.E. Brandt, A.L. Reingold, *Clinical Infectious Diseases*, **1998**, *27*, 1138.
7. F. Marco, S.R. Lockhart, M.A. Pfaller, C. Pujol, M.S. Rangel-Frausto, T. Wiblin, H.M. Blumberg, J.E. Edwards, W. Jarvis, L. Saiman, J.E. Patterson, M.G. Rinaldi, R.P. Wenzel, D.R. Soll, *Journal of Clinical Microbiology*, **1999**, *37*, 2817.
8. M. Bassetti, M. Merelli, E. Righi, A. Diaz-Martin, E.M. Rosello, R. Luzzati, A. Parra, E.M. Trecarichi, M. Sanguinetti, B. Posteraro, J. Garnacho-Montero, A. Sartor, J. Rello, M. Tumbarelli, *Journal of Clinical Microbiology*, **2013**, *51*, 12, 4167.
9. A. Lepak, D. Andes, *Critical Care Clinics*, **2011**, *27*, 123.
10. A. Grozav, V. Zaharia, C. Cristea, N.I. Fit, *Studia UBB Chemia*, **2015**, *60* (3), 283.
11. B. Brem, E. Gal, C. Cristea, L. Gaina, A. Grozav, V. Zaharia, L. Silaghi-Dumitrescu, *Studia UBB Chemia*, **2015**, *60* (2), 37.
12. P.A. Wayne, CLSI, Clinical Laboratory Standards Institute. Reference method for broth dilution antifungal susceptibility testing of yeast: fourth Informational Supplement, **2012**, M27-S4.

*Dedicated to Professor Luminița Silaghi-Dumitrescu
on the occasion of her 65th anniversary*

ELECTROCHEMICAL INVESTIGATION OF THE INHIBITING EFFECT EXERTED BY THE SULFURIC ACID DIAMIDE ON BRONZE CORROSION

**JULIETA DANIELA CHELARU^a, MARIA GAVRILOAE^a,
LIANA MARIA MURESAN^{a*}**

ABSTRACT. The present study is aiming to study the effect of sulfuric acid diamide (SAD) on corrosion of bronze CuSn8. In order to determine the optimal corrosion inhibiting effect SAD was tested at different concentrations. The inhibiting effect of the SAD was investigated by electrochemical methods, in a 0.2 g / L Na₂SO₄ + 0.2 g / L NaHCO₃ (pH = 5) solution simulating acid rain. The results show that SAD exerts a good protection in case of CuSn8.

Key words: bronze corrosion, inhibitor, acidic solutions, electrochemical techniques

INTRODUCTION

Because of increasing urban pollution in recent years, bronze statues exposed in these areas are subject to accelerated corrosion, resulting in the destruction of the protective layer formed over time (noble patina). The artistic aspect is also suffering due to the appearance of leaks, discoloration and the crystallization of impurities on the bronze surface.

For bronze protection against corrosion are used various inhibitors, most of them containing S and N in their molecules, such as thiadiazoles [1 - 7], imidazoles [1, 8 - 9], antibacterial drugs [10] etc. It is preferable that they do not modify the noble patina artistic appearance.

^a Department of Chemical Engineering, "Babes-Bolyai" University, 11 Arany Janos St., 400028 Cluj-Napoca, Romania,

*Corresponding author: limur@chem.ubbcluj.ro

In this context, in order to improve the corrosion resistance of bronze CuSn8 surface, the aim of this paper was to investigate the protective effect of sulfuric acid diamide (**SAD**) at different concentrations on bronze CuSn8 surface, in a solution containing $\text{Na}_2\text{SO}_4 + \text{NaHCO}_3$ (pH5) that simulated an acid rain in urban environment. The protective effect of **SAD** was investigated by electrochemical methods (potentiodynamic polarization measurements and electrochemical impedance spectroscopy).

RESULTS AND DISCUSSION

Open circuit potential measurement

In order to evaluate inhibiting properties of **SAD** at different concentrations, the experiments were started with the open circuit potential (OCP) measurements as a function of time. In Fig. 1 there are shown the OCP evolution for all concentrations of **SAD** studied, as well as in the absence of **SAD**, in the corrosion solution (pH 5). We can observe that all curves present a similar electrochemical behavior. In time, there is an increase of the values of OCP, but after approximately 15 minutes, it can be observed a regular evolution caused by a stable process at electrode / corrosive solution interface. It can be also observed that in the case of the presence of **SAD** OCP values are more negative than in the case of its absence, suggesting interactions of **SAD** molecules with the cathodic depolarization reaction [4].

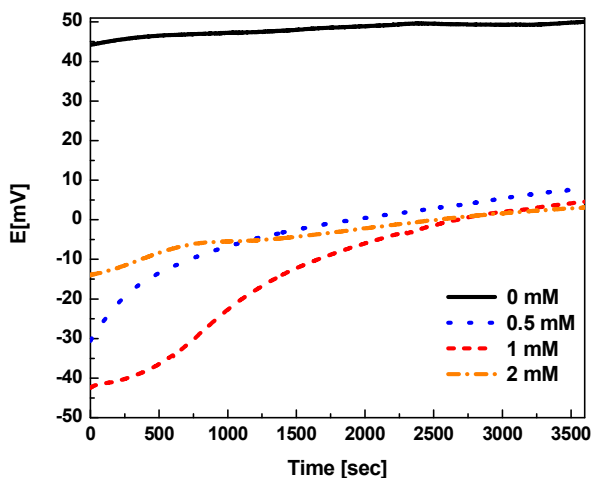


Figure 1. Open circuit potential measurements for the examined samples in absence / presence of **SAD**, immersed in corrosion solution, pH 5

Potentiodynamic polarization measurements

One hour after immersion of bronze electrodes in the corrosive solution in the presence or absence of various **SAD** concentrations (pH 5), the linear polarization curves were recorded at a potential scan rate of 10 mV / min., in the potential domain of ± 20 mV vs. the value of the open circuit potential (OCP). The polarization resistance values, R_p^* , calculated as the inverse of the slope of each curve in case of all **SAD** concentrations, are shown in Table 1.

To determine the kinetic parameters of the corrosion process, polarization curves were recorded in the potential range of ± 200 mV vs. OCP Fig. 2. The results obtained by Tafel interpretation are also shown in Table 1.

Table 1. Corrosion process parameters for the examined samples in 0.2 g/L NaSO₄ + 0.2 g/L NaHCO₃ (pH = 5)

C [mM]	i_{corr} [$\mu\text{A}/\text{cm}^2$]	E_{corr} [mV]	β_a [mV]	β_c [mV]	R_p^* [$\text{k}\Omega\text{cm}^2$]	IE [%]	
						i_{cor}	R_p^*
0	1.46	41.57	255.55	76.82	9.05	-	-
0.5	0.41	1.52	182.18	203.85	48.30	72	81
1	0.16	-6.65	106.86	313.72	176.00	89	95
2	0.39	1.14	406.10	168.29	44.85	73	80

Based on the corrosion current density (i_{corr}) the protection efficiencies IE, calculated with the formula (1) are highest when a 1mM solution of **SAD** was used.

$$IE[\%] = \frac{i_{corr}^0 - i_{corr}}{i_{corr}^0} \times 100 \quad (1)$$

i_{corr}^0 and i_{corr} are the values of the corrosion current densities in absence and in presence of the **SAD** at different concentrations, respectively.

IE was also calculated with the formula (2):

$$IE[\%] = \frac{R_p - R_p^0}{R_p} \times 100 \quad (2)$$

R_p^0 and R_p are the values of the polarization resistance in absence and in presence of the **SAD** at different concentrations, respectively. The results calculated by equation (2) are in accordance with the previous ones.

As shown in Table 1, the sulfuric diamide exerts a protective effect against bronze corrosion at all investigated concentrations. The best results were noticed at 1 mM **SAD**, this being suggested by the high value of the polarization resistance ($R_p=176.00$ [$k\Omega cm^2$]) and the low value of the corrosion current density ($i_{corr}= 0.16$ [$\mu A/cm^2$]). It can be assumed that the beneficial action of the organic compound is due to S and N heteroatoms from its molecules determining its adsorption on the bronze surface.

This behaviour it can be ascribed to the formation of the uniform and stable passive layer on bronze surface. According to Chiavari the layer of corrosion products formed, prevents especially the oxygen diffusion to the bronze surface [11].

Based on these results **SAD** can be considered an efficient corrosion inhibitor for bronze.

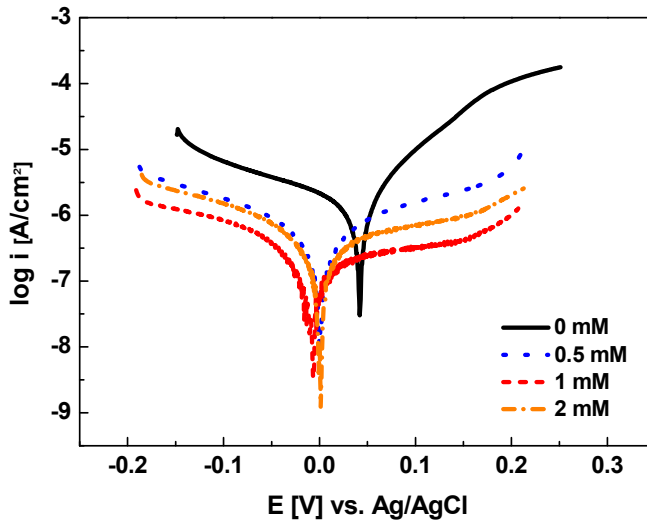


Figure 2. Polarization curves (± 200 mV vs. ocp) for the studied electrodes immersed in 0.2 g / L Na_2SO_4 + 0.2 g / L $NaHCO_3$ (pH = 5) at different concentrations of **SAD**, potential scan rate, 10 mV / min.

Electrochemical impedance spectroscopy

The corrosion behaviour of bronze after 1 h immersion in the corrosive solutions without and with various concentrations of **SAD** was more deeply investigated by electrochemical impedance spectroscopy (EIS). The measurements were conducted at 1 hour, 24, 48, respectively 72 hours from the immersion in the corrosive solution and the obtained Nyquist diagrams are presented in Fig. 3.

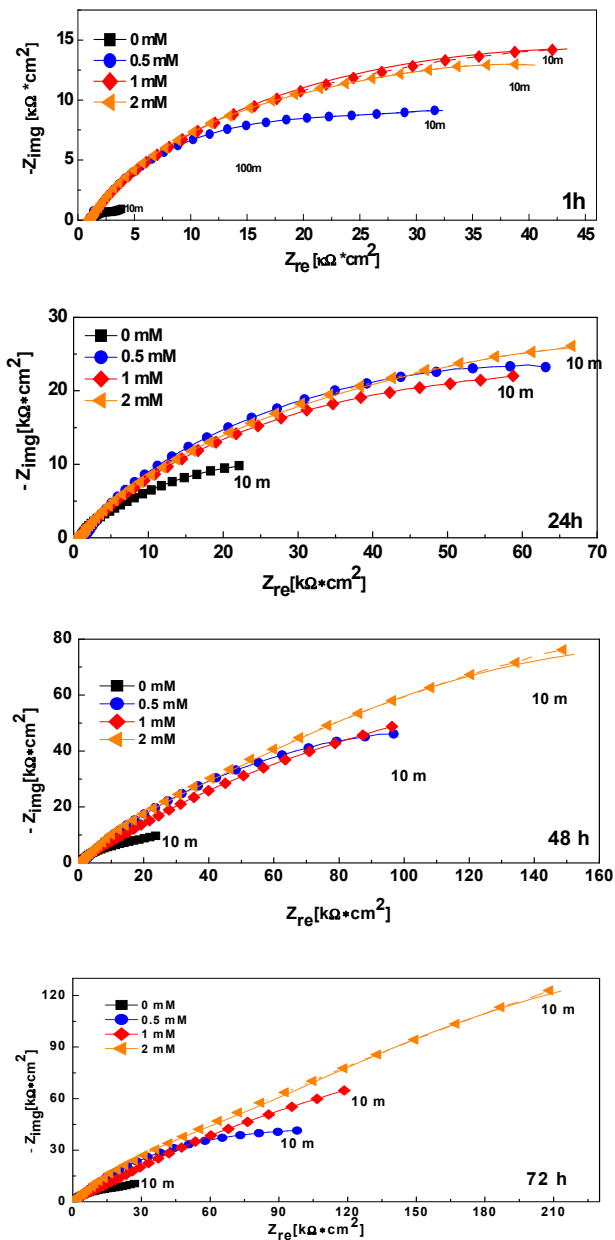


Figure 3. Nyquist impedance diagrams of bronze electrode in $Na_2SO_4 / NaHCO_3$ (pH 5) solution without / with various concentrations of **SAD** as a function of immersion time; the lines represent fitted data.

It can be noticed that the impedance spectra exhibit a capacitive behaviour in the whole frequencies domain. The experimental impedance spectra were analyzed by fitting to the (2RC) equivalent electrical circuit (Fig. 4), which was previously used to model bronze corrosion in the presence of corrosion inhibitors [10 - 12]. The origin of various variables used in the equivalent circuit from Fig. 4 is as follows: R_e : Electrolyte resistance; R_t : Charge transfer resistance; C_d : Double layer capacitance at the bronze | electrolyte interface; R_f : Faradic resistance of the corrosion products accumulated at the interface; C_f : Faradic capacitance due to an oxidation - reduction process taking place at the electrode surface, probable involving the corrosion products, n_d , n_f : Coefficient representing the depressed feature of the capacitive loop in *Nyquist* diagram ($n = [0.52 - 0.81]$).

The polarization resistance R_p , can be calculated as the sum $R_f + R_t$ [1], and is inversely proportional to corrosion rate. The protective effectiveness of the SAD calculated from R_p values (according to the relation 2), is presented in Table 2.

As can be observed, the used equivalent circuit suitably reproduce the experimental data corresponding to bronze corrosion in the absence and in the presence of **SAD** (Fig. 3). The parameters obtained by non - linear least square fitting and the calculated inhibition efficiencies are given in Table 2. It can also be observed that after 1 hour of immersion, the efficiency is also highest in case of addition of 1mM **SAD** (**92.22 %**), thus confirming the results obtained from the polarization curves. Generally, the inhibition efficiencies are higher at short immersion times and are situated around 90 %.

Table 2. Electrochemical parameters of bronze corrosion in $\text{Na}_2\text{SO}_4 / \text{NaHCO}_3$ (pH 5) solution obtained in the absence / the presence of various concentrations of **SAD**.

C [mM]	Time [h]	R_e [$k\Omega\text{cm}^2$]	R_t [$k\Omega\text{cm}^2$]	C_d [$\mu\text{F}/\text{cm}^2$]	R_f [$k\Omega\text{cm}^2$]	C_f [$\mu\text{F}/\text{cm}^2$]	R_p [$k\Omega\text{cm}^2$]	IE[%]
0	1	1.03	3.04	321.8	2.12	837	5.16	-
	24	0.937	11.67	48.55	34.58	678.4	46.25	-
	48	0.782	15.99	39.76	39.02	616.2	55.01	-
	72	0.675	18.17	27.48	43.90	608.2	62.07	-
0.5	1	1.22	19	29.58	21.67	301.8	40.67	87.31
	24	1.30	67.6	36.15	120.8	644.8	118.98	61.13
	48	0.93	80.4	35.2	156.3	33.16	192	71.35
	72	0.72	50.09	2.03	135.2	2.8	185.29	66.50
1	1	1.05	47.52	45.96	18.78	602.1	66.3	92.22
	24	0.752	49.95	30.40	59.97	222	109.92	57.92
	48	0.295	44.02	20.36	58.5	190.52	102.52	46.34
	72	0.303	36.57	22.73	233.6	10.12	270.17	77.03
2	1	0.97	33.69	26.79	31.35	480.4	65.04	92.07
	24	0.63	67.08	27.53	68.46	353.1	135.54	65.88
	48	0.51	85.73	7.1	286	71.99	371.73	85.20
	72	0.54	143.6	6.43	472	65.36	615.6	89.91

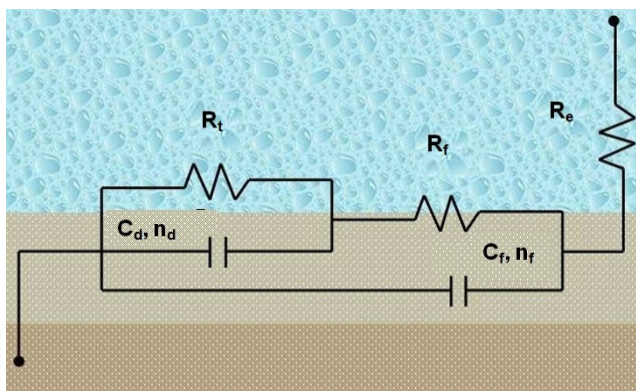


Figure 4. Equivalent electrical circuit used for fitting of the experimental results (2RC)

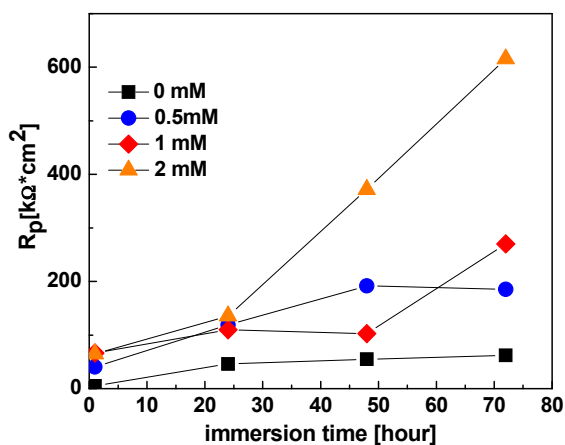


Figure 5. Variation of the polarization resistance in time at different **SAD** concentrations.

The increase in polarization resistance observed in the presence of various concentrations of **SAD** compared to the values obtained in the absence of **SAD** may be associated with the slowing down of corrosion process. It can be observed that the polarisation resistance values are changing during time for all **SAD** concentrations (Fig. 5). A relative stabilization in time is noticed only at 0.5 mM **SAD**, probably due to a stabilization of the corrosion products layer. At high concentrations, R_p increases in time suggesting a thickening of the protective inhibitor film formed on the electrode surface by its adsorption.

CONCLUSIONS

Inhibiting effect of the sulfuric acid diamide at different concentrations on artistic bronze were investigated in $\text{Na}_2\text{SO}_4 / \text{NaHCO}_3$ (pH 5) solution. Electrochemical investigations (polarization and impedance measurements) revealed that sulfuric acid diamide exerts a good protective effect against bronze corrosion in case of all various concentrations. The best anticorrosive effect was noticed after 1 hour of immersion in corrosion media when 1mM inhibitor was used, but after 72 hour immersion the best protection is exerted by 2 mM **SAD**.

The corrosion behaviour of the bronze immersed in $\text{Na}_2\text{SO}_4 / \text{NaHCO}_3$ (pH 5) solution can be simulated with a 2RC electric circuit.

EXPERIMENTAL

Materials

For the working electrodes was used a complex tin bronze alloy that contains a series of secondary alloying elements: 90.18 % copper, 8 % tin, 0.8 % zinc, 1 % lead and 0.02 % aluminium.

The working electrodes were made from a cylindrical bronze rod, placed in a PVC tube and embedded in an epoxy resin, so that only the disc-shaped cross section ($S = 2 \text{ cm}^2$) of the rod was exposed to the corrosive electrolyte. For electrical contact, a metal rod was attached. It were used four bronze electrodes. Before each electrochemical measurement, the bronze electrode was mechanically polished using successive grades of silicon carbide paper up to grade 2000 to obtain a planar and smooth surface. Finally, the bronze electrodes surface were rinsed with distilled water.

Corrosion inhibitor

The inhibitor used in the experiments was a non - toxic sulfonamide derivative, namely sulfuric acid diamide ($\text{H}_2\text{NSO}_2\text{NH}_2$) (Fig. 6). The inhibitor was dissolved in the corrosive solution at different concentrations respectively: 0.5 mM, 1 mM, 2 mM. The electrolyte solution for corrosion measurements was 0.2 g / L Na_2SO_4 + 0.2 g / L NaHCO_3 acidified to pH = 5 by the addition of a dilute sulfuric acid at room temperature.

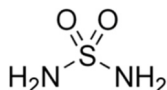


Figure 6. The molecular structure of the inhibitor

Experimental investigation

The electrochemical corrosion measurements were performed on a PC – controlled electrochemical analyzer AUTOLAB - PGSTAT 10 (Eco Chemie BV, Utrecht, The Netherlands) using a three electrodes cell containing a working electrode (bronze), an Ag/AgCl electrode as reference electrode and a platinum counter electrode. Anodic and cathodic polarization curves were recorded in a potential range of ± 20 mV (for R_p determination) and of ± 200 mV vs. the value of the open circuit potential (for Tafel interpretation), with a scan rate of 10 mV / min, after 1 hour immersion in the corrosive solution.

Electrochemical impedance spectroscopy measurements (EIS) were carried out at the open circuit potential after 1 h, 24 h, 48 h respectively 72 h immersion of the bronze electrode in the corrosive medium. The impedance spectra were acquired in the frequency range 10 kHz to 10 mHz at 10 points/decade with an AC voltage amplitude of ± 10 mV. The impedance data were interpreted based on equivalent electrical circuits, using the ZSimpWin V3.21 software for fitting the experimental data.

REFERENCES

1. L. Mureşan, S. Varvara, E. Stupnišek - Lisac, H. Otmačić, K. Marušić, S. Horvat - Kurbegović, L. Robbiola, K. Rahmouni, H. Takenouti, *Electrochimica Acta*, **2007**, 52, 7770 - 7779.
2. S. Varvara, L.M. Mureşan, K. Rahmouni, H. Takenouti, *Corrosion Science*, **2008**, 50, 2596.
3. J.D. Chelaru, L.M. Mureşan, *Studia UBB Chemia*, **2013**, 173 - 182.
4. J.D. Chelaru, L.M. Mureşan, *Studia UBB Chemia*, **2014**, 91-102.
5. S. Varvara, R. Bostan, L. Găină, L.M. Mureşan, *Materials and Corrosion*, **2014**, 65, 1202 - 1214.
6. El-S.M. Sherif, *Applied Surface Science*, **2006**, 252, 8615 – 8623.
DOI:10.1016/j.apsusc.2005.11.082.
7. A. Balbo, C. Chiavari, C. Martini, C. Monticelli, *Corrosion Science*, **2012**, 59, 204 - 212.
8. K. Marušić, H. Otmačić - Ćurković, Š. Horvat - Kurbegović, H. Takenouti, E. Stupnišek - Lisac, *Electrochimica Acta*, **2009**, 52, 7106 - 7113.
9. K. Marušić, H. Otmačić - Ćurković, H. Takenouti, *Electrochimica Acta*, **2011**, 56, 7491 - 7502.
10. I. Rotaru, S. Varvara, L. Găină, L.M. Mureşan, *Applied Surface Science*, **2014**, 321, 188 – 196.

11. C. Chiavari, A. Colledan, A. Frignani, G. Brunoro, *Materials Chemistry and Physics*, **2006**, 95, 252 – 259.
12. R. Bostan, S. Varvara, L. Găină, L.M. Mureșan, *Corrosion Science*, **2012**, 63, 275 – 286.

*Dedicated to Professor Luminița Silaghi-Dumitrescu
on the occasion of her 65th anniversary*

ELECTROCHEMICAL DETERMINATION OF DOPAMINE WITH GRAPHENE-MODIFIED GLASSY CARBON ELECTRODES

**ÁRPÁD FERENC SZÓKE^a, GRAZIELLA LIANA TURDEAN^{a*},
GABRIEL KATONA^a, LIANA MARIA MURESAN^a**

ABSTRACT. Two new glassy carbon modified electrodes were prepared by drop casting of chemically reduced graphene oxide (rGO) or graphene oxide (GO) on glassy carbon (GC) and then protected with a polymeric layer of Nafion or chitosan (Chit) (GC/Chit/rGO/Chit and GC/GO/Nafion). Their investigation by cyclic- and square-wave voltammetry for dopamine (DA) oxidation was aiming to estimate the analytical parameters that have the best values for GC/Chit/rGO/Chit electrode (*i.e.*, the highest sensitivity of $1.002 \pm 0.025 \mu\text{A}/\mu\text{M}$, a detection limit of $2.67 \mu\text{M}$, for a linear domain from 4 to $18 \mu\text{M}$ DA). The modified GC/Chit/rGO/Chit electrode was also used for the detection of dopamine in injection vials using the standard addition method with a recovery of 99.42%.

Keywords: graphene oxide, reduced graphene oxide, dopamine, cyclic voltammetry, square wave voltammetry

INTRODUCTION

Dopamine (DA) is a neurotransmitter with important roles in the function of central nervous, cardiovascular, renal and hormonal systems [1]. It is associated in human behaviours such as: reward, cognition, motor function, motivation, learning and memory [2]. Deficiency of DA may cause serious diseases like schizophrenia and Parkinson's disease, so its detection becomes necessary and helpful for correct diagnosis [3-4].

^a "Babeş-Bolyai" University, Faculty of Chemistry and Chemical Engineering, 11 Arany Janos St., RO-400028, Cluj-Napoca, Romania,

* Corresponding author: gturdean@chem.ubbcluj.ro

The detection of dopamine could be realized by capillary electrophoresis, liquid chromatography, calorimetric method, chemiluminescence, fluorescence etc. Because of its redox activity, dopamine is an interesting subject in electroanalysis, consequently electrochemical methods have gained more attention due to their advantages such as: selectivity, low-cost, portability, easy handling and less-time consuming [2].

However, in real body fluids, dopamine coexists with interfering substances (e.g., ascorbic acid and uric acid), having similar oxidation potential. In this context, for selective and discriminative detection of DA, surface modification of the working electrodes with appropriate agents such as graphene [5] and carbon nanotubes is a promising method [6].

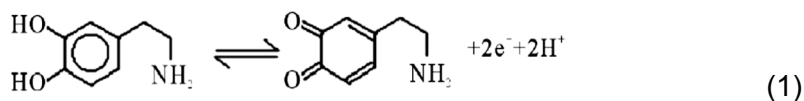
Graphenes, an atomically thin layer of sp²-bonded carbon atoms, stacked in a two-dimensional (2D) honeycomb lattice, belong to a new class of carbon nanomaterials [7] that display versatile properties including thermal/electrical conductivity, good mechanical properties, large surface area etc. [8]. Due to these properties, graphenes can be successfully used in electrochemical sensing devices for selective detection of chemical species. Nevertheless, it should be mentioned that graphene is electrochemically active only in its reduced form, but electrode modification with graphene oxide can also be achieved by the introduction of a pretreatment step, which reduces the graphene oxide to graphene. The reduction of GO to graphene can be done either chemically, electrochemically or thermally [2].

The present work was focused on the electrochemical studies of chemically reduced graphene oxide (rGO) and electrochemically reduced graphene oxide (GO) immobilized *via* drop-casting method [9] on glassy carbon (GC) electrodes and protect by either Nafion [10] or Chitosan [11] polymers. The obtained modified electrodes were used for studying dopamine oxido-reduction process by cyclic- and square-wave voltammetry.

RESULTS AND DISCUSSION

Electrochemical behaviour of dopamine at different glassy carbon modified electrodes

The oxido-reduction of 10⁻³ M DA at various modified electrodes was investigated by cyclic voltammetry (CV). As shown in figure 1, at both modified electrode a pair of peaks appeared at around +0.250 V vs. Ag/AgCl, KCl_{sat} and was attributed to the oxidation of dopamine to form dopaminequinone with the release of two electrons as described by the following reaction (1):



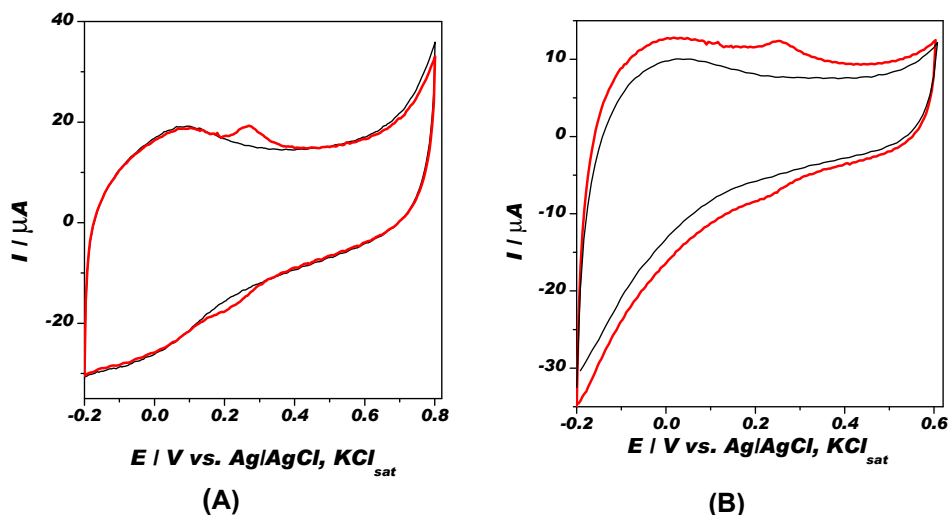


Figure 1. Cyclic voltammograms of 15 μM dopamine (thick) at GCE/GO/Nafion/(red) (A) and GCE/Chit/rGO/Chit (B) modified electrode. Experimental conditions: electrolyte, 0.1 M phosphate buffer (pH 7) (thin layer); scan rate, 50 mV/s; starting potential, -0.2 V vs. Ag/AgCl, KCl_{sat} .

Dopamine being an easily oxidizable catecholamine, the separation of redox peaks (ΔE_p , calculated as the difference between E_{pa} and E_{pc}) was found 0.046 V for GCE/GO/Nafion/(red) and 0.023 V for GCE/Chit/rGO/Chit electrode, respectively. On the other side, the $I_{\text{pa}}/I_{\text{pc}}$ ratio was found 1.68 (at GCE/GO/Nafion/(red) electrode) and 1.39 (at GCE/Chit/rGO/Chit electrode), suggesting a quasi-reversible reaction. Despite the fact that the peak potentials for GCE/Chit/rGO/Chit electrode are placed more closely one from another, the formal peak potential (E^0 , calculated as the midpoint of E_{pa} and E_{pc}) was estimated to be 0.242 V for both studied modified electrodes. The smaller value of ΔE_p and the $I_{\text{pa}}/I_{\text{pc}}$ ratio value closer to 1 confirm that the redox process occurring at GCE/Chit/rGO/Chit electrode is more reversible than that occurring at GCE/GO/Nafion/(red) electrode. The difference between the two modified electrodes could be explained by the different porosity of the protective polymeric membrane used (*i.e.*, chitosan and Nafion).

Influence of scan rate

The effect of scan rate on the peak current of dopamine was recorded in the range of 10 – 200 mV/s in order to investigate the electrode reaction kinetics and verify if diffusion is the only factor controlling the process (Fig 2A-B). As it can be seen in Fig 2A-B, for both studied electrodes the scan rate increasing leads to the increase of the peak current and the

anodic and cathodic peak potentials are slightly shifted towards the positive and negative direction, respectively [2].

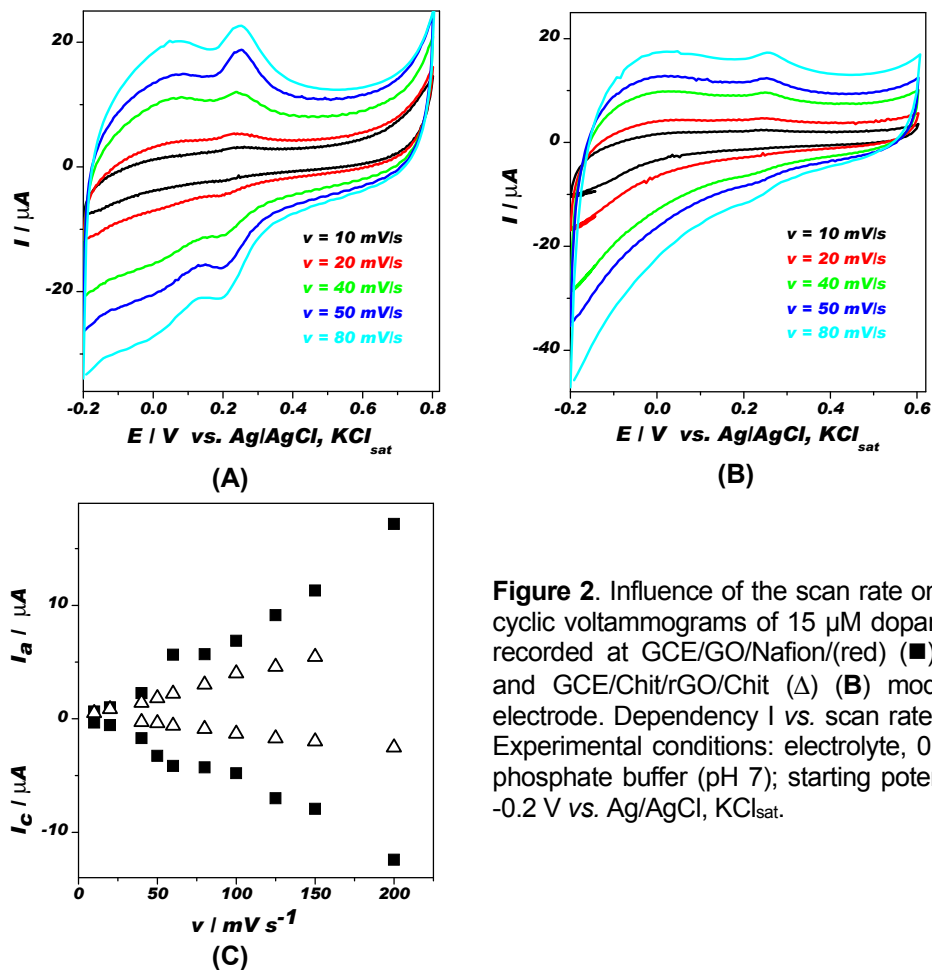


Figure 2. Influence of the scan rate on the cyclic voltammograms of 15 μM dopamine recorded at GCE/GO/Nafion/(red) (■) (A) and GCE/Chit/rGO/Chit (Δ) (B) modified electrode. Dependency I vs. scan rate (C). Experimental conditions: electrolyte, 0.1 M phosphate buffer (pH 7); starting potential, -0.2 V vs. Ag/AgCl, KCl_{sat} .

Fig 2C illustrates for both anodic and cathodic processes a linear relationship between $\log I_p$ and $\log v$ with a slope close to 1 (Table 1), proving a surface adsorption-controlled kinetics for oxidation of dopamine at the electrode surface during the experiment. Also, from Figure 2C it can be observed that the current intensities for GCE/Chit/rGO/Chit electrodes have lower values than those of GCE/GO/Nafion/(red) electrode. This behaviour, at the working pH 7, could be explained by an enhanced attractive interactions between the positively charged dopamine ($\text{pK}_a = 8.89$ [10]) and the negatively charged groups

(SO₄²⁻) of the Nafion protective polymers for GCE/GO/Nafion/(red) electrode. Such interactions could lead to an accumulation of DA on the surface of the modified electrode explaining the increase in peak current [4]. In the case of GCE/Chit/rGO/Chit electrode repulsive interactions between dopamine and the positively charged chitosan are noticed. Nevertheless, this effect is partially counteracted by the well-known phenomenon of swelling of Chit which increase the protective layer porosity [12].

Table 1: Influence of the potential scan rate on the voltammetric response of GCE/GO/Nafion/(red) and GCE/Chit/rGO/Chit modified electrodes. Experimental conditions: see Fig 2.

Electrode type	Slope of the log I _p – log v dependencies			
	oxidation	R ² /n	reduction	R ² /n
GCE/Chit/rGO/Chit	0.899 ± 0.034	0.9916 / 9	1.417 ± 0.056	0.9779 / 8
GCE/GO/Nafion/(red)	1.121 ± 0.07	0.9817 / 9	1.237 ± 0.092	0.9706 / 10

where: R is the correlation coefficient and n is the no. of experimental points.

Analytical parameters for dopamine detection

The analytical parameters were determined by using square-wave voltammetry (SQW).

Case of G/GO/Nafion electrode

The GCE/GO/Nafion electrodes were activated by electrochemical reduction of GO, consisting by cycling the electrode potential between -1 and 0 V vs. Ag/AgCl, KCl_{sat} for 10 cycles. This activation step was done before (*i.e.*, GCE/GO/(red)/Nafion) and after (*i.e.*, GCE/GO/Nafion/(red)) deposition of the protective layer of Nafion. Square-wave voltammetric measurements carried out at GCE/GO/Nafion electrodes in the absence and in the presence of dopamine (Figure 3A) allowed obtaining of calibration curves. Based on these curves (Figure 3B), the electroanalytical parameters of the modified electrodes were estimated (Table 2).

It is worth mentioning that the step of electrochemical reduction of GO before or after applying the protective layer of Nafion has a great influence on the electrode sensitivity. Comparing the slopes of the calibration curves we can observe an increase of the sensibility from 0.147 ± 0.004 μA/μM (for

GCE/GO/(red)/Nafion electrode) to $0.318 \pm 0.007 \mu\text{A}/\mu\text{M}$ (for GCE/GO/Nafion/(red) electrode). For GCE/GO/(red)/Nafion electrode the linear domain was between 2.5 - 70 μM DA and more narrow for GCE/GO/Nafion/(red) (*i.e.*, 1 - 40 μM DA).

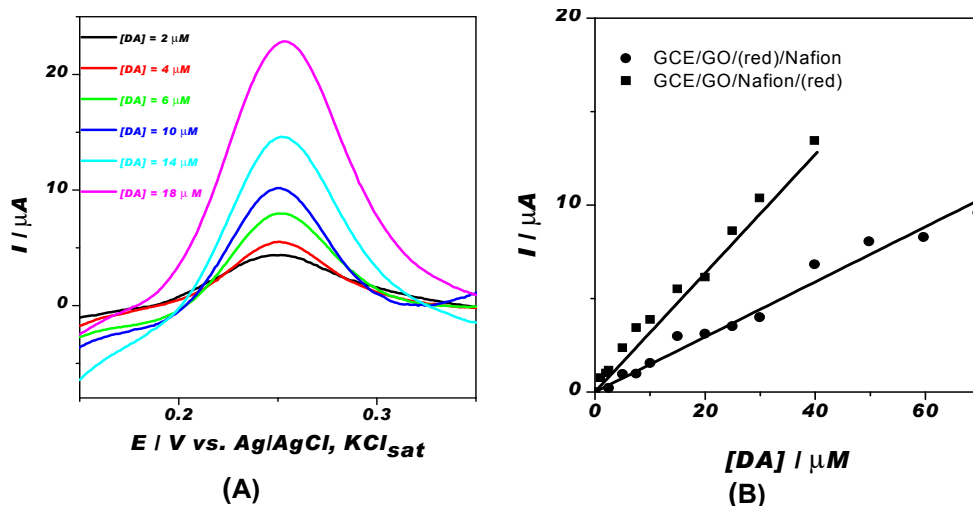


Figure 3. SQW voltammograms of dopamine (after baseline corrections) at GCE/GO/(red)/Nafion electrodes (A) and the corresponding calibration curve for dopamine detection at GCE/GO/(red)/Nafion (●) and GCE/GO/Nafion/(red) (■) (B). Experimental conditions: phosphate buffer 0.1 M (pH 7); frequency, 10 Hz; amplitude, 25 mV; step potential, 10 mV; starting potential -1 V vs. Ag/AgCl, KCl_{sat} .

Case of GCE/Chit/rGO/Chit electrode

In the case of GCE/GO/(red)/Nafion electrode, after a short time storage of the electrode surface, either by immersion in buffer solution or on air, the protective layer cracked. This is the reason for which Nafion was replaced by chitosan. In view to determine the ideal concentration of the chitosan solution used for surface protection, a concentrated (1%) solution and a diluted (0.1%) solution was used.

It was determined that the GCE/Chit/rGO/Chit electrode obtained using diluted solution shows a much higher sensitivity for detecting DA (*e.g.*, $1.0 \mu\text{A}/\mu\text{M}$) compared with those obtained with concentrated one (*e.g.*, $0.04 \mu\text{A}/\mu\text{M}$). Such high sensitivity can be obtained with a much lower limit of detection (*i.e.*, $2.67 \mu\text{M}$ compared to $6.6 \mu\text{M}$ DA) (results not shown).

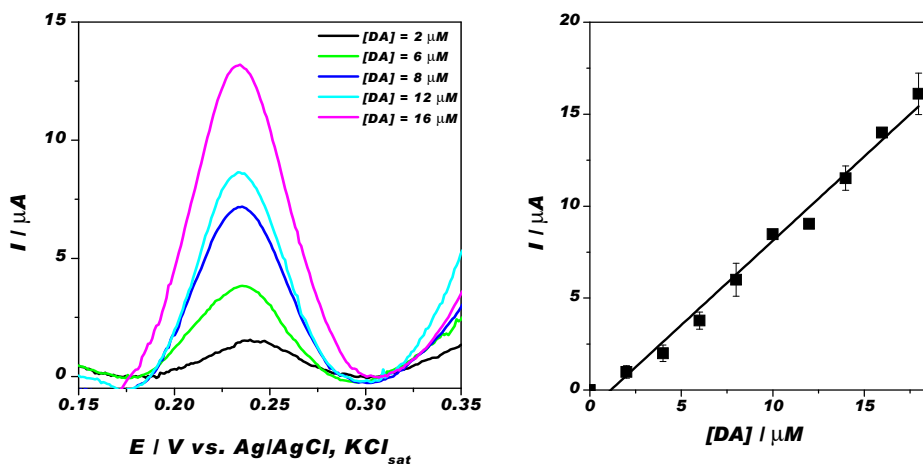


Figure 4. SQW voltammograms of dopamine (after baseline corrections) at GCE/Chit/rGO/Chit electrodes (A) and the corresponding calibration curve for dopamine. Experimental conditions: phosphate buffer 0.1 M (pH 7); frequency, 10 Hz; amplitude, 25 mV; step potential, 10 mV; starting potential -1 V vs. Ag/AgCl, KCl_{sat} ; error bars: mean of measurements with 3 different electrodes.

The analytical parameters of the mean measurements with 3 different GCE/Chit/rGO/Chit electrodes are summarised in table 2.

In the case of three measurements with 3 different electrodes of 18 μM DA at GCE/Chit/rGO/Chit in 0.1 M phosphate buffer pH 7, the mean peak intensity is $16,11 \pm 1.955 \mu A$, with a RSD of 12.14% and the mean peak potential is $0.234 \pm 0.006 V$ vs. Ag/AgCl, KCl_{sat} , with a RSD of 2.65%, respectively. The obtained RSD values indicate a good reproducibility of the obtained electrode, recommending the GCE/Chit/GO/Chit as a good sensor for DA detection.

Real sample analysis

To investigate the application potential of the GCE/Chit/GO/Chit electrodes for the detection of DA, the injections vials of DA (5 mg/ml) were analyzed by the standard addition method in order to overcome possible matrix effects.

Table 2. Electroanalytical parameters of the G/GO/Nafion and GCE/Chit/rGO/Chit modified electrodes. Experimental conditions: see fig. 3 and 4.

Electrode type	Sensitivity $\mu\text{A} / \mu\text{M}$	Linear range/ μM	LOD* / μM	R^2 / n
GCE/GO/(red)/Nafion)	0.147 ± 0.004	2.5 - 70	$1.35 \mu\text{M}$	0.9980/ 9
GCE/GO/Nafion/(red)	0.318 ± 0.007	1 - 40	$0.69 \mu\text{M}$	0.9980/10
GCE/Chit/GO/Chit **	1.002 ± 0.025	4 -18	$2.67 \mu\text{M}$	0.9969/ 7

* calculated using Miller approach and SMAC software based on the confidence bands of the calibration function; ** mean of 3 measurements obtained with 3 different electrodes.

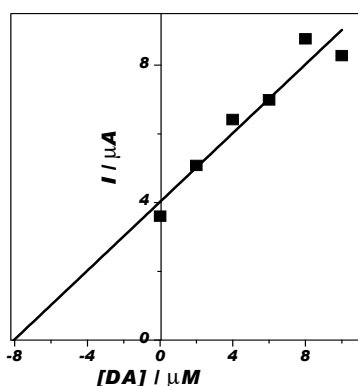


Figure 5. Standard addition method for determination of DA concentration from injection vials using GCE/Chit/GO/Chit electrode. Experimental conditions: see fig 4.

The linear equation for GCE/Chit/GO/Chit electrode obtained with standard addition method was $I/\mu\text{A} = (4.023 \pm 0.435) + (0.5 \pm 0.072) [\text{DA}]/\mu\text{M}$ ($R^2 = 0.9236$ $n = 6$), and lead to calculate the unknown concentration of the DA, which was estimated as $8.046 \mu\text{M}$ DA, for an added concentration of $8 \mu\text{M}$ DA. The value is in good agreement with that indicated by the producer and confirms that the proposed method could be efficiently used for the determination of DA in injection vials with a recovery of 99.42%.

EXPERIMENTAL SECTION

Reagents

The graphene oxide (GO) were prepared by dr. C. Cotet at the Faculty of Chemistry and Chemical Engineering and was a kindly gift which is gratefully thanked here. The reduced graphene oxide (rGO) was provided by Chengdu Organic Chemicals Co. Ltd., Chinese, Academy of Sciences. Dopamine hydrochloride 99% and the glacial acetic acid were provided by Alfa Aesar and by Merck, respectively. The $\text{Na}_2\text{HPO}_4 \cdot 2 \text{H}_2\text{O}$, $\text{NaH}_2\text{PO}_4 \cdot 12 \text{H}_2\text{O}$ and high viscosity chitosan were provided by Sigma Aldrich. The 5% Nafion in ethanol solution was supplied from Sigma Aldrich and ethanol 100% from Reactivul Bucuresti, respectively. All chemicals were of analytical grade and used without any purification step. For avoiding DA polymerization, stock solutions of dopamine were prepared fresh every day. The DA injection vials were produced by Zentiva with a specified content of DA of 5 mg/ml.

The graphene oxide (GO) 1 mg/mL solutions were prepared from flakes dissolved in distilled water during 30 minutes in a vortex mixer followed by 30 minutes sonication.

The 1 mg/mL dispersion of reduced graphene oxide (rGO) was obtained by mixing the appropriate quantity of powder for 30 minutes on a vortex mixer, followed by sonication (2 hours) and mixing (30 minutes on a vortex mixer). Before every usage, the stored dispersion was further sonicated, and then mixed for 30 minutes.

A 0.1 % chitosan solution was prepared by dissolving appropriate quantity of salt in 0.1 M acetic acid solution.

A 0.1 M phosphate buffer solution was prepared by using appropriate amounts of Na_2HPO_4 and NaH_2PO_4 and adjusting the pH values with 0.1 M H_3PO_4 or NaOH solutions, respectively.

Methods

Electrochemical measurements were performed with a PGStat 12 computer controlled potentiostat (Autolab, The Netherlands). An undivided electrochemical cell containing the modified glassy carbon electrode (GCE, 3 mm diameter) as the working electrode, a platinum wire as the counter and a $\text{Ag}/\text{AgCl}/\text{KCl}_{\text{sat}}$ as reference electrode was connected to the potentiostat. All experiments were carried out at room temperature.

Electrode preparation

The cleaning of glassy carbon electrodes (GCE) surfaces consist in polishing with 1200 abrasive paper and Al_2O_3 powder, followed by ultrasonication for 3 minutes. Between each step the electrode surface was rinsed with distilled water and inspected *via* microscope. The modified electrodes were prepared by drop casting.

GCE/GO/Nafion was obtained by dropping 5 μL of 1 mg/mL of GO solution on the clean GC surface and dried in air for solvent evaporation. After that the electrode surface was covered with 5 μL of 1.25% Nafion solution. The active form of GO was obtained by cycling the potential between -1 and 0 V vs. $\text{Ag}/\text{AgCl}/\text{KCl}_{\text{sat}}$ for 10 cycles either before (**GCE/GO/(red)/Nafion**) or after (**GCE/GO/Nafion/(red)**) protection with Nafion membrane.

GCE/Chit/rGO/Chit was prepared by successive deposition of 2 μL Chit, and a mixture of 5 μL rGO dispersion and 3 μL Chit solutions, respectively. Between each deposition steps, the solvent was evaporated in air drying. This alternation was needed to eliminate the significant differences in surface structure of glassy carbon electrodes, thus obtaining a "universal" procedure that would yield matching results on all used GC electrodes.

CONCLUSIONS

Modified GCE/GO/Nafion and GCE/Chit/rGO/Chit electrodes were prepared by drop casting method and investigated for studying the dopamine oxido-reduction process by cyclic voltammetry. The electrochemical parameters (ΔE_p , E^o , I_{pa}/I_{pc} , influence of scan rate) are in accordance with the literature data describing a $2e^-/2H^+$ reversible electrode process.

The prepared GCE/GO/Nafion and GCE/Chit/rGO/Chit electrodes, tested by square-wave voltammetry, exhibit greater sensitivity and selectivity for the determination of DA with a wide linear range and a low detection limit.

The GCE/Chit/rGO/Chit electrode was also used for detection of DA in real samples and satisfactory results were obtained.

REFERENCES

1. M. Heien, A. Khan, J. Ariansen, J. Cheer, P. Phillips, K. Wassum, M. Wightman, *Proceedings of the National Academy of Sciences of the United States of America*, **2005**, *102*, 10023.
2. S. Sakthinathan, H.F. Lee, S.-M. Chen, P. Tamizhdurai, *Journal of Colloid and Interface Science*, **2016**, *468*, 120.
3. Z. Zhao, M. Zhang, X. Chen, Y. Li, J. Wang, *Sensors*, **2015**, *15*, 16614.
4. S. Hou, N. Zheng, H. Feng, X. Li, Z. Yuan, *Analytical Biochemistry*, **2008**, *179*, 179.
5. Y. Wang, Y. Li, L. Tang, J. Lu, J. Li, *Electrochemistry Communications*, **2009**, *11*, 889.
6. L. Jiang, C. Liu, L. Jiang, Z. Peng, G. Lu, *Analytical Sciences*, **2004**, *20*, 1055.
7. D. Konios, M. M. Stylianakis, E. Stratakis, E. Kymakis, *Journal of Colloid and Interface Science*, **2014**, *430*, 108.
8. H. Wang, X. Yuan, G. Zeng, Y. Wu, Y. Liu, Q. Jiang, S. Gu, *Advances in Colloid and Interface Science*, **2015**, *221*, 41.
9. Y.-R. Kim, S. Bong, Y.-J. Kang, Y. Yang, R.K. Mahajan, J.S. Kim, H. Kim, *Biosensors and Bioelectronics*, **2010**, *25*, 2366.
10. S. Ku, S. Palanisamy, S.-M. Chen, *Journal of Colloid and Interface Science*, **2013**, *411*, 182.
11. C. Liu, J. Zhang, Y.E., J. Yue, L. Chen, D. Li, *Electronic Journal of Biotechnology*, **2014**, *17*, 18.
12. Y.-T. Shieh, H.-F. Jiang, *Journal of Electroanalytical Chemistry*, **2015**, *736*, 132.
13. V. Loryuenyong, K. Totepvimarn, P. Eimburanaprat, W. Boonchompoo, A. Buasri, *Advances in Materials Science and Engineering*, **2013**, <http://dx.doi.org/10.1155/2013/923403>.

*"Dedicated to Professor Luminița Silaghi-Dumitrescu
on the occasion of his 65th anniversary"*

REMOVAL OF LEAD FROM INDUSTRIAL WASTEWATER BY ELECTROCOAGULATION USING SACRIFICIAL ALUMINIUM ELECTRODES

SZABOLCS FOGARASI^a, FLORICA IMRE-LUCACI^b,
ADINA GHIRIȘAN^a, BARBU RADU HORĂȚIU MIȘCA^a,
ÁRPÁD IMRE-LUCACI^{a,c,*}

Abstract. The aim of this study was to develop an ecological method for the removal of Pb²⁺ ions from industrial wastewater. The electrocoagulation (EC) process of Pb²⁺ has been studied, using an electrolytic flow cell (flow rate of 20, 40, 60 mL/min) equipped with sacrificial Al electrodes, operated under galvanostatic mode (current density of 5, 10 and 15 mA/cm²). In all experimental conditions the concentration of Pb²⁺ was lowered below the maximum allowable concentration (0.5 ppm). The experimental results showed that the performances of the process are more strongly dependent on the applied current density than on the applied flow rate. The electrolytic flow cell has proved to be quite effective, allowing the complete removal of lead with a specific energy consumption of 3.08 kWh/kg Pb removed.

Keywords: lead contamination, sacrificial Al electrodes, lead removal, electrocoagulation.

^a Faculty of Chemistry and Chemical Engineering, Babeș-Bolyai University, 11 Arany Janos Street, Cluj-Napoca, RO-400028, Romania

^b Physico-Chemical Analyses Center, Interdisciplinary Research Institute on Bio-Nano-Sciences, Babeș-Bolyai University, 42 Treboniu Laurian Street, Cluj-Napoca, RO-400271, Romania

^c Research Institute for Sustainability and Disaster Management based on High Performance Computing (ISUMADECIP), Babeș-Bolyai University, 30 Fântânele Street, Cluj-Napoca, RO-400294, Romania

*Corresponding author: aimre@chem.ubbcluj.ro

INTRODUCTION

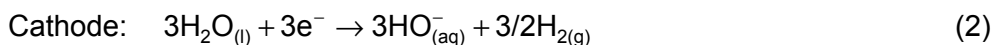
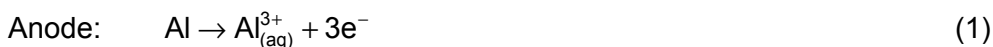
In the recent decades, the development of different types of industries, especially in Asian countries increased the amount of directly or indirectly discharged wastewaters into the environment [1, 2]. In many situations these wastewaters have high heavy metal concentrations, even exceeding the maximum allowable concentration, causing important environmental issues. The most of metals such as copper, nickel, lead, zinc and chromium tend to accumulate in living organisms leading to several health problems [3, 4]. Among the heavy metals, lead is one of the most dangerous since it is a neurotoxin that can accumulate in the soft tissues and bones through ingestion, causing serious brain disorders [5, 6]. There are different sources of lead pollution such as plating industries, depleted lead mines, dyes and refineries [7, 8]. Another major source of pollution is attributed to the uncontrolled degradation of electronic waste materials such as lead batteries or waste printed circuit boards [9, 10]. As a result, various techniques have been employed for the removal of heavy metals from industrial wastewaters among which the most important are: precipitation, adsorption, biosorption, ion-exchange, electrochemical and ion-exchange assisted membrane separation [11-14]. It is well known that an advanced removal of heavy metals can be achieved by means of electrochemical treatment, ion-exchange and reverse osmosis [15, 16]. The last two techniques are more expensive than electrochemical methods such as electrowinning, electro dialysis, and electrocoagulation (EC), which have been more frequently applied for heavy metal removal [17-19]. EC is a simple and efficient method where the flocculating agent is generated *in situ* by electro-oxidation of a sacrificial anode such as iron or aluminum [10, 20]. Moreover, EC offers an attractive and promising alternative considering its low environmental impact, high energy efficiency and the fact that it can be performed with minimal involvement of auxiliary materials. Thus, the treatment is done without adding any chemical coagulant or/and flocculants, preventing the generation of other wastewaters [21].

For the above reasons this study assesses the influence of current density and flow rate on the efficiency of lead removal *via* electrocoagulation. The most adequate operating conditions for the process were determined based on key technical performance indicators such as removal and cathodic current efficiency and specific energy consumption.

RESULTS AND DISCUSSION

Theoretical background

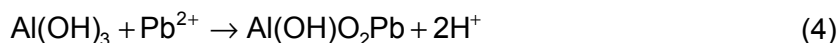
The removal of Pb^{2+} ions through electrocoagulation involves the following main electrochemical reactions:



At the cathode in parallel with hydrogen evolution the electrodeposition of lead can also take place as a secondary reaction:

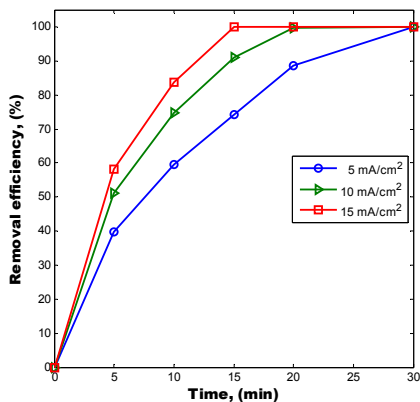


The HO^{-} formed at the cathode can react with Al^{3+} and Pb^{2+} ions, inducing their precipitation and co-precipitation as corresponding hydroxides. Freshly formed amorphous $\text{Al}(\text{OH})_{3(\text{s})}$ (sweep flocs) have large surface areas, which are beneficial for the adsorption and trapping of Pb^{2+} ions. According to the literature [10], the adsorption of Pb^{2+} ions on $\text{Al}(\text{OH})_3$ flakes can be described by the following reaction:

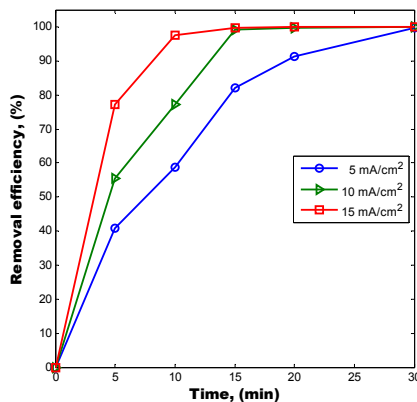


The influence of current density and flow rate on process performances

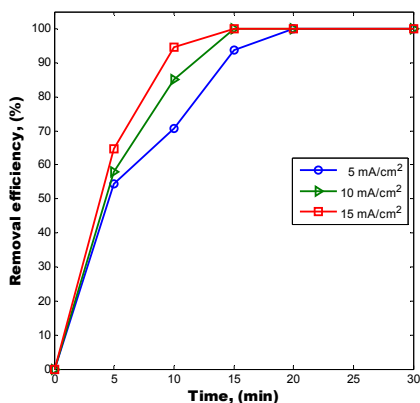
The removal efficiency of Pb^{2+} ions was evaluated under batch electrocoagulation using different current densities and flow rates. It was found that the increase of current density lead to more rapid removal of Pb^{2+} ions regardless the applied flow rate. Figure 1 shows that the removal efficiency values obtained at 5 and 15 mA/cm^2 differ most in the initial stage of the process, being with 40 % higher after the first 5 minutes for the current density of 15 mA/cm^2 .



a



b



c

Figure 1. Removal efficiency for various current densities at different flow rates: a - 20 mL/min; b - 40 mL/min; c - 60 mL/min.

It can be also observed that the difference in removal efficiency values between the highest and the lowest current densities decreases in time and with flow rate increase, reaching a minimum of 10 % after 20 minutes. This tendency can be accounted to the fact that current density determines the generation rate of metal hydroxides and the growth of flocs. Therefore the amount of produced coagulating agent increases as current density increases. However, the removal efficiency does not follow linearly the increase of current density considering that an increase of current density by three times did not increase the removal efficiency three times. This can be explained considering that the adsorption of Pb^{2+} ions is a much slower step than the generation of $Al(OH)_3$ flocs. As a result, the

removal efficiency values increase only moderately with the increase of current density, even if the amount of coagulant agent and available surface area for Pb^{2+} ion adsorption increases. It can be also observed that the removal efficiency reached 100 % in just 30 minutes for all the combinations of current density and flow rate values. On the other hand, the period of time in which a complete removal of Pb^{2+} ions was achieved decreased as the applied current density and flow rate increased.

Still, operating at high current densities has negative impact on the process considering the dependency of electrode potentials and cell voltage on the applied current density. As the data from Table 1 indicates, electrode potentials increase with the increase of current densities. This can be attributed to the increase of cathode over potential for hydrogen evolution and more advanced passivation of the aluminum anode. Similar tendency can be noticed in the case of the cell voltage which also increases with the increase of current density due to the higher ohmic drop. In contrast, the increase of flow rate has a positive effect on the electrochemical parameters of the process which can be accounted to the more intensive mass transport of electroactive species.

Table 1. Electrode potentials and cell voltage vs. electrolyte flow rate and current density

Flow rate, (mL/min)	U_b , (V)			U_{el} , (V)			U_{ce} , (V)		
	i , (mA/cm ²)			i , (mA/cm ²)			i , (mA/cm ²)		
	5	10	15	5	10	15	5	10	15
20	5.10	7.07	9.29	2.11	2.75	3.09	-1.88	-2.13	-3.81
40	4.97	7.09	9.16	2.03	2.67	2.76	-1.72	-2.14	-2.89
60	4.88	7.07	9.00	2.04	2.08	2.45	-1.63	-1.84	-2.23

According to eq. (3) the removal of Pb^{2+} ions from the solution also involved the electrodeposition of metallic lead. In order to quantify the importance of lead electrowinning compared to the removal of Pb^{2+} ions by electrocoagulation a new performance criteria was introduced. The extraction efficiency was defined as the ratio between the amount of electrodeposited Pb and the total amount of Pb removed from the solution. The results from Table 2 show that at the lowest flow rate and current density almost 5 % of Pb^{2+} ions were removed by electrowinning. Also as it was expected the extraction efficiency drops as flow rate and current density increases. The extraction

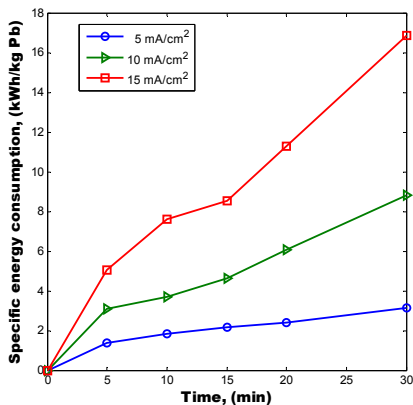
efficiency values are decreasing with 63 % by increasing the current density from 5 to 15 mA/cm² and with 17 % by increasing the flow rate from 20 to 60 mL/min. The more significant influence of current density can be accounted to enhancement of hydrogen evolution with the increase of current density while flow rate increase involves only the intensification of Pb²⁺ ions adsorption. This is also sustained by the cathodic current efficiency which follows the same tendency as the extraction efficiency. The low values of these two parameters it is also related to the fact that Pb²⁺ ions concentration is very low and decreasing during the process.

Table 2. Extraction and current efficiency vs. electrolyte flow rate and current density

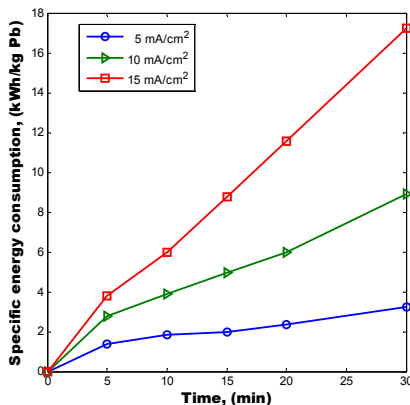
Flow rate, (mL/min)	Extraction efficiency, (%)			Current efficiency, (%)		
	<i>i</i> , (mA/cm ²)			<i>i</i> , (mA/cm ²)		
	5	10	15	5	10	15
20	4.62	2.80	1.67	1.89	0.58	0.23
40	4.39	2.38	1.49	1.80	0.49	0.21
60	3.82	1.93	1.42	1.56	0.40	0.20

In order to determine the combined effect of the previously discussed parameters the specific energy consumption for the removal of Pb²⁺ ions was also evaluated for all the experimental conditions. The specific energy consumption was defined as the amount of energy consumed for the removal of one kg of Pb²⁺ ions from the treated effluent. Figure 2 shows that the specific energy consumption increases in time regardless the applied flow rate or current density. This can be attributed to the fact that the amount of Pb²⁺ ions removed decrease in time, especially during the second part of the experiment. Moreover, as flow rate increases the difference between the specific energy consumption after 5 and 30 min of processing become even larger due to the faster removal of Pb²⁺ ions at higher flow rates.

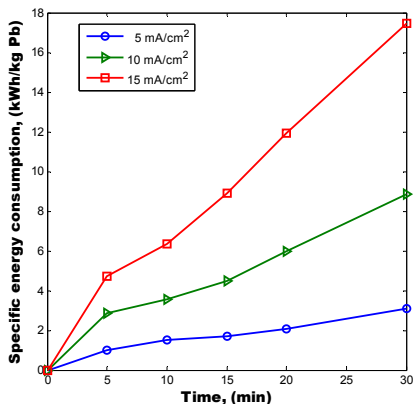
At constant current density, specific energy consumption increases by 200 % for the flow rate of 60 mL/min while for the other two flow rates it only doubles between the initial and final stages of the experiment. The results also revealed that specific energy consumption depends more on the applied current density than on the flow rate considering that it increased by 5 times between the lowest and highest current densities.



a



b



c

Figure 2. Specific energy consumption for various current densities at different flow rates: a – 20 mL/min; b – 40 mL/min; c – 60 mL/min.

CONCLUSIONS

The study proved that the complete removal of Pb^{2+} ions from aqueous solutions can be performed efficiently by EC using an electrolytic flow cell in batch operation. The results revealed that in parallel with the precipitation of Pb^{2+} ions the process also involved the electrodeposition of metallic lead which accounted to 1.5-4 % of the removed Pb^{2+} ions. It was found that process performance is more strongly dependent on current density than electrolyte flow rate or duration of the experiment.

As it was expected, the increase of current density increases the amount of flocs which makes the removal of lead ions to be done in a shorter time but with higher specific energy consumption. Nevertheless, the increase of flow rate even if reduces the requested time for the removal of Pb^{2+} ions with less extent than current density it decreases the specific energy consumption as well.

Considering the importance of the specific energy consumption it can be concluded that the complete removal of Pb^{2+} ions, in the applied experimental conditions, can be done the most efficiently at 60 mL/min and a current density of 5 mA/cm².

EXPERIMENTAL SECTION

EC experiments were performed using a plexiglas undivided electrochemical reactor equipped with parallel Al plate electrodes with a nominal surface area of 12.5 cm² (Figure 3). The inter-electrode gap between the electrodes was 20 mm. Cathode and anode potentials were measured using two Ag/AgCl/KCl_{sat} reference electrodes.

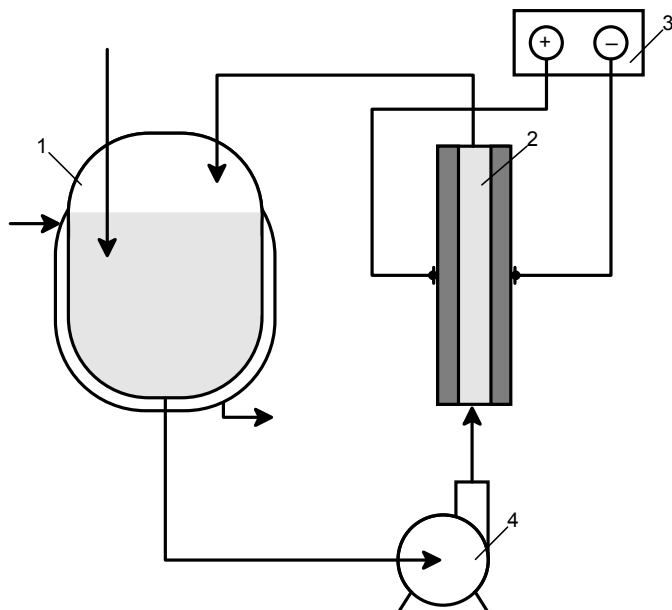


Figure 3. The experimental set-up for the EC process using sacrificial Al electrodes: 1 - thermoregulated reservoir; 2 - electrochemical cell; 3 - power supply; 4 - pump

Tests were performed under galvanostatic conditions, at different values of applied current densities ($i = 5, 10, 15 \text{ mA/cm}^2$), using a computer controlled DXC 236 potentiostat (Datronix Computer) equipped with a PCI 6024E (National Instruments, U.S.A.) data acquisition board. All experiments were performed at room temperature over a period of 30 minutes using 100 mL synthetic wastewater solutions containing 500 mg/L Pb^{2+} and 1 g/L NaNO_3 . The solutions were made by using analytical grade chemicals and double distilled water. The electrolyte containing 500 mg/L Pb^{2+} ions was recirculated through the electrochemical reactor at a flow rate of 20, 40 and 60 mL/min by using a Reglo-Digital-Ismatec peristaltic pump. During the EC process, the electrolyte was sampled at different time intervals in order to determine the evolution of Pb^{2+} ion concentration in time. At the end of each experiment the cathodic deposit was dissolved in concentrated HNO_3 solution. The Pb content of the samples and of the solution with the cathodic deposits was quantified by an atomic absorption spectrophotometer (Avanta PM - GBC).

REFERENCES

1. X. Wei, B. Gao, P. Wang, H. Zhou, J. Lu, *Ecotoxicology and Environmental Safety*, **2015**, 112, 4, 186.
2. H. Chen, Y. Teng, S. Lu, Y. Wang, J. Wang, *The Science of the Total Environment*, **2015**, 512-513, 143.
3. B.H. Robinson, *The Science of the Total Environment*, **2009**, 408, 2, 183.
4. V. Khandegar, A.K. Saroha, *Journal of Environmental Management*, **2013**, 128, 949.
5. M. Kazemipour, M. Ansari, S. Tajrobehkar, M. Majdzadeh, H.R. Kermani, *Journal of Hazardous Materials*, **2008**, 150, 2, 322.
6. E. Igberase, P. Osifo, *Journal of Industrial and Engineering Chemistry*, **2015**, 26, 340.
7. X. Wang, Q. Chen, Z. Yin, M. Wang, B. Xiao, F. Zhang, *Hydrometallurgy*, **2011**, 105, 3-4, 355.
8. B. Pospiech, *Hydrometallurgy*, **2015**, 154, 88.
9. H.J. Mansoorian, A.H. Mahvi, A.J. Jafari, *Separation and Purification Technology*, **2014**, 135, 165.
10. M.M.S.G. Eiband, K.C. de A. Trindade, K. Gama, J.V.D. Melo, C.A. Martínez-Huitle, S. Ferro, *Journal of Electroanalytical Chemistry*, **2014**, 717-718, 213.

11. F. Akbal, S. Camcı, *Desalination*, **2011**, 269, 1-3, 214.
12. M.S. Oncel, A. Muhcu, E. Demirbas, M. Kobya, *Journal of Environmental Chemical Engineering*, **2013**, 1, 4, 989.
13. O. Hanay, H. Hasar, *Journal of Hazardous Materials*, **2011**, 189, 1-2, 572.
14. A.L. Ghirisan, S.L. Dragan, A. Pop, M. Simihaian, V. Miclaus, *Can. J. Chem. Eng.*, **2007**, 85, 6, 900.
15. M.M. Emamjomeh, M. Sivakumar, *Journal of Environmental Management*, **2009**, 90, 5, 1663.
16. I. Petrinic, J. Korenak, D. Povodnik, C. Hélix-Nielsen, *Journal of Cleaner Production*, **2015**, 101, 292.
17. I. Kabdasli, T. Arslan, T. Olmez-Hanci, I. Arslan-Alaton, O. Tunay, *Journal of Hazardous Materials*, **2009**, 165, 1-3, 838.
18. S. Caprarescu, M.C. Corobea, V. Purcar, C.I. Spataru, R. Ianchis, G. Vasilievici, Z. Vuluga, *Journal of Environmental Sciences*, **2015**, 35, 27.
19. F. Imre-Lucaci, S.-A. Dorneanu, P. Ilea, *Studia Universitatis Babeș-Bolyai Chemia*, **2009**, 54, 105.
20. B. Khaled, B. Wided, H. Béchir, E. Elimame, L. Mouna, T. Zied, *Arabian Journal of Chemistry*, **2015**, doi:10.1016/j.arabjc.2014.12.012.
21. A. de Mello Ferreira, M. Marchesiello, P.X. Thivel, *Separation and Purification Technology*, **2013**, 107, 109.

*Dedicated to Professor Luminița Silaghi-Dumitrescu
on the occasion of her 65th anniversary*

HYDROGEN PEROXIDE ELECTROSYNTHESIS AND DETECTION IN SULPHATE MEDIA

**ANA-DOMNICA MĂRINCEAN^a, SORIN-AUREL DORNEANU^{a,*},
PETRU ILEA^a**

ABSTRACT. The increase of the graphite electrocatalytic activity toward hydrogen peroxide (HP) electrosynthesis (HPE) by the partial electroreduction of O₂ can be achieved by *in-situ* electroactivation (EA). Our previous studies completed in strong alkaline media (1 M NaOH) by galvanostatic multi-sequence EA techniques (MSETs) revealed that an adequate graphite EA can improve HPE current efficiency (CE) up to 35 % compared to the unmodified graphite. In order to implement the optimised operational parameters to a micro-pilot scale electrochemical reactor, in a first step, several systems for the on-line HP concentration monitoring were designed and tested. Unfortunately, the preliminary test, even in moderate alkaline media (0.1 M NaOH) revealed that, at concentrations greater than 50 ppm, the HP decomposes intensively in contact with the setup components, disallowing the HP accumulation. As a consequence, for all further experiments, the alkaline supporting electrolyte was replaced with 0.1 M Na₂SO₄. In these new conditions, two models of HP on-line detectors (spectrophotometrical and amperometrical) were designed and tested, presenting adequate limit of detection (L.O.D. = 10 ppm and L.O.D. = 0.23 ppm, respectively). Also, the HPE process was studied in sulphate media, using a Pt/graphite wall-jet ring disk electrode system, revealed that the CE can reach a 46 % value for the unmodified electrode and increases up to 52 % when the auto-adaptive galvanostatic MSETs protocol is used.

Keywords: *hydrogen peroxide electrosynthesis, graphite electroactivation, hydrogen peroxide on-line monitoring, wall-jet ring disk electrode, auto-adaptive techniques*

^a Babes-Bolyai University, Faculty of Chemistry and Chemical Engineering, 11 Arany Janos str., RO-400028, Cluj-Napoca, Romania

* Corresponding author: dorneanu@chem.ubbcluj.ro

INTRODUCTION

Hydrogen peroxide (HP) is widely used in many industrial areas, like chemical industry and environmental protection, but represents also a potential energy carrier. During the last decades, in order to counteract the main drawbacks of the consecrated anthraquinone based process for the HP production [1], significant efforts have been dedicated to develop efficient and *on-sitelin-situ* HP production technologies, which can reduce considerably the cost for synthesis, separation, transport, storage and handling [2]. The methods based on the direct HP synthesis from H_2 and O_2 in plasma assisted [3] or catalytic [4] reactors allow the decentralized production of HP in continuous mode but still present the potential risk of H_2/O_2 gas mixture explosion. The HP electrosynthesis (HPE) by the partial electroreduction of O_2 represents another extremely studied alternative. In spite of the fact that, in special conditions, the concentration of the accumulated HP can reach values up to 3.6 M (~ 122 g/L) [5], in almost all other studies, final concentrations between 3 ppm [6] and 700 ppm [7] were reported. Even at low HP accumulated concentrations, below 50 ppm, the interest for the HPE remains high due to the fact that, at this reduced level, HP allows the direct degradation of certain pollutants [8] and the generation of the electro-Fenton reagent, a more powerful and versatile depolluting agent [9 - 13]. Irrespective to the design of the electrochemical reactor used for the HPE process (*i.e.* divided or undivided batch reactors, filter-press, flow-through or wall-jet micro-reactors [14]), in almost all studies, the modified or unmodified carbonaceous materials, in 2D or 3D shapes, were used as cathode. Among them, the compact graphite electrodes present major advantages (*i.e.* inexpensive and facile production, high selectivity and conductivity), recommending them for the design of reliable small scale plants for *on-site* and/or *in-situ* HPE. Unfortunately, the low specific surface of the compact graphite requires consistent studies dedicated to the increase of its electrocatalytic activity toward HPE by chemical, physical or electrochemical activation (EA).

In this context, the results of our previous studies [14] accomplished in strong alkaline media (1 M NaOH) by auto-adaptive galvanostatic multi-sequence electroactivation techniques (MSETs) revealed that the adequate graphite EA can improve HPE current efficiency (CE) up to 35 % compared to the unmodified compact graphite. In consequence, we decided to implement the optimal operational parameters at a micro-pilot scale electrochemical reactor with recirculation and HP accumulation capability. In order to accomplish this goal and better understand the influence of the new experimental parameters on the HPE process, we found out that is mandatory to design and validate an accurate and reliable flow-through detector able to monitor, *on-line* and *in-situ*, the concentration of accumulated HP.

Unfortunately, the preliminary test, accomplished in a moderate alkaline media (0.1 M NaOH) revealed that, at HP concentration over 50 ppm, it decomposes intensively in contact with the setup components (PTFE and PVC tubes and cells), disallowing the HP accumulation. As a consequence, for all further experiments, the alkaline supporting electrolyte was replaced with a weakly acidic one consisting in 0.1 M Na₂SO₄ (pH ~ 4.2). In these new conditions, two models of HP *on-line* detectors (a spectrophotometrical and an amperometrical one) were designed and tested, presenting adequate sensitivity and limit of detection. Also, the HPE process was studied in sulphate media, using a Pt/spectral graphite (Pt/SG) wall-jet ring disk electrode (WJRDE) system, revealing that the CE can be improved using an auto-adaptive galvanostatic MSETs protocol. Additional tests indicate that a symmetrical divided reactor with periodic inversion of the electrodes cannot be used for sulphate media.

RESULTS AND DISCUSSION

Design and validation of the flow-through HP detectors

Our previous results revealed that, even in optimal conditions, the increase of the electrosynthesized HP concentration during each passage of the electrolyte through the electrochemical reactor can reach a maximum value of 0.07 ppm ($\sim 2 \times 10^{-6}$ M). In these conditions, in order to evaluate rigorously the influence of the EA parameters on the HPE efficiency and also the kinetic of the accumulation process, a very sensitive method of HP detection must be used. Many consecrated techniques (*i.e.* the Iodometric-molybdate, Titanium oxalate, Peroxidase enzyme-DPD or Copper-DMP method) [15] accomplish these requirements but are inadequate for flow analysis, especially if the accumulation process is envisaged due to the requirement of permanent addition of specific reagents. In order to overcome this problem, we decided to evaluate the possibility to estimate the HP concentration by spectrophotometry without addition of specific reagents, exploiting the ability of HP to present an intense absorption in the UV range. The preliminary tests were accomplished, at a wavelength (λ) of 225 nm, in a flow-through spectrometric cell with an optical path length of 10 mm, at a flow rate (V_f) of 10 mL/min, using dilute standard solution of HP (10, 20, 50, 100, 250 and 500 ppm) prepared in bi-distilled water. As indicated in Figure 1 and Table 1, if a second order polynomial fitting function ($Y = A + B1 \cdot X + B2 \cdot X^2$) is used, this method presents acceptable analytical parameters in the studied concentrations range ($R = 0.9999$ and L.O.D. = 6.5 ppm for a signal to noise ratio (S:N) of 3:1), but the accuracy is poor at concentrations less than 20 ppm.

In the next step, we tried to repeat the same set of measurements in the presence of 0.1 M NaOH in the standard solutions. Unfortunately, during the measurements, we observed, for the standard solutions having concentrations equal to or higher than 50 ppm, an intense HP decomposition, indicated by the gaseous oxygen evolution. This phenomenon, that appeared at the contact between the concentrated standard solutions and the setup elements (PVC and PTFE tubes, spectrophotometric cell), indicates that the available components and materials included in the structure of the designed micro-pilot scale electrochemical reactor are not compatible with the alkaline HP solutions, making, practically, impossible the accumulation of the electrosynthesized HP. In these conditions and based on literature data [9-13], we decided to replace, for all the further experiments, the alkaline supporting electrolyte with a weakly acidic one, consisting in a 0.1 M Na₂SO₄ solutions, having a intrinsic pH of around 4.2.

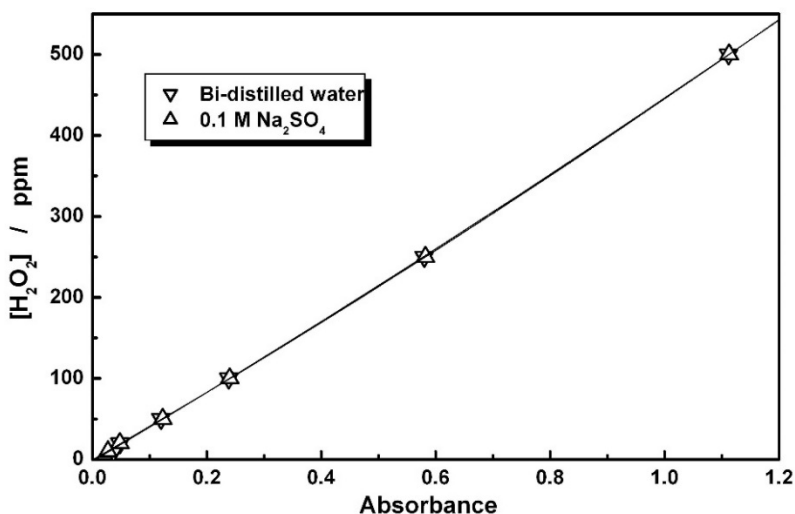


Figure 1. Spectrophotometric calibration curves for HP recorded in flow conditions in bi-distilled water and 0.1 M Na₂SO₄. ($\lambda = 225$ nm, $V_f = 10$ mL/min.)

Table 1. Analytical parameters evaluated for the UV spectrophotometric detection of HP in flow conditions in bi-distilled water and 0.1 M Na₂SO₄.

Solution	A	B1	B2	R	L.O.D.
Bi-distilled water	-2.3±1.7	420±11	28±9	0.99995	6.5 ppm
0.1 M Na ₂ SO ₄	-0.5±0.4	410±3	36±2	0.99999	10 ppm

At this point, in order to verify that the new supporting electrolyte does not interact with the HP in the investigated concentrations range, the previous measurements were repeated in the presence of 0.1 M Na₂SO₄. As it can be seen from Figure 1 and Table 1, the new calibration curve is quasi-identical with that recorded in bi-distilled water and the analytical parameters preserved very similar values, excepting the L.O.D. that degraded slightly. In these conditions, we conclude that the designed HP detection method can be used successfully during the accumulation experiments, but only at concentration greater than 10 ppm. Moreover, the detector is, practically, insensitive to the electrolyte flow rate, but presents failures risk if gaseous bubbles remain entrapped inside of the optical path.

As pointed before, in order to quantify rigorously the increase of the electrosynthesized HP concentration after each passage of the electrolyte through the electrochemical reactor, a more sensitive detector must be used. In order to fulfil this requirement, an original dedicated 3-electrodes flow-through amperometric detector (described in the EXPERIMENTAL SECTION) was designed and tested. Using this new detector, 5 calibration curves were recorded at flow rates of 2, 5, 10, 15 and 20 mL/min., in an extended range of standard HP solutions (5, 10, 20, 50, 75, 100, 250 and 500 ppm) prepared in 0.1 M Na₂SO₄. As indicated in Figure 2 and Table 2, if a similar second order polynomial fitting function is used, this new method presents excellent analytical parameters in the studied concentrations and flow rates ranges: R between 0.99996 and 0.99999 and L.O.D. between 0.15 and 0.23 ppm for a S:N of 3:1.

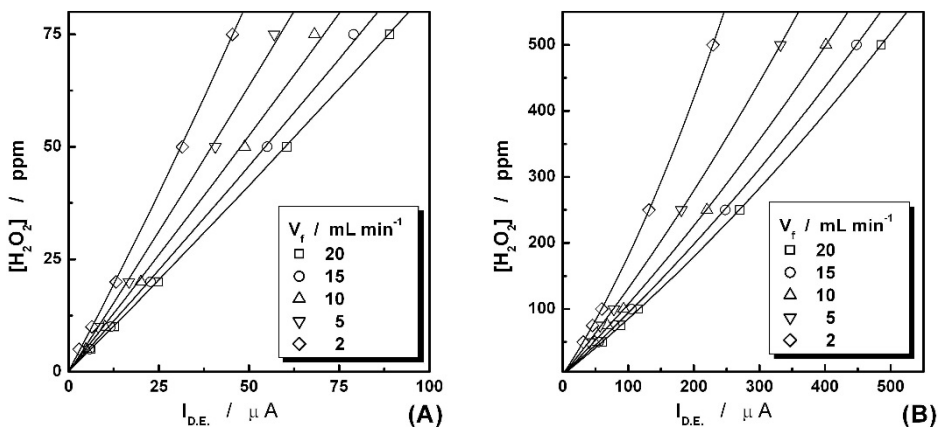


Figure 2. Amperometric calibration curves for HP recorded in 0.1 M Na₂SO₄ at different flow rates in the domain of reduced (A) and increased (B) concentrations ($E_{D.E.} = 0.7$ V vs. Ag/AgCl/KCl_{SAT})

Table 2. Analytical parameters evaluated for the amperometric detection of HP in flow conditions in 0.1 M Na₂SO₄.

V _f [mL/min.]	A	B1	B2*10 ⁴	R	L.O.D. [ppm]
2	0.003±0.3	1.512±0.010	29±0.44	0.99999	0.23
5	-0.22±0.8	1.233±0.016	8.2±0.50	0.99997	0.18
10	0.17±0.9	1.016±0.017	5.7±0.42	0.99996	0.15
15	0.07±0.7	0.887±0.011	5.1±0.24	0.99998	0.14
20	0.005±0.5	0.803±0.007	4.6±0.13	0.99999	0.15

Based on the obtained result, we conclude that the designed HP amperometric detector can be used successfully during the HPE experiments, with or without accumulation. Obviously, the detector response depends on the flow rate, but the HP concentration can be easily calculated based on the corresponding calibration curve. Also, the vertical position of the detecting electrode reduces the failures risk due to the gaseous bubbles fixation on the electrode surface.

HPE tests using 0.1 M Na₂SO₄ as supporting electrolyte

Prior to the HPE experiments, the collecting efficiency (N) of the WJRDE system was evaluated by hydrodynamic voltammetry with linear scan of the potential (HVLSP), at flow rates of 1, 2.5, 5 and 10 mL/min, using the fero/feri redox system. Based on the calculated N values, the CE values for the HPE process in sulphate media were evaluated by HVLSP at the same flow rates, the obtained results being presented in Figure 3.

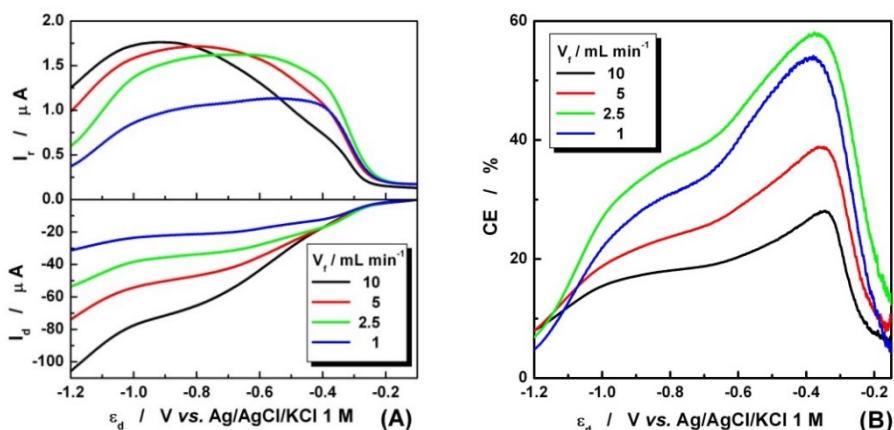


Figure 3. Voltamograms recorded by HVLSP on the Pt/SG WJRDE at different V_f in 0.1 M Na₂SO₄ air saturated solution (A) and the corresponding CE evolution (B). (v = 5 mV/s, ε_r = 0.7 V vs. Ag/AgCl/KCl 1 M)

As it can be seen from Figure 3, a maximal CE value of $\sim 58\%$ can be obtained at a flow rate of 2.5 mL/min. and a disc potential (ϵ_d) of -0.38 V , corresponding to a disc current (I_d) of $-16\ \mu\text{A}$. Supplementary, these evolutions of the ring currents (I_r) and the CE values suggest that, in sulphate media, the adsorption of the dissolved O_2 on the electrode surface and desorption of the HPE products is considerable slower than in alkaline media, requiring additional studies able to elucidate the corresponding mechanism.

Based on the promising results obtained by HVLSP, we decided to test if the EA protocols optimised in alkaline media can be applied in sulphate media. After several preliminary measurements (results not shown), we found that the best results can be obtained following the auto-adaptive galvanostatic MSETs protocol, the corresponding results and the optimised parameters being presented in Figure 4, where the invoked terms are explained in our previous work [14].

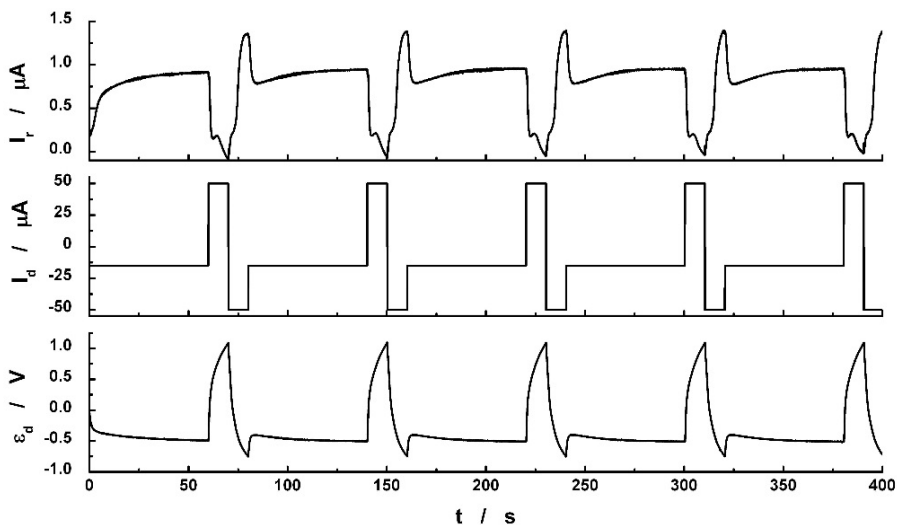


Figure 4. The evolution of I_r , I_d and ϵ_d during 5 cycles of galvanostatic auto-adaptive EA and HPE in 0.1 M Na_2SO_4 solution. ($V_f = 2.5\text{ mL/min.}$; $\epsilon_{AS, \text{MAX}} = +1.2\text{ V}$; $\epsilon_{PRS, \text{MIN}} = -0.8\text{ V}$; $T_{PS} = 60\text{ s}$; $I_{AS, +} = +50\ \mu\text{A}$; $I_{PRS, -} = -50\ \mu\text{A}$; $I_{PS, -} = -15\ \mu\text{A}$)

Based on the recorded data included in Figure 4, we found that, during the first cycle (corresponding to the inactivated graphite), the CE reached a global value of 46 % and increase to 52 % after 5 cycles of EA. These values are clearly superior to those of 28 % reported for a HPE continuous test accomplished using an unmodified graphite electrode, in very similar condition (0.05 M Na_2SO_4 as supporting electrolyte, $\text{pH} = 3$, $j = 0.25\text{ mA cm}^{-2}$) [16].

Finally, in order to check the possibility to use the sulphate media for HPE in a symmetrical divided reactor with periodic inversion of the electrodes, we made complementary measurements using rectangular asymmetrical or symmetrical current profiles. The comparison between the signals recorded in these conditions, presented in Figure 5, reveals that, if the symmetric profile current is imposed through the disc electrode, the recorded ring current decrease continuously, from cycle to cycle, indicating an advanced deactivation of the graphite electrode surface. In these conditions, we conclude that the idea of a symmetrical divided reactor with periodic inversion of the electrodes is not applicable when the sulphate media is used.

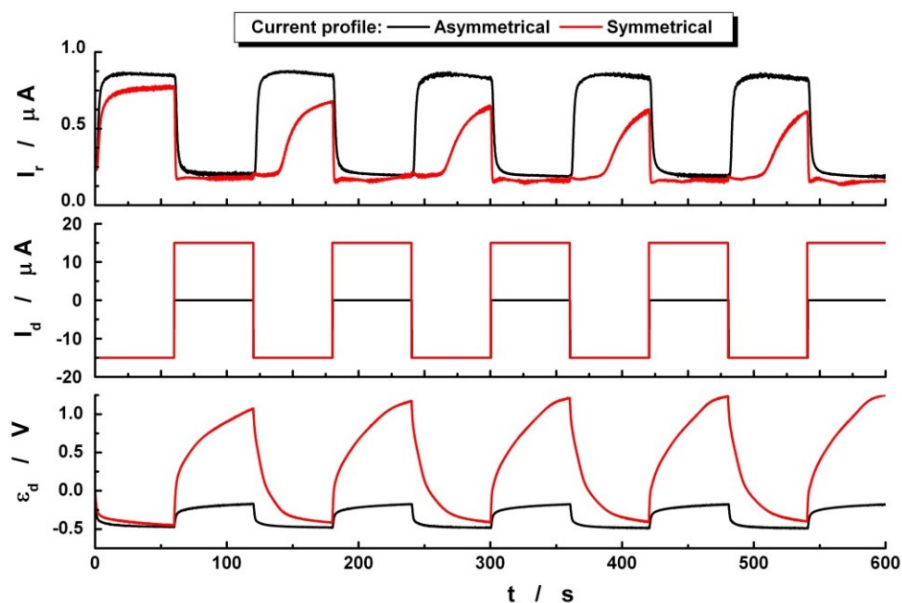


Figure 5. Comparison between the evolutions of I_r , I_d and ε_d recorded in 0.1 M Na_2SO_4 solution for asymmetrical and symmetrical current profiles. ($V_f = 2.5 \text{ mL/min.}$, $\varepsilon_r = 0.7 \text{ V vs. Ag/AgCl/KCl } 1 \text{ M}$)

CONCLUSIONS

Obviously, HPE represents an attractive and eco-friendly alternative for *on-place* and/or *in-situ* production of HP and, consequently, extremely numerous researches are dedicated to this process. All these studies reveal that the evaluation of the HP concentration is a mandatory and

essential task, accomplished mainly by periodic sampling and *ex-situ* analysis of the extracted samples using consecrated analytical techniques. In order to eliminate these complicated and time-consuming procedures, we decided to design and validate an accurate and reliable flow-through detector able to monitor *on-line* the concentration of electrosynthesized and accumulated HP. In a first attempt, exploiting the ability of HP to present an intense absorption in the UV range, we proposed a spectrophotometrical flow-through HP detector that works without addition of specific reagents. The preliminary tests, accomplished at a wavelength of 225 nm and using HP standard solutions prepared in bi-distilled water, revealed that, implementing a second order polynomial fitting function, the original designed method presents, for concentrations between 10 and 500 ppm, acceptable analytical parameters ($R = 0.9995$ and L.O.D. = 6.5 ppm at S:N = 3:1), but the accuracy is unsatisfactory at concentrations less than 20 ppm. The subsequent test, accomplished in a moderate alkaline media (0.1 M NaOH) revealed that, for HP concentrations over 50 ppm, it decomposes intensively in contact with the setup components (PTFE and PVC tubes and cells), compromising the HP accumulation tests. As a consequence, for all further experiments, we decided to replace the alkaline supporting electrolyte with a weakly acidic one consisting in 0.1 M Na_2SO_4 with an intrinsic pH of ~ 4.2 . In these new conditions, the proposed original detection method presents very similar analytical parameters ($R = 0.9999$ and L.O.D. = 10 ppm at S:N = 3:1).

In order to improve the L.O.D. value, another original amperometric flow-through HP detector was designed and tested. In the studied concentrations and flow rates ranges, the new detection method presents excellent analytical parameters: R between 0.99996 and 0.99999 and L.O.D. between 0.15 and 0.23 ppm evaluated for a S:N of 3:1.

Finally, using the Pt/SG WJRDE system, the HPE process was studied in sulphate media, using different protocols. The experiments revealed that, for the unmodified electrode, the CE of HPE can reach a value of 46 %, but increases up to 52 % when the auto-adaptive galvanostatic MSETs protocol is used. Unfortunately, additional measurements lead to the conclusion that the idea of a symmetrical divided reactor with periodic inversion of the electrodes cannot be applied when the sulphate media is used as supporting electrolyte.

For future developments, in order to validate the very promising obtained results, the best experimental parameters will be implemented and tested at a micro-pilot scale electrochemical reactor.

EXPERIMENTAL SECTION

For the spectrophotometric studies, a modular spectrometer (model UV-VIS USB4000), a miniature UV-VIS-NIR light source (model DT-MINI-2-GS), 2 UV optical fibres (model QP600-025-SR) and a flow spectrometric cell (model FIA-Z-SMA-ML-PE), all from Ocean Optics (SUA), were used.

The amperometric detector consists in a cylindrical PTFE flow channel of 3 mm inner diameter in which is fixed a coil (10 turns, 2.5 mm external diameter) of 0.1 mm diameter Pt wire as counter-electrode and, perpendicular to the flow direction, another Pt wire (0.8 mm diameter and 0.5 mm length) as detecting electrode (D.E.). Supplementary, in the superior wall of the channel is fixed a VYCOR® pill that inter-connects the flow channel with an external chamber for the reference electrode, of Ag/AgCl/KCl_{SAT} type.

All the electrochemical measurements, including the calibration of the amperometric HP detector, were carried out in controlled hydrodynamic conditions, using the experimental setup described in detail in our previous work [14, 17]. In the wall-jet cell (WJC), the injector to disc electrode distance was fixed at 1 mm in order to achieve a planar laminar flow. For the HPE experiments, an air saturated ([O₂] ~ 8 ppm) 0.1 M Na₂SO₄ aqueous solution was pumped in the WJC at V_F of 1, 2.5, 5 or 10 mL/min. Before each set of HPE experiments, the RDE surface was polished on waterproof emery paper of 1200 grit (Struers, Denmark) and intensively washed with doubly distilled water. All measurements were performed at room temperature (25 ± 1 °C).

REFERENCES

1. J.M. Campos-Martin, G. Blanco-Brieva, J.L.G. Fierro, *Angewandte Chemie - International Edition*, **2006**, *45*, 6962.
2. Y. Liu, X. Quan, X. Fan, H. Wang, S. Chen, *Angewandte Chemie - International Edition*, **2015**, *54*(22), 6837.
3. Y. Yi, J. Zhou, H. Guo, J. Zhao, J. Su, L. Wang, X. Wang, W. Gong, *Angewandte Chemie - International Edition*, **2013**, *52*, 8446.
4. R. Dittmeyer, J. -D. Grunwaldt, A. Pashkova, *Catalysis Today*, **2015**, *248*, 149.
5. G.A. Kolyagin, V.L. Kornienko, *Russian Journal of Electrochemistry*, **2014**, *50*(8), 798.
6. S. Cotillas, J. Llanos, M.A. Rodrigo, P. Canizares, *Applied Catalysis B: Environmental*, **2015**, *162*, 252.
7. C. Zhang, M. Zhou, G. Ren, X. Yu, L. Ma, J. Yang, F. Yu, *Water Research*, **2015**, *70*, 414.

8. R. Darvishi Cheshmeh Soltani, A. Rezaee, A. R. Khataee, H. Godini, *Research on Chemical Intermediates*, **2013**, 39, 4277.
9. X. Yu, M. Zhou, G. Ren, L. Ma, *Chemical Engineering Journal*, **2015**, 263, 92.
10. S. Qiu, D. He, J. Ma, T. Liu, T. D. Waite, *Electrochimica Acta*, **2015**, 176, 51.
11. O. Scialdone, A. Galia, C. Gattuso, Sabatino, B. Schiavo, *Electrochimica Acta*, **2015**, 182, 775.
12. Y. Zhang, M-M. Gao, X-H. Wang, S-G. Wang, R-T. Liu, *Electrochimica Acta*, **2015**, 182, 73.
13. G. Xia, Y. Lu, H. Xu, *Electrochimica Acta*, **2015**, 158, 390.
14. C. Vlaic, S. A. Dorneanu, *Studia UBB Chimia*, **2015**, LX(3), 141.
15. P.J. Brandhuber, G. Korshin, "Methods for the Detection of Residual Concentrations of Hydrogen Peroxide in Advanced Oxidation Processes", WateReuse Foundation, Alexandria, VA, **2009**, chapter 2.
16. E. Peralta, R. Natividad, G. Roa, R. Marin, R. Romero, T. Pavon, *Sustainable Environment Research*, **2013**, 23(4), 259.
17. C. Vlaic, S.A. Dorneanu, P. Ilea, *Studia UBB Chimia*, **2011**, LIV(2), 167.

*Dedicated to Professor Luminița Silaghi-Dumitrescu
on the occasion of her 65th anniversary*

THE USE OF CHEMICALLY ACTIVATED FIR CONE CARBON IN THE REMOVAL OF Pb²⁺ CONTAMINATED AQUEOUS SOLUTIONS

CARMEN MÂNZATU^a, CORNELIA MAJDIK^a and BOLDIZSÁR NAGY^{a,*}

ABSTRACT. Fir cone biomass was used as a precursor for the preparation of activated carbon by sulfuric acid treatment and activation. It is known that the activated carbon from different biomass sources has a wide range of applications in water treatment. Therefore, fir cone activated carbon (FCAC) was prepared from raw fir cone by chemical treatment and used in various experiments to test its functions for the removal of Pb²⁺. The influences of different parameters like contact time, initial lead concentration, initial pH, biomass quantity and temperature were studied. Adsorption isotherm and kinetic models were used to analyze the equilibrium data. It was found that the Freundlich isotherm model and pseudo-second-order model describe better the Pb²⁺ biosorption process. The changes in morphological structure after lead ions-biomass interactions were evaluated by SEM analysis. From these studies, it can be concluded that the fir cone activated carbon could be a promising and effectively employed bioadsorbent for the removal of Pb²⁺ ions from aqueous solutions.

Keywords: *Fir cone activated carbon, Lead, Biosorption, Isotherms*

INTRODUCTION

Nowadays, the heavy metal pollution has become one of the most serious environmental problems. Unlike organic pollutants, heavy metals are non-biodegradable and so their removal is extremely important regarding the

^a Babeş-Bolyai University, Faculty of Chemistry and Chemical Engineering, Department of Chemistry, 11 Arany János st., 400028 Cluj Napoca, Romania

* Corresponding author: bnagy@chem.ubbcluj.ro

health of living specimens [1]. The heavy metal ions are stable and persistent environmental contaminants, since they cannot be degraded and destroyed. These metal ions represent a threat for human health as well for the aquatic ecosystem [2].

Among all the existing metals, Pb^{2+} may be found in wastewaters from many industries involving metal plating, painting, mining operations, battery manufacture and mining operations [3, 4]. Industrialists and environmentalists usually have the challenge of developing safe and effective disposal methods for these wastewaters containing heavy metals [5]. The long term Pb^{2+} exposure may cause several diseases such as: mental disturbance, retardation, semi-permanent brain damage, liver damage and can accumulate in animal tissues such as kidneys [6, 7, 8, 9, 10]. The World Health Organization (WHO) recommends that the amount of Pb^{2+} should be 0.01 mg/L for safe drinking water while the permissible level of Pb^{2+} in wastewater given by the Environmental Protection Agency (EPA) is 0.05 mg/L [11, 12].

Many physico-chemical methods such as extraction, ion exchange, chemical precipitation, membrane filtration, adsorption, and electro dialysis have been developed for the removal of heavy metals from aqueous solutions, but most of these methods have significant disadvantages (high operational costs and high specific consumption of reagent and energy) [13, 14].

Among the methods noted above, biosorption is preferred as a well-organized technique for the removal of heavy metals from aqueous wastes [15, 16]. This biosorption technique has advantages over other conventional methods due to its unique properties, such as simple design, the use of non-toxic and low cost materials, and the high efficiency in removing pollutants at low level concentrations, fast operation and favorable performance [17].

The biosorption with activated carbon is widely used to remove contaminants in water treatment processes because of its huge specific surface area, heterogeneous surface and well-developed pore structures [18, 19]. One of the major advantages of using activated carbon is that many water treatment and remediation facilities already have granular activated carbon (GAC) filtration systems in place [20].

The removal of heavy metals from aqueous waters using different biomasses [21] such as waste tea leaves [13], orange peel [14], hazelnut shell sago [22], sawdust [23], waste banana, orange peels [24], cocoa shells [25], coffee residue [26], rice husk [27], olive stone waste [28], grape stalk [29] as well as modified papaya seed [30] were also reported to have good biosorption abilities for Pb^{2+} but the potential of other waste agricultural by-products after chemical modification is yet to be entirely explored [31].

Wood products, especially products of fir wood have been treated using different kinds of chemical solutions to improve their surface properties, mechanical strength, chemical resistance and the ability to incorporate organic and inorganic compounds. Many of the recent studies show that these methods

have been applied for wood materials used as bioadsorbents for the removal of heavy metals [32]. Frequently, activated carbon surfaces are modified by oxidation, acidic treatment, ammonization or heating to enhance the biomass adsorption capacity [33, 34].

The main objective of the present work is to investigate the potential biosorption of the FCAC prepared by sulfuric acid treatment and activation from the fir cone biomass. The influence of contact time, initial Pb²⁺ concentration, initial pH, biomass quantity and temperature were investigated in detail. SEM microscopy studies were also used for the extensive characterization of the biomass surface morphology. This study also evaluates the use of the FCAC as a new, low cost and effective bioadsorbent material for the removal of Pb²⁺ from aqueous solutions.

RESULTS AND DISCUSSION

Biosorption experiments

SEM analysis

The SEM micrographs of FCAC carbon samples, before and after the Pb²⁺ biosorption, are given in Fig. 1. SEM enables a direct observation of any surface microstructure changes in the samples that would have occurred due to the biosorption of Pb²⁺. Some slight differences at the micrographs are noticeable. The number and shape of cracks and attached fine particles over the carbon surface clearly differ before (Fig. 1a) and after biosorption (Fig. 1b). A minor decrease in the size of the particles after biosorption is visible.

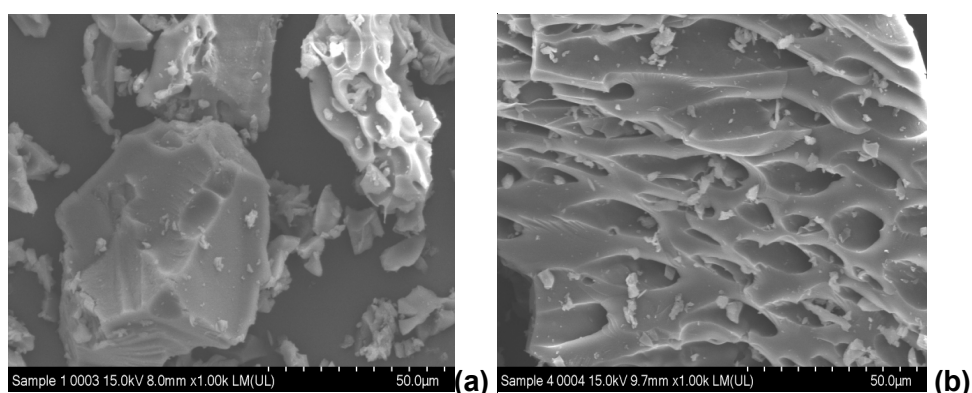


Figure 1. Scanning electron microscope (SEM) images of the (a) unloaded FCAC and (b) FCAC loaded with Pb²⁺.

The effects of contact time and initial Pb^{2+} concentration

The effects of contact time and initial concentration on biosorption of Pb^{2+} by FCAC are presented in (Fig. 2). The amount of Pb^{2+} adsorbed increased with the increase in contact time and reached equilibrium in about 240 min. The equilibrium time is independent of initial Pb^{2+} concentration, but in the first 20 min, the initial rate of biosorption was greater for higher initial Pb^{2+} concentration. After that, it gradually decreases until equilibrium is reached. The rate of percent metal removal is higher at the beginning due to the large number of biosorption sites available and high surface area of the FCAC, while towards the end of the experiment fewer sites are available for biosorption. Therefore an equilibrium time of 240 min was assumed for all further experiments.

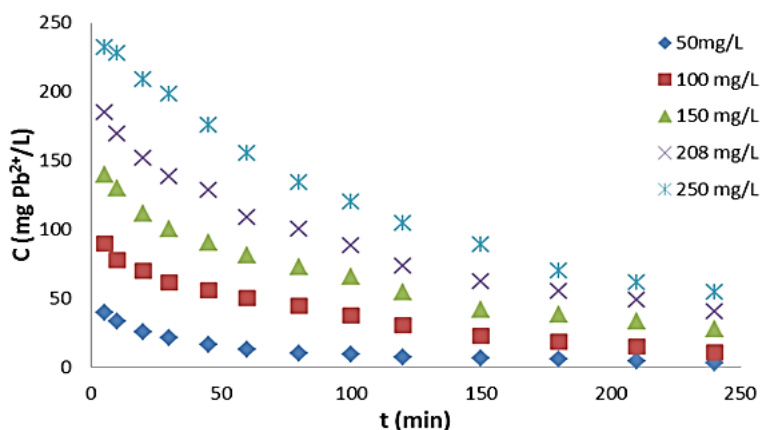


Figure 2. The effect of contact time and initial concentration on the biosorption of Pb^{2+} on FCAC; pH = 5.0, $d = 150 - 300 \mu\text{m}$, 296 K, 0.5 g biomass, 200 rpm.

The effect of initial Pb^{2+} concentration on the adsorption capacity was analyzed within the range of 50-250 mg/L. Fig. 3 shows that the adsorption capacity increases with an increase of lead concentration. The increase in adsorption capacity occurs due to the higher biosorption rate and the utilization of all the available active sites for biosorption at higher heavy metal concentration. Moreover, higher initial concentration provides increased driving force to overcome all mass transfer resistance of lead ions between aqueous and solid phase. It was noted that initial concentration increased the sorption of Pb^{2+} as is generally expected due to the equilibrium process. A further increase in the initial metal ion concentration does not lead to any other modifications in the adsorption capacity.

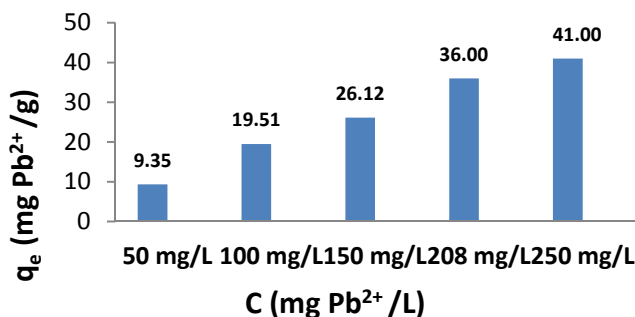


Figure 3. Influence of the initial Pb^{2+} concentration over the adsorption capacity of FCAC; 0.5 g biomass, $d = 150 - 300 \mu m$, 296 K, pH 5.0, 200 rpm.

The effects of biomass quantity

The amount of the FCAC added to the metal solutions varied between 0.1 and 0.5 g, while the total volume, initial concentration of the metal solution, temperature and the pH value were kept constant. The result of variation of biosorption removal with quantity of FCAC is shown in (Fig. 4). The amount of Pb^{2+} biosorption increased with an increase in bioadsorbent quantity. This result can be explained by the fact that for optimum biosorption, extra sites must be available for biosorption reaction, whereas by increasing the biomass of the already available sites for biosorption, the site increased. However, a further increase of the bioadsorbent quantity did not lead to better results in the removal efficiency values at these experimental conditions; therefore, the optimum biomass was taken as 0.5 g for further batch experiments.

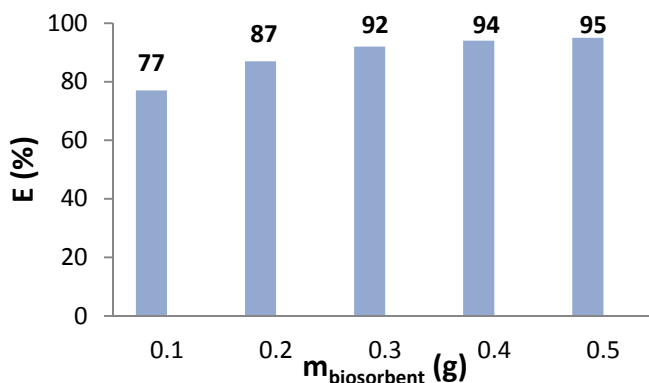


Figure 4. The effect of the FCAC quantity on Pb^{2+} biosorption over the removal efficiency; $C_i = 50 \text{ mg } Pb^{2+}/L$, 296 K, $d = 150 - 300 \mu m$, 5.0 pH, 296 K and 200 rpm.

The effect of initial pH of solution

The effect of initial pH of solution is an important factors in biosorption studies, which controls the biosorption process, particularly, the adsorption capacity and removal efficiency [35]. The effect of the pH on the amount of lead removed from the solution was assessed by performing experiments in acid/base pH scale and the results are shown in Fig. 5. The results point out that lead removal was 90.73% at initial pH of 2.0, which increased to 94.56% at initial pH 5.0. An appreciable decrease in percentage removal of Pb^{2+} was observed after pH 5.0. At lower pH values, the removal of Pb^{2+} was inhibited as a result of competition between hydrogen and metal ions on the sorption sites. Thus, the electrostatic repulsive forces between positively charged H_3O^+ and Pb^{2+} ions inhibited the Pb^{2+} removal at lower pH. As pH is increased, the active sites on the adsorbents are exposed to increasing negative charge density on the surface and the resultant is an increasing attraction of metal cation onto the surface. Consequently, an initial pH value of 5.0 was used as the optimum pH throughout the experimental work to avoid the formation of metal hydroxides.

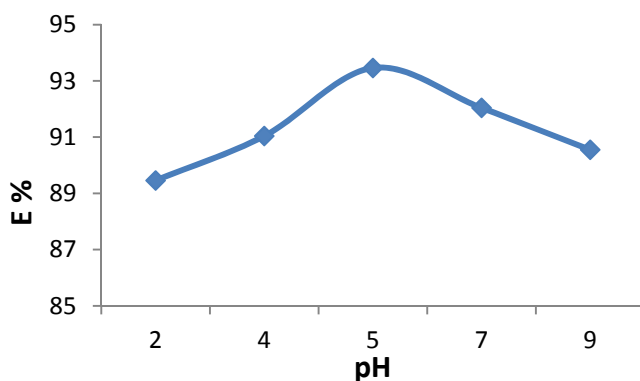


Figure 5. The effect of initial pH values on Pb^{2+} biosorption using FCAC; $C_i = 50 \text{ mg } Pb^{2+} / L$, 0.5 g biomass , $d = 150 - 300 \text{ } \mu\text{m}$, 296 K and 200 rpm .

The effects of temperature

The amount of Pb^{2+} adsorbed on FCAC as function of solution temperature is shown in Fig. 6. As the figure shows, the removal efficiency decreased as the temperature increased from 23 to 53°C, showing that low temperature favors the Pb^{2+} removal from aqueous solutions. It was observed that the maximum biosorption was found at 23°C with a maximum removal percentage of 94%. The observed increase in biosorption of Pb^{2+} with decrease

in temperature is indicative of the fact that the biosorption process is exothermic in nature. The general trend in decrease of biosorption for FCAC with an increase in temperature may be attributed to the Pb²⁺ escaping from the solid phase with a rise in temperature. The optimum temperature of 23°C was used for all further experiments.

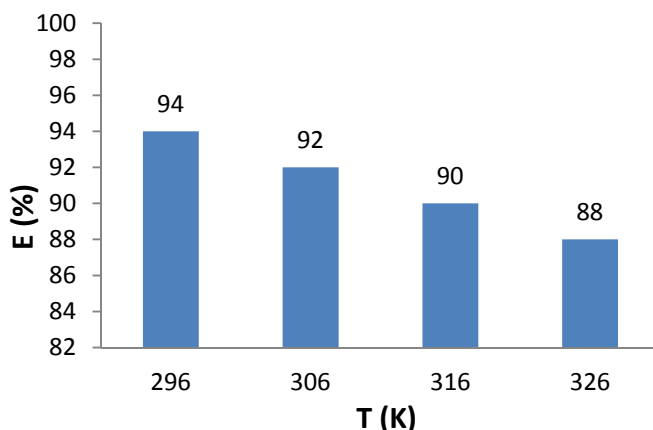


Figure 6. Temperature influence over the removal efficiency of Pb²⁺ on FCAC C_i=50 mg Pb²⁺/L, d =150 – 300 μm, 0.5 g biomass, 5.0 pH, 296 K and 200 rpm.

Adsorption isotherms

Isotherm equations have been used for the equilibrium modeling of adsorption systems. The adsorption data have been subjected to different adsorption isotherms, namely; Langmuir, Freundlich, Dubinin–Radushkevich (D–R) and Temkin required for Pb²⁺ biosorption from simulated wastewaters onto FCAC.

The Freundlich isotherm assumes that adsorption takes place on a heterogeneous surface which involves a multilayer adsorption of metal ions. The Freundlich isotherm linear equation can be expressed as [36]:

$$\log q_e = \log K_F + \frac{1}{n} \times \log C_e \quad (1)$$

where, K_F is related to the adsorption capacity and n is related to the intensity of adsorption. The $\log q_e$ versus $\log C_e$ plot allows the determination of the Freundlich constants.

The Langmuir isotherm model describes the monolayer adsorption onto the surface of an adsorbent with finite number of identical sites and is the most widely used isotherm for adsorption studies in recent years. The linear form of the Langmuir isotherm model [37] can be represented by:

$$\frac{1}{q_e} = \frac{1}{q_m b} \times \frac{1}{C_e} + \frac{1}{q_m} \quad (2)$$

where, C_e (mg/L) is the equilibrium concentration, q_e is the amount of metal ion adsorbed at equilibrium, q_m is the maximum adsorption capacity and b is the equilibrium Langmuir constant.

The Freundlich constants n and K_F , Langmuir constants b and q_m , and their corresponding correlation coefficients, R^2 are given in Table 1.

The adsorption constants were calculated for concentration ranges between 50 and 250 mg/L the results are presented in Table 1. Based on the correlation coefficients (R^2), it is clear that the biosorption of lead ions onto FCAC is best fitted to the Freundlich adsorption isotherm for the entire range of concentrations. The fact that the Freundlich isotherm fits the experimental data very well may be due to heterogeneous distribution of active sites on the carbon surface, since the Freundlich equation assumes that the surface is heterogeneous.

The n value indicates the degree of nonlinearity between solution concentration and adsorption as follows: if $n = 1$, then adsorption is linear; if $n < 1$, then adsorption is a chemical process; if $n > 1$, then adsorption is a physical process. The values of n for Freundlich isotherm were found to be greater than 1, which indicates that the adsorption system is a favorable one and suggesting physical adsorption.

The Temkin isotherm equation assumes that the fall in the heat of adsorption of all the molecules in the layer decreases linearly with coverage due to adsorbent-adsorbate interactions, and that the adsorption is characterized by a uniform distribution of the binding energies up to some maximum binding energy [38]. The Temkin isotherm has been applied in the following form:

$$Q_e = B \ln A_T + B \ln C_e \quad (3)$$

$$B = \frac{RT}{b_T} \quad (4)$$

where, b_T is the Temkin isotherm constant, T is the absolute temperature in Kelvin and R is the universal gas constant (8.314 J/mol K). The model constants A_T and B are determined by the linear plot of q_e versus $\ln C_e$. The Temkin isotherm assumes that the heat of adsorption of the molecules in a layer decreases linearly due to adsorbent-adsorbate interaction and that the binding energies are uniformly distributed. The Temkin constants are presented in Table 1.

The Dubinin–Radushkevich (D–R) model is given by [39]:

$$\ln q_e = \ln q_m - \beta \varepsilon^2 \quad (5)$$

where, q_e is the whole amount of metal ions adsorbed on per unit weight of biomass (mol/g), q_m is the maximum adsorption capacity (mol/g), β is the activity coefficient related to biosorption mean free energy (mol²/J²) and ε is the Polanyi potential. This energy E is determined by the following equation [40]:

$$E = \frac{1}{\sqrt{-2\beta}} \quad (6)$$

The isotherm constants q_m and β were obtained from the intercept and the slope of the plot $\ln q_e$ vs. ε^2 . It is known that the magnitude of apparent adsorption energy E is useful for estimating the type of adsorption and, if this value is below 8 kJ/mol, the adsorption type can be explained by physical adsorption, between 8 and 16 kJ/mol, the adsorption type can be explained by ion exchange, and, over 16 kJ/mol, the adsorption type can be explained by a stronger chemical adsorption than ion exchange [41, 42]. The values of E are found to be below 8 kJ/mol (Table 1) which correspond to physical adsorption [43].

Table 1. Langmuir, Freundlich, Dubinin-Radushkevich and Temkin calculated coefficients using linear regression analysis for Pb²⁺ removal using FCAC; C_i = 50-250 mg/L, 0.5 g biomass, d = 150 – 300 μ m, 296 K, pH 5.0, 200 rpm.

Langmuir			Freundlich			Dubinin-Radushkevich			Temkin		
K _L (L/mg)	q _{max} (mg/g)	R ²	n	K _F (mg ^(1-1/n) L ^{1/n} /g)	R ²	β (mol ² /kJ)	E (kJ/mol)	R ²	A _T (L/g)	B (J/mol)	R ²
10.01	48.54	0.981	1.70	4.76	0.997	2×10 ⁻⁵	5	0.885	2.89	2×10 ⁻⁶	0.807

Adsorption kinetics

The adsorption kinetics is one of the most important data in understanding the mechanism of the adsorption and in assessing the performance of the adsorbents. Different kinetic models including pseudo-first-order [44] and pseudo-second-order [45] were applied for the experimental

data to predict the adsorption kinetics of Pb^{2+} . The linear form of the pseudo-first-order and pseudo-second-order rate equation is given as:

$$\ln(q_e - q_t) = \ln q_e - k_1 t \quad (7)$$

$$\frac{dq_t}{dt} = k_2 (q_e - q_t)^2 \quad (8)$$

where, q_t and q_e (mg/g) are the amounts of the adsorbed lead ions at equilibrium time (mg/g) and t (min), respectively and the values of k_1 (min^{-1}) and k_2 (g/mg min) are the adsorption rate constants of the pseudo-first-order and pseudo-second-order models.

The experimental value of solid phase concentration of adsorbate at equilibrium ($q_{e,exp}$) and the calculated value of solid phase concentration of adsorbate at equilibrium ($q_{e,calc}$) for the pseudo-first-order and pseudo-second-order models are also presented in Table 2. The $q_{e,exp}$ and the $q_{e,calc}$ values from the pseudo-second-order kinetic model are very close to each other, and also the calculated coefficients of determination, R^2 are also closer to unity for pseudo-second-order kinetics than that for the pseudo-first-order kinetics. Therefore, the adsorption kinetic could be approximated more favorably by pseudo-second-order kinetic model for the biosorption of Pb^{2+} by FCAC.

Table 2. Pseudo-first-order and pseudo-second-order rate constants, calculated and experimental q_e values for Pb^{2+} removal by FCAC biomass using different initial concentrations; $C_i = 50\text{-}250$ mg/L, $d = 150 - 300$ μm , 0.5 g biomass, 296 K, pH 5.0, 200 rpm.

C (mg/L)	q_e (exp) (mg/g)	Pseudo-first-order			Pseudo-second-order		
		k_1 (1/min)	q_e (calc) (mg/g)	R^2	k_2 (g/mg-min)	q_e (calc) (mg/g)	R^2
Fir cone activated carbon							
50	9.35	1.01×10^{-2}	0.002	0.6625	1.98×10^{-2}	9.40	0.999
100	19.51	1.75×10^{-2}	0.066	0.9356	5.4×10^{-3}	19.54	0.994
150	26.12	1.96×10^{-2}	1.216	0.9048	1.9×10^{-3}	26.22	0.994
200	36.00	1.82×10^{-2}	1.343	0.8788	3.8×10^{-3}	37.00	0.997
250	41.00	1.94×10^{-2}	1.576	0.8994	1.5×10^{-3}	40.87	0.998

Desorption experiments

In wastewater treatment, the regeneration and reusability of the bioadsorbent material is very important from an economic point of view, and it also helps to protect the environment and recycling of adsorbate (Pb^{2+} ions) and bioadsorbent (fir cone activated carbon). The biosorption-desorption

processes were repeated consecutively to designate the reusability of the fir cone. The biosorption process was performed under the optimal batch conditions previously determined. Also, desorption studies help in process design systems by giving information on the mechanism and recovery process of the adsorbates from industrial wastewater and the bioadsorbent. In the present work, different concentrations of HCl (0.1, 0.2, 0.3 and 0.4 M) as stripping agents were used for the desorption studies. The experiments were performed in order to determine the optimum concentration of the HCl solution and to attained the maximum desorption efficiency. The desorption process were repeated three times consecutively and the biosorption-desorption efficiencies of FCAC after each cycle were determined separately (Fig. 6). It can be observed that the desorption rate decreases with the increase in HCl concentration, where at concentration of 0.1 M, more than 80% were desorbed from FCAC. This can be explained by the fact that low concentration acidic treatment activates and opens the pore spaces in the surface of the bioadsorbent [46, 47]. Further biosorption-desorption cycle experiments can be performed in order to show the reusability by saturation of FCAC with Pb²⁺ ions at each cycle.

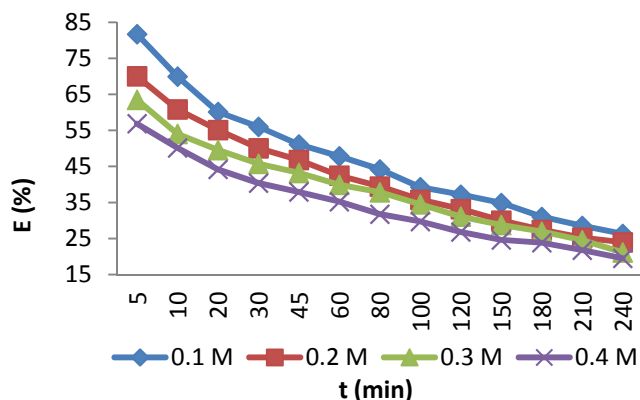


Figure 6. Desorption of Pb²⁺ ions from FCAC; C_i=50 mg Pb²⁺/L, d =150 – 300 μm, 0.5 g biomass, 5.0 pH, 296 K and 200 rpm.

CONCLUSIONS

This study presented the results obtained at Pb²⁺ ions biosorption where the fir cone biomass was used as a precursor for the preparation of fir cone activated carbon (FCAC) by sulfuric acid treatment and activation. The biosorption of Pb²⁺ on FCAC was found to be depending on factors such as initial pH, bioadsorbent quantity, initial lead concentration and temperature.

The following important results can be mentioned:

- pH 5.0 was deduced as optimum for the removal of Pb^{2+} for the FCAC biomass.
- Following the biosorption process, a contact time of 240 min was necessary to reach equilibrium, depending on lead ions initial concentration.
- The biosorption rate increased with increasing bioadsorbent quantity and decreased with increasing of Pb^{2+} ion concentration.
- Equilibrium was best described by Freundlich isotherm model ($R^2=0.9971$).
- The maximum adsorption capacity obtained from Langmuir model was 48.54 mg/g.
- From the values of activation energy of the process calculated according to Dubinin-Radushkevich and Temkin models, it is suggested that biosorption of Pb^{2+} by FCAC biomass is physical in nature.
- Kinetic study showed that the biosorption follows pseudo-second-order kinetic model.
- The biosorption is favorably influenced by a decrease in temperature of the operation.
- Desorption experiments showed that more than 80% can be desorbed at 0.1 M concentration of HCl.

In conclusion, the experimental results entail that the FCAC is a reasonably good, low cost and promising bioadsorbent for the efficient removal of Pb^{2+} from contaminated aqueous media.

EXPERIMENTAL SECTION

Preparation of biomass

Fir tree (*Abies alba*) cones were obtained from a botanical garden in Cluj-Napoca, Romania. The cones were washed to remove impurity such as sand and leaves, and then the washed cones were dried at 105°C for 24 h. The scales on the cones were then removed and crushed using a bead mill. Prior to being used, the fir cone biomass was washed with distilled water several times until it yielded colorless filtered water. The dried fir cone biomass were then soaked in concentrated sulphuric acid (98%) at 1:1 (W:V) ratio for 48 h at normal temperature and pressure. After treatment, the reaction product was soaked in 1% sodium bicarbonate solution overnight

(for neutralization) and washed with distilled water again until a neutral pH. The samples were then carbonized in a Muffle furnace at 600°C and at a heating rate of 10°C and held at this temperature for 1 h. The prepared FCAC material was sieved (150 – 300 µm) and used as bioadsorbent for the removal of Pb²⁺ from aqueous solutions.

Preparation of Pb²⁺ solutions

The stock solution of 1000 mg/L was prepared by dissolving Pb(NO₃)₂ in deionized water. Pb²⁺ solutions of different concentrations in range between 50-250 mg/L were prepared by serial dilution of the stock solution using deionized water. Before mixing the adsorbent, the pH of each test solution was adjusted to the required value with 0.1 M KOH or 0.1 M HCl. All chemicals used during the experiments were of analytical grade.

Biosorption experiments

Batch biosorption experiments were carried out in conical Erlenmeyer flasks containing 100 mL of Pb²⁺ solutions. The flasks with bioadsorbent quantity of 0.5 g were stirred at 200 rpm, 23°C and pH 5.0. In order to establish the evolution of the removal process, samples of 500 µL were collected at different time intervals (0-240 min). The collected samples at predetermined time intervals were filtered (ME cellulose 0.45 µm microfilter) and the remaining concentration in aqueous phase was determined using an Atomic Absorption Spectrometer (SensAA Dual GBS Scientific Equipment, Australia).

In order to evaluate the amount of lead ions retained per unit mass of biomass, the adsorption capacity and efficiency was calculated using the following equations:

$$E, (\%) = \frac{C_i - C_f}{C_i} \cdot 100 \quad (9)$$

$$q_t, (mg/g) = \frac{(C_i - C_f) V}{m} \quad (10)$$

where $E, (\%)$ represents the efficiency, C_i and C_f the initial and final concentration of lead (mg/L) in the aqueous solution, the q_t (mg/g) represents the amount of lead ions adsorbed onto unit weight of biomass, V (L) means the volume of lead ions in aqueous solution and m (g) the bioadsorbent quantity.

In order to study the pH influence over the biosorption process, the initial pH was adjusted using 0.1 M HCl and 0.1 M KOH solutions. The relationship between temperature and removal efficiency values for Pb²⁺ biosorption were established and performed at different temperatures (296, 306, 316 and 326 K) using a thermostat water bath. All the experiments were repeated three times, the values presented were calculated using averaged concentration values.

Desorption experiments

In order to consider the practical use fullness of the bioadsorbent, desorption experiments were performed. For the desorption study 0.5 g biomass was contacted with 100 mL of Pb²⁺ solution (50 mg/L). After the biosorption test, the biomass was collected by filtration and washed with deionized water two times to remove excess Pb²⁺ residual on the surface. Then, it was treated with 100 mL of 0.1, 0.2 0.3 and 0.4 M HCl each and stirred at 200 rpm for 240 min and 23°C. Supernatants were collected and Pb²⁺ analysis were done. For the best eluent, the biosorption and desorption steps were repeated three times. All of the experiments were carried out in duplicate and the average values were used in the calculations.

Scanning electron microscopy (SEM) analysis

Scanning electron microscopy is utilized for characterizing surface microstructures, porosity and fundamental physical properties of different adsorbents. The surface morphology of FCAC was determined using a scanning electron microscope JEOL JSM 5510 LV (Japan). Prior to the analysis, the bioadsorbent samples were mounted on a stainless stab with a double stick tape. Then they were coated with a thin layer of gold under vacuum to improve electron conductivity and image quality.

REFERENCES

1. K. Naiya, A.K. Bhattacharya, S. Mandal, S.K. Das, *Journal of Hazardous Materials*, **2009**, 163, 1254.
2. W.S. Peternele, A.A. Winkler-Hechenleitner, E.A. Gomez Pineda, *Bioresource Technology*, **1999**, 68, 95.

3. J. Crittenden, R. Trussel, D. Hand, K. Howe, G. Tchobanoglous, *New Jersey*, **2005**, pp. 266–267.
4. L. Wang, J. Zhang, R. Zhao, Y. Li, C. Li, C. Zhang, *Bioresource Technology*, **2010**, *101*, 5808.
5. WHO, Environmental Health Criteria. No. 200, Lead exposure. Ch-1211, **1998**, Geneva 27, Switzerland.
6. A.T. Paulino, L.B. Santos, J. Nozaki, *Reactive and Functional Polymers*, **2008**, *68*, 634.
7. P.S. Kumar *Environmental Progress and Sustainable Energy*, **2013**, *33*, 1, 55.
8. T.A. Saleh, V.K. Gupta *Environmental Science and Pollution Research*, **2012**, *19*, 4, 1224.
9. N.M. Mubarak, S. Daniel, M. Khalid, J. Tan, *Journal of Chemical and Environmental Engineering*, **2012**, *3*, 1.
10. G. Garcia-Rosales, A. Colin-Cruz, *Journal of Environmental Management*, **2010**, *91*, 2079.
11. H. Lalhrualtuanga, K. Jayaram, M.N.V. Prasad, K.K. Kumar, *Journal of Hazardous Materials*, **2010**, *175*, 311.
12. J. Goel, K. Kadirvelu, C. Rajagopal, V.K. Garg, *Journal of Hazardous Materials*, **2005**, *B125*, 211.
13. M.K. Mondal, *Journal of Environmental Management*, **2009**, *903*, 266.
14. Z. Xuan, Y. Tang, X. Li, Y. Liu, F. Luo, *Journal of Biological Engineering*, **2006**, *31*, 160.
15. S.M. Lalhmunsiana, Le, D. Tiwari, *Chemical Engineering Journal*, **2013**, *225*, 128.
16. F.N. Azad, M. Ghaedi, K. Dashtian, M. Montazerzohori, S. Hajati, E. Alipanahpour, *RSC Advances*, **2015**, *75*, 61060.
17. M. Ghaedi, M.N. Biyareh, S.N. Kokhdan, Sh. Shamsaldini, R. Sahraei, A. Daneshfar, S. Shahriyar, *Materials Science and Engineering*, **2012**, *32*, 725.
18. W. Zhang, Q. G. Chang, W.D. Liu, B.J. Li, W.X. Jiang, L.J. Fu, *Environmental Progress*, **2007**, *26*, 289.
19. T. Bohli, N. Fiol, I. Villaescusa, A. Ouederni, *Journal of Chemical Engineering & Process Technology*, **2013**, *4*, 1.
20. M.F. Rahman, S. Peldszus, B.W. Anderson, *Water Research*, **2014**, *50*, 318.
21. E. Pehlivan, T. Altun, S. Parlayıcı, *Journal of Hazardous Materials*, **2009**, *164*, 982.
22. G. Cimino, A. Passerini, G. Toscano, *Water Research*, **2000**, *34*, 2955.
23. B. Nagy, A. Măicăneanu, C. Indolean, S. Burca, L. Silaghi-Dumitrescu, C. Majdik, *Acta Chimica Slovenica*, **2013**, *60*, 2, 263.
24. G. Annadurai, R.S. Juang, D.J. Lee, *Water Science and Technology*, **2003**, *47*, 185.
25. N. Meunier, *Journal of Environmental Engineering ASCE*, **2003**, *129*, 693.
26. F. Boudrahem, F. Aissani-Benissad, H. Aït-Amar, *Journal of Environmental Management*, **2009**, *90*, 3031.
27. Q. Feng, Q. Lin, F. Gong, S. Sugita, M. Shoya, *Journal of Colloid and Interface Science*, **2004**, *278*, 1.

28. N. Fiol, I. Villaesscusa, M. Martinez, N. Miralles, J. Poch, J. Serarols, *Separation and Purification Technology*, **2006**, 50, 132.
29. M. Martinez, N. Miralles, S. Hidalgo, N. Fiol, I. Villaeseasa, *Separation and Purification Technology*, **2006**, B133, 203.
30. S.K. Yadav, D.K. Singh, S. Sinha, *Journal of Environmental Chemical Engineering*, **2014**, 2, 9.
31. S.K.R. Yadanaparthi, D. Graybill, R. Wandruszka, **2009**, *Journal of Hazardous Materials*, 171, 1.
32. B. Nagy, C. Mânzatu, A. Măicăneanu, C. Indolean, L. Silaghi-Dumitrescu, C. Majdik, *Journal of Wood Chemistry and Technology*, **2014**, 34, 301.
33. J. Rivera-Utrilla, M. Sánchez-Polo, V. Gómez-Serrano, P.M. Álvarez, M.C.M. Alvim-Ferraz, J.M. Dias, *Journal of Hazardous Materials*, **2011**, 187, 1.
34. Y. Chun Yang, A.M. Kheireddine, W.M.A.W. Daud, *Separation and Purification Technology*, **2007**, 52, 403.
35. M. Moyo, L. Chikazaza, B.C. Nyamunda, U. Guyo, *Journal of Chemistry*, **2013**, 1.
36. H.M.F. Freundlich, *Zeitschrift für Physikalische Chemie*, **1906**, 57(A), 385.
37. I. Langmuir, *Journal of American Chemical Society*, **1918**, 40, 1361.
38. M.J. Temkin, V. Pyzhev, *Acta Physico-Chimica Sinica*, **1940**, 12, 217.
39. M.M. Dubinin, *Chemical Reviews*, **1960**, 60, 235.
40. S.M. Hasany, M.H. Chaudhary, *Applied Radiation and Isotopes*, **1996**, 47, 467.
41. C.C. Wang, L.C. Juang, C.K. Lee, T.C. Hsua, J.F. Leeb, H.P. Chaob, *Journal of Colloid and Interface Science*, **2004**, 280, 27.
42. P. Djomgoue, M. Siewe, E. Djoufac, P. Kenfack, D. Njopwouo, *Applied Surface Science*, **2012**, 258, 7470.
43. S. Elsherbiny, T.A. Fayed, *Journal of Physics and Chemistry of Solids*, **2010**, 71, 952.
44. S. Lagergren, *Kungliga Svenska Vetenskapsakademiens, Handlingar, Band, 1898*, 34, 451.
45. Y.S. Ho, G. McKay, *Process Biochemistry*, **1999**, 34, 451.
46. K.G. Akpomie, F.A. Dawodu, K.O. Adebowale, *Alexandria Engineering Journal*, **2015**, 54, 757.
47. E. Igberase, P. Osifo, A. Ofomaja, *Journal of Environmental Chemical Engineering*, **2014**, 2, 362.

*Dedicated to Professor Luminița Silaghi-Dumitrescu
on the occasion of her 65th anniversary*

ADSORPTION, EQUILIBRIUM AND KINETIC STUDY OF MALACHITE GREEN REMOVAL FROM AQUEOUS SOLUTIONS USING FIR (*ABIES NORDMANNIANA*) CONES BIOMASS

**ANA-MARIA SĂCARĂ^a, CERASELLA INDOLEAN^{a*},
LIANA MARIA MUREȘAN^a**

ABSTRACT. Adsorption of Malachite Green (MG) dye on a biomass prepared from fir (*Abies nordmanniana*) cones, followed by UV–Vis detection has been studied. The biomass was characterized using scanning electron microscopy (SEM). The maximum adsorption capacity of MG onto fir cones biomass was determined to be 2.197 mg/g. The influence of pH on the removal of the MG dye was investigated and the results showed that the best adsorption capacity were obtained in the most acidic environment (pH=2). The adsorption rates were evaluated by fitting the experimental data to conventional kinetic models such as pseudo- first- and pseudo-second-order models. From the Dubinin–Radushkevich isotherm model, a 5.95 kJ/mol value for the mean free energy was calculated, indicating that MG adsorption could include an important physisorption stage.

Keywords: *adsorption, cones biomass, Abies nordmanniana, kinetics, dyes, malachite green*

INTRODUCTION

Malachite green (MG) is a cationic dye used extensively in the textile finishing industry for dyeing cotton, silk, wool and leather products [1] as well as in aquaculture to treat parasites, fungal and bacterial infections [2].

^a Babeș-Bolyai University, Faculty of Chemistry and Chemical Engineering, 11 Arany Janos str., RO-400028, Cluj-Napoca, Romania,

* Corresponding author cella@chem.ubbcluj.ro

Due to its potential carcinogenicity, mutagenicity and teratogenicity [3] MG should be removed from wastewater and this process has become an important environmental issue.

One of the simplest and most cost-effective techniques to remove MG from aqueous effluents consists in its adsorption on different materials such as zeolites [4], clays [5], compost [6], active carbon prepared from different biomaterials such as pine sawdust [7], oak wood [8], olive stones [9] cherry stones [10] etc., but mostly on biosorbents derived from renewable resources [11-14]. By contrast with carbon-based and other inorganic adsorbents, biosorbents have some significant advantages. They exhibit excellent adsorption capacity, fast adsorption kinetics and simplicity of design together with low cost and availability [15].

Numerous physicochemical factors affect dye adsorption, including: (i) characteristics of the adsorbent (*i.e.* surface area, pore structure, surface treatments, particle size); (ii) characteristics of the dye molecule, and (iii) operational conditions, such as pH, temperature, contact time etc. [16]. The interactions occurring between the adsorbate and adsorbent have to be also taken into consideration.

In this context, adsorption of MG dye on biomass prepared from fir tree (*Abies nordmanniana*) cones biomass, followed by UV–Vis detection has been developed for the removal of the dye from aqueous solutions. The biomass was subsequently characterized using scanning electron microscopy (SEM). The influence of pH on the removal of MG was investigated. The adsorption rates were evaluated by fitting the experimental data to conventional kinetic models such as pseudo first- and second-order models.

RESULTS AND DISCUSSION

SEM characterization of the biomass

Scanning electron microscopy (SEM) images of the biomass surface were taken before and after the adsorption of MG. As can be seen from figure 1a, the crevices and the pores of the adsorbent offer good conditions for dye adsorption. Figure 1b shows clearly a smoother surface, resulted after filling the crevices with dye molecules.

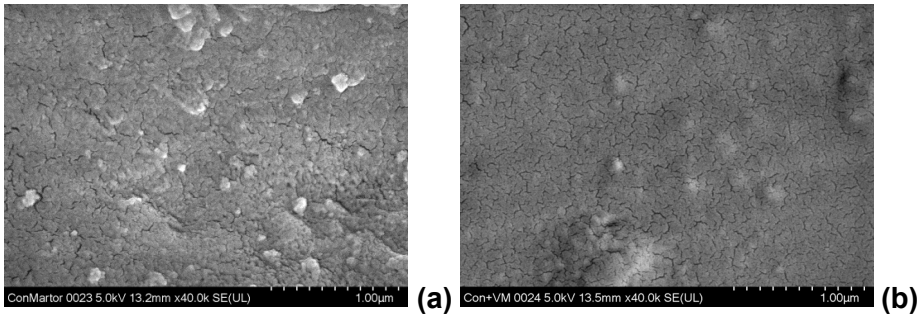


Figure 1. SEM images of the fir cones biomass before (a) and after (b) MG adsorption

Effect of pH

Initial pH of the solution can significantly influence the dye adsorption on the adsorbent surface. Consequently, the effect of pH was investigated in the range of 2 to 6 imposed by the solubility of MG, which is better at acidic pHs. At basic pH values, new species of the dye can form [17] which could impede on the accuracy of the experimental results.

It was observed that the best adsorption capacities were obtained in the most acidic environment, as can be seen in Figure 2. These results are different from those of some similar studies on MG [18], but are in agreement with the observations of some authors relative to other basic dyes, such as Maxilon Blue [19]. This could be attributed to the better solubility of MG, as could be observed during the experiments.

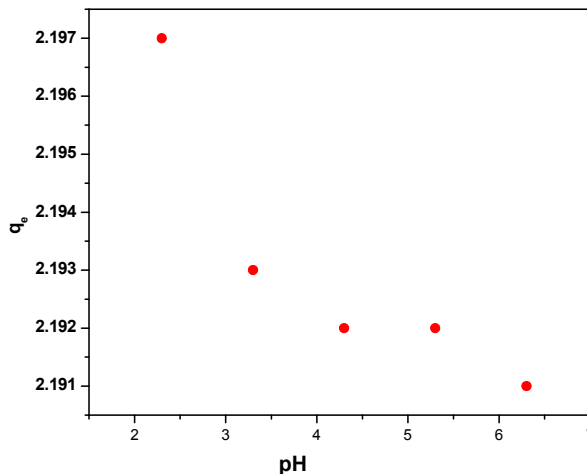


Figure 2. Initial pH influence on MG adsorption capacity of cones biomass, 5g, 0.2-0.4 mm, $t=20^{\circ}\text{C}$, $C_0=100\text{mg/L}$ MG, 100mL solution

Moreover, the fir cone biomass was observed to have a notable buffering effect on the solutions with pH between 3 and 6 (figure 3), by shifting the solution pH toward 6, irrespective to the initial pH value. At this pH, adsorption of MG is favored and involves interactions of the dye with the functional groups of the adsorbent [20]. At strong acidic environments, the MG acts itself as an acid according to its pKa (6.9) [21], counteracting the buffering effect of the biomass (Figure 3).

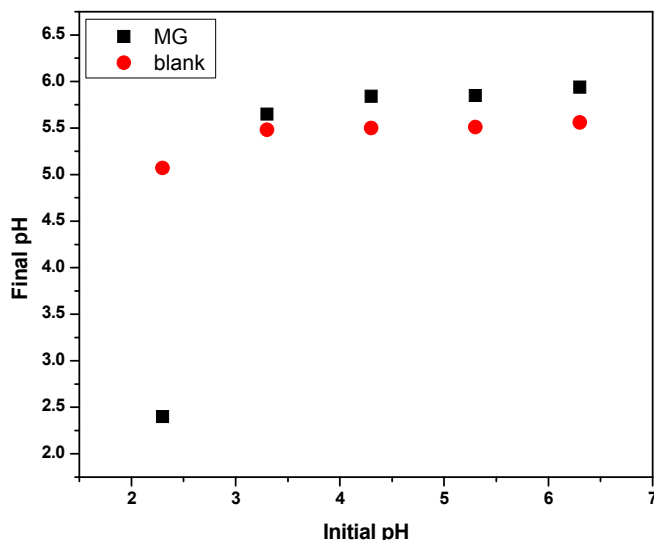


Figure 3. Initial pH influence over final pH for blank and MG adsorption, 5g biomass, 0.2-0.4 mm, $t=20^{\circ}\text{C}$, $C_0=100\text{mg/L}$ MG, 100mL solution.

Blank sample (shown in Figure 3) refers to the values obtained in batch experiments conducted under identical conditions (biomass:solution ratio, temperature and contact time) with distilled water instead of MG solution, in order to establish the contribution of MG on the global pH shift.

Adsorption isotherms

In order to characterize the adsorption process, the experimental data were analyzed according to the linear forms of Langmuir, Freundlich, Temkin and Dubinin-Radushkevich (D-R) equilibrium isotherms (Figure 4).

Langmuir isotherm proposes that the adsorption sites on the surface are identical, the final result being a monolayer of adsorbate.

Freundlich isotherm assumes that a heterogeneous adsorption occurs, the active sites are different by nature and energy and that there is a link between adsorption capacity (q_e) and dye concentration at equilibrium. [17]

Temkin isotherm takes into account adsorbent-adsorbate interactions, assuming that the heat of adsorption, expressed as a function of temperature, decreases linearly with coverage [22] while D-R isotherm model is applied to uncover the nature of the process, as physical or chemical sorption [23].

Characteristic parameters were calculated and are shown in Table 1. The values are comparable to results obtained in other similar studies [24, 25]

In Table 1, A_T is Temkin isotherm constant, dm^3/mol ; B_D - Dubinin-Radushkevich isotherm constant, mol^2/J^2 ; b_T -Temkin isotherm constant; C_e - is the adsorbate concentration at equilibrium mg/dm^3 ; E - free energy of sorption, J/mol ; K_L - Langmuir isotherm constant, dm^3/g ; K_F - Freundlich isotherm constant; n_F - Freundlich isotherm exponent; q_e is the equilibrium adsorption capacity (mg/g) and the other symbols have the usual significance.

From the Dubinin–Radushkevich isotherm model, a 5.95 kJ/mol value for the mean free energy was calculated, indicating that MG adsorption could be a physisorption process [26, 27].

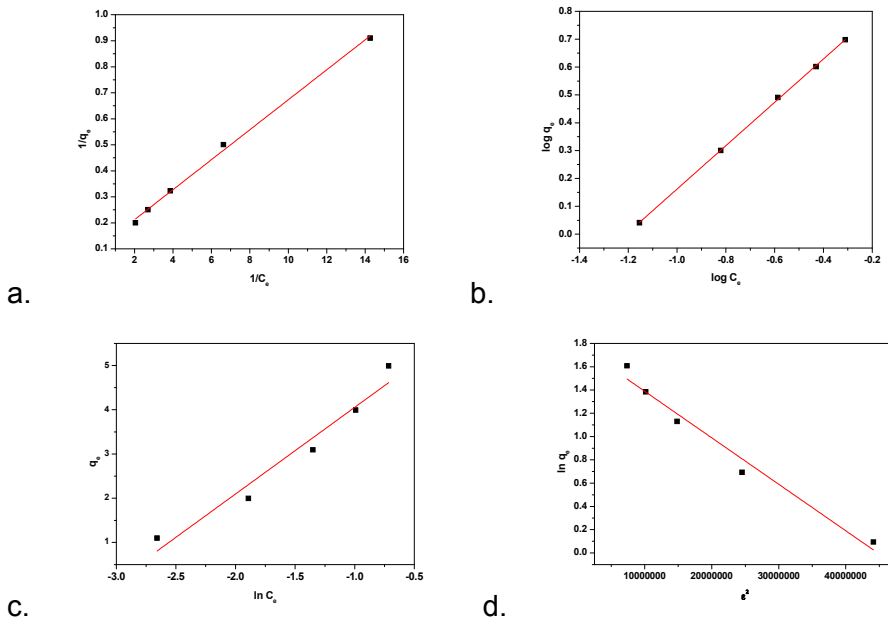


Figure 4. Isotherm models: Langmuir (a), Freundlich (b), Temkin (c) and Dubinin-Radushkevich (d), for MG adsorption on *Abies nordmanniana* cones biomass, 5g, 0.2-0.4 mm, $t=20^\circ\text{C}$, $C_0=100\text{mg}/\text{L}$ MG, 100mL solution.

After examining the similarity between the different adsorption isotherms models and the experimental results, it seems that Freundlich isotherm is most adapted for the fitting of MG adsorption, as encountered in many similar studies [28].

Table 1. Characteristic parameters of adsorption isotherms

Isotherm	Equation	R ² /N	Parameters	Values
Langmuir	$1/q_e = 1/q_m K_L C_e + 1/q_m$	0.9976/5	q_m (mg/g)	10.27
			K_L (dm ³ /g)	1.69
Freundlich	$\lg q_e = \lg K_f + 1/n \lg C_e$	0.9998/5	n_F	1.29
			K_F	2.56
Temkin	$q_e = RT/b_T \ln(A_T C_e)$	0.9577/5	b_T (J/mol)	1244.77
			A_T (dm ³ /mol)	3.00
Dubinin-Raduskevich	$\ln q_e = \ln q_D - B_D R^2 T^2 [\ln(1+1/C_e)]^2$ $*\ln(1+1/C_e) = \varepsilon$ for graph 4d	0.9755/5	B_D (mol ² /kJ ²)	1.41×10^{-6}
			E (kJ/mol)	5.95
			q_D (mg/g)	5.88

Kinetics of adsorption

Kinetics of adsorption is one of the most important characteristics in defining the adsorption efficiency. In order to describe the mechanism of MG removal on fir cones biomass, pseudo-first and pseudo-second order kinetics as well as film layer and intra-particle diffusion were taken into consideration.

It is common knowledge that, if the adsorption is the only phenomenon occurring on the surface, the variation of the reaction rate should be proportional to the first power of adsorbate concentration (pseudo-first-order kinetics) [26, 29]. Lagergren suggested a first-order equation for the adsorption of liquid/solid system based on solid capacity, which can be expressed in linear form as follows [26, 27]:

$$\ln(q_e - q_t) = \ln q_e - k_1 t \quad (1)$$

where, q_e and q_t are the amounts of adsorbate for 1 g of adsorbent (mg/g) at equilibrium and time t , respectively, t is time (min), k_1 is the rate constant of the first order adsorption (1/min).

If diffusion (both on the adsorbent's surface and through its pores) has a contribution to the global mechanism, limiting the adsorption process, the dependence between the concentration and rate will not be linear.

The pseudo-second-order kinetic model is derived on the basis of the adsorption capacity of the solid phase. The linear form of the model is expressed as follows [28, 30]:

$$\frac{t}{q_t} = \frac{1}{k_2 q_e^2} + \frac{t}{q_e} \quad (2)$$

where, q_e and q_t are the amounts adsorbed at equilibrium and time t , respectively (mg/g), t is time (min), k_2 is the rate constant of the second order adsorption (g/mg·min).

An analysis of the experimental data allowed us to conclude that the q_e value calculated based on the pseudo-second order model compared to q_e values obtained from experimental data are closer. Also taking into consideration the fact that the correlation coefficient is $R^2 = 0.999$, for all five initial concentrations (55, 100, 155, 200 and 250 mg MG/L), (Figure 5, Table 2), in the case of pseudo-second-order model, we concluded that this model describes the considered adsorption process.

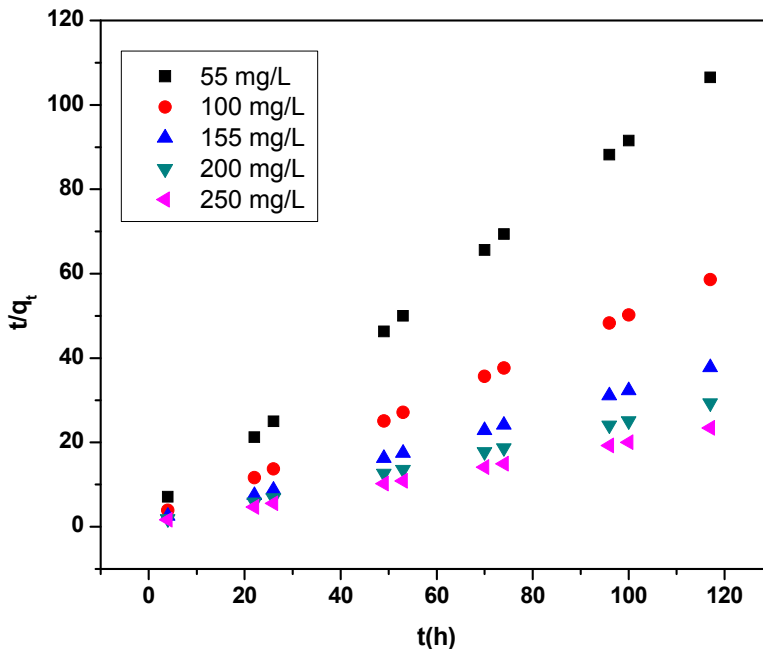


Figure 5. Pseudo-second order kinetics for MG adsorption on *A. nordmanniana* cone biomass, 5g, 0.2-0.4 mm, $t=20^{\circ}\text{C}$, $C_0=55\text{-}250\text{mg MG/L}$, 100mL solution.

Table 2. The correlation coefficient (R^2) for pseudo-first and pseudo-second order models and different initial MG concentrations.

Kinetic model	Initial MG concentration [mg MG/L]	R^2
Pseudo-first order	55	0.448
	100	0.447
	155	0.445
	200	0.444
	250	0.463
Pseudo-second order	55	0.999
	100	0.999
	155	0.999
	200	0.999
	250	0.999

The results are in agreement with most adsorption studies concerning MG [28-31].

As already mentioned, adsorption processes are accompanied by two types of diffusion: one on the material's surface (liquid layer, or external diffusion) and the other through the pores of the adsorbent (internal diffusion). One of these two types is often rate determining for the entire process, therefore determining their implication is important.

To identify the diffusion mechanism involved in MG retention on cones biomass, the model based on the theory of Weber and Morris was considered and can be written as follows: [32].

$$q_t = k_{ip} \cdot t^{0.5} \quad (3)$$

where, k_{ip} is the intra-particle diffusion rate constant ($\text{mg/g} \cdot \text{min}^{0.5}$).

According to this theory, if intraparticle diffusion is the rate determining step, the adsorbate uptake, q_t should be directly proportional to $t^{1/2}$ and the plot q_t vs. $t^{1/2}$ passes through the origin. If the plots do not pass through the origin, it is possible that intraparticle diffusion is not the only rate controlling step.

By examining the plot it could be seen that it not linear, meaning that the intraparticle diffusion is not the rate determining step, therefore results are not shown, but the correlation coefficients (R^2) and intercept values for intra-particle and liquid layer diffusion can be seen in Table 2.

As expected, at the beginning, the adsorption is fast, the high adsorption rate being due to the availability of the uncovered surface area of the adsorbent [19].

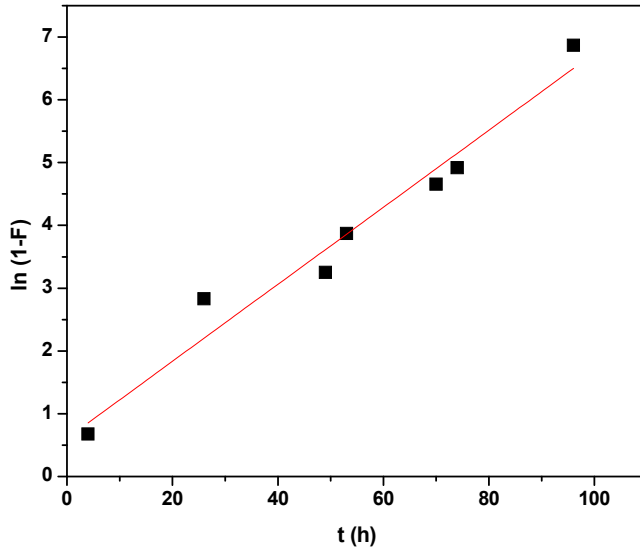


Figure 6. Liquid layer diffusion pattern of MG on fir cone biomass, 5g, 0.2-0.4 mm, $t=20^{\circ}\text{C}$, $C_0=100\text{mg/L}$ MG, 100mL solution.

Regarding the liquid layer (external) diffusion, the kinetic data have been analyzed using the model proposed by Boyd et al. [33]:

$$\ln(1-F) = -B_t - \ln\left(\frac{6}{\pi^2}\right) \quad (4)$$

where F represents the fraction of solute adsorbed at any time t (min), $F = q_t/q_0$ and B_t is a mathematical function of F .

Analyzing the experimental plot it suggests that intra-particle diffusion has a more important contribution to the global process.

The fact that the R^2 value is higher (0.9748) and the intercept is different, but closer to 0 (0.173 compared to 0.32 for liquid layer diffusion) confirms that in the given experimental conditions the intra-particle diffusion is most probably the rate determining step.

Table 3. The correlation coefficients (R^2) and intercept values for intra-particle and liquid layer diffusion

Diffusion type	R^2	Intercept
Intra-particle	0.9748	0.173
Liquid layer	0.9568	0.32

CONCLUSIONS

Fir (*Abies nordmanniana*) cones biomass was successfully used as a low cost adsorbent for the removal of toxic MG dye from aqueous solutions. The maximum adsorption capacity was determined to be 2.197 mg/g.

Four isotherms were used to model the adsorption of MG on the fir cones biomass. The classification of the models obtained by simulation of the corresponding equations and correlation with the experimental data was Freundlich > Langmuir > Dubinin-Radushkevich > Temkin. Between the four isotherm models considered, Freundlich model describes better MG dye adsorption onto fir cones biomass ($R^2 = 0.9998$). From the Dubinin-Radushkevich isotherm model, a 5.95 kJ/mol value for the mean free energy was calculated, indicating that MG adsorption could be a physisorption process.

Kinetic studies showed that the adsorption followed a pseudo-second-order kinetic model, with a correlation coefficient of 0.999 for all five initial concentrations (55, 100, 155, 200 and 250 mg MG/L, respectively).

EXPERIMENTAL SECTION

Preparation of dye solution

Analytical grade triphenylmethane dye MG ($\lambda = 618$ nm) in oxalate salt form was procured from Penta - Ing. Petr Švec, Czech Republic. Stock solution was obtained by dissolving 1 g of anhydrous powder in 1L of distilled water. Experimental solutions of different concentrations (55, 100, 155, 200 and 250 mg MG/L) were realised by subsequent dilutions.

Preparation and characterisation of adsorbent

The fir (*Abies nordmanniana*) cones used in this study were collected from a natural forest biotope in Cluj-Napoca, Cluj county, Romania. The cones were washed with tap water and left to dry out naturally, then grounded with a ball mill. The resulting material was boiled for 20 min to extract the natural colorant, then washed with distilled water and dried at 65-75°C for 3 days and sieved into five particle size fractions (<0.2, 0.2-0.4, 0.4-0.6, 0.6-1, 1-1.25 mm).

SEM images of the biomass were obtained on a with a JEOL (USA) JSM 5510 LV apparatus.

Adsorption studies

The MG adsorption on fir cones biomass was studied using the batch technique, with immobilized phases. Experiments were carried out by contacting different quantities of adsorbent, at 23°C, with 100 mL MG in aqueous solutions, with different initial concentrations (55–250 mg/L), until the equilibrium was reached.

Samples were collected and the residual concentration of MG was determined with a UV-Vis spectrophotometer Cintra 202 (GBC Scientific Equipment Ltd.) at 618 nm.

The amount of adsorbed MG dye (adsorption capacity q_e , mg/g) was calculated using Equation (5). Removal efficiency (E, %), Equation (6) was also calculated, in order to establish the effectiveness of the considered biomass in the Cd (II) removal process.

$$q_e = \frac{(C_0 - C_e)}{w} \times \frac{V}{1000} \quad (5)$$

$$E, (\%) = \frac{C_0 - C_e}{C_0} \times 100 \quad (6)$$

where, C_0 is the initial MG concentration (mg/L), C_e is MG concentration at equilibrium (mg/L), $V = 100$ mL, and w is the quantity of the adsorbent (g). [27].

The influence of initial pH (2-6) on the adsorption efficiency was studied. Its initial value was altered with 0.1M NaOH or 0.1M HCl solution, respectively.

ACKNOWLEDGMENTS

Ana-Maria Sacara thanks for the financial support received from National Scholarship Program of the World Federation of Scientists (WFS).

REFERENCES

1. D. Wang, L. Liu, X. Jiang, J. Yu, X. Chen, *Colloids and Surfaces A: Physicochemical and Engineering Aspects*, **2015**, 466,166.
2. N. Hidayah, F. Abu Bakar, N.A. Mahyudin, S. Faridah, M.S. Nur-Azura, M.Z. Zaman, *International Food Research Journal*, **2013**, 20, 1511.
3. S.J. Culp, F.A. Beland, *Journal of American College Toxicology*, **1996**, 15, 219.
4. S. Wang., E. Ariyanto, *Journal of Colloid and Interface Science*, **2007**, 314, 25.
5. S. Arellano-Cárdenas, S. López-Cortez, M.I. Cornejo-Mazón, J.C. Mares-Gutiérrez, *Applied Surface Science*, **2013**, 280, 74.
6. T. Bhagavathi Pushpa, J. Vijayaraghavan, S.J. Sardhar Basha V. Sekaran K. Vijayaraghavan, J. Jegan *Ecotoxicology and Environmental Safety*, **2015**, 118, 177.

7. C. Akmil-Basar, Y. Onal, T. Kilicer D. Eren, *Journal of Hazardous Materials*, **2005**, B127, 73.
8. S.Hajati, M. Ghaedi, S. Yaghoubi, *Journal of Industrial and Engineering Chemistry*, **2015**, 21, 760.
9. I. Ghouma, M. Jeguirim S. Dorge, L. Limousy, C. Matei Ghimbeu, A. Ouederni, *Comptes Rendus Chimie*, **2015**, 18, 63.
10. P. Nowicki, J. Kazmierczak, R. Pietrzak, *Powder Technology*, **2015**, 269, 312.
11. E.J. Lara-Vásquez, M. Solache-Ríos, E. Gutiérrez-Segur, *Journal of Environmental Chemical Engineering*, **2016**, 4, 1594.
12. F. Hemmati, R. Norouzbeigi, F. Sarbisheh, H. Shayesteh, *Journal of the Taiwan Institute of Chemical Engineers*, **2016**, 58, 482.
13. H. Saygılı, F. Güzel, *Chemical Engineering Research and Design*, **2015**, 100, 27.
14. S. Banerjee, G.C. Sharma, R.K. Gautam, M.C. Chattopadhyaya, S.N. Upadhyay, Y.C. Sharma, *Journal of Molecular Liquids*, **2016**, 213, 162.
15. W.-T. Tsaia, H.-R. Chen, *Journal of Hazardous Materials*, **2010**, 175, 844.
16. L. Pereira, M. Alves, *Dyes-Environmental Impact and Remediation in "Environmental Protection Strategies for Sustainable Development Strategies for Sustainability series"* A. Malik and E. Grohmann eds. Springer, New York, **2012**, 111-162.
17. A. Sartape, A. Mandhare, V. Jadhav, P. Raut, M. Anuse, S. Kolekar, *Arabian Journal of Chemistry*, **2014**, doi.org/10.1016/j.arabjc.2013.12.019.
18. V. K. Garg, R. Kumar, R. Gupta, *Dyes and Pigments*, **2004**, 62, 1.
19. A.M. Aljeboree, A.N. Alshirifi, A.F. Alkaim, *Arabian Journal of Chemistry*, **2014**, doi.org/10.1016/j.arabjc.2013.12.019.
20. K. Reena, M. Goyal, M. Bhagat, G. Chaudhary, M. Sharma, *Indian Journal of Chemical Technology*, **2013**, 20, 87.
21. R.W. Sabnis, *Handbook of Acid-Base Indicators*, CRC Press, Boca Raton, **2007**, 212.
22. A.O. Dada, A.P. Olalekan, A.M. Olatunya, O. Dada, *Journal of Applied Chemistry*, **2012**, 3, 38.
23. D. Fatih, *Environmental Progress & Sustainable Energy*, **2015**, DOI 10.1002/ep.
24. J.C. Igwe, *Terrestrial and Aquatic Environmental Toxicology*, **2007**, 1, 60.
25. T. Bhagavathi, J. Vijayaraghavan, S. Sardhar, V. Sekaran, *Ecotoxicology and Environmental Safety*, **2015**, 118, 177.
26. S. Lagergren, *Kungliga Svenska Vetenskapskad. Handl.*, **1898**, 24, 1.
27. J.R. Njimou, A. Măicăneanu, C. Indolean, C. Péguy Nanseu-Njiki, E. Ngameni, *Environmental Technology*, **2016**, 37(11), 1369.
28. M. Hema, S. Arivoli, *Journal of Applied Science and Environment*, **2008**, 12, 43.
29. T.K. Sen, S. Afroze, H.M. Ang, *Water Air Soil Pollution*, **2011**, 499.
30. Y. S. Ho, G. McKay, *Process Biochem.* **1999**, 34, 451.
31. S. Burcă, A. Măicăneanu, C. Indolean, *Rev. Roum. Chim.*, **2015**, 60(11), in press.
32. W.J. Weber, J.C. Morris, *Journal of the Sanitary Engineering Division*, **1963**, 89, 31.
33. J.B. Boyd, M.D. Golino, K.E. Shawk, C.J. Osgood, M.M. Green, *Genetics*, **1981**, 97, 607.

*Dedicated to Professor Luminița Silaghi-Dumitrescu
on the occasion of her 65th anniversary*

PHYSICO-CHEMICAL PROPERTIES AND CRYSTAL VIOLET ADSORPTION PERFORMANCES OF H₃PO₄ - MODIFIED MANGO SEEDS KERNEL

GHISLAIN ARNAUD MOUTHE ANOMBOGO^{a,b,c},
ANDRADA MĂICĂNEANU^{b,*}, JEAN BAPTISTE BIKE MBAH^a,
CHRISDEL CHANCELICE NDJEUMI^{a,b,c}, LIVIU COSMIN COTEȚ^b,
RICHARD KAMGA^a

ABSTRACT. This study investigated the removal of Crystal Violet (CV) from aqueous solutions using H₃PO₄-modified mango seeds kernel (H₃PO₄-MSK). The adsorbent was characterized using elemental analysis, thermal analysis (TGA), scanning electron microscopy (SEM), specific surface area and pore size distribution (BET) and Fourier Transformed Infrared Analysis (FTIR). X-ray diffraction (XRD) analysis showed that H₃PO₄-MSK is a type II cellulose crystal structure, while SEM and BET analysis confirmed the macroporosity of the adsorbent. The removal efficiency of CV increased with an increase in adsorbent quantity and temperature. The adsorption capacities increased from 23.94 to 87.23 mg/g for an increase in temperature from 30 to 50°C. Adsorption kinetics analysis indicated that pseudo-second-order and Elovich equations fitted very well the adsorption of CV onto H₃PO₄-MSK. The adsorption process followed the Temkin and Langmuir isotherm models. Isotherm modelling showed that CV is loosely bound to H₃PO₄-MSK. Further thermodynamic analysis revealed that the removal of CV from aqueous solution by H₃PO₄-MSK was a spontaneous and endothermic process. The proposed adsorption mechanism involves -OH, -NH₂ and -COOH groups from the H₃PO₄-MSK surface.

Key words: *H₃PO₄-modified mango seeds kernel, adsorption, Crystal Violet, kinetics, equilibrium, thermodynamics*

^a *Laboratoire des Matériaux et Chimie Industrielle Inorganique, National Advanced School of Agro-Industrial Sciences, University of Ngaoundere, P.O. BOX 455 Ngaoundere, Cameroon.*

^b *Department of Chemical Engineering, Babeş-Bolyai University, 11 Arany Janos st., Cluj-Napoca, RO-400028, Romania.*

^c *Department of Environmental Sciences, Higher Institute of the Sahel, University of Maroua, P.O. BOX 46 Maroua, Cameroon*

*Corresponding author: andrada@chem.ubbcluj.ro

INTRODUCTION

Contamination of water is a worldwide environmental concern. This contamination is generated by urbanization, agriculture and industries, and particularly, in case of dyes, textile industries [1]. Textile industry is one of the main industries in Cameroon. This industry produces a large amount of wastewater which contain high amount of coloring dyes. Many methods have been developed to remove organic and inorganic pollutants from water. They include coagulation-flocculation [2,3], chemical oxidation [4-6], adsorption [7-9], etc. Among these methods, adsorption is considered to be easy to use, low cost and with high efficiency in wastewater treatment [7,8].

Many adsorbents have been used for the removal of undesirable substances from aqueous solution [10-13]. Among these adsorbents, activated carbon is found to be the most efficient. However, the high cost of production and of regeneration of activated carbon limits its use as adsorbent and encourage its substitution by low cost materials. Recent studies have demonstrated that a wide variety of low cost adsorbents, such as agricultural residues, can be employed, with minimum treatment, as biosorbents for the removal of organic and inorganic pollutants from wastewaters [14-16]. The implication of untreated fruit and vegetable wastes as adsorbents tends to generate several problems such as low adsorption, high Chemical Oxygen Demand (COD) and Biochemical Oxygen Demand (BOD) as well as total organic carbon due to release of soluble organic compounds from the plant materials, which eventually leads to depletion of oxygen content in water and threaten aquatic life. Therefore, plant wastes need to be modified or treated prior to their use in water purification. Chemical modifications involve treatment of the adsorbents with an array of chemicals for the elimination of undesired substances, enhancement of binding groups, elimination of inhibiting groups and graft copolymerization [17].

A recent study indicated that mango leaves, pits, seeds and husks are potential adsorbents for the removal of dyes from aqueous solutions [18-22]. Cameroon is an important producer of mango (*Mangifera Indica*) in Central Africa Region [23, 24] and the waste residues of this fruit are abundant. These residues can be used with minimum treatment as adsorbent for textile dye removal from aqueous solution. The purpose of this work was to study the physico-chemical characteristics of H_3PO_4 -modified mango seeds kernel (Kent specie), H_3PO_4 -MSK, and their use for the removal of Crystal Violet (CV) from aqueous solution.

2. RESULTS AND DISCUSSION

Physico-chemical characterization of H₃PO₄-MSK

Elemental analysis. Carbon, hydrogen nitrogen and oxygen content of the H₃PO₄-MSK were determined to be as follows C: 56.03%, H: 5.21%, N: 2,53% and O: 36.23%. These values are similar to those usually found in lignocellulosic materials [18,25,26].

Thermal analysis. The TG curve for H₃PO₄-MSK showed three distinct patterns of weight loss (Fig. 1). In the temperature range of 25 to 160°C there is a gradual weight loss, in the range of 160 to 900°C there is a steep weight loss and a continuous decrease of weight is observed at temperature higher than 900°C. Associated numerical values of these weight losses are presented in Table 1. DTG curve showed two main endothermic peaks. The first peak between 25 and 160°C corresponds to the H₃PO₄-MSK powder dehydration. The second peak between 160°C and 900°C with a maximum at 372°C is an overlapping peak with two shoulders observed at 240°C and 320°C. Many phenomena are associated to this second peak. These phenomena could be evaporation of water condensed in the pores, evaporation of volatile organic compounds, dehydroxylation and degradation of H₃PO₄-MSK powder. The peak at 372°C could be associated with the degradation of cellulose, while those appearing at 240 and 320°C could be associated to the degradation of starch and lignin respectively [18,20].

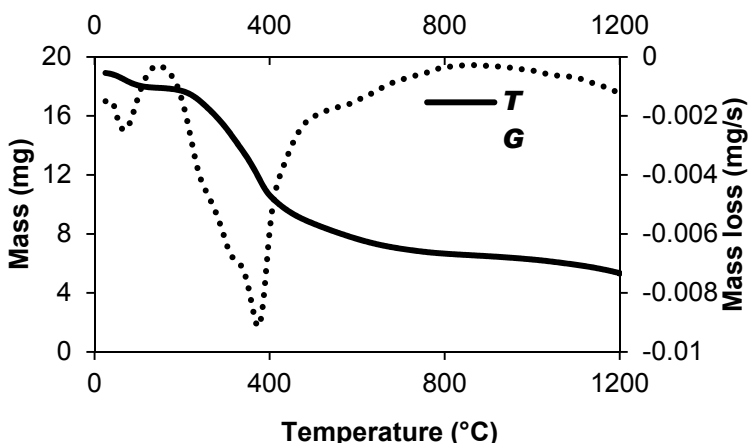
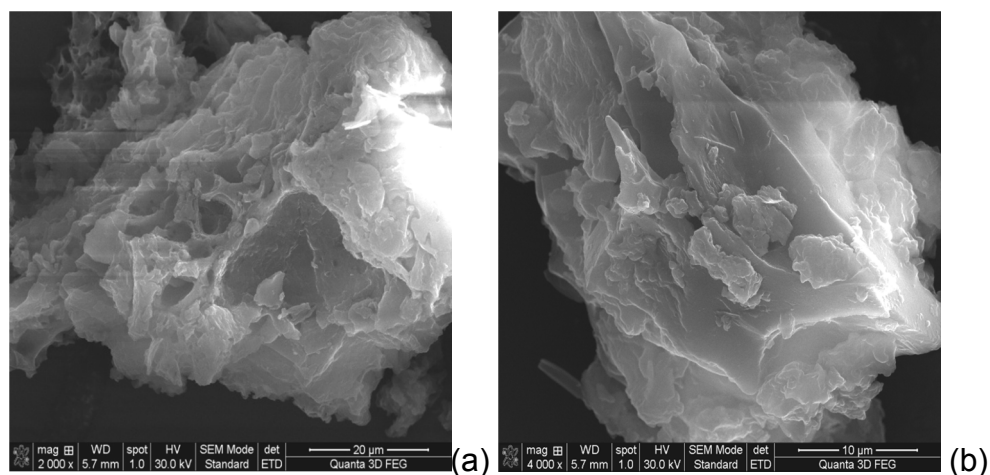


Figure 1. TG and DTG graphs of H₃PO₄-MSK.

Table 1. Thermogravimetric and derivative analysis (TG and DTG) of H₃PO₄-MSK.

Amount (mg)	Total mass loss (%)	Temperature interval (°C)	Partial mass loss (%)	T _{max} (°C)
18.91	71.4	25 - 160	5.2	67
		160 - 900	60.3	372
		900 - 1200	5.9	Continuous

Structural analysis. SEM micrographs of H₃PO₄-MSK are presented in Fig 2. Images showed a lamellate structure (Fig 2a) and a heterogeneous surface of the H₃PO₄-MSK sample (Fig 2b).

**Figure 2.** SEM micrographs of H₃PO₄-MSK.

Morpho-structural properties of H₃PO₄-MSK. The specific volume and specific surface area values of H₃PO₄-MSK are 10.24 cm³/g and the BET surface 44.57 m²/g, respectively.

XRD analysis. The XRD studies showed that the apparently amorphous material presents a crystalline structure even if it does not present properties like angle and crystal face usually associated to the crystal structure [27]. The diffraction patterns of H₃PO₄-MSK exhibited a mixture of polymorphs I and cellulose II, with a remarkable predominance of type II cellulose (Fig. 3). The

presence of type II cellulose is reflected by peaks at $2\theta = 19.40^\circ$ (plane 100) and 21.57° (plane 002) [28]. Reticular distances were 4.57 and 4.11 Å, respectively. The presence of type II cellulose in this work is associated with the regeneration of cellulose after hydrolysis.

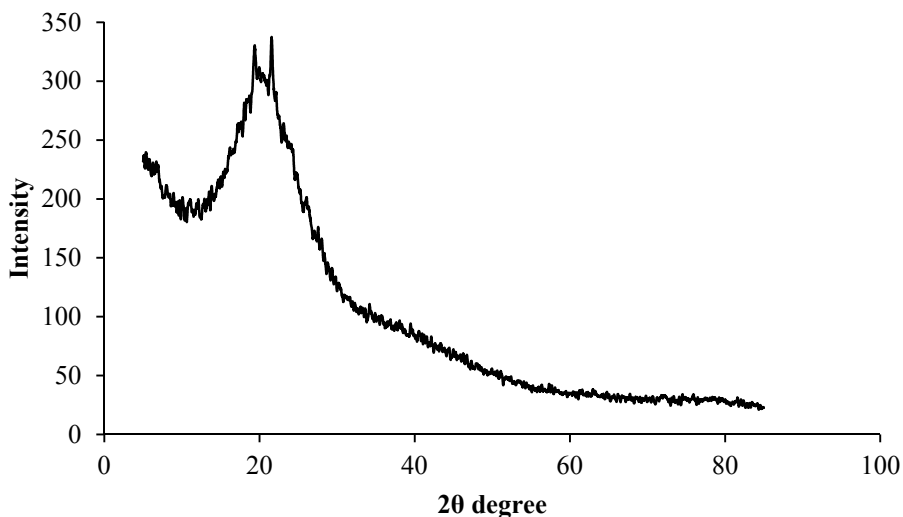


Figure 3. XRD diffractogram of H₃PO₄-MSK.

Surface chemistry. The FTIR spectral analysis is important to identify the different functional groups of the adsorbent surface. Peaks appearing in the FTIR spectrum of MSK (Fig. 4a) and H₃PO₄-MSK (Fig. 4a) were assigned to various chemical groups and bonds in accordance with their respective wavenumber as reported in the literature. The FTIR spectral of MSK and H₃PO₄-MSK are very similar. However, at low wavelengths ($<1800\text{ cm}^{-1}$) the spectra of MSK, have its peaks more intense than those of H₃PO₄-MSK ones. This difference can be attributed to the presence of hydrogen bonds among substances present in the crude mango seeds kernel. H₃PO₄ treatment of mango seeds leads to the removal of some fatty acids compounds and to the rupture of some H-bonds. The region at high wavelengths, between 3000 cm^{-1} and 3400 cm^{-1} showed a broad and strong band stretch, indicative of the presence of $-\text{NH}_2$ groups and free or hydrogen bonded O-H groups [29]. The narrow peaks at 2920.61 cm^{-1} and 2851.54 cm^{-1} showed the asymmetric C-H bond of methyl and methylene groups [30] and N-H vibration, respectively. The peak at 1772.19 cm^{-1} can be attributed to unionized C-O stretching of the carboxylic acid. The peak at 1650.97 cm^{-1} was attributed to COO^- , C=O and C-N peptidic bond of proteins [31]. The

peak at 1455.12 cm^{-1} , was correlated with the symmetric bending of CH_3 [32]. The bands at 1211.16 cm^{-1} might be attributed to phosphonate (P-OH) group stretching [33,34]. The bands appearing between 950 and 1200 cm^{-1} might be attributed to C-O group stretching [32]. We noticed that peaks at 1211.16 , 1772.29 , 285.54 and 2920.61 cm^{-1} are strong for H_3PO_4 -MSK. It can be thereby noted that the IR spectrum of the powdered MSK and H_3PO_4 -MSK supported the presence of O-H , COOH , $\text{C}=\text{O}$, C-N , C-H , C-O , $-\text{NH}_2$ and P-OH as functional groups. The diversity of functional groups indicated the presence of cellulose, lignin, starch and proteins [30].

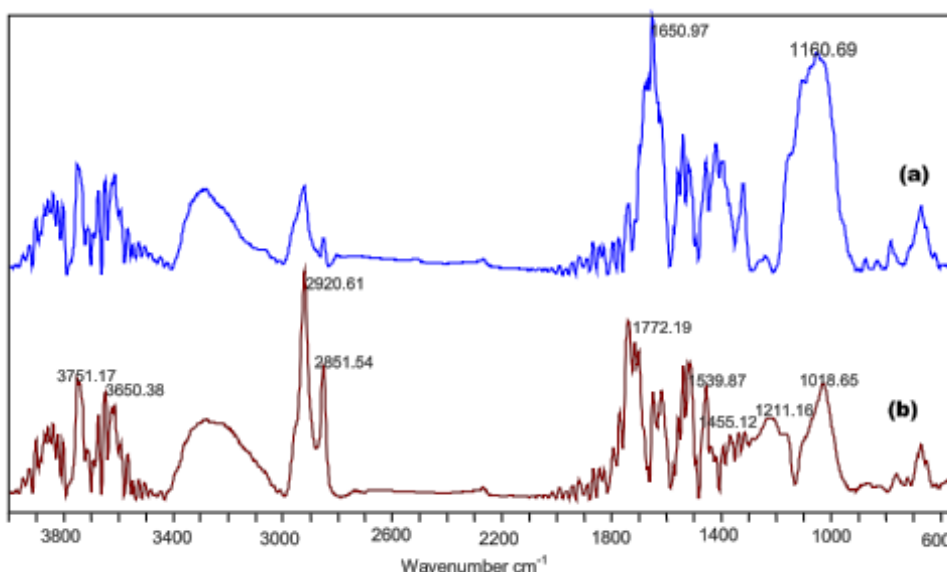


Figure 4. FTIR spectra of (a) crude MSK and (b) H_3PO_4 -MSK.

Point of zero charge and pH influence. The pH where, the sum of charges at the surface of an adsorbent are equal to zero, is generally known as the point of zero charge (pH_{PZC}). The pH_{PZC} of H_3PO_4 -MSK is 5.4 as presented in the Fig. 5. At $\text{pH} > \text{pH}_{\text{PZC}}$ the adsorbent is negatively charged and the adsorbed species are positively charged. Such a situation improves the electrostatic attraction between the adsorbate and the negatively charged surface of the adsorbent. At $\text{pH} < \text{pH}_{\text{PZC}}$ the surface of the adsorbent is positively charged.

Data presented in the Fig. 6 show the influence of the pH on the CV adsorption onto H_3PO_4 -MSK. The adsorbed amount presents two major domains. When the pH is between 3 and 8 the adsorbed amount increased,

while when the pH is higher than 8 the adsorbed amount decreased. The increase of the amount adsorbed with the pH indicates a weak electrostatic attraction during the adsorption process. If the electrostatic attraction was strong, we would have had an interruption of the evolution of the amount adsorbed at pH 5.4 which is the point of zero charge. This situation is unfavorable for electrostatic attraction. This increase of the adsorbed amount suggests that the adsorption could also involve surface complexation.

The formed complex might be instable at pH greater than 8, which leads to the decrease on the adsorbed amount [36].

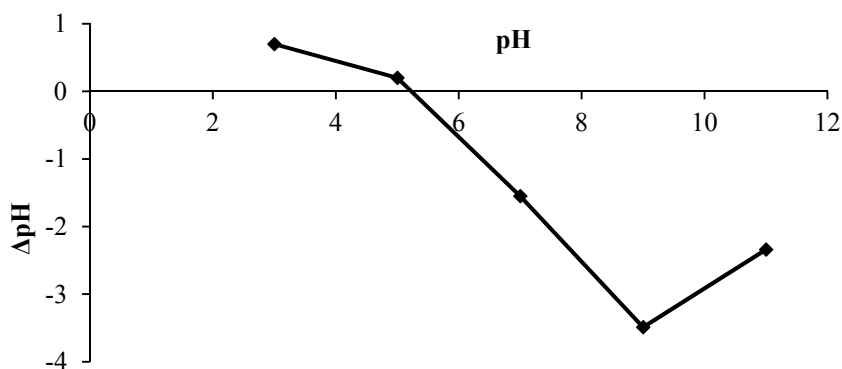


Figure 5. H_3PO_4 -MSK point of zero charge.

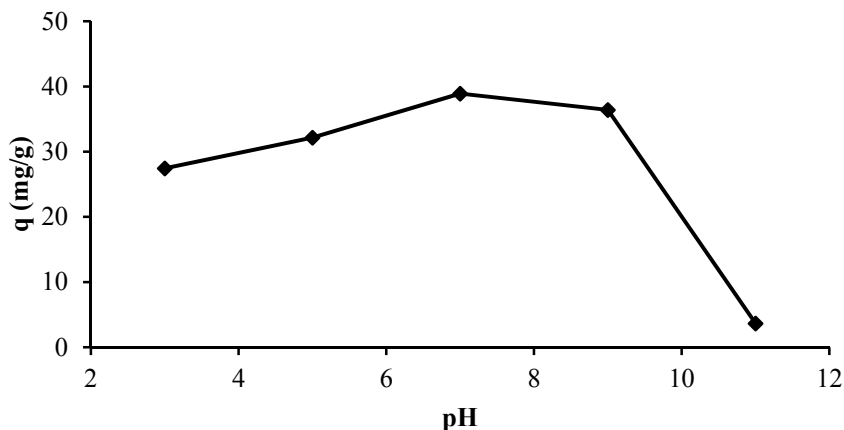


Figure 6. Effect of the pH on the CV adsorption on H_3PO_4 -MSK. (50 mg/L, 25°C, 0.1g, 240 min)

Kinetic studies

Effect of adsorbent quantity. The adsorption of CV is relatively fast in the first 50-100 min, then the adsorption rate decreases and progresses much slower thereafter towards the equilibrium (240 min), irrespective to the adsorbent quantity, (Fig. 7). The amount of CV adsorbed per gram of adsorbent, decreases as the adsorbent quantity increases (Fig 7a). This shows that surface diffusion became rate-determining step due to particle agglomeration, which leads to difficult access to the adsorption sites. The relative amount of CV adsorbed at equilibrium is 78, 85 and 93% for 0.1, 0.2 and 0.3 g of adsorbent, respectively (Fig 7b). This indicates that a better efficiency will be obtained if CV solution would be treated successively with 0.1 g of adsorbent than one step treatment with 0.3 g of adsorbent.

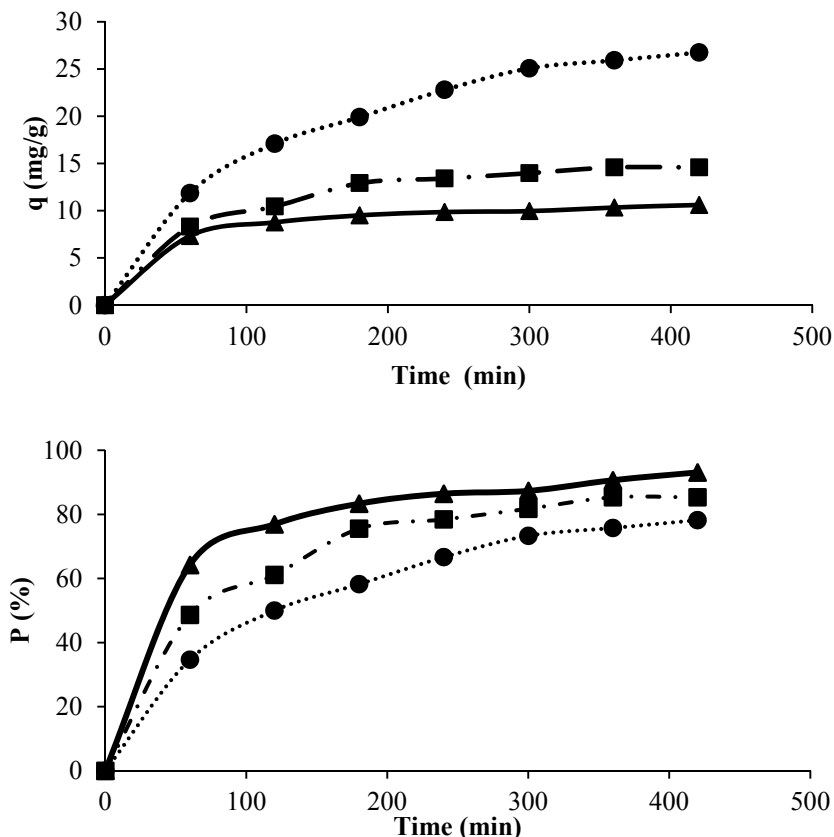


Figure 7. Adsorption kinetics of CV onto H₃PO₄-MSK (a) adsorbed amount and (b) relative amount adsorbed, for different adsorbent quantities, ●0.1 g, ■0.2 g and ▲0.3 g (50 mg/L, 25°C, pH 6).

Kinetic modeling. In order to analyze the adsorption kinetics of CV, the pseudo-first- and pseudo-second-order and simple Elovich models were applied to the experimental data.

The pseudo-first-order rate equation or Lagergren equation is derived on the assumption of one step reaction [37] and is expressed as:

$$\ln(q_e - q_t) = \ln q_e - k_1 t \quad (3)$$

where, q_e is the amount of dye adsorbed at equilibrium (mg/g), q_t is the amount of dye adsorbed at time t (mg/g), k_1 is the pseudo-first-order reaction rate constant (1/min).

Pseudo-second-order equation based on two step reaction is usually expressed in the form [38,39]:

$$\frac{t}{q_t} = \frac{1}{k_2 q_e^2} + \frac{t}{q_e} \quad (4)$$

where, k_2 is the pseudo-second-order reaction rate equilibrium constant (g/mg·min).

The simple Elovich model may be expressed in the form:

$$q_t = A + B \ln t \quad (5)$$

where, A and B (mg/g·min) are Elovich constants, related to the initial adsorption rate and to the number of available site for adsorption. B is related to the extent of surface coverage and activation energy for chemisorption.

Based on the fact that pseudo-second-order equation is derived on the assumption of a two-step reaction, we concluded that CV adsorption takes place as a two-step reaction scheme. The pseudo-second-order model is build based on the assumption that the rate-controlling step is chemical adsorption involving valence force by sharing or exchange of electrons between adsorbent and adsorbate [40]. Therefore, a satisfactory fitness of this model suggested that chemisorption was the rate-controlling step [41]. A and B parameters derived from Elovich equation are used to estimate the reaction rates. It was suggested that an increase in A value and/or decrease in B value would increase the rate of the adsorption process. The obtained R^2 values for H₃PO₄-MSK for all the dosage were high, suggesting that Elovich model describes this adsorption system.

The estimated model and the related statistic parameters for CV adsorption onto H₃PO₄-MSK are presented in Table 2. Based on linear regression analysis, correlation coefficient (R^2) values, we concluded that the kinetics of CV onto the considered adsorbent is well described by pseudo-second-order and Elovich models. The amount of adsorbed CV

determined from the two mentioned equations fitted very well with the experimental values (Table 2).

The negative value of k_1 indicated that the pseudo-first-order model cannot be applied to describe the adsorption of CV on H_3PO_4 -MSK.

Intra-particle diffusion. The common diffusion model usually designated as intra particle model is expressed as [42]:

$$q_t = k_{int}t^{1/2} + D \quad (6)$$

where, k_{int} is the intra-particle diffusion rate constant ($mg/L \cdot min^{1/2}$) and D the constant. The fitting of the experimental data with this model was checked using so-called Weber and Morris plot of q versus $t^{1/2}$. According to intra-particle diffusion model, a plot of uptake, q versus the square root of time, $t^{1/2}$, should be linear if intra-particle diffusion is involved in the adsorption system and if this line passes through the origin, then intra-particle diffusion is the rate controlling step [43]. In this study, the relative plot of q and $t^{1/2}$ obtained for Crystal Violet dye adsorption on H_3PO_4 -MSK did not go through the origin. Also it was indicative of some degree of boundary layer control and this further indicated that the intra-particle diffusion was not the only rate controlling step; other mechanisms were simultaneously operating during the adsorption of CV on H_3PO_4 -MSK.

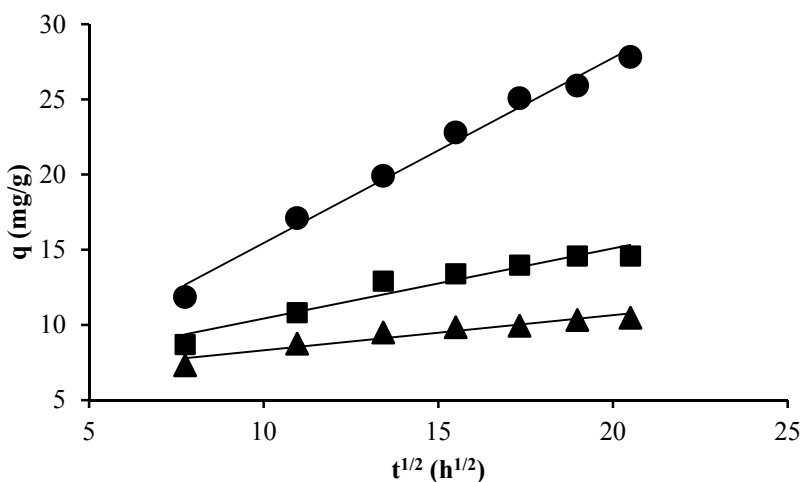


Figure 8. Intra-particle diffusion model for CV adsorption onto H_3PO_4 -MSK, for different adsorbent quantities, ●0.1 g, ■0.2 g and ▲0.3 g (50 mg/L, 25°C, pH 6).

Table 2. Kinetic parameters for the adsorption of CV onto H₃PO₄-MSK (50 mg/L, 25°C, pH 6); q_{exp} and q_{cal} are the experimental and calculated amount of CV adsorbed per gram of adsorbent

Kinetic models	Parameters	Experiment		
		0.1 g	0.2 g	0.3 g
Pseudo-first-order	q _{exp} (mg/g)	22,80	13,40	9,80
	k ₁ × 10 ⁻² (1/min)	-0.15	-0.07	-0.06
	q _e (mg/g)	38.53	25.39	15.50
	q _{cal} (mg/g)	22.61	11.17	7.22
	R ²	0.9748	0.8744	0.8633
Pseudo-second-order	k ₂ × 10 ⁻² (min·g/mg)	0.70	1.70	3.00
	q _e (mg/g)	0.52	0.53	0.57
	q _{cal} (mg/g)	23.16	13.47	9.87
	R ²	0.9956	0.9987	0.9960
Elovich	A	-21.92	-4.10	1.01
	B	8.17	3.17	1.59
	q _{cal} (mg/g)	22.87	13.25	9.73
	R ²	0.99	0.99	0.99
Intra-particle diffusion	k _{int} (1/min)	1.23	0.47	0.23
	D	3.14	5.75	5.98
	q _{cal} (mg/g)	22.21	12.98	9.6
	R ²	0.9955	0.9782	0.9776

Equilibrium studies

Isotherm modeling. Adsorption isotherms modeling are prerequisites to understand the nature of the interaction between adsorbate and the adsorbent. In order to successfully represent the equilibrium adsorption behavior, it is important to have a satisfactory description of the equation state between the two phases of the adsorption system. Three well known phenomenological equations were tested to fit the experimental data, namely Langmuir, Freundlich and Temkin equations [42,44]. They are expressed as follows:

$$\text{Langmuir equation: } \frac{1}{q_e} = \frac{1}{q_{\max} K_L} \cdot \frac{1}{C_e} + \frac{1}{q_{\max}} \quad (7)$$

$$\text{Freundlich equation: } \ln q_e = \ln K_F + \frac{1}{n} \ln C_e \quad (8)$$

$$\text{Temkin equation: } q_e = B \ln A + B \ln C_e \quad (9)$$

where q_e , q_{max} and C_e , are, the amount adsorbed at equilibrium (mg/g), the amount adsorbed at the monolayer (mg/g) and the equilibrium concentration of CV (mg/L), respectively. K_L is the Langmuir adsorption equilibrium constant (L/mg), K_F is the Freundlich constant related to the adsorption capacity ($mg^{(1-1/n)} L^{1/n}/g$) and n is the Freundlich constant related to the adsorption energy. B is Temkin constant related to adsorption energy (J/mol) and A is the Temkin constant (L/mg).

Considering the correlation coefficient (R^2) values, Table 3, the following series was obtained for CV adsorption onto H_3PO_4 -MSK: Langmuir > Temkin > Freundlich. The adsorption of CV on H_3PO_4 -MSK is favorable as n takes value in the range of 1 to 10. However, the small value of B indicates that CV is loosely bond to H_3PO_4 -MSK, therefore the adsorption is physical in nature. The essential characteristic of Langmuir isotherm can be expressed in terms of dimensionless separation factor of equilibrium parameter, R_L , defined by the equation [44]:

$$R_L = \frac{1}{1 + K_L C_0} \quad (10)$$

where, C_0 is the highest dye concentration in solution (mg/L). The values of R_L indicates the type of isotherm to be irreversible ($R_L=0$), favorable ($0 < R_L < 1$), linear ($R_L=1$) or unfavorable ($R_L > 1$). The calculated value of R_L for the highest concentration of 300 mg/L obtained for H_3PO_4 -MSK indicates (Table 3) that is a suitable adsorbent for CV removal from aqueous solutions.

Table 3. Isotherms parameter values for the adsorption of CV onto H_3PO_4 -MSK (50-300 mg/L, 0.1 g, pH 6).

Isotherm models	Constants	Values
Langmuir	K_L (L/mg)	0.38
	q_{max} (mg/g)	112.44
	R_L	0.0087
	R^2	0.9907
Freundlich	K_F ($mg^{(1-1/n)} L^{1/n}/g$)	34.48
	n	2.40
	R^2	0.9474
Temkin	A (L/mg)	34.93
	B (J/mol)	21.72
	R^2	0.9849

Fig. 9 shows the plot of the amounts of CV adsorbed versus equilibrium dye concentrations. The amount of dye adsorbed increased from 23.94 to 87.25 mg/g for an increase in initial dye concentration from 50-300 mg/L, whereas the percent dye removal decreases from 79 to 33% for an increase in initial dye concentration from 50-300 mg/L. The adsorption isotherm has the L form considering Giles classification [45].

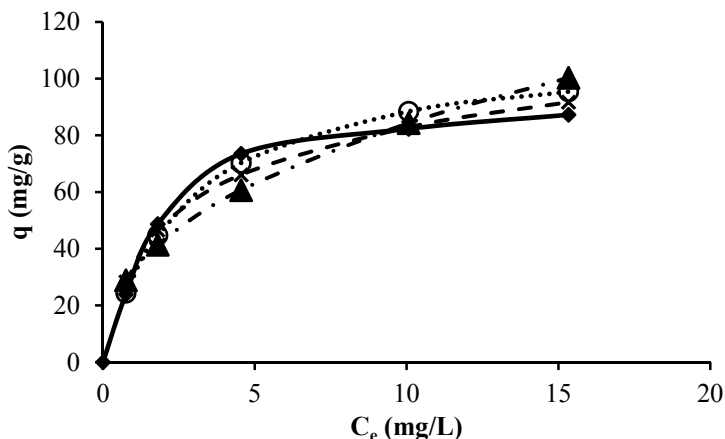


Figure 9. Isotherms of CV adsorption onto H₃PO₄-MSK (◆Experimental values, ○Langmuir, ▲Freundlich; ×Temkin).

Thermodynamics

Effect of temperature. Experiments were performed at different temperatures 30, 40 and 50°C for the initial concentration of 50 mg/L. The CV adsorbed amount (mg/L) increases as temperature increases (Fig. 10). The results showed that the adsorption was endothermic in nature. Since adsorbent is porous and CV diffusion in pores plays an important role in the adsorption process, increase in the adsorption with the rise of temperature may be diffusion controlled, which is an endothermic process, i.e. the rise of temperatures favors the CV transport within the pores of the adsorbent. The increased adsorption with the rise of temperature is also due to the increase in the number of the adsorption sites generated because of the breaking of some internal bonds near the edge of the active surface sites of the adsorbent [46,47].

Thermodynamic parameters. Standard thermodynamic parameters such as change in free energy (ΔG°), enthalpy (ΔH°) and entropy (ΔS°) were calculated using the following equations:

$$K_c = \frac{C_a}{C_e} \quad (11)$$

$$\Delta G^\circ = -RT \ln K_c \quad (12)$$

$$\ln K_c = -\frac{\Delta H^\circ}{RT} + \frac{\Delta S^\circ}{R} \quad (13)$$

where, K_c is the equilibrium constant, C_a and C_e are the equilibrium concentration (mg/L) of CV on the adsorbent and in solution, respectively, T is the temperature (K) and R is the universal gas constant (kJ/K·mol). ΔH° and ΔS° were obtained from the slope and the intercept of van't Hoff plot of $\ln K_c$ versus $1/T$ and values are presented in Table 4. The negative free energy values indicate that the adsorption process is spontaneous. It was also noted a decrease in the free energy values with an increase in temperature corresponding to an increase of the adsorbed CV amount. The positive values of the enthalpy further confirm the endothermic nature of the process whereas the positive values of entropy reflect good affinity of the dye towards H_3PO_4 -MSK [48,49]. When the CV is adsorbed on the surface of the adsorbent, water molecules previously bonded to the dye cation are released and dispersed in the solution, which leads to the increase of the entropy [50].

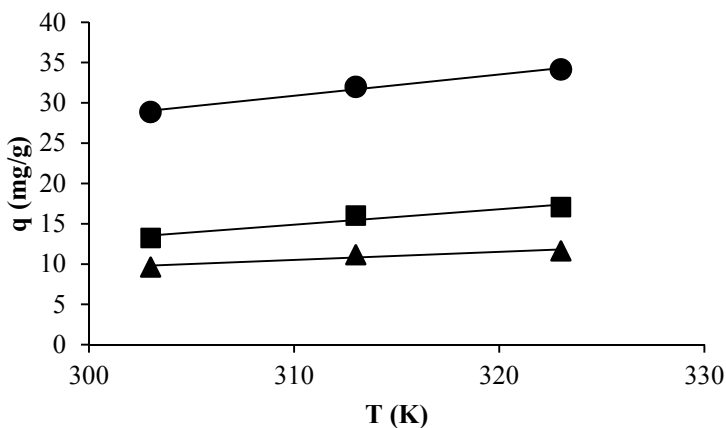


Figure 10: Effect of temperature on the adsorption of CV onto H_3PO_4 -MSK at 25°C, 50mg/L, time 240 min, pH 6 (●0.1g, ■0.2g and ▲0.3g).

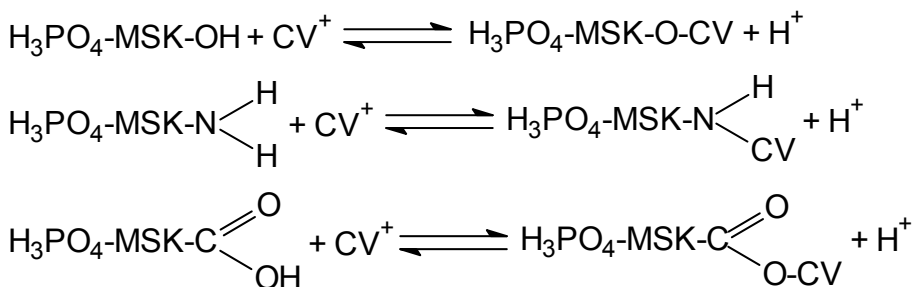
Table 4. Thermodynamic parameters for CV adsorption onto H_3PO_4 -MSK.

Samples	R^2	Temperature (K)	ΔG° (kJ/mol)	ΔH° (J/mol)	ΔS° (J/mol·K)
0.1 g	0.96	303	-4.19	142.86	482.95
		313	-6.79		
		323	-13.94		
0.2 g	0.98	303	-3.07	170.06	569.41
		313	-6.88		
		323	-14.55		
0.3 g	0.98	303	-3.20	185.29	622.28
		313	-7.55		
		323	-14.34		

Adsorption mechanism

The binding mechanisms of dyes by adsorption could be explained by the physical and chemical interactions between cell wall ligands and adsorbates by ion exchange, complexation, coordination and micro-precipitation. The diffusion of the dye from the bulk solution to active sites of the adsorbents occurs predominantly by passive transport mechanisms, while various functional groups such as carboxyl, hydroxyl, amino and phosphate existing on the cell wall can bind the dye molecules. The adsorption dynamics can be described by the following three consecutive steps, which are as follows [22]: transport of the dye molecules from bulk solution through the liquid film to the adsorbent exterior surface, migration on the adsorbent surface and diffusion into the pore of the adsorbent, and adsorption on the interior pores surfaces of the adsorbent.

The last step is considered to be an equilibrium reaction. Out of three steps, the third step is assumed to be rapid. Therefore, the adsorption of CV onto H₃PO₄-MSK is probably controlled by a two-step reaction scheme. The adsorption of CV onto H₃PO₄-MSK was proposed to take place according to the following chemical mechanism:



CONCLUSION

The ability of H₃PO₄-MSK to retain dyes with high molecular weight was investigated for CV dye using kinetic, equilibrium and thermodynamic models. The kinetics of CV onto H₃PO₄-MSK was studied using the pseudo-first-order, pseudo-second-order and Elovich kinetic models. The results indicated that the pseudo-second-order and Elovich models provided the best correlation with the experimental data. Then, CV adsorption rate is governed by two-step reaction scheme. The adsorption process followed well Temkin and Langmuir models. Calculated thermodynamic parameters

indicated that the adsorption in this system was a spontaneous and endothermic process. These results suggest that H_3PO_4 -MSK is a potential low-cost adsorbent for dye removal from industrial wastewaters.

EXPERIMENTAL

Material

Mango seeds kernel (MSK) used as adsorbent in this study was collected from Ngaoundere a city, in the Adamawa Region, Cameroon. MSK was treated by concentrated phosphoric acid (H_3PO_4), then washed with deionized water and dried at $110^\circ C$ for 24 h. The dried H_3PO_4 -MSK was grounded to fine powder and sieved to a particle size $< 50\mu m$.

Crystal Violet (CV) dye was of commercial grade (M_F : $C_{25}H_{30}N_3Cl$, M_W : 408, λ_{max} : 586 nm) and it was used without further purification (Fig. 11). Stock solution was prepared by dissolving 1g of the CV powder in 1000 mL distilled water. For adsorption experiments this solution was diluted to the desired initial concentrations ranging from 50-300 mg/L. The initial solution pH was adjusted to the desired value by adding drop wise HCl, 0.1M or NaOH, 0.1M solutions.

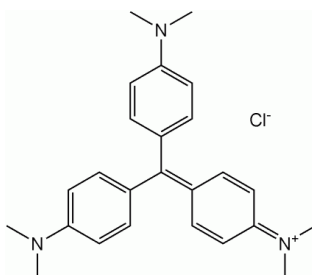


Figure 11. Structural formula of Crystal Violet.

Adsorbent characterization

Elemental analysis (C, H, N, S) was performed using a CHN CARLO ERBA EA 1108 Elemental Analyzer. The oxygen percentage was estimated by difference.

The thermal behavior of the H_3PO_4 -MSK sample was studied using a TGA/SDTA 851, $1600^\circ C$ Mettler-Toledo analyzer. Experimental conditions were as follows: initial mass of the sample was 18.91 mg, initial temperature $25^\circ C$, final temperature $800^\circ C$, heating rate of $10^\circ C/min$ and nitrogen flow of 50 mL/min. The DTG and TG curves were obtained by calculating the derivative simultaneously.

The X-ray diffraction (XRD) was used to determine the crystalline structure of the H₃PO₄-MSK sample. The X-ray diffractograms were obtained at room temperature within a 2θ ranging from 5 to 40 and a scan rate of 1°/min. The equipment used was a Bruker Advance D8 diffractometer, operating at a power of 40 kV with a current of 30 mA and Cu K α radiation (1.5406 Å). Before performing the analysis the sample was dried at 50°C for 12 h in an air-circulating oven.

The surface structure of H₃PO₄-MSK was analyzed using Scanning Electron Microscopy (SEM Quanta 2000 - Philips) at an electron acceleration voltage of 25 kV. Prior to scanning, the unloaded and dye-loaded H₃PO₄-MSK sample was mounted on a stainless steel stab with double stick tape and coated with a thin layer of gold in a high vacuum condition.

Infrared spectra were recorded using a Nicolet Magna FT-IR-750 spectrometer thoroughly mixing MSK and H₃PO₄-MSK with KBr matrix.

Specific surface area and pore specific volume for the H₃PO₄-MSK were determined by the Brunauer–Emmett–Teller (BET) method using a Sorptomatic ADP-nitrogen adsorption analyzer (Thermo Electron-Corp.). Prior to N₂ adsorption, samples were out gazed for 20 h at 105°C.

The pH of the point of zero charge (pH_{pzc}) corresponds to the pH where the sum of all the electrical charges at the surface of the adsorbent are equal to zero. pH_{pzc} determination method consist in the preparation of a solution of desired pH in the 2-11 range. HCl 0,01M solution was dropwise to a 50 mL NaCl 0,01M solution until de pH value was reached. 0,05 g of adsorbent were then added to the prepared solution. The mixture is then stirred at 50 rpm for 24 h. The pH of the solution is noted and the graph of the pH versus the variation of the pH is drawn. The value at the intersection of the obtained curve with the x-axis gives the pH_{pzc} of the adsorbent [51].

Batch adsorption experiments

A predetermined amount of H₃PO₄-MSK was added into 100 mL conical flasks filled with 25 mL of CV solution of known concentration. The flasks were then placed in a shaking water bath (50 cycles/min) at room temperature for 24 hours. The samples were then withdrawn at predetermined time interval and the residual concentration of CV was determined by UV-Visible spectroscopy. The absorbance was measure at 586 nm with 1 cm optical path length quartz cell. TG Instrument T-70 UV-Vis spectrophotometer was used for this purpose. The concentration of CV was determined from the calibration curve.

The adsorbed amount of CV per gram of adsorbent (q , in mg/g) and the relative amount adsorbed (P , in %) were expressed as:

$$q = (C_0 - C_f) \cdot \frac{V}{m} \quad (1)$$

$$P = \frac{C_0 - C_f}{C_0} \cdot 100 \quad (2)$$

where, C_0 is the initial concentration of CV (mg/L), C_f is the final concentration of CV (mg/L), V is the volume of the solution (L) and m the amount of adsorbent (g).

Statistical analysis

In order to ensure the accuracy and reliability, all experiments were performed in triplicate, and the mean values were used in data analysis. Relative standard deviations were found to be within $\pm 3\%$. Microsoft Office Excel program was employed for data processing. Linear regression analysis was employed to fit experimental data with theoretical models.

ACKNOWLEDGEMENTS

This work was carried out with financial support from the Romanian Ministry of Foreign Affairs and the Agence Universitaire de la Francophonie, Bureau of Central and Eastern Europe (BECO), Bucharest, Romania. Ghislain Arnaud MOUTHE ANOMBOGO wish to express sincere thanks to the Romanian Government for the Fellowship "EUGEN IONESCU" offered.

REFERENCES

1. J. Atchana, G.M. Simu, S.G. Hora, M.E. Grad, J.B. Tchatchueng, B.L. Benguella, R.Kamga, *Journal of Food, Agriculture & Environment*, **2011**, 9, 457.
2. G. Bogoeva-Gaceva, A. Bužarovska, B. Dimzoski, *G. U. Journal of Science*, **2008**, 21, 123.
3. A. Aygun, T. Yilmaz, *International Journal of Chemical and Environmental Engineering*, **2010**, 1, 97.
4. H. Valdes, H.P. Godoy, C.A. Zaror, *Journal of International Association of Water Pollution Research*, **2010**, 61, 2973.
5. F-R. Xiu, F-S. Zhang, *Journal of Hazardous Materials*, **2009**, 172, 1458.
6. A.R. Khataee, M. Fathinia, S. Aber, M. Zarei, *Journal of Hazardous Materials*, **2010**, 181, 886.

7. U. Singh, R.K. Kaushal, *International Journal of Technical & Non-Technical Research*, **2013**, 4, 33.
8. G.Z. Kyzas, F. Jie, K. A. Matis, *Materials*, **2013**, 6, 5131.
9. M.A. Mohammed, A. Shitu, M. A. Tadda, M. Ngabura, *International Research Journal of Environment Sciences*, **2014**, 3, 62.
10. R. Kamga R., G.J. Kayem, P.G. Rouxhet, *Journal of Colloid and Interface Science*, **2000**, 232, 198.
11. J.B. Bike Mbah, R. Kamga, J. P. Nguetnkam, J. Fanni, *European Journal of Lipid Science and Technology*, **2005**, 107, 387.
12. A. Bhatnagar, A. K. Minocha, *Indian Journal of Technology*, **2006**, 13, 203.
13. G. Bayramoglu, B. Altintas, M. Yakup Arica, *Chemical Engineering Journal*, **2009**, 152, 339.
14. G. Crini, *Journal of Biotechnology*, **2006**, 97, 1061.
15. L.S. Oliveira, A.S. Franca, in "Food Science and Technology: New Research" L.V. Greco, M.N. Bruno, editors, Nova Publishers, New York, **2008**, chapter 3.
16. A.E. Ofomaja, *Chemical Engineering Journal*, **2008**, 143, 85.
17. D. Park, Y-S. Yun, J.M. Park, *Biotechnology and Bioprocess Engineering*, **2010**, 15, 86.
18. M.P. Elizalde-Gonzalez, V. Hernandez-Montoya, *Biochemical Engineering Journal*, **2007**, 36, 230.
19. A.S. Franca, L.S. Oliveira, P.I.A. Santos, S.A Saldanha., S.A. Salum, *Journal of Biotechnology*, **2008**, 136, S655.
20. M.M. Davila-Jimenez, M.P. Elizalde-Gonzalez, V. Hernandez-Montoya, *Bioresource Technology*, **2009**, 100, 6199.
21. T. Murugan, A. Ganapathi, R. Valliappan, *E-Journal of Chemistry*, **2010**, 7, 669.
22. K.K. Vasanth, A. Kumaran, *Biochemical Engineering Journal*, **2005**, 27, 83.
23. FAO report, "Situation actuelle et perspectives à moyen terme pour les fruits tropicaux", FAO Data Base, **2004**.
24. E.B. Djantou Njantou, "Optimisation du broyage des mangues séchées (*Mangifera indica* var Kent): Influence sur les propriétés physicochimiques et fonctionnelles des poudres obtenues", Thèse de Doctorat PhD, INP de Lorraine et Université de Ngaoundéré, **2006**.
25. G.G Stavropoulos., A.A. Zabaniotou, *Microporous and Mesoporous Materials*, **2005**, 82, 79.
26. M.T Uddin, M. Rukanuzzaman, M.M.R. Khan, M.A. Islam, *Journal of Environmental Management*, **2009**, 90, 3443.
27. M.A. Henrique, H.A. Silvério, W.P. Flauzino Neto, D. Pasquini, *Journal of Environmental Management*, **2013**, 121, 202.
28. W.P. Flauzino Neto, H.A. Silverio, N.O. Dantas, D. Pasquini, *Industrial Crops and Products*, **2013**, 42, 480.
29. C.J. Duran-Valle, M. Gomez-Corzo, J. Pastor-Villegas, V. Gomez-Serrano, *Journal of Analytical and Applied Pyrolysis*, **2005**, 73, 59.
30. A. Saeed, M. Sharif, M. Iqbal, *Journal of Hazardous Materials*, **2010**, 179, 564.
31. O. Gulnaz, A. Kaya, S. Dincer, *Journal of Hazardous Materials*, **2006**, 134, 190.
32. A. Khaled, A.E. Nemr, A. El-Sikaily, O. Abdelwahab, *Journal of Hazardous Materials*, **2009**, 165, 100.

33. X.N. Li, Q.Y. Xu, G.M. Han, W.Q. Zhu, Z.H. Chen, X.B. He, *Journal of Hazardous Materials*, **2009**, 165, 469.
 34. S. Sadhasivam, S. Savitha, K. Swaminathan, F. H. Lin, *Journal of the Taiwan Institute of Chemical Engineering*, **2009**, 40, 394.
 35. W. Jianlong, Z. Xinmin, D. Decai, Z. Ding, *Journal of Biotechnology*, **2001**, 87, 273.
 36. G. Mckay, Y.S. Ho, *Process Biochemistry*, **1999**, 34, 451.
 37. R. Ansari, Z. Mosayebzadeh, A. Mohammad-Khah, *Journal of Advanced Scientific Research*, **2011**, 2, 25.
 38. P.D. Saha, S. Chakraborty, S. Chowdhury, *Colloids and Surfaces B: Biointerfaces*, **2012**, 92, 262.
 39. D.K. Mahmoud, M.A. Mohd Salleh, W.A.W. Abdul Karim, A. Idris, Z.Z. Abidin, *Chemical Engineering Journal*, **2012**, 181-182, 449.
 40. I. Kula, M. Ugurlu, H.C. Karaoglu, A. Elik, *Bioresource Technology*, 2008, 99, 492–501.
 41. Y.S. Ho, G. McKay, *Water Research*, **2000**, 34, 735–742.
 42. R. Ahmad, *Journal of Hazardous Materials*, 2009, 171, 767.
 43. W.T. Tsai, K.J. Hsien, J.M. Yang, *Journal of Colloid and Interface Science*, **2004**, 275, 428–433.
 44. K. Porkodi, K.K. Vasanth, *Journal of Hazardous Materials*, **2007**, 143, 311.
 45. G. Limousin, J.P. Gaudet, L. Charlet, S. Szenknect, V. Barthes, M. Krimissa, *Applied Geochemistry*, **2007**, 22, 249.
 46. S. Chakraborty, S. Chowdhury, P. D. Saha, *Carbohydrate Polymers*, **2011**, 86, 1533.
 47. P.D. Saha, S. Chakraborty, S. Chowdhury, *Colloids and Surfaces B: Biointerfaces*, **2012**, 92, 262.
 48. H.C. Chu, K.M. Chen, *Process Biochemistry*, **2002**, 37, 1129.
 49. R.K. Gautam, A. Mudhoo, M.C. Chattopadhyaya, *Journal of Environmental Chemical Engineering*, **2013**, 1, 1283.
 50. S. Senthilkumar, P. Kalaamani, C. V. Subburaam, *Journal of Hazardous Materials*, **2006**, 136, 800.
- P.C.C. Faria, J.J.M. Orfao, M. F. R. Pereira, *Water Resources*, **2004**, 38, 2043.

*Dedicated to Professor Luminița Silaghi-Dumitrescu
on the occasion of her 65th anniversary*

DEVELOPMENT OF THE SOUR WATER PLANT DYNAMIC SIMULATOR FOR IMPROVING DESIGN AND OPERATION

ANETTA VAIDA^a, VASILE-MIRCEA CRISTEA^{a*}

ABSTRACT. Sour water system (SWS), as vital part of refineries, is aimed to process wastewater produced during different refining processes. Sour water contains contaminated water with H₂S and NH₃ and/or alkali metals or hydrocarbon traces. The main objective of SWS is to reduce the concentration of these contaminants below undesirable level and to make possible water reuse in the refinery. H₂S is generally stripped from the sour water and sent to the Claus Unit. The paper reviews two possible designs for SWS. The first one corresponds to the traditional design of the SWS unit, while the second design uses an internal stream to heat up the feed flow. For analyzing the two different design configurations, dynamic simulators were developed in Aspen-Hysys using industrial and literature data. Different operating scenarios were tested, also involving the SWS control loops. Dynamic simulation results reveal incentives for the second analyzed design from the energy cost reduction perspective, as external need of heat utilities is diminished and this is associated to an improved separation of the contaminants.

Keywords: *sour water system, dynamic model, design, pollution, energy consumption*

INTRODUCTION

Oil and gas production use a significant amount of water. The source of water may have different origin: surface, rain, ground water, water in crude or recycled water. Figure 1 reveals the raw balance of the water in a refinery

^a *Babeş-Bolyai University, Faculty of Chemistry and Chemical Engineering, 11 Arany Janos str., RO-400028, Cluj-Napoca, Romania,*

**Corresponding author: mcristea@chem.ubbcluj.ro*

[1]. Sour water is produced by different plants, such as: crude, vacuum, catalytic cracker, delayer coker, visbreaker, hydrotreater, hydrocracker and sulphur plant units, or in the isomerization, Claus and alkylation processes [1, 2]. Sour water contains water contaminated with hydrogen sulfide (H_2S), ammonia (NH_3), traces of CO_2 , salts, phenols, caustic. Non-phenolic sour water contains exclusively H_2S and NH_3 . It is produced exclusively by hydro-treating processes and it is usually recycled in the upstream process. Phenolic sour water is generally not recycled for reuse because it contains contaminants which can undesirably affect the upstream process [3].

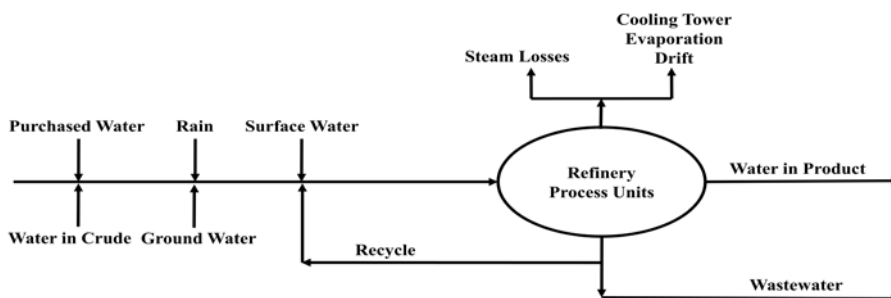


Figure 1. Water balance in a refinery [1].

The main concern with sour water is the H_2S content. Commonly, the concentration of the H_2S has to be kept below 1ppm [2, 3]. Presence of ammonia is also undesired. The treated water has to contain limited amount of NH_3 as its concentration must lie between 30-80 ppm [2-4].

The process of treating sour wastewater contains two main steps. In the first step H_2S is eliminated in a Sour Water (SW) Stripper. In the second stage the water is introduced in an absorption column where the remained NH_3 is separated. The vapor streams separated at the top of the SWS columns are sent to the Claus Unit, where the H_2S is broken down to its elemental molecules H_2 and S , for later use in other industrial processes.

Nowadays, SWS gets more attention in industrial plants [5]. The process is important because of the increasing emphasis on regulating the quality of the effluent water and saving energy [6-10].

RESULTS AND DISCUSSIONS

The paper presents two dynamic models for differently designed SWSs. The models represent the first step of the wastewater purification, which is performed in the SW Stripper. Figure 2 shows a traditional SWS design

and its schematic representation. The contaminated water from the refinery enters the Flash Drum where the gases are separated from the liquid part (water and oil). The gas is sent directly to the top of the SW Stripper. The liquid is directed by the Feed Pump to the Feed Heat Exchanger where the inlet stream is heated up to the desired temperature, using hot water as heating agent. The heated sour water is sent to the SW Stripper. During the distillation (stripping) process the dissolved H_2S and NH_3 leave at the top of the SW Stripper and the purified water at the bottom. The heat for the distillation is provided by live steam injection at the bottom of the column. High efficiency of the SW Stripper is provided by a pump around consisting in a controlled recycled flow which leaves one tray of the column, it is cooled down by an air cooler and sent back to an upper tray. The stripped water bottom product is driven by the Stripper Water Pump to a cooler and sent downstream to the absorption column for separation. This first design and model will be further referred as Model A.

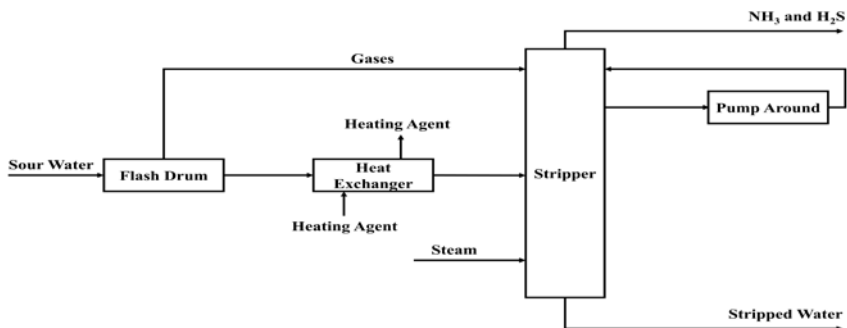


Figure 2. SWS flow sheet for Model A.

Table 1 lists the equipment of the SWS simulator.

Table 1. SWS equipment description [11].

Equipment Name	Description
SWS - V - 001	Flash Drum
SWS - P - 001A	Feed Pump
SWS - HX - 001	Feed Heat Exchanger
SWS - C - 001_TOP	SW Stripper
SWS - C - 001_MIDDLE	
SWS - C - 001_BOTTOM	
SWS - P - 003A	Pump-Around Pump
SWS - EA - 001	Pump-Around Air Cooler
SWS - P - 002A	Stripper Water Pump
SWS - EA - 002	Stripped Water Air Cooler

Figure 3 represents the second investigated design for the SWS, in which the heating agent for the Feed Heat Exchanger of Model A was replaced by the stripped water from the bottom of the SW Stripper. This new design recovers heat and is intended to spare costs with the heating agent. This second design and model will be further referred as Model B. Figure 4 presents the SWS simulator implemented in Aspen Hysys for the SWS setup described in Figure 3.

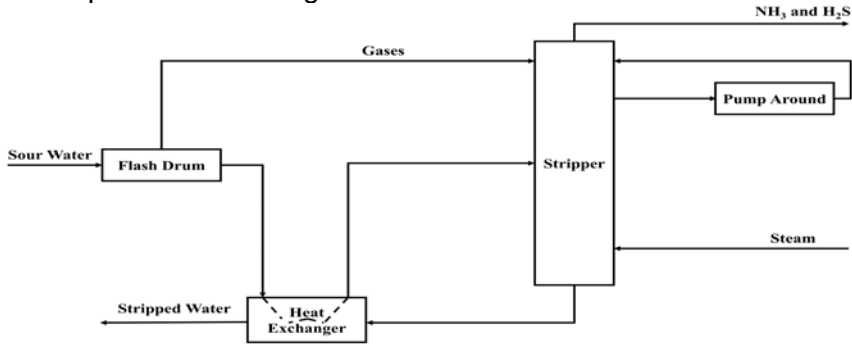


Figure 3. SWS flow sheet for Model B.

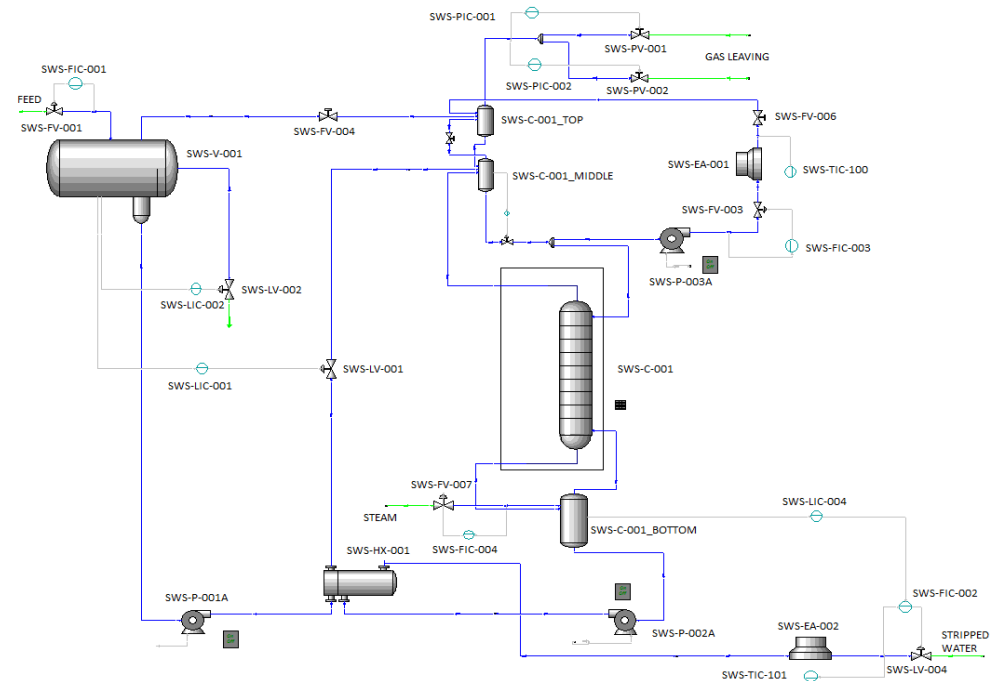


Figure 4. Model B implemented in Aspen Hysys.

Table 2 presents the feed stream composition [12-18]. The main parameters of the feed stream are: inlet feed pressure of 300 kPa, inlet feed temperature of 62.3 °C and mass flowrate of 19860 kg/h.

The most important and complex equipment of a SWS is the SW Stripper. Generally, the SWS stripper is modeled as a series of equilibrium stages [2, 3, 6, 7, 16]. The SW Stripper in both Model A and Model B, contains 50 equilibrium trays. Sieve trays were used for modeling the internal part of the column. The feed stream enters the column at tray 5. Tray 5 is critical because the pump around flow also leaves at this level and it is important to maintain the tray level. The pump around flow reenters the column in tray 1, where the vapors coming from the Flash Drum also enter the column.

Table 2. SWS feed stream composition.

Components	Mass Fraction
Hydrogen	0.0002064
i-Butane	0.0000107
n-Butane	0.0000251
Propane	0.0000352
Ethane	0.0000402
Methane	0.0000956
H ₂ O	0.9459771
H ₂ S	0.0344657
Ammonia	0.0191440

Model A and Model B designs contain the controllers listed in Table 3.

Table 3. Controllers used in Models A and B.

Controller Name	Description
SWS - FIC - 001	Inlet flow controller in the Flash Drum
SWS - LIC - 001	Water level controller in the Flash Drum
SWS - LIC - 002	Oil level controller in the Flash Drum
SWS - PIC - 001	Top pressure controllers for the SW Stripper
SWS - PIC - 002	
SWS - FIC - 003	Flow controller for the pump around flow of the SW Stripper (SWS-EA-001)
SWS - TIC - 100	Temperature controller for the pump around of the SW Stripper
SWS - LIC - 004	Master loop of the bottom level controller for the SW Stripper which has as slave loop SWS – FIC - 002
SWS - TIC - 101	Temperature controller for the stripper water after EA-002
SWS - FIC - 002	Flow controller for the stripper water (slave loop of the bottom level controller, is in cascade with SWS – LIC - 004)
SWS - FIC - 004	Flow controller for the live steam injected at the bottom of the SW Stripper

Controllers are important because they affect the dynamics of the process [18, 19]. Most of them are PID controllers. Two types of control systems were used: feed-back control and cascade control. Cascade control was used for controlling the level in the SW Stripper.

Comparison of the two dynamic models

Model B design uses the hot water stream from the bottom of the SW Stripper to heat the Feed stream, instead of the external hot water utility of Model A. This new design shows energy saving incentives. The Models have been undertaken to several analyses in order to determine the design most appropriate for industrial implementation. Table 4 shows the main temperature, pressure and flow variables of the inlet and outlet streams, revealing also the overall mass balance of the plant.

Table 4. Main variables and mass balance of the plant for both Models A and B.

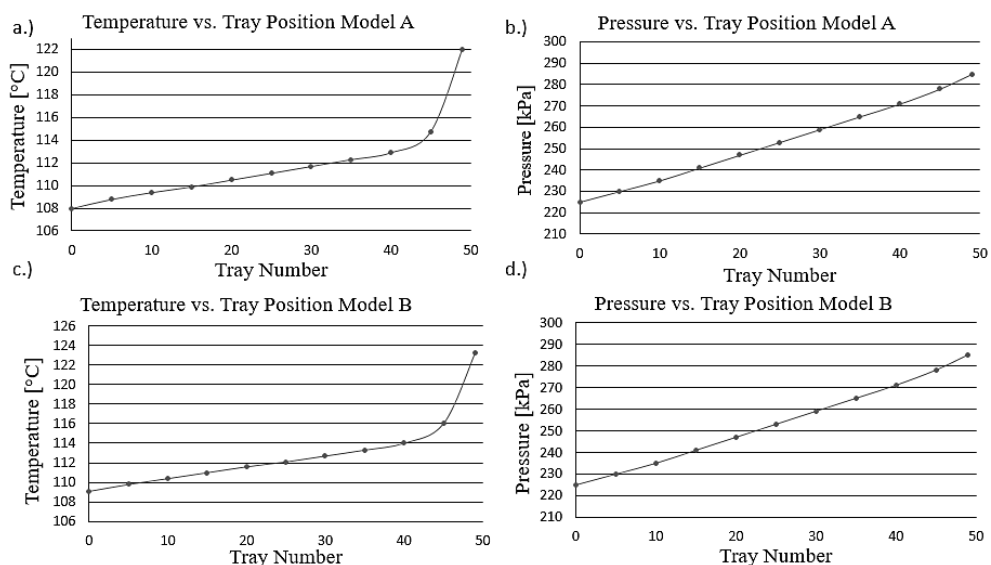
	INLET			OUTLET	
		Live steam	Feed Heat	Gas	Stripped
Model A	FEED	Injected	Exchanger External Agent	Leaving	Water
Temperature [°C]	62.3	150	122	73.83	89.94
Pressure [kPa]	300	290	1800	225	600
Molar Flow [kmol/h]	1087	120.3	498.6	32.52	1175
TOTAL Flow	1207.3			1207.52	
		Live steam	Feed Heat	Gas	Stripped
Model B	FEED	Injected	Exchanger External Agent	Leaving	Water
Temperature [°C]	62.3	150	-	78.58	60.21
Pressure [kPa]	300	290	-	225	400
Molar Flow [kmol/h]	1087	119.1	-	35.1	1171
TOTAL Flow	1206.1			1206.1	

As expected, Model A presents higher bottom temperature and higher pressure, compared to Model B. Model A shows lower temperature at the top of the SW Stripper. The Feed stream temperature to the SW Stripper is controlled with the Stripped Water flow, as the latter is already used for the bottom level cascade control (in the slave loop). Consequently, the temperature of the inlet stream in the SW Stripper of Model B is about 4 °C higher than in Model A. Table 5 presents the outlet streams composition.

Table 5. Mass fraction composition of the outlet streams from the SW Stripper.

Components	Model A		Model B	
	Gas Leaving	Stripped Water	Gas Leaving	Stripped Water
Hydrogen	0.0627	0	0.0579	0
i-Butane	0.0001	0	0.0001	0
n-Butane	0.0003	0	0.0002	0
Propane	0.0005	0	0.0005	0
Ethane	0.0008	0	0.0008	0
Methane	0.0036	0	0.00034	0
H ₂ O	0.1572	0.9843	0.1919	0.9861
H ₂ S	0.619	0	0.5722	0
Ammonia	0.1558	0.0157	0.1731	0.0139

Table 5 shows that all light hydrocarbons are found in the gas phase leaving the top of the SW Stripper. H₂S separation is very efficient as the whole H₂S amount can be found in the gas phase that is sent to further operations. The stripped water is free of H₂S but there is a small amount of NH₃ (1.39%). It is worthy to notice that NH₃ concentration is lower in the case of Model B design, favouring the separation. Figure 5 shows temperature and the pressure profiles of the SW Stripper along the column height.

**Figure 5.** Temperature and pressure profiles of the SW column in function of the tray position (0 is the top of the column and 50 is the bottom of the column).

As expected, both the temperature and the pressure decrease from the bottom to the top of the column. The overall temperature profile is higher in the case of Model B. The main difference between the two models consists in their energy efficiency perspective. Model A uses utility water with the temperature of 122 °C, pressure of 1800 kPa and flow of 8984 kg/h in order to warm up the feed stream for the SW Stripper. Model B uses the bottom stripped water to warm up the feed stream to the SW stripper. The stripped water leaves the column at temperature of 127 °C and pressure of 1743 kPa. This makes possible to replace the warm water utility with a process stream leading to a significant energy saving of about 59 GJ/day.

Based on the above results it is relevant to conclude that Model B is more efficient than Model A and demonstrates incentives for industrial application. As a result, further analysis will be made on Model B.

Effects of changing the feed temperature

In order to show the SWS simulator behavior several operating scenarios were investigated. Two of them are presented in the following.

The operating scenario presented in Figure 6, shows effects of an increasing step change in the inlet feed temperature, from 63 °C to 80 °C. As the stripping temperature increases, more of the heavier components, such as H₂O and NH₃, leave at the top of the column, Figure 6.c. and Figure 6.d. The quantity of the H₂S removed remains the same at the top of the column, although Figure 6.b shows a decreasing profile. The latter is due to the fact that mass of the other top column components are increasing and consequently, the H₂S concentration is decreased.

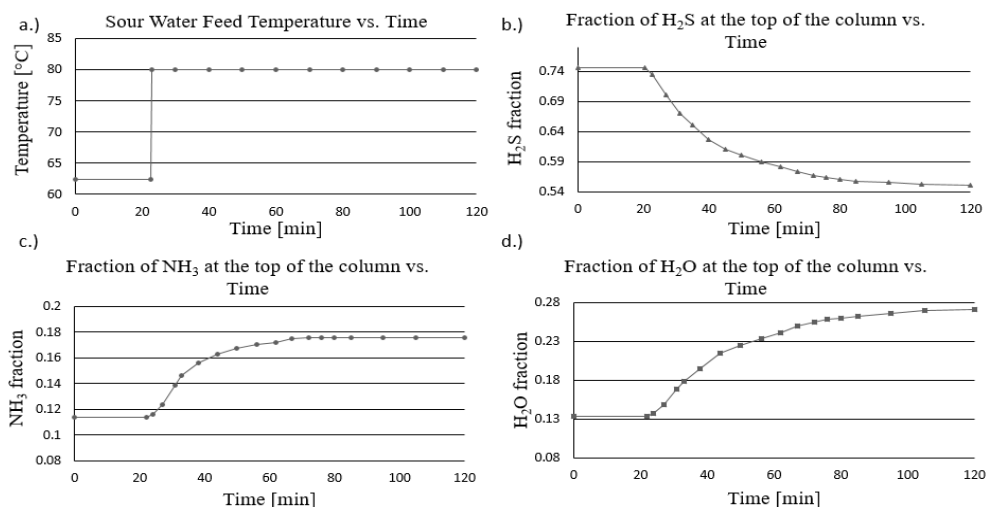


Figure 6. Effects of changing the SWS inlet temperature on the mass fraction of the components at the top of the column.

Effects of changing the pump around flow rate on the top column gas composition

In normal operating conditions, part of liquid leaves tray 5 of the column and after it is cooled down from the temperature of 100°C to the temperature of 60 °C it enters again the top of the column. This pump around increases the efficiency of the column. The operating scenario reveals the effects of decreasing followed by increasing of the pump around flow. Due to the pump around flow decrease from the value of 7800 kg/h to the value of 2000 kg/h, Figure 7.a, the top temperature of the column increases and higher amount of NH₃ component leaves at the column top.

During the reverse action, when at 77 minutes the pump around flow is increased from the value of 2000 kg/h to the value of 12000 kg/h, the temperature at the top of the column decreases and consequently, higher amount of the heavier components is condensing. Figure 7.b reveals an increase of the H₂S mass fraction due to the fact that both NH₃ and H₂O condensate and the vapor phase which leaves at the top of the column contains more H₂S compared to the other components.

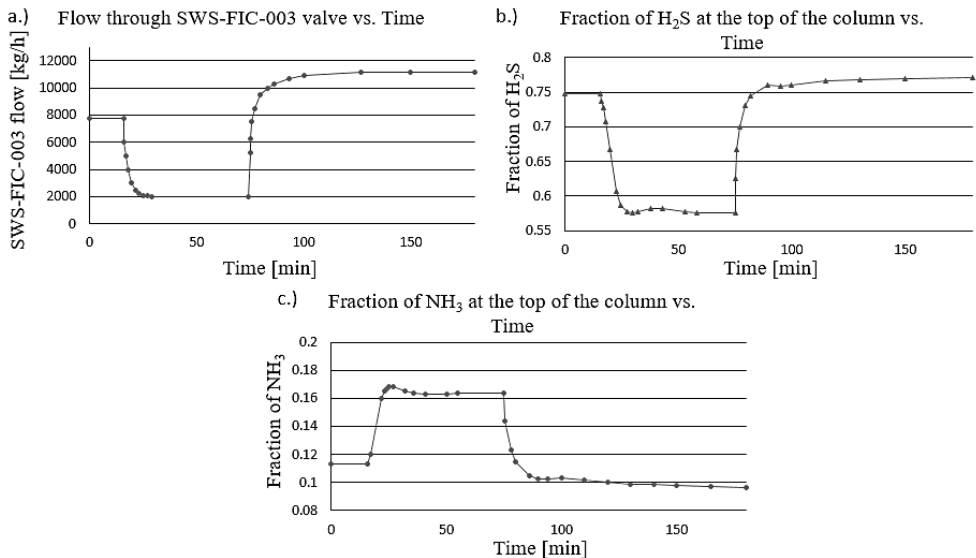


Figure 7. Effects of decreasing followed by increasing the pump around flow of the SW Stripper on the H₂S and NH₃ mass fractions at the top of the column.

Efficiency of the SWS-LIC-004 cascade loop

The bottom level in the SW Stripper is controlled by a cascade level control system. Cascade control loops have two measurement signals to control the primary level variable. The output (OP) of the primary controller (level master loop) determines the set-point (SP) for the secondary flow loop (level slave loop). The master loop of the controller is the SWS-LIC-004 and the slave loop of the system is the SWS-FIC-002.

In order to check the operation of the cascade level control system the set-point of the level in the bottom of the SW Stripper was changed from the value of 3 m to the value of 2.5 m. Figure 8 shows the result of this last operating scenario.

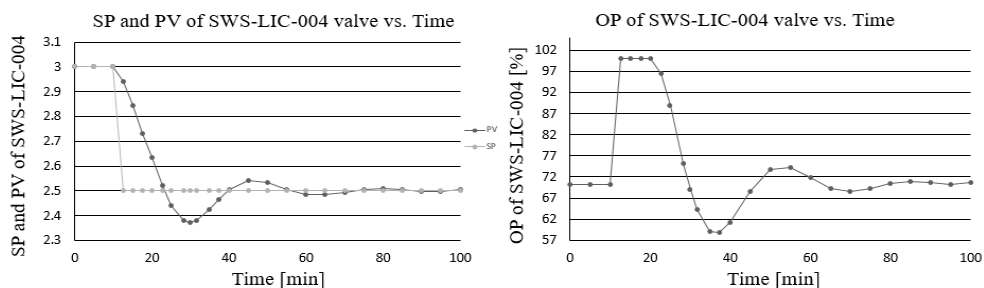


Figure 8. Effect of the level set-point change for the cascade control SWS-LIC-004; a. Changes of the level set-point variable SP and level process variable PV; b. Change of the master controller output (OP).

As a result of the level set-point SP change, Figure 8.a, the output of the level master controller opening percentage OP increases, Figure 8.b. Following a damped oscillation, the level PV is brought to the new set-point with zero offset and reduced overshoot, Figure 8.a.

CONCLUSIONS

Design and operation of the sour water stripping plant were investigated. Two dynamic models and their associated dynamic simulators were developed and implemented in Aspen Hysys simulation software. The results of the dynamic simulations are consistent with the data from the literature and with the measured data from the real plant.

Two dynamic models were investigated. Model A corresponds to the traditional design of the SWP unit, while Model B design uses an internal stream to heat up the feed flow. Investigated operating scenarios revealed that Model B is more efficient than Model A, as the former shows incentives from energetic perspective for reducing heat utilities and sparing costs. Better separation of the hazardous components is also achieved by the proposed Model B design. The same amount of H₂S is sent to the top of the column in both models but the NH₃ mass fraction concentration of 0.0157 remains in the stripped water stream for the case of Model A, while a diminished NH₃ concentration of 0.0137 is obtained for the Model B design.

Different control loops were proposed and implemented in the simulators for controlling pressure, level, flow and temperature, in either feedback of cascade configuration. Tests were run and results showed their effectiveness.

The developed simulators may be further exploited for the design of advanced control systems, elaboration of operator training software, operational optimization and investigation of new design improvements.

EXPERIMENTAL SECTION

The SWS models have been implemented in Aspen Hysys version V8.0 flowsheet simulation software. Model A and B parameters were calibrated on the basis of the literature data and data measured from the real plant [6, 12, 14-16].

REFERENCES

1. International Petroleum Industry Environmental Conservation Association, IPIECA, "Petroleum refining water/wastewater use and management", AECOM, UK, **2010**, chapter 2.
2. L. Addington, C. Fitz, K. Lunsford, L. Lyddon, M. Siwek, *Bryan Research and Engineering Inc.*, **2010**, 1.
3. R.H. Weiland, N.A. Hatcher. Sour Water Strippers Exposed, Laurance Reid Gas Conditioning Conference, Oklahoma, **2012**.
4. J.S. Eow, *Environmental Progress*, **2002**, 21, 143.
5. M. Zhu, L. Sun, G. Ou, K. Wang, K. Wang, Y. Sun, *Engineering Failure Analysis*, **2016**, 62, 93.

6. S.Y. Lee, J.M. Lee, D. Lee, I.B. Lee. *Korean Journal of Chemical Engineering*, **2004**, 21, 549.
7. C.M. Torres, M. Gadalla, J.M. Mateo-Sanz, L. Jiménez, *Journal of Cleaner Production*, **2013**, 44, 56.
8. N. Quirante, J.A. Caballero, *Computers and Chemical Engineering*, **2016**, 92, 143.
9. V.M. Cristea, E.D. Bagiu, P.S., *Computer Aided Chemical Engineering*, **2010**, 28, 985.
10. Ani E.C., Cristea V.M., Agachi P.S., Kraslawski A., *Revista de Chimie*, **2010**, 11, 1108.
11. L. C. Hardison, U.S. Patent, 4784775, Nov. 15, **1988**.
12. R. Thiele, R. Faber, J. -U. Repke, H. Thielert, G. Wozny, *Chemical Engineering Research and Design*, **2007**, 85, 74.
13. Z. Nasri, H. Binous, *Journal of Chemical Eng. of Japan*, **2007**, 40, 534.
14. J.E.F. Inverno, E. Correia, P. Jimenez-Asenjo, J.A. Feliu, *Computer Aided Chemical Engineering*, 18, **2004**, 211.
15. W.E. Luetzelschwab, U.S Patent, 3821110, June 28, **1974**.
16. R. Houser, T. Kirkey, AIChE 2003 Spring National Meeting, New Orleans, **2003**.
17. D. Sujo-Nava, L.A. Scodari, C.S. Slater, K. Dahm, M.J. Savelski, *Chemical Engineering and Processing*, **2009**, 48, 892.
18. N. Alsop, J.M. Ferrer, AIChE 2006 Spring National Meeting, Orlando, **2006**.
19. R.H. Weiland, M.S. Sivasubramanian, J.C. Dingman, 53rd Annual Laurance Reid Gas Conditioning Conference, Norman, **2003**.

*Dedicated to Professor Luminița Silaghi-Dumitrescu
on the occasion of her 65th anniversary*

CALCULATION OF THE EFFECTIVE MASS TRANSFER AREA IN TURBULENT CONTACT ABSORBER

SIMION DRĂGAN^a

ABSTRACT. One of the most important efficiency parameters for separation columns is the effective interfacial mass transfer area. In this study the effective mass transfer area in gas-solid-liquid turbulent contact absorber was determined using the chemical absorption of carbon dioxide into sodium hydroxide aqueous solution. The effective mass transfer area determined in this study was found to be from three to six times higher than the geometric area of the solid packing.

Keywords: *Three phase fluidized bed, gas-solid-liquid turbulent contact absorber, effective mass transfer area, chemical methods*

INTRODUCTION

In order to obtain maximum absorption efficiency it is necessary to use proper equipments to maximize gas-liquid contact, such as new columns with three phase fluidized beds [1,2]. Gas-solid-liquid three phase fluidized bed absorber is mass transfer equipment in which the bed of low density packing is fluidized by the counter current flow of gas continuous phase and liquid as a dispersed phase.

The efficiency of the mass transfer depends on many factors such as the effective interfacial mass transfer area, mass transfer coefficients and liquid holdup.

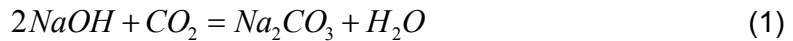
The effective mass transfer area (a_e) is not identical either to the geometric area (a) or to the wetted area of the packing (a_w). The measurement of the specific geometric area of packing is straightforward but is not a design parameter. The wetted area is that part of geometric area over which there is a liquid film.

^a *Babes-Bolyai University, Faculty of Chemistry and Chemical Engineering, Arany Janos 11, 400028, Cluj-Napoca, sdragan@chem.ubbcluj.ro*

The most popular absorption system employed for determining interfacial mass transfer area with the use of the chemical method is the reactive absorption of CO₂ into aqueous solutions of sodium hydroxide [3-6]. The liquid phase reaction is considered to fall in the fast reaction regime with the mechanism given by Tsai [7, 8].

CALCULATION OF GAS-LIQUID CONTACT AREA

The effective mass transfer area can be calculated using a reactive absorption system such as air-CO₂-NaOH. A pseudo-first order reaction has been chosen as model reaction in this study, due to the fact that the kinetics of the system is well-known and the chemicals are easy to handle. When the NaOH is in excess, the reaction between the dissolved CO₂ and the NaOH in solution can be expressed as:



The concentration profiles of the two reactants in the liquid film are described by the next differential equations:

$$D_{CO_2} \frac{\partial^2 C_{CO_2}}{\partial x^2} + k_2 \cdot C_{CO_2} \cdot C_{HO^-} = 0 \quad (2)$$

$$D_{HO^-} \frac{\partial^2 C_{HO^-}}{\partial x^2} + 2k_2 \cdot C_{CO_2} \cdot C_{HO^-} = 0 \quad (3)$$

with these boundary conditions:

$$\text{at } x = 0; C_{CO_2} = C_{CO_2}^i \text{ and } \frac{dC_{HO^-}}{dx} = 0 \quad (4)$$

$$\text{at } x = \delta; C_{CO_2} = C_{CO_2}^0 \text{ and } C_{HO^-} = C_{HO^-}^0$$

The analytical solution of the system (2)-(4) leads to the enhancement factor concept, E. This solution is available only if the reaction (1) is considered to be pseudo-first-order, i.e., the concentration of NaOH is not depleted in the liquid film ($C_{HO^-} = C_{HO^-}^0$). According to Danckwerts mass-transfer model the reaction rate can be expressed as [8]:

$$v_{abs} = a_e C_{CO_2}^i \left(k_1 D_{CO_2} + k_L^2 \right)^{1/2} \quad (5)$$

The mass-transfer process of the absorption of CO₂ is controlled by the liquid film, according to Henry's law:

$$C_{CO_2}^i = H \cdot P_{CO_2} \quad (6)$$

In the fast reaction regime, defined by $Ha > 5$, the enhancement factor equals the Hatta number and rapid chemical reaction is not sensitive to liquid side mass transfer coefficient k_L , the equation of the reaction rate becomes:

$$v_{abs} = a_e \cdot H \cdot P_{CO_2} \left(k_1 D_{CO_2} \right)^{1/2} \quad (7)$$

The solubility coefficient of CO₂ in the electrolyte solution can be estimated as follows [9]:

$$\lg \frac{H}{H_0} = -K_s \cdot I \quad (8)$$

$$K_s = i_+ + i_- + i_g = i_{Na^+} + i_{HO^-} + i_{CO_3^{2-}} + i_{CO_2} \quad (9)$$

For the system CO₂-NaOH-H₂O, ion coefficients are [3]:

$$\begin{aligned} i_{Na^+} &= 0.091; \\ i_{HO^-} &= 0.066; \\ i_{CO_3^{2-}} &= 0.021 \\ i_{CO_2} &= -0.019 \end{aligned} \quad (10)$$

So, $K_s = 0,159$ and equation (8) become:

$$\lg \frac{H}{H_0} = -0.159 \cdot I \quad (11)$$

The solubility coefficient of CO₂ in pure water, H_0 , depends only on temperature and can be calculated with relation (12) [9]:

$$\lg H_0 = \frac{1140}{T} - 5.30 \quad (12)$$

The rate constant of the pseudo-first-order reaction is k_1 and its relationship with temperature and ionic concentration is given by equation (13) [10]:

$$k_1 = k_2 \cdot C_{HO^-} \quad (13)$$

where k_2 is the pseudo-second-order rate constant:

$$\lg\left(\frac{k_2}{k_2^\infty}\right) = 0.1987I - 0.012I^2 \quad (14)$$

$$\lg k_2^\infty = 11.895 - \frac{2382}{T} \quad (15)$$

The formula for the ionic strength is as follows:

$$I = \frac{1}{2} \sum C_i \cdot Z_i^2 = C_{NaOH}^0 \quad (16)$$

Using the equation system (17) it can be determine the concentration of CO_2 at interface $C_{CO_2}^i$.

$$\begin{aligned} C_{CO_2}^i &= H \cdot P_{CO_2} \\ H &= H_0 \cdot 10^{-0.159C_{NaOH}^0} \\ \lg H_0 &= \frac{1140}{T} - 5.30 \end{aligned} \quad (17)$$

In the fast reaction regime, the enhancement factor $E = Ha$ and the equation of the absorption rate becomes:

$$v_{abs} = a_e \cdot C_{CO_2}^i \left(k_2 \cdot C_{HO^-}^0 \cdot D_{CO_2} \right)^{1/2} \quad (18)$$

The effective mass transfer area can be determined from the slope of the straight line, passing through the origin, obtained by the representation of equation (18).

RESULTS AND DISCUSSION

The carbon dioxide concentration at the inlet and outlet of system was determined. With these values and height of the fluidized bed, the absorption rate for the two concentrations of NaOH solution and two gas rates were determined:

$$v_{ab} = \frac{273}{293} \cdot \frac{w_g}{22.4} \cdot \frac{1}{H_{sf}} \left(Y_{CO_2}^i - Y_{CO_2}^f \right) \quad (19)$$

The reaction constant k_2 was calculated by the relations of:

Barett equation [11]:

$$\lg k_2 = 11.8609 - \frac{2338.28}{T} + 0.1317 \cdot C_{NaOH}^0 \quad (20)$$

Astarita equation [12]:

$$\lg k_2 = 13.635 - \frac{2895}{T} + 0.160 \cdot C_{NaOH}^0 \quad (21)$$

Pohorecki equation [13]:

$$\lg k_2 = 11.895 - \frac{2382}{T} + 0.221 \cdot C_{NaOH}^0 - 0.016 \left(C_{NaOH}^0 \right)^2 \quad (22)$$

The obtained values are presented in the table 1.

Table 1. Values of reaction constant k_2 [l / mol s] at T=293 K

Equation→ C_{NaOH}^0 ↓	(20)	(21)	(22)
0.0 N	7593.154	5681.381	5825.151
0.5 N	8836.335	6830.522	7444.014
1.0 N	10283.06	8212.094	9339.146

The values of k_2 obtained with Pohorecki equation are approximated the mean value of values obtained with equations (20) and (21), therefore these values are used.

The CO_2 diffusivity in pure water depends on the temperature as follows:

$$\lg D_{CO_2}^0 = -8.1764 + \frac{712.5}{T} - \frac{2.591 \cdot 10^5}{T^2} \quad (23)$$

While the diffusivity of the CO_2 in the NaOH aqueous solution was calculated by the equation (24):

$$D_{CO_2} = D_{CO_2}^0 \cdot \left(\frac{\eta_{H_2O}}{\eta_{NaOH}} \right)^{0.637} \quad (24)$$

Using equations (23), (24) and the viscosity values of NaOH aqueous solutions has been calculated the diffusion coefficient D_{CO_2} .

Henry constant of CO₂ in NaOH aqueous solutions has been calculated. These values are presented in table 2.

Table 2. Diffusion coefficient D_{CO_2} in NaOH aqueous solutions and Henry constant H at $T=293$ K

C_{NaOH}^0 [mol/l]	0	0.5	1
$D_{CO_2} \cdot 10^9$ [m ² / s]	1.76	1.74	1.62
$H \cdot 10^2$ [atm · l/mol]	3.897	3.245	2.7

In the tables 3 to 6 the concentrations of carbon dioxide at interfaces, the absorption rates and X coordinate from equation (18) are presented.

Table 3. Experimental results for the absorption in three phase fluidized bed of CO₂ into 0.5 N NaOH aqueous solution at $v_g = 1.1$ [m/s].

C_{CO_2}	$C_{CO_2}^i$	$C_{CO_2}^i \sqrt{k_2 \cdot C_{HO^-} \cdot D_{CO_2}}$	v_{ab} [Kmol/m ³ s]	Liquid flow [l/h]
0	0	0	0	L=100
5%	1.6200E-03	4.1940E-06	0.006221753	
8%	2.6000E-03	6.7300E-06	0.010433075	
10%	3.2400E-03	8.3900E-06	0.012784895	
0	0	0	0	L=200
5%	1.6200E-03	4.1940E-06	0.006815129	
8%	2.6000E-03	6.7300E-06	0.011182052	
10%	3.2400E-03	8.3900E-06	0.013601283	

Table 4. Experimental results for the absorption in three phase fluidized bed of CO₂ into 1.0 N NaOH aqueous solution at $v_g = 1.1$ [m/s].

C_{CO_2}	$C_{CO_2}^i$	$C_{CO_2}^i \sqrt{k_2 \cdot C_{HO^-} \cdot D_{CO_2}}$	v_{ab} [Kmol/m ³ s]	Liquid Flow [l/h]
0	0	0	0	L=100
5%	1.3500E-03	5.2300E-06	0.006636536	
8%	2.1600E-03	8.3700E-06	0.011128613	
10%	2.7000E-03	1.0500E-05	0.013637221	
0	0	0	0	L=200
5%	1.3500E-03	5.2300E-06	0.007520142	
8%	2.1600E-03	8.3700E-06	0.012338816	
10%	2.7000E-03	1.0500E-05	0.014539302	

Table 5. Experimental results for the absorption in three phase fluidized bed of CO₂ into 0.5 N NaOH aqueous solution at v_g = 2.11 [m/s].

C _{CO2}	C ⁱ _{CO2}	$C_{CO_2}^i \sqrt{k_2 \cdot C_{HO^-} \cdot D_{CO_2}}$	V _{ab} [Kmol/m ³ s]	Liquid Flow [l/h]
0	0	0	0	L=100
5%	1.6200E-03	4.1940E-06	0.011137704	
8%	2.6000E-03	6.7300E-06	0.017339647	
10%	3.2400E-03	8.3900E-06	0.019845364	
0	0	0	0	L=200
5%	1.6200E-03	4.1940E-06	0.013427058	
8%	2.6000E-03	6.7300E-06	0.019669209	
10%	3.2400E-03	8.3900E-06	0.024171189	

Table 6. Experimental results for the absorption in three phase fluidized bed of CO₂ into 1.0 N NaOH aqueous solution at v_g = 2.11 [m/s].

C _{CO2}	C ⁱ _{CO2}	$C_{CO_2}^i \sqrt{k_2 \cdot C_{HO^-} \cdot D_{CO_2}}$	V _{ab} [Kmol/m ³ s]	Liquid Flow [l/h]
0	0	0	0	L=100
5%	1.3500E-03	5.2300E-06	0.012622731	
8%	2.1600E-03	8.3700E-06	0.020329241	
10%	2.7000E-03	1.0500E-05	0.024097942	
0	0	0	0	L=200
5%	1.3500E-03	5.2300E-06	0.015217332	
8%	2.1600E-03	8.3700E-06	0.022947411	
10%	2.7000E-03	1.0500E-05	0.029005427	

The effective mass transfer area was determined as a slope of the straight line from representation of equation (18):

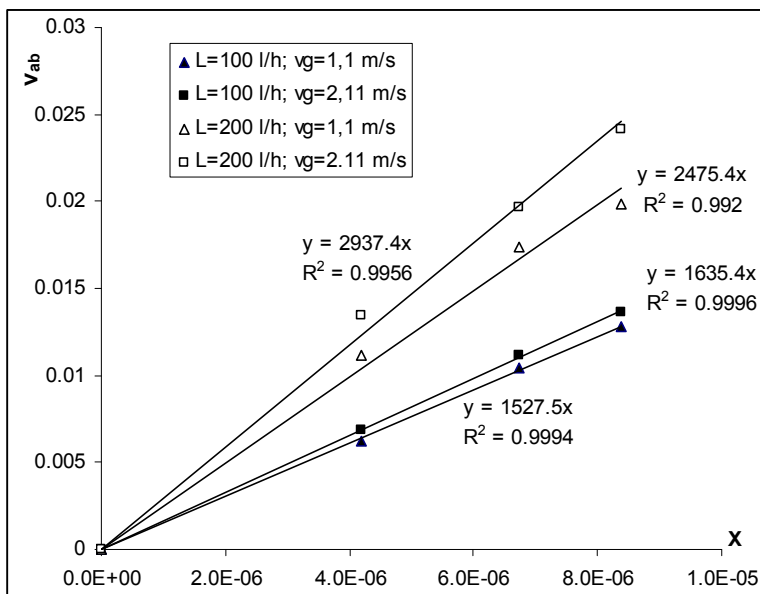


Figure 1. Absorption rate versus X at $C^0_{HO^-}=0.5 \text{ mol/l}$, $T=293\text{K}$

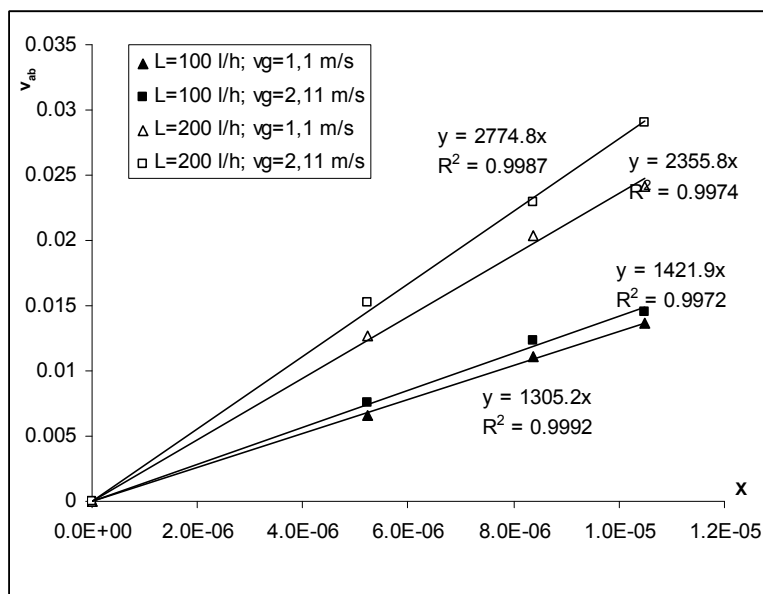


Figure 2. Absorption rate versus X at $C^0_{HO^-}=1 \text{ mol/l}$, $T=293\text{K}$

The numerical values of the determined effective mass transfer area from figures 1-2 are centralized in table 7.

Table 7. Effective mass transfer area in three phase fluidized bed (a_e , [m²/m³])

C_{HO}^0 / L [l/h]	100	200	
0.5 [mol/l]	1527.5	1635.4	$V_g=1.10$ [m/s]
1.0 [mol/l]	1305.2	1421.9	
<i>Average</i>	<i>1416.3</i>	<i>1528.6</i>	
0.5 [mol/l]	2475.4	2937.4	$V_g=2.11$ [m/s]
1.0 [mol/l]	2355.8	2774.8	
<i>Average</i>	<i>2415.6</i>	<i>2856.1</i>	

At a constant concentration of NaOH solution and constant liquid flow rate, effective mass transfer area increases more with gas velocity, from 1527.5 m²/m³ ($C_{NaOH} = 0.5$ mol/l, $v_g = 1.10$ m/s and $L = 100$ l/h) at 2475.4 m²/m³ ($C_{NaOH} = 0.5$ mol/l, $v_g = 2.11$ m/s and $L = 100$ l/h).

At a constant concentration of NaOH solution and constant gas velocity, the effective mass transfer area increases low with the increase of the liquid flow, from 2475.4 m²/m³ ($C_{NaOH} = 0.5$ mol/l, $v_g = 2.11$ m/s and $L = 100$ l/h) at 2937.4 m²/m³ ($C_{NaOH}=0.5$ mol/l, $v_g=2.11$ m/s and $L=200$ l/h). The increase of liquid flow determines the increase of packing buoyancy and a better fluidization is obtained.

At a constant liquid flow rate and constant gas velocity, effective mass transfer area decreases with the increase of NaOH concentration, from 1527.5 m²/m³ ($C_{NaOH} = 0.5$ mol/l, $v_g = 1.1$ m/s and $L = 100$ l/h) at 1305.2 m²/m³ ($C_{NaOH} = 1$ mol/l, $v_g = 1.1$ m/s and $L = 100$ l/h). This phenomenon can be explained using the two-film theory. The reaction of CO₂ and NaOH takes place in liquid boundary layer, so CO₂ has to diffuse through gas film and enter in liquid film to reach the NaOH solution. The increase of NaOH concentration causes the viscosity liquid increase, thus CO₂ diffusion in liquid phase is slower and mass transfer area is decrease.

CONCLUSION

The effective mass transfer area in turbulent contact absorber with low density solid particles has been determined. The absorption of carbon dioxide from the mixture of air-CO₂ into 0.5 N and 1.0 N aqueous NaOH solutions was employed as model reaction of known kinetics.

The effective mass transfer area increases when gas velocity and liquid flow increase and decreases when the concentration of the NaOH solution increases.

The effective mass transfer area in turbulent contact absorber with three phase fluidized bed is from three to six times higher than the geometric area of the solid packing.

EXPERIMENTAL

In order to determine the effective mass transfer area in turbulent contact absorber with low density inert solid packing, the rate absorption of carbon dioxide from air-CO₂ mixture into the NaOH solution was measured. The flow diagram of the experimental equipment used for the absorption rate is represented in the figure 7.

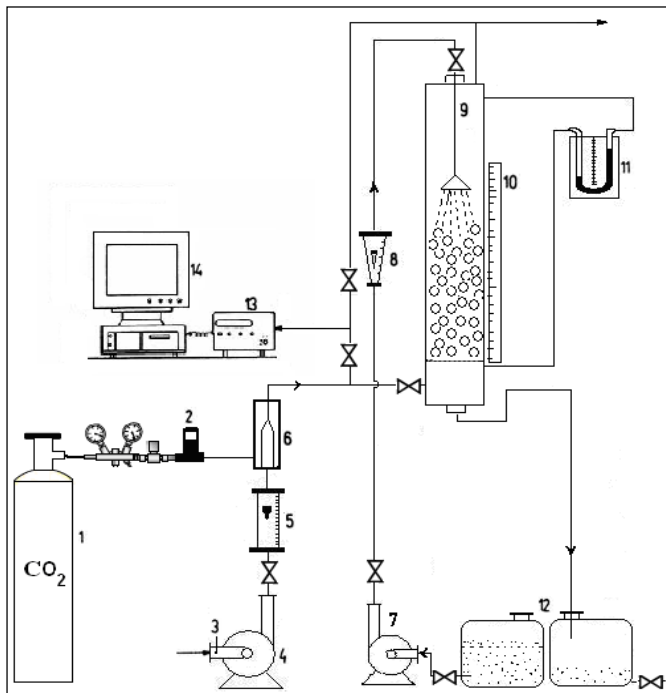


Figure 7. Flow diagram of the experimental equipment

1-carbon dioxide cylinder, 2-carbon dioxide mass flow meter, 3-air temperature controller, 4-air blower, 5-gas rotameter, 6-gas mixing tube, 7-liquid pump, 8-liquid rotameter, 9-three phase fluidized bed absorber column, 10-graduet scale, 11-manometer, 12-slution tanks, 13-gas analyzer, 14-IBM computer.

The column was made of glass with an interior diameter of 0.14 m and high 1.10 m. The glass column was used for better visual observation of the phenomena occurring in the fluidized bed. Gas mixture is the continuous phase and was introduced at predetermined flow rate into the column. NaOH solution of specified concentration as dispersed phase was sprayed from the liquid distributor over the top of the fluidized bed.

The solid materials which were used as solid phase are plastic hollow balls of 1.0 cm diameter and with the density of 170 kg/m³. The experiments were conducted in a fully fluidized state. The fluidized bed height was read on the scale. The liquid and air flow rates were measured by rotameters and carbon dioxide flow rate was measured and controlled by mass flow meter. The composition of carbon dioxide in the entering and leaving gas phase was measured using a calibrate BINOS 120 gas analyzer. The experimental conditions are presented in table 8.

Table 8. The experimental conditions (T = 293 K, P = 1 bar)

Variable	Range
Column diameter D_c [m]	0.14
Diameter of solid particle d_p [m]	0.01
Solid particle density [Kg/m ³]	170
Static solid bed height H_0 [m]	0.12
Gas velocity v_g [m/s]	1.1; 2.11
CO ₂ mole fraction in the gas mixture	0.05; 0.08; 0.1
Liquid flow [l/h]	100; 200
Concentration of NaOH solution, [mol/l]	0.5; 1.0

The absorption rate has been calculated from the measured inlet ($Y_{CO_2}^0$) and outlet (Y_{CO_2}) concentration of the carbon dioxide in the gas phase.

REFERENCES

1. A. Shabani, S.T. Asl and B.H.Shahraki, *International Journal of Chemical Engineering and Application*, **2010**, 1(1), 117.
2. S. Dragan, *Stud. Univ. Babeş-Bolyai, Chemia*, **2015**, 60, 3, 183.
3. P.V. Danckwerts, "Gas-Liquid Reactions", New York, McGraw-Hill, **1970**, Chap.9, 206.
4. G.H. Joosten and P. Danckwerts, *Chem. Eng. Science*, **1973**, 28, 453.

5. M. Drăgan, S. Drăgan, I. Siminiceanu. *Stud. Univ. Babes-Bolyai, Chemia*, **2000**, 45 (1-2), 11.
6. M.H. de Brito, U. von Stockar, A.M. Bangerter and M. Laso. *Ind. Eng. Chem. Res.*, **1994**, 33 (3), 647.
7. E.R.Tsai, P.Schultheis, A. Kettner, J.C.Lewis, A.F. Seibert, R.B.Eldridge and G.T. Rochelle, *Ind. Eng. Chem. Res.*, **2008**, 47, 1253.
8. R. Tsai, PhD Dissertation, Austin, University of Texas. **2010**.
9. M.M., Sharma, P.V. Danckwerts, *Br.Chem.Eng.*, **1970**, 15, 522.
10. K. Yang, G. Chu, H. Zou, B. Sun, L., J.F. Shao, *Chem. Eng. Journal*, **2011**, 168, 1377.
11. P.V.L. Baret, PhD Thesis, University of Cambridge, **1967**.
12. G. Astarita, D.V. Savage, A. Bisio, "Gas treating with chemical solvents", John Wiley & Sons, **1983**. Chap. 9, 210.
13. R. Pohorecki, W. Moniuk, *Chem. Eng. Sci.*, **1988**, 43 (7), 1677.

*Dedicated to Professor Luminița Silaghi-Dumitrescu
on the occasion of her 65th anniversary*

INFLUENCE OF MgO/SiO₂ RATIO AND ADDITIVES ON BIONANOFORSTERITE POWDERS CHARACTERISTICS

LILIANA BIZO^a, MARIA GOREA^{a,*}, GABRIEL KATONA^a

ABSTRACT. Forsterite (Mg₂SiO₄) powders were synthesized by solid state reaction from basic magnesium carbonate and silicon dioxide. The MgO/SiO₂ molar ratio was established at 2:1, 2:1.05 and 2:1.10. In order to realize a complete reaction between compounds and avoiding the MgO (periclase) presence in the final product, an excess of SiO₂ was added. Boric acid in small quantity was used as a mineralizer. The six mixtures were designed and prepared in the laboratory. After a good homogenization and mechanical activation, the raw mixtures were thermally treated at 800 °C, 900 °C, 1000 °C, 1200 °C, 1300 °C and 1350 °C with a heating rate of 2 °C/min and one hour plateau at maximum temperature. The grain size distribution of the powders obtained at 800 °C, 900 °C and 1000 °C, according to the particle analyzes, are in the nanometer range. Increasing the temperature the size of grains is increased at micrometer dimensions indicating the presence of agglomerates. The mineralogical compositions evidenced by X-ray powder diffraction (XRPD) showed as the main crystalline compound the forsterite beginning of 1200 °C temperature. The crystallinity index of forsterite depends on the thermal treatment conditions, being highest at 1350 °C. A small quantity of MgO at the maximum temperature in compositions without boric acid was identified. The shape and morphology of forsterite crystals were evidenced by TEM analyses.

Keywords: *nano forsterite, biomaterial, synthesis*

^a Babeş Bolyai University, Faculty of Chemistry and Chemical Engineering, 11 Arany Janos str., RO-400028, Cluj-Napoca, Romania,

* Corresponding author: mgorea@chem.ubbcluj.ro

INTRODUCTION

Due to the increasing interest in silicon and magnesium based bioceramic materials, much research was carried out recently on forsterite (Mg_2SiO_4) ceramics for medical applications [1-2]. Naghiu et al demonstrated that presence of MgO in small quantity does not affect the forsterite powder biocompatibility [3].

It was previously demonstrated that magnesium and silicon play an important role in human body processes: magnesium is one of the most important elements in the human body, closely associated with mineralization of calcined tissues and indirectly influences mineral metabolism, whereas silicon is an essential element in skeletal development. Recent research has shown that the compounds in the MgO–SiO₂ system are biocompatible, thus they are suitable to be used for dental and orthopaedic prosthetic materials.

Forsterite nanostructured ceramics show improved biocompatibility, superior mechanical properties and increased osteoblast adhesion and proliferation over normal materials [4]. Because nanoparticle ceramics show more attractive properties than microstructured ceramics, like high diffusion rates or mechanical properties, many methods have been employed for obtaining forsterite nanoparticles. These methods included sol–gel method [5-8], polymer precursor method [9], co-precipitation [10], or conventional solid-state reaction [11-16]. During the synthesis by the ceramic method, a reaction in solid phase, at high temperature between, MgO and SiO₂ takes place [17]. The formation of a single phase, forsterite, in the oxide systems MgO–SiO₂, is difficult to obtain. It is always accompanied by secondary phases like enstatite (MgSiO_3) and/or periclase (MgO). The mechanical activating of raw mixtures was demonstrated to be an efficient method to increase the chemical homogeneity of the product and to reduce the reaction temperature [18-20]. In this work boric acid as a mineralizing agent and a small excess of SiO₂ were used in order to enhance the nanostructure forsterite formation.

The aim of this work is to study the parameters of synthesis and characterization of nanoforsterite powders with a small excess of silicon dioxide. The effect of MgO/SiO₂ ratio and additives on bionanoforsterite powders characteristics will be investigated by different methods: X-ray powder diffraction (XRPD), particle size analysis and transmission electron microscopy (TEM).

RESULTS AND DISCUSSION

X-ray powder diffraction

X-ray powder diffraction (XRPD) patterns show the formation of well-crystallized forsterite in the samples thermally treated at 1350 °C. Beside of a forsterite phase, small quantities of periclase and enstatite were

detected in tested samples depending on composition and thermal treatment. The presence of the secondary phases could be assigned to an incomplete reaction or insufficient homogeneity of the precursor mixtures.

Figure 1 showed the XRPD pattern for samples DPI which is similar to DPII, composition without boric acid. It can observe that in the pattern of samples thermally treated at low temperatures (800 °C, 900 °C, 1000 °C) the presence of forsterite crystals is not evidenced. The only crystalline phase is periclase resulted from magnesium carbonate decomposition. In the samples treated at higher temperatures, 1200 °C, 1300 °C and 1350 °C, the specific peaks for forsterite as the main crystalline compound, and small quantities of enstatite and periclase were identified. In conclusion, in composition DPI and DPII, the reaction between reactants is no completed at 1350 °C temperature.

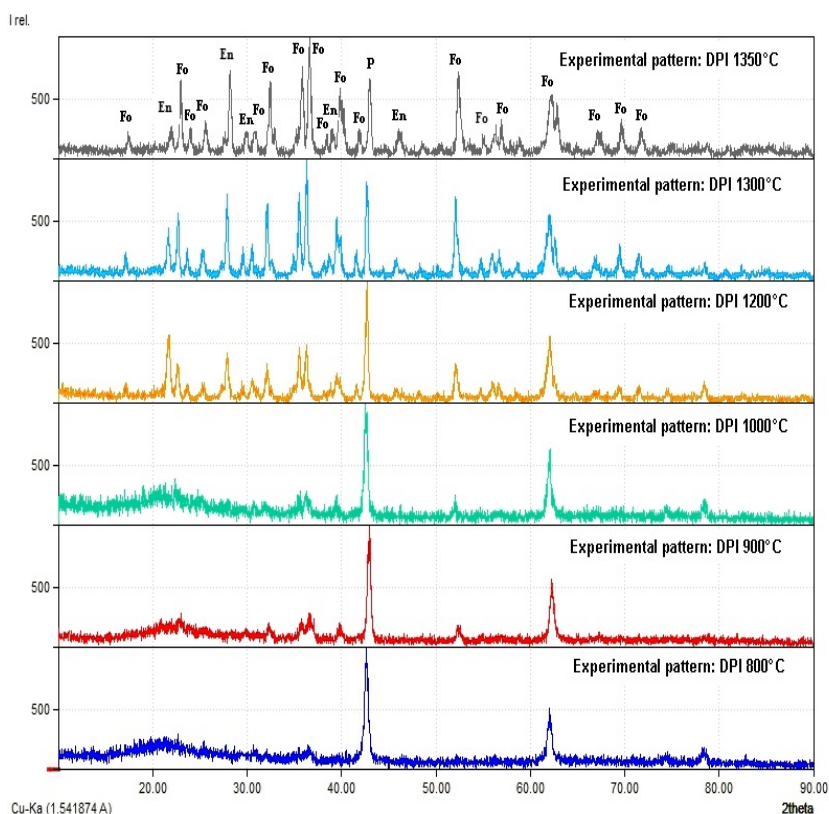


Figure 1. XRPD patterns of DPI samples treated at 800 °C, 900 °C, 1000 °C, 1200 °C, 1300 °C and 1350 °C, respectively (Fo-forsterite, En-enstatite, P-periclase)

In Figure 2 are presented the specific XRPD patterns of sample DPIII which are similar to DPIV at different temperatures.

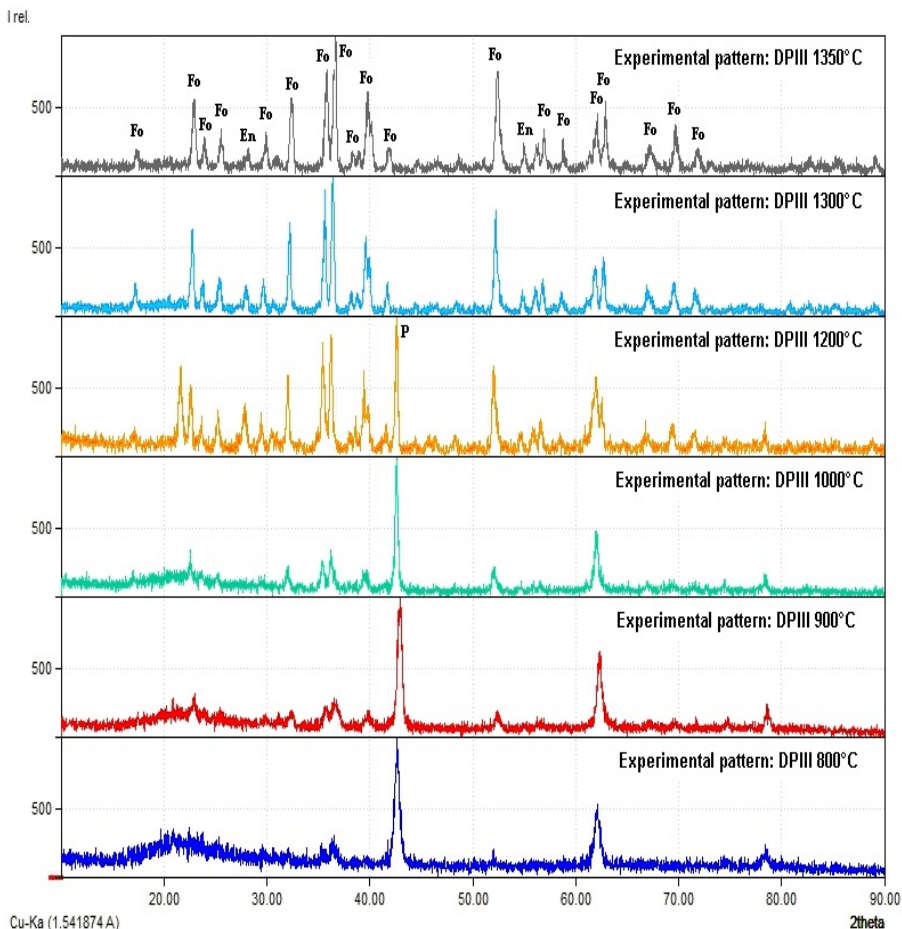


Figure 2. XRPD patterns of DPIII samples treated at 800 °C, 900 °C, 1000 °C, 1200 °C, 1300 °C and 1350 °C, respectively (Fo-forsterite, En-enstatite, P-periclas)

At low temperatures (800 °C, 900 °C, 1000 °C), the well crystalline phase evidenced is periclas and the enstatite and forsterite crystals are poorly crystalline. Beginning with 1200 °C temperature, the enstatite and forsterite phases were identified besides of periclas. At 1350 °C temperature the specific peaks of periclas and enstatite disappeared. This fact demonstrated that the presence of additives (boric acid) determines a complete reaction between reactants.

Figure 3 shows the XRPD specific pattern for samples DPV (similarly with DPVI) thermally treated at different temperatures.

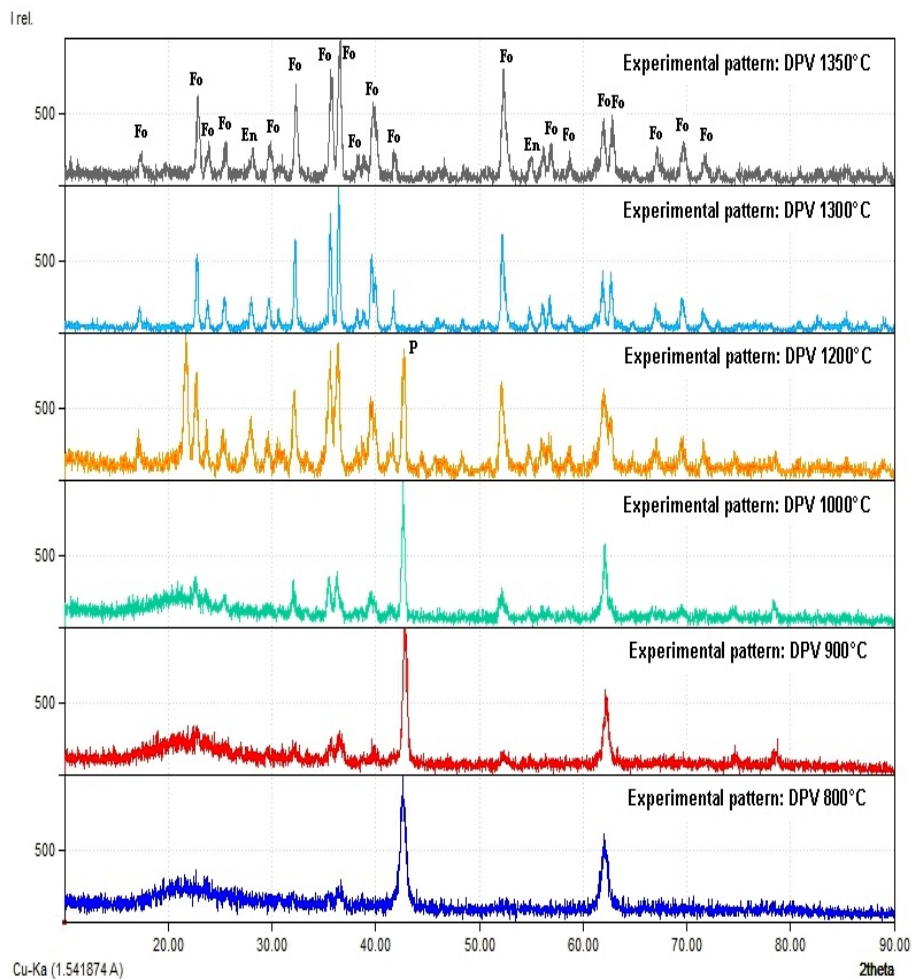


Figure 3. XRPD patterns of DPV samples treated at 800 °C, 900 °C, 1000 °C, 1200 °C, 1300 °C and 1350 °C, respectively (Fo-forsterite, En-enstatite, P-periclase)

The crystalline components evidenced by X-ray diffraction are similar to those detected in sample DPV. At 1350 °C temperature only the forsterite and enstatite crystals were identified. It could be concluded that a small excess of SiO₂ and mainly a proper additive determine a complete reaction and obtaining of forsterite of nanometer size besides of small amounts of enstatite.

In table 1 are listed the crystallite values of forsterite calculated from XRPD data using Scherrer formula at 1200 °C, 1300 °C and 1350 °C, respectively temperatures.

Table 1. Calculated crystallite sizes D (nm)

Sample	D [nm]		
	1200 °C	1300 °C	1350 °C
DPI	21.90	25.43	23.87
DPII	29.21	24.63	21.30
DPIII	23.90	27.18	20.20
DPIV	26.28	26.28	21.30
DPV	14.08	29.20	19.70
DPVI	20.22	24.63	20.73

The calculated crystallite values for all the tested samples are in the 20 nm and 30 nm range size excepting the value of 14.08 nm for DPV sample.

Transmission Electron Microscopy – TEM

TEM microscopy evidenced the morphology and sizes of the crystallites from the synthesized powders (figure 4).

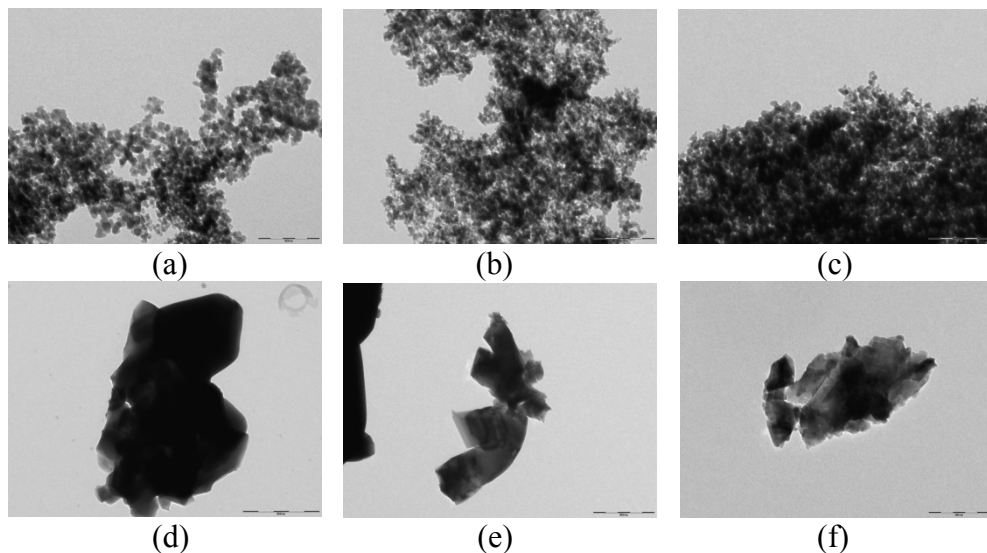


Figure 4. TEM images of forsterite powders at different temperatures: (a) DPIV at 800 °C, (b) DPVI at 900 °C, (c) DPII at 1000 °C and (d) DPI at 1350 °C, (e) DPIII at 1350 °C, (f) DPV at 1350 °C

The TEM images show two types of crystal mixtures. In the samples fired at low temperatures very small and poorly crystalline phases are evidenced. The grain agglomerate and no individual crystal are illustrate (figure 4 a, b and c). In the case of samples fired at 1350 °C temperature the crystals orthoromboidal bipyramidal with a high crystallinity index specific for forsterite are identified. The crystal size are in the nanometer interval.

Grain size distribution

The grain size distribution of experimented composition thermally treated at 800 °C, 900 °C, 1000 °C is presented in figure 5.

The grain sizes of samples free of boric acid, DPI and DP11, are smaller than the others. This fact could be explained by agglomerates formation. The boric acid in the forsterite samples emphasizes the particles aggregation; due to agglomeration, there could not be stabilized a correlation between grain size and synthesis temperature.

The mean grain sizes of all treated samples with boric acid were situated in the 0.021-17.604 μm range, confirming that this technique measures the agglomerates and not individual particles. TEM measurements confirm the agglomerates formation at low temperatures. For this reason, the analyses of grain size distribution for samples thermally treated at higher temperatures were not realized.

CONCLUSIONS

Nanoforsterite was successfully synthesized by solid state reaction from basic magnesium carbonate and silicon dioxide with and without boric acid and a small excess of silicon dioxide. The XRD patterns showed that forsterite represents the main crystalline phase in samples thermally treated at 1350 °C. The forsterite crystals are well crystallized and the sizes are in the nanometer range. At this temperature, only enstatite as crystalline phases is detected. Small amounts of periclase and enstatite at 1200 °C and 1300 °C temperatures are identified. The mainly crystalline phase in samples fired at low temperatures (800 °C, 900 °C and 1000 °C) is periclase. The crystallites sizes calculated by Scherrer formula for samples fired at high temperatures fall in the nanometer interval. The particles sizes of the treated samples measured by particle size analyzer were situated both in nano and micrometer interval due to the presence of the agglomerates. TEM measurements evidenced the morphology and sizes of forsterite crystals and agglomeration of particles; the size of the individual particles is in the nanometer range.

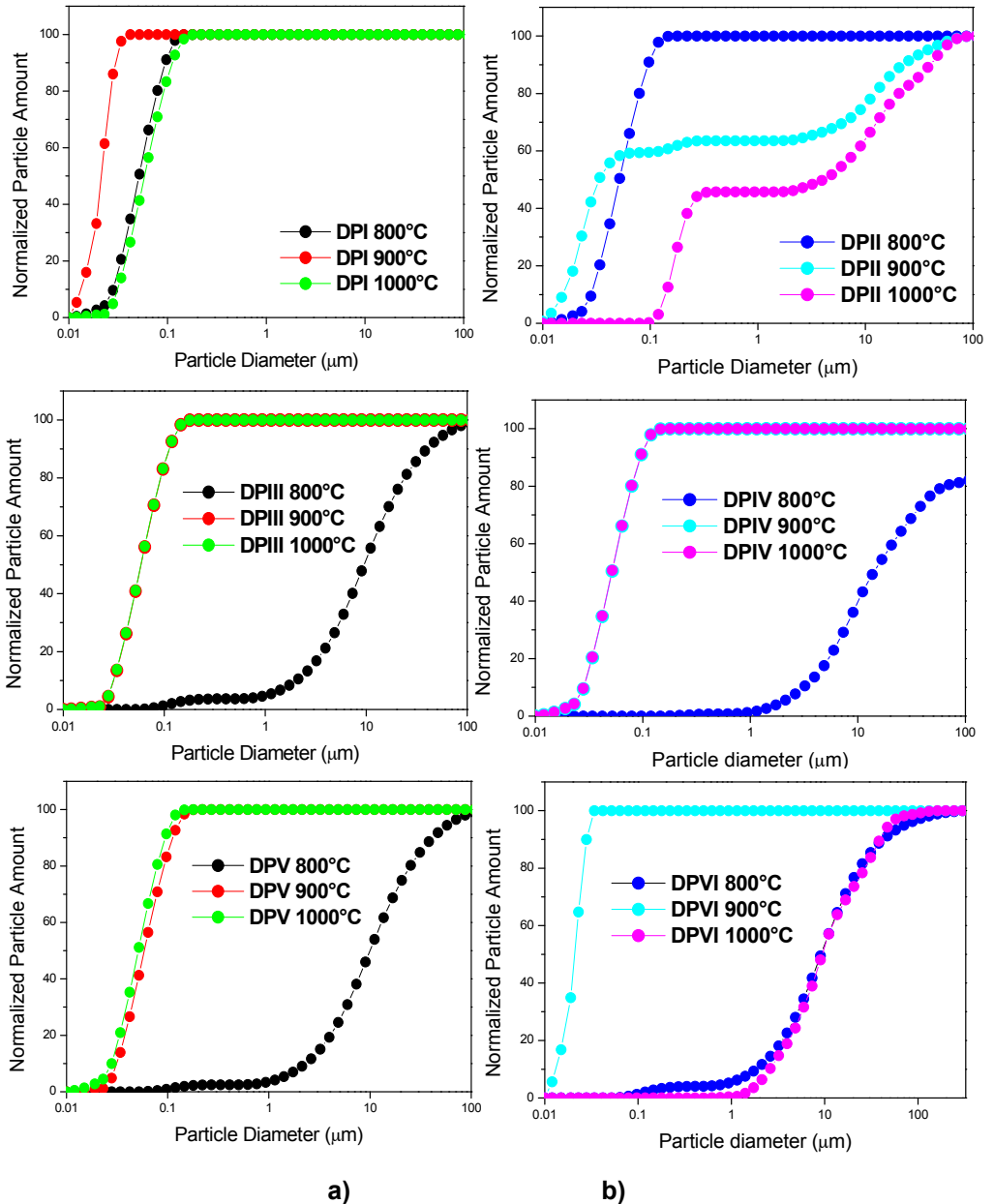


Figure 5. Grain size distributions (cumulative curves) for the forsterite nanopowders synthesized at 800 °C, 900 °C and 1000 °C, (a) samples DPI, DPIII and (b) DPV and DPII, DPIV and DPVI, respectively

EXPERIMENTAL SECTION

Samples preparation

Forsterite (Mg₂SiO₄) powders were synthesized by solid state reaction from basic magnesium carbonate and silicon dioxide. The MgO/SiO₂ molar ratio was established at 2:1, 2:1.05 and 2:1.1. In order to realize a complete reaction between compounds, avoiding the MgO (periclase) presence, and to study the influence of silicium on forsterite biocompatibility a small excess of SiO₂ was added. Boric acid in small quantity was used as a mineralizer. The six mixtures were designed and prepared in laboratory. DPI, DPIII and DPV samples were prepared in a molar ratio of MgO : SiO₂ 2:1.05, whereas in DPII, DPV and DPVI samples the molar ratio was 2:1.10. H₃BO₃ was added, 0.4%wt in DPIII and DPV, and 0.8%wt in DPV and DPVI, respectively.

A dry homogenization and mechanical activation 4 hours in a Pulverisette laboratory ball mill at ratio material/balls of 1/1.3 was performed. The mean grain size of raw mixtures is ranged between 50-60 nm. The raw mixtures were thermally treated at 800 °C, 900 °C, 1000 °C, 1200 °C, 1300 °C and 1350 °C with a heating rate of 2 °C/min and one hour plateau at maximum temperature.

The schematic flow chart for obtaining forsterite nanometer powder is presented in figure 6.

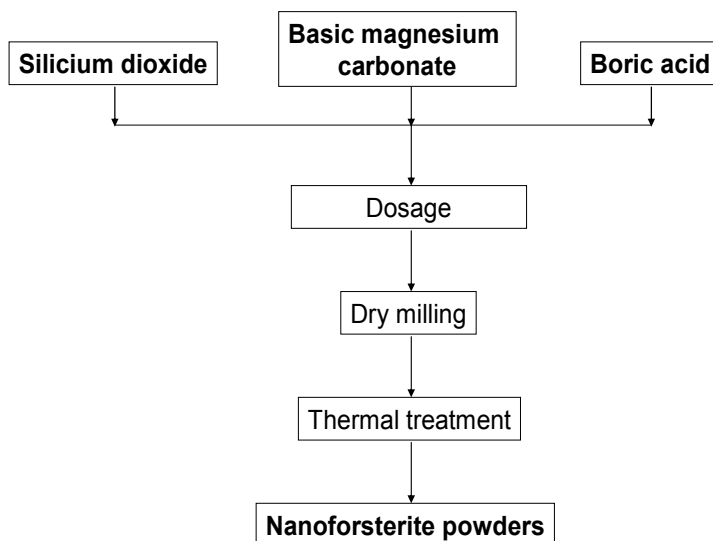


Figure 6. Schematic flow chart of the nanoforsterite synthesis

CHARACTERIZATION METHODS

The prepared materials were characterized by specific oxide materials methods.

X-ray diffraction (XRD)

XRD measurements were performed by a Shimadzu XRD-6000 diffractometer, using CuK α radiation ($\lambda=1.5418$ Å), with Ni-filter with a speed of 2°/ min. Scans were conducted from 10 to 90°.

Crystallite size was calculated from XRD data using the Scherrer approximation (Cullity, 1978), according to equation (1):

$$D = K\lambda / h_{1/2} \cos\theta \quad (1)$$

where d is the crystallite size, as calculated for the (hkl) reflections, λ is the wavelength of CuK α radiation, and k is the broadening constant varying with crystal habit and chosen as 0.9 [21].

Particle size analyses

A Shimadzu Sald-7101 laser granulometer was used for investigating the grain size distribution of raw mixtures and forsterite powders. Using this apparatus, serial measurements based on the same measurement principle are possible for particle changing across the 10 nm to 300 μ m measurement range.

Transmission Electron Microscopy (TEM)

The size and shape of forsterite crystallites were investigated by transmission electron microscopy (TEM) on HITHACHI H-7650 equipment.

REFERENCES

1. M. Diba, Q.-M. Goudouri, F. Tapia, A.R. Boccaccini, *Current Opinion in Solid State and Materials Science*, **2014**, *18*, 147.
2. M.A. Naghiu M. Gorea, F. Kristay, M. Tomoaia-Cotisel, *Ceramics – Silikáty*, **2014**, *58(4)*, 303.
3. M.A. Naghiu, M. Gorea, E. Mutch, F. Kristaly, M. Tomoaia-Cotisel, *J. Mater. Sci. Technol.*, **2013**, *29*, 628

4. C.Y. Tan, R. Singh, Y.C. Teh and Y.M. Tan, *Int. J. Appl. Ceram. Technol.*, **2015**, *12*, 437-442.
5. S.A. Hassanzadeh-Tabrizi, A. Bigham, M. Rafienia, *Materials Science and Engineering C*, **2016**, *58*, 737.
6. M. Kharaziha, M.H. Fathi, *Ceram. Int.*, **2009**, *35*, 2449.
7. M. Kharaziha, M.H. Fathi, *Journal of the Mechanical Behavior of Biomedical Materials*, **2010**, *3*, 530.
8. K.P. Sanosh, A. Balakrishnan, L. Francis, T.N. Kim, *Journal of Alloys and Compounds*, **2010**, *495*, 113.
9. M.H.E. Martin, M., C. K. Ober, C. R. Hubbard, W. D. Porter, O. B. Cavin, *Journal of the American Ceramic Society*, **1992**, *75*, 1831.
10. O. Yamaguchi, Y. Nakajima, K. Shimizu, *Chem. Lett.*, **1976**, *5*, 401.
11. Y. Chen, J. Yu, J. Gao, *Bull. Chin. Ceram. Soc.*, **2012**, *31*, 622.
12. M. Ando, K. Himura, T. Tsunooka, I. Kagomiya, H. Ohsato, *Jpn. J. Appl. Phys.*, **2007**, *46*, 7112.
13. L. Chen, G. Ye, Q. Wang, B. Blanpain, A.Malfiet, M. Guo, *Ceram. Int.*, **2015**, *41*, 2234.
14. S. Sano, N. Saito, S. Matsuda, N. Ohashi, H. Haneda, Y. Arita, M. Takemoto *J. Am. Ceram. Soc.*, **2006**, *89*, 568.
15. A.V. Belyakov, N.T. Andrianov, S. S. Strel'nikova, *Inorg. Mater.*, **2012**, *48*, 176.
16. M. Gorea, M.A. Naghiu, M. Tomoiaia-Cotisel, G. Borodi, *Ceramics – Silikáty*, **2013**, *57(2)*, 87.
17. G.W. Brindley, R. Hyami, *Philos Mag.*, **1965**, *12*, 505.
18. F. Tavangarian, R. Emadi, *Powder Technology*, **2010**, *203*, 180.
19. L. Chen, G. Ye, W. Zhou, J. Dijkmans, B. Sels, A. Malfiet, M. Guo, *Ceramics International*, **2015**, *41*, 12651.
20. F. Tavangarian, R. Emadi, *Materials Research Bulletin*, 2010, *45*, 388.
21. H.P. Klug, L.E. Alexander, "X-ray diffraction procedures", Wiley, New York, USA, **1956**.

*Dedicated to Professor Luminița Silaghi-Dumitrescu
on the occasion of her 65th anniversary*

MATHEMATICAL MODELING OF THE VARIATION IN WATER QUALITY ALONG THE NETWORK OF WATER SUPPLY OF SATU MARE MUNICIPALITY, ROMANIA

**THOMAS DIPPONG^a, CRISTINA MIHALI^a, FIRUTA GOGA^{*,b},
GHEORGHE ARDELEAN^c**

ABSTRACT. Drinking water quality in the water network supply of the Satu Mare municipality was investigated, aiming to quantify the variation of some physico-chemical parameters with the distance from the water treatment plant. Usually, water quality decreases in the drinking water distribution systems due to unwanted physical, chemical and biochemical reactions occurring in the distribution systems. The variation of the main physicochemical parameters of drinking water such as turbidity, pH, oxidability, chlorides and free residual chlorine concentration, conductivity, iron content, water hardness and nitrates concentrations was studied. The drinking water samples were collected weekly during the year 2013 from 16 fixed points of the distribution network of Satu Mare. The statistical analysis of the results was accomplished and presented. Univariate and bivariate regression models of the water quality variation with the distance from the water treatment plant were proposed. The distance from the water treatment plant to the each sampling point was established by measuring the length of pipelines crossed by water until that sampling point. The sampling points were chosen on the main routes of water distribution pipes in the main districts of the city of Satu Mare. These mathematical models attempted to capture the variation of the physico-chemical parameters of drinking water along the water network supply. An increasing trend of turbidity, water conductivity, water hardness and nitrates content of water was observed while the free chlorine content showed a decreasing trend.

Keywords: *drinking water; free chlorine; supply network; oxidability; turbidity.*

^a *Technical University of Cluj Napoca, Faculty of Science, Department of Chemistry and Biology, 76 Victoriei Street, 430122, Baia Mare, Romania*

^b *Babeş-Bolyai University, Faculty of Chemistry and Chemical Engineering, 11 Arany Janos str., RO-400028, Cluj-Napoca, Romania*

^c *Technical University Of Cluj Napoca, Faculty Of Science, Department Of Mathematics And Computer Sciences, 76 Victoriei Street, 430122, Baia Mare, Romania*

* *Corresponding author: fgoga@chem.ubbcluj.ro*

INTRODUCTION

Water is an important component of the environment and it is absolutely necessary to life, including human life. Access to safe drinking water is fundamental to human life, health and wellness. Therefore, obtaining drinking water with an adequate quality is an important objective of urban and rural communities. The assessment of water quality is an essential aspect in the case of raw water sources and also of drinking water. A water quality index (WQI) is a common tool for the quantitative assessment of water quality [1,2]. This activity needs synergetic actions and efforts from many partners such as: water resources managers, water plants, water distribution systems, communities and water consumers. To gain a proper understanding and control of water quality, the partners might bring together their different scientific backgrounds towards a comprehensive understanding of all the parameters involved [3,4].

The treatment process of raw water for obtaining drinking water includes a chemical oxidation aiming to ensure the disinfection and oxidation of undesired compounds. Through chemical oxidation the taste and odor of water are improved and micro-pollutants are removed [5]. Chlorine is one of the most used chemical oxidants in the disinfection process due to its very effective disinfectant action [6,7,8]. The chlorine dose in the water is selected depending on the chemical and microbiological characteristics of the treated water (organic substances content and microbiological load) in order to ensure a residual chlorine content after the disinfection process at the drinking water entrance in the distribution network system [9,10]. The most studied halogenated disinfection by-products are trihalomethanes and haloacetic acids. These compounds could be found in low concentrations in the water treated by chlorine if it also contains organic substances [11,12].

Water quality usually degrades with time and space in the drinking water distribution systems. The water quality decreases due to unwanted physical, chemical and biochemical reactions that occur when the residence time in the distribution systems is increased [13,14].

Water quality may decrease in the distribution system of drinking water and consequently the water quality has to be assessed also in several points of the water supply network. The network of drinking water supply is a complex installation composed of pumps, reservoirs, pipes, that contains zones of consumption and portions where water sometimes stagnates [15].

Corrosion processes could occur in the water supply network generating corrosion scale on the inner walls of the pipes in the water distribution system. The physico-chemical properties of the corrosion scale depend on the metallic material of pipes, on the water quality transported through the pipes and also on the hydraulic conditions. The water quality parameters that influence the corrosion process are: pH, natural organic matter, temperature, oxygen content etc [16,17].

Satu Mare, located in the North-West of Romania is a relative small municipality, with about 100000 residents. The water source for drinking water is groundwater extracted from wells with a depth of 110 - 120 m. The treatment process consists of filtration to reduce the iron and manganese content and chlorination for water disinfection. Residual chlorine should prevent the reinfection during the leakage of drinking water through the distribution network. Nitrates occur in groundwater related to human activities such as fertilizers application. The drinking water samples were collected weekly during a year (2013), from 16 fixed points of the distribution network of Satu Mare. 1728 physico-chemical analyses were performed in order to evaluate the variation tendency along the main distribution direction in the distribution network. The distance from the water treatment plant to the sampling points was measured along the pipelines travelled by water to each sampling points. The sampling points were selected along the main distribution routes that ensures the water supply in the main districts of the city of Satu Mare.

The experimental results were statistically analyzed with the purpose of finding the best mathematical models that most accurately describe the variation of the main physico-chemical parameters of drinking water in the distribution network [18,19]. Mathematical models which describe the variation of the main physico-chemical parameters of drinking water with the distance from water treatment in the distribution network system were proposed.

RESULTS AND DISCUSSION

Samples were taken during the year 2013 from 16 sampling points from the drinking water network of Satu Mare as shown in Fig. 1.

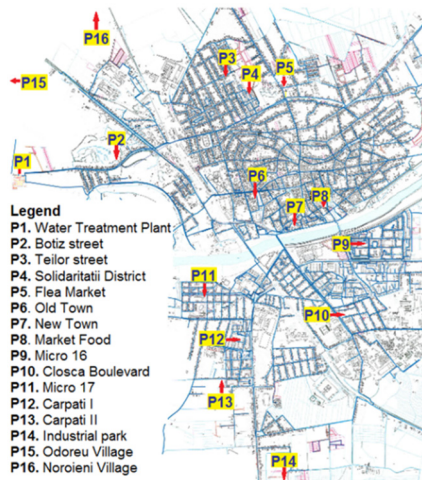


Figure 1. The locations of the sampling points in the network of drinking water supply of Satu Mare city

The average values of the physicochemical parameters were calculated and presented in Table 1. The studied physicochemical parameters of the drinking water are under the maximum allowable limit according to Romanian legislation. The obtained average values presented in Table I were compared with the maximum allowable limit by law 458/2002 and 311/2004 (of Romanian legislation). Physico-chemical parameters of drinking water in the distribution system were analyzed. The extent of their changing depending on the distance from the water plant to the sampling point was investigated.

Table 1. Average values of the main physicochemical parameters from 16 sampling points in the water distribution network.

Point	Turbidity /NTU	pH	Cond./ $\mu\text{S/cm}$	Oxidab/ mgO_2/L	$c_{\text{Cl}^-}/\text{mg/L}$	Total hardness / $^\circ\text{dh}^a$	$c_{\text{FreeCl}_2}/\text{mg/L}$	$c_{\text{NO}_3^-}/\text{mg/L}$	$c_{\text{Fe}}/\text{mg/L}$	Distance/ <i>m</i>
P1	0.110	7.24	323.9	0.087	4.52	8.84	0.43	0.313	0.0005	0.0000
P2	0.096	7.34	335.4	0.101	4.81	8.74	0.35	0.338	0.0029	5110.810
P3	0.081	7.34	336.8	0.132	5.05	8.60	0.28	0.343	0.0025	4010.821
P4	0.103	7.37	338.1	0.166	5.35	8.57	0.24	0.348	0.0031	4318.333
P5	0.098	7.30	339.9	0.261	5.67	8.53	0.16	0.354	0.0037	4789.037
P6	0.103	7.30	335.2	0.111	4.62	8.51	0.35	0.329	0.0038	4487.877
P7	0.116	7.31	336.8	0.123	4.84	8.48	0.29	0.336	0.0046	4583.907
P8	0.120	7.55	338.1	0.137	5.03	8.44	0.25	0.341	0.0063	6600.837
P9	0.115	7.37	338.7	0.148	5.25	8.43	0.20	0.346	0.0063	5697.981
P10	0.121	7.34	340.8	0.216	5.51	8.42	0.12	0.353	0.0063	5308.837
P11	0.120	7.30	335.2	0.123	4.96	8.64	0.33	0.335	0.0041	3341.417
P12	0.071	7.32	336.8	0.135	5.19	8.54	0.27	0.341	0.0049	3978.653
P13	0.166	7.38	339.0	0.171	5.34	8.49	0.17	0.346	0.0056	4039.944
P14	0.152	7.87	343.6	0.249	5.70	8.37	0.10	0.352	0.0157	8028.581
P15	0.188	7.41	342.2	0.177	5.40	8.55	0.11	0.348	0.0070	4878.448
P16	0.234	7.28	350.2	0.265	5.83	8.69	0.10	0.365	0.0124	11563.04
Limit ^b	≤ 5	6.5-9.5	≤ 2500	≤ 5	≤ 250	Min 5	0.1-0.5	≤ 50	0.2	

^a Total hardness is expressed in $^\circ\text{dh}$ -German degree; ^b the maximum allowable limit or range according to Romanian legislation (Law 458/2002 and 311/2004) .

Figure 2 shows the concentration of the residual free chlorine in three series of the sampling points arranged in the ascending order of the distance from the water plant. As the distance from the water plant increases, the concentration of residual free chlorine in the distribution system decreases. At lower values the regrowth of bacterial could occur. If the chlorine concentration in water distribution system falls below 0.1 mg L^{-1} , it is

necessary to install chlorination systems to restore free residual chlorine in the legal range of 0.1-0.5 mg L⁻¹. At higher values, the reaction of chlorine with dissolved organic matter and bromine ions take place generating potentially harmful disinfection by-products like trihalomethanes [9]. The excess of chlorine confers the drinking water an unpleasant specific taste and odor. The decrease of chlorine concentration in the water distribution network is due both to the reaction with natural organic matter quantified by water oxidability that occurred in the bulk phase and to the reaction with iron released from pipe corrosion that took place to the boundary layer at the pipe wall [20]. Similar variations were reported by Mandel [21] after a continuous monitoring of the free chlorine concentration in the distribution network over the course of two weeks. Mandel concluded that chlorine concentration measurements are much less homogeneous, but rapid and important variations such as peaks are generally seen on all probes.

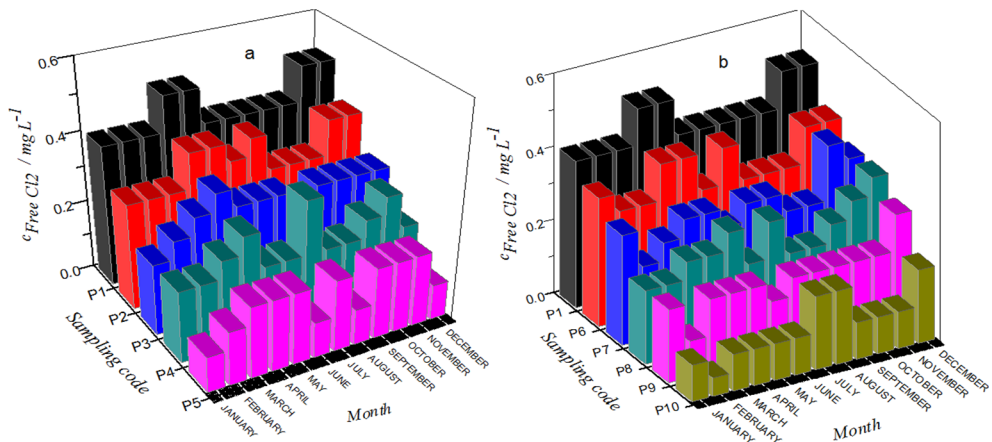


Figure 2. Evolution of free residual chlorine concentration between the sampling points P1-P2-P3-P4-P5 (a) and P1-P6-P7-P8-P9-P10 (b)

The electric conductivity of water is a measure of its content in ionic substances. In the case of two of the three series of sampling points (Fig. 3) the electric conductivity first showed a slight increase with the distance in the distribution network followed by a slight decrease. These fluctuations could be explained by the possible solubilization-deposition processes of some ionic substances contained in the corrosion scale of the pipes [16,20,21].

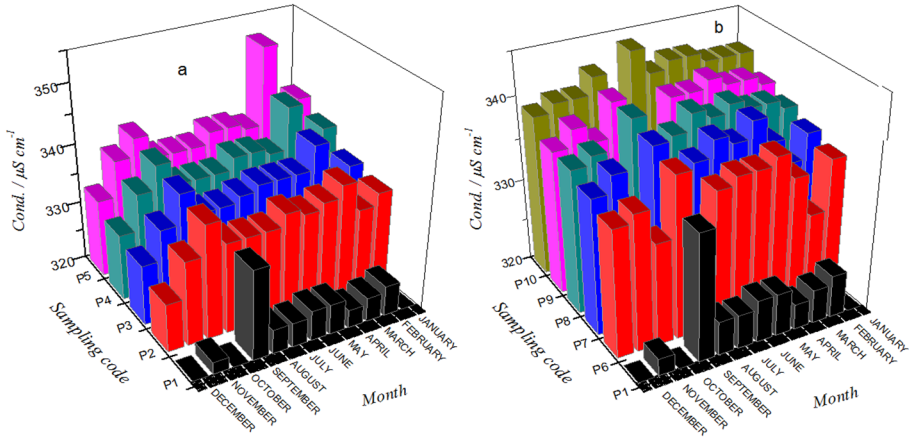


Figure 3. Evolution of the electric conductivity between the sampling points P1-P2-P3-P4-P5 (a), P1-P6-P7-P8-P9-P10 (b)

The water oxidability that is due to the remaining organic substances in the water after the chlorination step of the water treatment showed a tendency to increase along the water supply network (Fig. 4). This increasing trend was observed for the majority of the sampling points in the case of all the sequences: P1-P2-P3-P4-P5 and P1-P11-P12-P13-P14. Water oxidability varied between 0.05 and 0.3 $\text{mg (O}_2\text{)}\text{L}^{-1}$. The variation of water quality parameters such as pH, alkalinity, dissolved oxygen, natural organic matter, microorganisms, temperature, could disturb the solid-liquid equilibrium between corrosion scale and water phase, and consequently iron is released in the drinking water transported through the distribution systems [16.21].

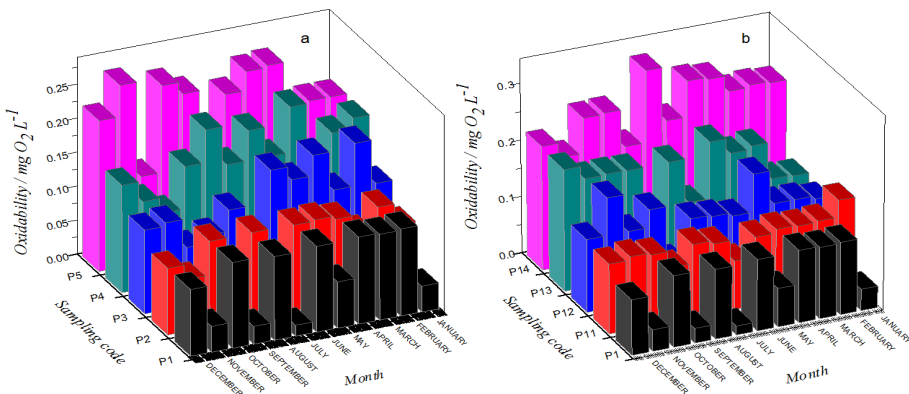


Figure 4. Evolution of oxidability between the sampling points P1-P2-P3-P4-P5 (a), P1-P11-P12-P13-P14 (b)

Mathematical models

A mathematical model is a mathematical description of a physical, chemical or biological state or process. Using a model we can design better experiments and interpret the results. When we fit a model to the data, we obtain the best-fit values that we can interpret in the context of the model that could guide further experiments. The mathematical models for the variation of the conductivity and free chlorine depending on the distance from the sampling points to the water treatment plant are given by nonlinear functions generated by the program, and the coefficients were determined.

The mathematical model for the variation of conductivity depending on the distance of sampling points P1-P11-P12-P13-P14 to the water plant ($r^2=0.850$, $F = 106.15$) is given by the equation (1):

$$f(x)=a + bx^{2.5} + cx^3 + dx^{0.5} \tag{1}$$

where x is the distance and the coefficients are:

$$a = 323.917, \quad b = 2.196 \cdot e^{-8}, \quad c = 2.241, \quad d = 0.0955$$

The mathematical model for the variation of free chlorine concentration depending on the distance of sampling points to the water plant ($r^2=0.8726$, $F=43.683$) is given by the equation (2). The mathematical model describing the evolution of free chlorine concentration with the distance was a nonlinear function.

$$f(x) = a + bx^{0.5} + cx + dx^{1.5} + ex^2 + fx^{2.5} \tag{2}$$

$$a = 0.433, \quad b = 9.793, \quad c = -0402 \quad d = 10.00347, \quad e = 2.478e^{-5}, \quad f = -6.429e^{-8}.$$

For the study of variation of distance to the water plant depending on free chlorine and the chloride concentrations, a two independent variables model was elaborated using *TableCurve3D* program. The graph resulted is presented in Fig. 5 and it is a nonlinear equation.

The mathematical model for variation of chloride concentration depending on the distance to the water plant and free chlorine concentration ($r^2=0.6894$, $F=48.105$) is given by the function (3):

$$z = f(x,y) = a + b \ln x + c(\ln x)^2 + e/y + f/y^2 \tag{3}$$

and the values of coefficients are:

$$a = 4.9889, \quad b = -1.112, \quad c = 0.0522, \quad e = 4.884, \quad f = -8.854$$

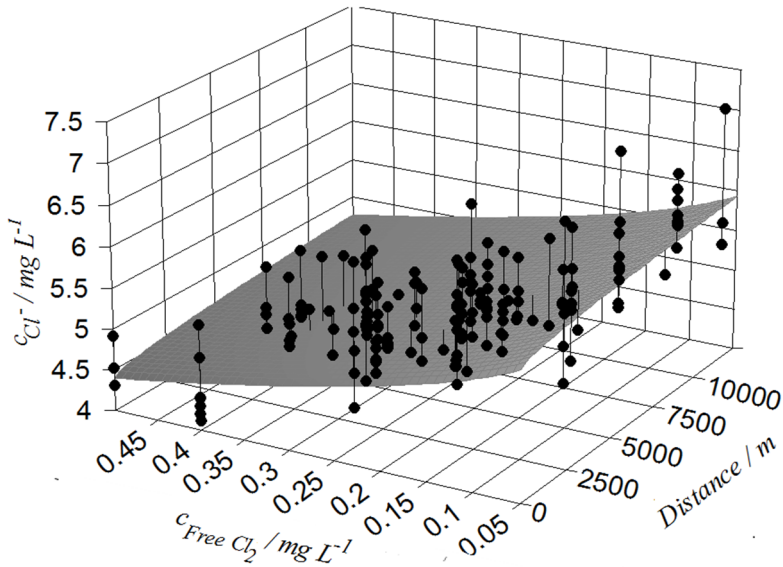


Figure 5. Variation of of chloride concentration (z) depending on the distance (x) to the water plant (P1) and free chlorine concentration (y)

The concordance between the results generated by the mathematical model and the experimental ones shows that we can use the model to approximate the value of conductivity when we know the value of water hardness and the distance to the water plant, by using the function $f(x,y)$.

The mathematical model for variation of distance to the water plant depending on conductivity and the total hardness ($r^2=0.7138$, $F=76.9022$) is given by the function (4):

$$z = f(x,y) = a + bx + c/y + d/y^2 \quad (4)$$

The values of the coefficients are:

$$a = 201.744, \quad b = 0.00759, \quad c = 2032.142, \quad d = -8423.956.$$

The corresponding graph is presented in Fig. 6. An increase tendency could be explained by the substances dissolved form the pipes walls depositions that increased with the distance traveled by water. The increase of the conductivity is more evident for lower water hardness due to a higher power of solvation of the soft water.

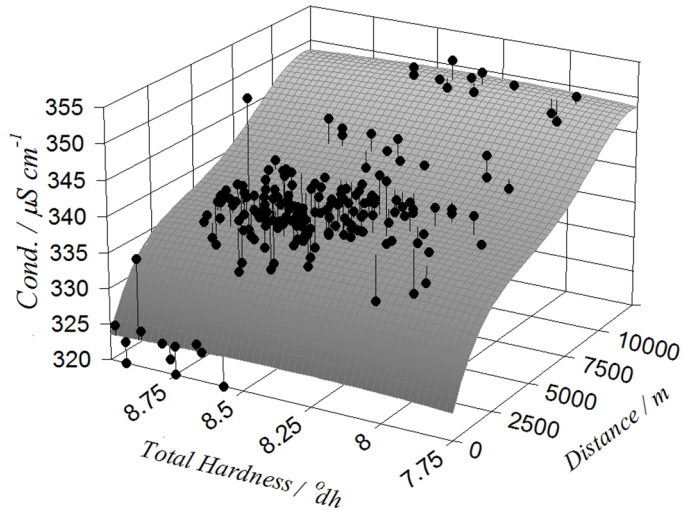


Figure 6. Variation of conductivity (z) depending on the distance (x) of the sampling points to the water plant and water total hardness (y) (°dh – german degree of hardness)

Usually, variation of the water demand occurs in the water distribution network. The variation of temperature and pressure modify the chemical equilibrium in which carbon dioxide is involved associated with carbonates depositions or solvation of previous carbonate deposits. At the end of the water distribution network, an increase of conductivity with 10-15 $\mu\text{S}/\text{cm}$ was observed.

CONCLUSIONS

The paper is a comprehensive study that investigates the way in which the main physico-chemical parameters of water are influenced when it travels through the water supply network in Satu Mare municipality. An increase of turbidity was observed with the increase of the distance from the water treatment plant to the sampling points. Conductivity showed a slight increase along the water supply network.

The residual chlorine concentration decreased with the distance from the drinking water plant. Also the nitrates concentration registred a decrease. Other indicators of water quality such as pH, oxidability and water hardness showed slight fluctuations compared with the initial value registred at the entrance in the water distribution network.

The physico-chemical parameters showed a very good quality of water at the entrance in the distribution system as well as at its end.

Also during the water passing through the pipes, fluctuations of the parameter occurred due to the presence and action of free chlorine that oxidized a part of the easily oxidizable substances present in water

The mathematical models developed in the present work show the variation of some physicochemical parameters, and can be used to a good approximation of these parameters, for drinking water in the network of Satu Mare city.

EXPERIMENTAL SECTION

Water sampling and analysis

The water samples were collected weekly in 16 points of the distribution network of drinking water in Satu Mare municipality. The analysis of the physicochemical parameters was carried out within a maximum of 48 hours after the sampling. Turbidity was measured immediately after sampling using a portable turbidimeter. The physico-chemical parameters analysed were: turbidity, pH, electric conductivity, oxidability, chloride, free chlorine, total hardness, iron and nitrate anion.

The studied microbiological parameters were: *Escherichia coli* (according to STAS 3001-91), faecal streptococci (STAS 3001-91), coliforms (ISO 4831/2009 European standard) and total number of germs (TNG) according to SR EN ISO 6222/2004. These microorganisms were absent in the samples of drinking water.

pH was determined using a Hanna Instruments pH meter HI 253 equipped with a combined pH electrode according to EN ISO10523 -2012 standard. The electric conductivity was measured using a WTW INOLAB 740 conductometer according to SR EN 27888/1997.

The measurements of water samples turbidity were performed with a WTW portable turbidimeter, model 355 IR according to the Romanian standard STAS 6323/88. Turbidity was expressed in NTU units. Oxidability was determined by back titration with potassium permanganate in presence of sulfuric acid after the addition of a known amount of oxalic acid (SR EN ISO 8467:2001). Chloride concentration in drinking water was measured by precipitation titration with silver nitrate according to ISO 9297-2001 standard while free chlorine was analysed by titration with methyl orange solution in acidic medium (according to the STAS 6364/78 standard). Iron was analysed by spectrometry according to SR ISO 6332/2011 standard.

The analysis of nitrate was made by the spectrophotometric method according to the SR ISO 7890-1-1998 standard using a UV-VIS T-60 PG Instruments spectrophotometer.

Water hardness was measured by EDTA titrimetric method according to SR ISO 6059/2008 standard.

Models development

Aiming to study the variation of the different physico-chemical parameters of water in the sampling points depending on distance from the sampling points to the water treatment plant, we used TableCurve Windows program, which applies the nonlinear regression method in order to obtain best-fit values of the parameters. Regression analysis was used to develop empirical models that relate some physico-chemical parameters of water such as oxidability, conductivity, free chlorine concentration to the distance from the water treatment plant. Also some correlations among the parameters were developed.

REFERENCES

1. 1. F. Yan, L. Liu, Y. Li, Y. Zhang, M. Chen, X. Xing, *Ecological Indicators*, **2015**, *57*, 249-258.
2. X. Zhao, W.H. Hool, G. Yun, *Water Research*, **2002**, *36*, 851-858.
3. M. Abtahi, N. Golchinpour, K. Yaghmaeian, M. Rafiee, M. Jahangiri-rad, A. Keyani, R. Saeedi, *Ecological Indicators*, **2015**, *53*, 283-291.
4. A. Scheili, M.J. Rodriguez, R. Sadiq, *Science of the Total Environment*, **2015**, *508*, 514-524.
5. M. Deborde, U von Gunten, *Water Research*, **2008**, *42*, 13-51.
6. S. Poleneni, E.C. Inniss, *Journal of Water Resource and Protection*, **2013**, *5*, 35-41.
7. M. Chiba, A. Sinohara, M. Sekine, S. Hiraishi S., *Journal of radioanalytical and Nuclear Chemistry*, **2006**, *269*, 519-526.
8. M. Lim, C. Delehomme, J. Capece, "Removal of Residual Chlorine from Drinking-Water by Solar Radiation (UV) and Activated Carbon Filtration", Intelligentisia International, Inc. **2008**.
9. P. Hua, E. Vasyukova, W. Uhl W., *Water Research*, **2015**, *75*, 109-122.
10. I. Fisher, G. Kastl, A. Sathasivan A., *Water Research*, **2012**, *46*, 3293-3303.
11. C.M. Shanks, J-B. Sérodes, M.J. Rodriguez, *Water Research*, **2013**, *47*, 3231-3243.
12. S. Parvez, Z. Rivera Núñez, A. Meyer, J.M. Wright, *Environmental Research*, **2011**, *111*, 499-509.
13. H. Tong, P. Zhao, H. Zhang, Y. Tian, X. Chen, W. Zhao, M. Li, *Chemosphere* **119** (2015) 1141-1147.

14. M. Al-Zahrani, K. Moied, *Water Science & Technology: Water Supply* **14** (2014) 1076-1086.
15. M. Benallouch, G. Schutz, D. Fiorelli, M. Boutayeb, *Journal of Process Control*, **2014**, *24*, 924-938.
16. F. Yang, B. Shi, J. Gu, D. Wang, M. Yang, *Water Research*, **2012**, *46*, 5423-5433.
17. B. Majkić-Dursun, A. Petković, M. Dimkić, *Journal of the Serbian Chemical Society*, **2015**, *80*, 947-957.
18. T. Todinca, M. Geantă, "Modeling and simulation of chemical processes", Politehnica Publishing house, Timișoara, Romania, **1999**.
19. S.B. Vardeman, "Statistics for engineering problem solving", Politehnica Publishing house, Timișoara, Romania, **1994**.
20. L.A. Rossman, "Water Supply and Water Resources Division, National Risk Management Research Laboratory", EPANET 2, Cincinnati, OH 45268, **2000**.
21. P. Mandel, M. Maurel, D. Chenu, *Water Research*, **2015**, *87*, 89-78.
22. Y. Zhu, H. Wang, X. Li, C. Hu, M. Yang, J. Qu, *Water Research*, **2014**, *60*, 174-181.
23. C-Y. Peng, G.V. Korshin, L. Richard R.L. Valentine, A.S. Hill, M.J. Friedman, H. Steve, S.H. Reiber S.H., *Water Research*, **2010**, *44*, 4570-4580.
24. X. Li, H. Wang, Y. Zhang, C. Hu, M. Yang, *International Biodeterioration & Biodegradation*, **2014**, *96*, 71-79.

*Dedicated to Professor Luminița Silaghi-Dumitrescu
on the occasion of her 65th anniversary*

INFLUENCE OF THE THERMAL TREATMENT ON THE COLOUR OF $RO \cdot Al_2O_3$ (R=Co, Ni) TYPE SPINEL PIGMENTS PREPARED BY A MODIFIED SOL – GEL METHOD

**FIRUTA GOGA^a, ROXANA DUDRIC^b,
LILIANA BIZO^a, ALEXANDRA AVRAM^{a,*},
THOMAS DIPPONG^c, GABRIEL KATONA^a,
GHEORGHE BORODI^d, ANDREEA ANTON^a**

ABSTRACT. This paper presents the results obtained through the synthesis of spinel - structured, ceramic pigment nanopowders ($CoAl_2O_4$ si $NiAl_2O_4$), using a modified sol – gel method. This study focuses on the influence of the thermal treatment, applied during gel calcination, on the properties of the obtained powders. The behavior of the dried gels during calcination was studied by differential thermal analysis. The formation of the spinel structure after the thermal treatment, was analyzed using X-ray diffraction. The colour of the powders was characterized by UV–VIS spectroscopy, determining the absorption spectra. Additionally, the trichromatic coordinates were determined, and the corresponding pigment positions were fixed on the chromaticity diagram.

Keywords: *ceramic pigment nanopowders, cobalt spinels, nickel spinels, sol–gel method, sucrose, pectin.*

^a Babeş-Bolyai University, Faculty of Chemistry and Chemical Engineering, 11 Arany Janos Street, RO-400028, Cluj-Napoca, Romania

^b Babeş-Bolyai University, Faculty of Physics, 1 M. Kogalniceanu Street, RO-400084, Cluj-Napoca, Romania

^c Technical University of Cluj-Napoca, Faculty of Science, Department of Chemistry and Biology, 76 Victoriei Street, RO-430122, Baia Mare, Romania

^d National Institute for Research and Development of Isotopic and Molecular Technologies, nr. 103, 67 Donath Street, Cluj-Napoca RO-400293, Cluj-Napoca, Romania

* Corresponding author: aavram@chem.ubbcluj.ro

INTRODUCTION

Oxide materials with a spinel structure are employed in a large number of fields due to their refractory, magnetic, semiconductor, and optical properties [1]. Spinel structured oxides are one of the most important classes of pigments, primarily due to their high thermal and chemical stability and their capacity to “host” different cations, which leads to a great variety of colours and colour shades [2, 3].

Synthetic blue pigments are widely used in the ceramics industry as colouring agents for glazes or porcelain stoneware. The traditional source of blue colour in a ceramic pigment, remains the divalent cobalt ion (Co^{2+}) in the tetrahedral coordination site - Co_2SiO_4 (olivine), $(\text{Co,Zn})_2\text{SiO}_4$ (willemite) and CoAl_2O_4 (cobalt spinel). However, recent publications have focused on the elaboration of aluminate spinels for cyan pigments (one primary colour in the subtractive system) with Ni^{2+} as a chromophore ion [4].

The development of the blue colour, specific to the Co^{2+} and Ni^{2+} chromophores, tetra-coordinated in spinel structures, relies on their inclusion into the “host” crystalline lattice, in a uniform distribution. This raises the necessity for a better homogeneity of the raw materials, as well as a high synthesis temperature to ensure the proper arranging of the crystalline network. In the case of the classical method, based on a mechanical mixture of salts or oxides, reaching a good homogenization proves difficult. Another problem with this approach would be the high temperatures needed in order to obtain the desired colour (over $1200\text{ }^\circ\text{C}$) [5]. Due to these difficulties, unconventional synthesis methods were developed. These methods, such as co-precipitation, hydrothermal synthesis, microemulsion and sol-gel method, utilize advanced homogeneous precursors. The sol-gel method is commonly used in the synthesis of oxide nanomaterials, its advantages consisting of mixing the raw materials at a molecular level, low temperature processing, and a better control over the obtained nanomaterials [6, 7].

The sol-gel method entails the reaction of the precursors in the solution, with the purpose of creating the nanometric units, “sols”, which, further assemble to form a three – dimensional lattice, “gel”. The liquid phase of the gel fills the open pores of the structure. The structure of the gel is uniform, as both the constituent particles and pores are nanometric in scale. This homogeneity ensures an evenness of the materials properties [6].

In the present paper, for the synthesis of the CoAl_2O_4 and NiAl_2O_4 spinels, a modified sol – gel method was applied, using metal nitrates as well as sucrose and pectin as organic precursors. This modified method was successfully utilized in the synthesis of other oxide compounds as nanometric powders [8-10]. Sucrose and pectin are inexpensive materials, as well as nontoxic, making their use instead of other organic components, beneficial.

RESULTS AND DISCUSSIONS

Differential thermal analysis

The diagrams for the two gels are presented in figures 1 and 2. The thermal analysis for the cobalt gel indicates an endothermic process up to 150°C , with a mass loss of approximately 15%, represented by the loss of residual water present in the pores. Between 150 and 548°C , two exothermic processes, with an important mass loss, can be seen. This is due to the calcination of the organic compounds with a formation of volatile components. The first exothermic process, present between $150 - 443^\circ\text{C}$, is more intense, having a mass loss of 60.30%. The second one, seen between $443 - 548^\circ\text{C}$, has a loss of only 9.06%. At temperatures higher than 548°C , the mass loss is insignificant (1.18%).

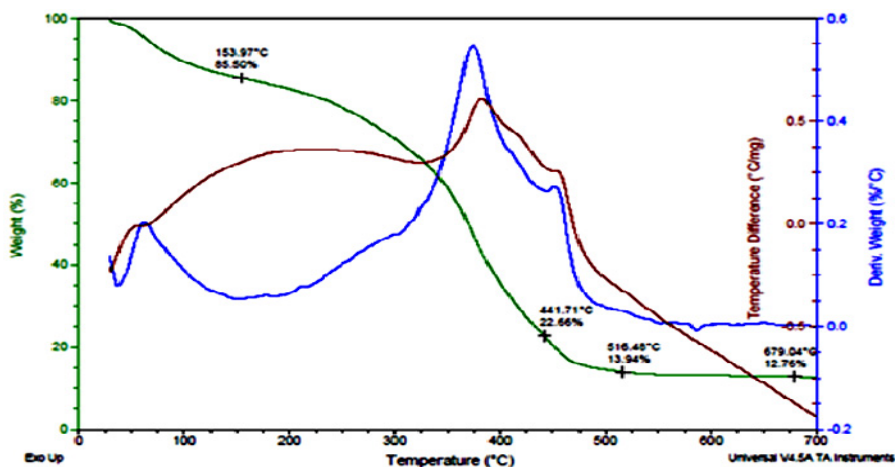


Figure 1. TG – DTG – DTA diagram for the CoAl_2O_4 gel

The thermal behaviour of the NiAl_2O_4 gel is similar to that of CoAl_2O_4 . The residual water is eliminated in two steps, up until 144°C , and the oxidation of the organic compounds takes place between $144 - 520^\circ\text{C}$. It manifests with two exothermic processes, one less intense, at $144 - 190^\circ\text{C}$, and the second one, more so, at $190 - 520^\circ\text{C}$. The mass loss due to the calcination of the organic precursors consists of 77.76%. Prior to 700°C , a small mass loss of 1.03% is attributed to the volatile compounds formed and remained inside the materials pores. According to the thermal analysis, the oxidation and elimination of the organic compounds takes place up until a temperature of 550°C . The thermal treatment on the dried gels was performed at $600 - 1000^\circ\text{C}$, with a 30 minutes plateau at maximum temperature.

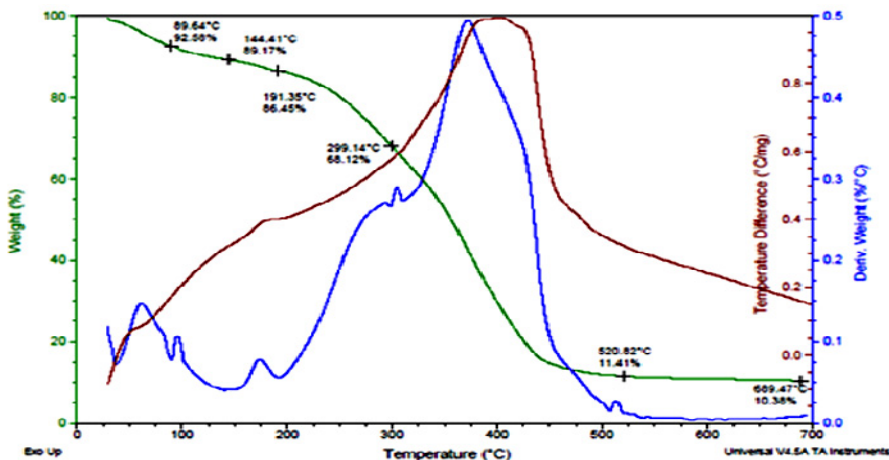


Figure 2. The TG – DTG – DTA diagram for the NiAl_2O_4 gel

X – ray diffraction analysis

X – ray diffraction analysis performed on samples thermally treated at 600, 700, 800 and 1000 °C respectively, are illustrated in figures 3 and 4. The CoAl_2O_4 patterns indicate that all samples are well crystallized, with the spinel structure already evidenced for samples thermally treated at a 600 °C temperature. At higher temperatures, the crystallinity of CoAl_2O_3 is increased. Conversely, the NiAl_2O_4 pattern shows a lower crystallization temperature of the spinel phase. The patterns for the samples thermally treated at lower temperatures, 600 and 700°C, respectively, illustrate only three of the specific reflexes of the spinel structure. This indicates a weak index of crystallization, the amorphous phase being predominant. No other crystalline phases are evidenced. In the case of the powder obtained at 800 °C, (figure 5) there are two spectral lines barely visible that tend to intensify with a longer thermal treatment time. The consolidation of the crystalline structure of NiAl_2O_4 can be seen on the 1000 °C diffraction pattern that shows a high crystallinity index. According to the results presented in [11] the arrangement of the NiAl_2O_4 structure, begins at 900°C. An increase of the spinel structure lattice parameter with the increase of the thermal treatment temperature can be noted for both CoAl_2O_4 and NiAl_2O_4 samples, as presented in table 1.

The sizes of the CoAl_2O_4 crystallites, calculated using the Debye-Scherrer formula, are in the range of 28–39 nm (table 1). The NiAl_2O_4 crystallite sizes are smaller than those of CoAl_2O_4 . The nanometric crystallite sizes represent an important factor in the case of pigments, an increase the coloration capacity being dependent on the specific surface.

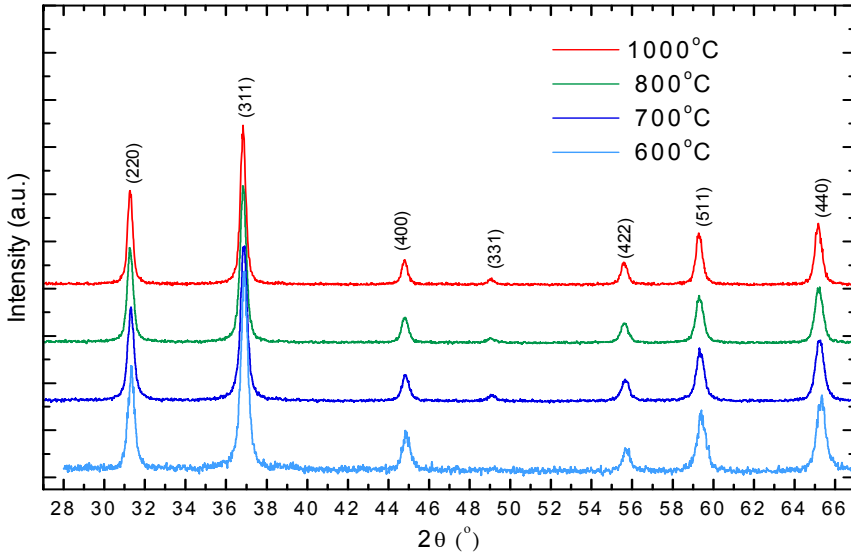


Figure 3. The X-ray diffraction pattern for $CoAl_2O_4$ thermally treated for 30 minutes at 600, 700, 800 and 1000 °C

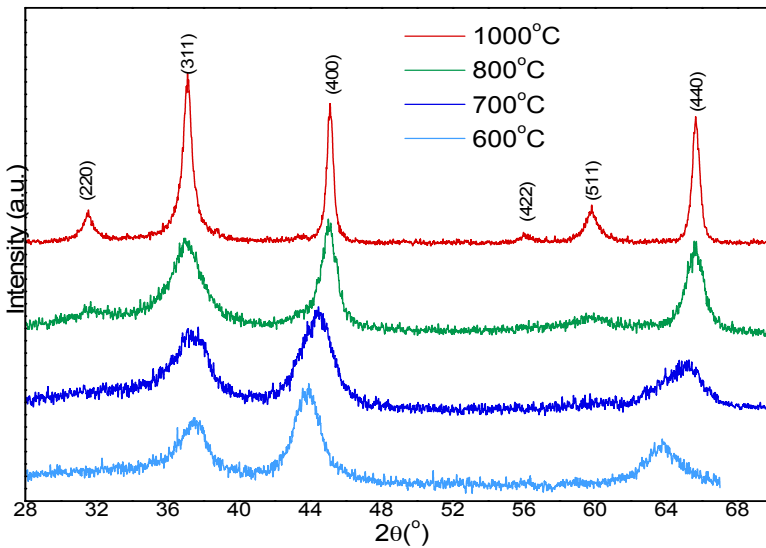


Figure 4. The X-ray diffraction pattern for $NiAl_2O_4$ thermally treated for 30 minutes at 600, 700, 800 and 1000 °C

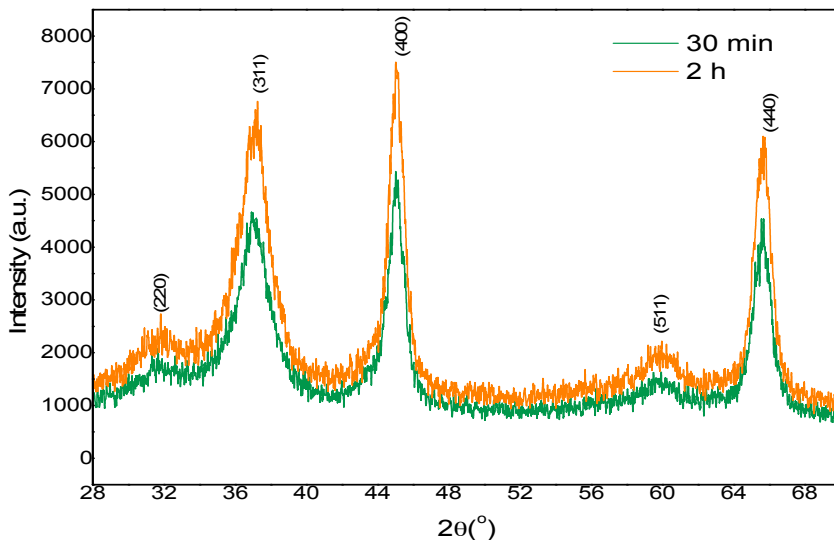


Figure 5. The X-ray diffraction pattern for NiAl₂O₄ thermally treated for 30 minute and 2 hours at 800 °C

Table1. XRD values for the structural lattice parameter and the crystalline particles diameter, correlated to the calcination time

Thermal treatment temperature °C	a (Å)		D (nm)	
	CoAl ₂ O ₄	NiAl ₂ O ₄	CoAl ₂ O ₄	NiAl ₂ O ₄
600°C	8.081		28±1	
700°C	8.092		30±1	
800°C	8.098	8.033	33±1	9±1
1000°C	8.102	8.044	39±1	23±1

Colour characterization of the obtained pigments

The pigment colour is in the blue range for CoAl₂O₄ and cyan for NiAl₂O₄, being strongly influenced by calcination temperatures.

The absorption spectra for CoAl₂O₄ and NiAl₂O₄ are shown in figure 6 and 7, respectively.

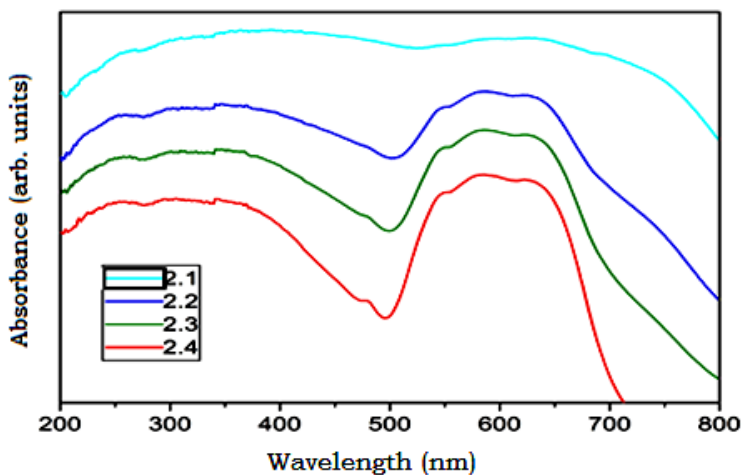


Figure 6. The absorption spectra of $CoAl_2O_4$ powders, obtained by calcination, for 30 min at : 2.1 – 600 °C, 2.2 – 700 °C, 2.3 – 800 °C, 2.4 – 1000 °C

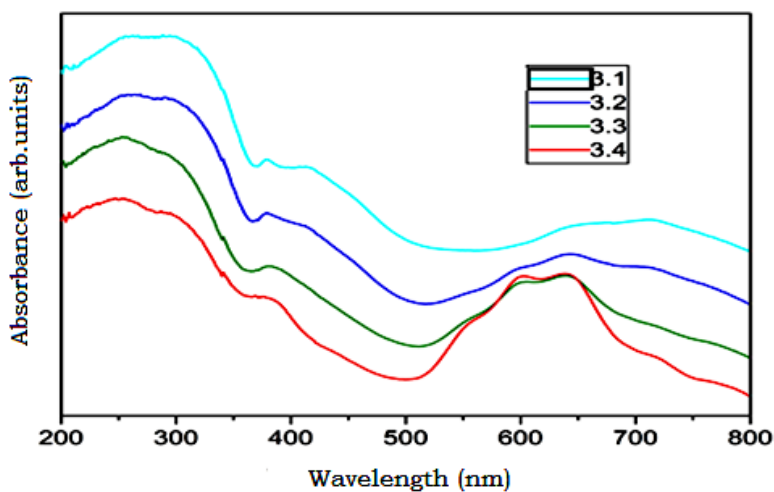


Figure 7. The absorption spectra of $NiAl_2O_4$ powders, obtained by calcination, for 30 min at : 3.1 – 600 °C, 3.2 – 700 °C, 3.3 – 800 °C, 3.4 – 1000 °C

In the case of $CoAl_2O_4$ thermally treated at 600 °C, the colour is dark green, almost black and has a tendency of becoming blue with a raise in temperature. The blue colour observed at 700 °C becomes clearer, and more luminous at 800 and 1000 °C. This is accordingly to the UV – VIS absorption spectra, that, at 600 °C, shows high intensity absorption almost on the entirety of the visible spectrum. In the case of the powders thermally treated at 700,

800 and 1000 °C, the spectra shows an absorption broadband at 500 – 700 nm, with maximums at 580 and 640 nm, that accordingly to literature data [1,2,4, 5,12] can be attributed to the ${}^4A_2(F) \rightarrow {}^4T_1(P)$ transition of Co^{2+} (d^4) in Td configuration. The rise in temperature leads to a narrowing of the absorption broadband, which indicates a high purity of colour.

The colour of $NiAl_2O_4$ powders varies among yellowish green for the 600 °C sample, bluish green for the 700, 800 °C one, and cyan blue for the 1000 °C sample. The absorption spectra for the powders calcined at 800 and 1000 °C show well contoured absorption bands with maximums at 370, 600, 640 nm, a characteristic of tetracoordinated Ni^{2+} . According to literature data [1,11,13,14], the absorption bands at 600 – 640 nm, correspond to the $3T_1(F) \rightarrow 3T_1(P)$ transition, a feature specific to Ni^{2+} tetracoordinated. The bands from 710 and 760 nm correspond to the $3A_2g(F) \rightarrow 3T_1g(F)$ transition, attributed to Ni^{2+} octahedrally coordinated, and the 370, 430 nm maximums correspond to the transfer in charge [11]. The experimental spectra do not show significant values for the absorbance at wavelengths greater than 700 nm, so it can be concluded that the amount of Ni^{2+} octahedrally coordinated is very small.

The determination of the tricromatic coordinates and the location of the representative points on the chromicity diagram confirms that the obtained colours belong in the blue domain in the case of $CoAl_2O_4$ and the cyan one, in the case of $NiAl_2O_4$ (figure 8).

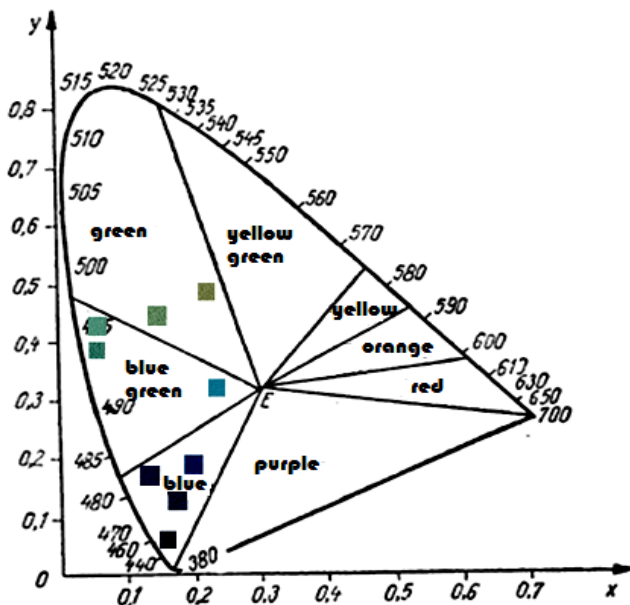


Figure 8. The Chromicity diagram. The fixed positions for the $CoAl_2O_4$ and $NiAl_2O_4$ pigments calcined between 600 – 1000 °C

CONCLUSIONS

The modified sol – gel method, utilizing sucrose and pectin as organic precursors, leads to the formation of powders with crystallite dimensions under 50 nm, when applied to $CoAl_2O_4$ and $NiAl_2O_4$ spinels. Sucrose and pectin are inexpensive and nontoxic both in terms of an economical, as well as an environmental point of view.

After XRD analysis on powders obtained by gel calcination at temperatures ranging between 600 – 1000 °C, it is found that the structure of $CoAl_2O_4$ spinel arranges itself easily. The diffraction pattern indicates a consolidated crystalline structure even at a lower temperature as 600 °C. The crystalline structure of $NiAl_2O_4$ arranges itself with more difficulty, at 600 °C the amorphous phase being predominant. The ordering of the crystalline structure begins at 800 °C.

The crystallite dimensions, determined with the Debye – Scherrer formula, indicate values in the range of 9 – 39 nm. These values rise with the rise in temperature, from about 28 nm for $CoAl_2O_4$ fired at 600 °C to about 39 nm for $CoAl_2O_4$ fired at 1000 °C. Comparatively, the crystallite dimension for $NiAl_2O_4$ is approximately 9 nm for the 800 °C sample and about 23 nm for the 1000 °C one. The differences shown are due to the differences in the ordering of the crystalline structure for the two pigments

The colour of the powder is characteristic for the two spinel structures: blue in the case of $CoAl_2O_4$ and cyan for $NiAl_2O_4$. The UV – VIS absorption spectra shown specific maximums in conformity to the literature data. The colour of the powders is dependent on the calcination temperature – for $CoAl_2O_4$ there can be observed a dark green, almost black colour for the 600 °C sample, dark blue for the 700 °C one, colour that becomes more luminous at higher temperature calcination. The colour for $NiAl_2O_4$ varies from a yellowish green, obtained at 600 °C to a bluish green at 700 - 800 °C and finally cyan, for the sample fired at 1000 °C.

EXPERIMENTAL SECTION

The sol – gel process is based on the formation of a solution that contains metal salts or alkoxides, followed by the conversion of the gel, by hydrolysis and condensation, into the oxide gel lattice. The hydrolysis is accomplished under a strict control of the temperature, pH, concentration, water/ alcohol ratio. By controlled drying and calcination, the gel becomes an oxide [2,6]. This mechanism, and the role played by sucrose and pectin in the formation of the oxide structures, is discussed in more detail in reference [8,9,10]. The addition of sucrose, and pectin, to the solution of the

metal cations, forms a polymer matrix in which the Co^{2+} and Al^{3+} respectively Ni^{2+} and Al^{3+} cations are distributed through the polymeric network structure. Sucrose, which is always in excess, acts as a strong chelating agent and as a pattern material. The sucrose solution contains NO_3^- ions that help hydrolyze the sucrose molecule into glucose and fructose, and afterwards, oxidize it to gluconic acid, or polyhydroxyl acid. Gluconic acid contains carboxylic acid groups and hydroxyl groups which can participate in the complexation of metal ions and may form branched polymer with pectin. Pectin chains form long layers and sucrose molecules may bind between these layers. In the present process, metallic ions are bound by the sucrose molecule and the resulting complex molecule is trapped between pectin layers. During calcination this polymeric metal ion complex is decomposed into CO_2 and H_2O and a large amount of heat is generated preventing agglomeration by ensuring that the mixture remains porous [9].

For obtaining CoAl_2O_4 and NiAl_2O_4 spinels, $\text{Co}(\text{NO}_3)_2 \cdot 2\text{H}_2\text{O}$, $\text{Al}(\text{NO}_3)_3 \cdot 9\text{H}_2\text{O}$ and $\text{Ni}(\text{NO}_3)_2 \cdot 6\text{H}_2\text{O}$ were used. The salts were dissolved in water, to obtain concentrated solutions. The solutions were stirred in with the sucrose for 1 hour (with a 2:1 molar ratio for sucrose: oxides), at 40 – 45 °C and with a pH corrected to 1 – 1.5. After stirring, the mixture is left in a repose state, at 60 °C, for 24 h, to ensure the formation of the gel lattice, with the elimination of the water present in the pores and the final formation of a porous structure. The thermal treatment of the dried gels was done in an electric furnace, in porcelain crucibles. The furnace temperature had an increase rate of 300°C/h, with an isothermal plateau of 30 minutes, at 600, 700, 800, 1000 °C. At 800 °C an additional thermal treatment for 2 hours was realized.

The behavior of the gels during heating was studied with a Differential Thermal Analysis, done with a TA Instruments SQD 600 analyzer, on an interval of 30 – 700 °C, and a heating rate of 10°C/min, in alumina crucibles and a dynamic air atmosphere.

The structural characterization was carried out at room temperature by powder X-ray diffraction using a Bruker D8 Advance AXS diffractometer with Cu K α radiation. The crystallite-sizes were calculated using the Debye – Scherrer formula:

$$D = \frac{k\lambda}{\beta \cos \theta} \quad [1],$$

where β is the peak full width at half maximum (in radians) at the observed peak angle θ , k is the crystallite shape factor (was considered 0.94) and λ is the X-ray wavelength.

The characterization of the pigment colour was realized by measuring the absorption in UV - VIS and by determining the trichromatic coordinates (X, Y, Z), with an MOM colorimeter. The UV-visible absorption spectra were recorded with a Jasco V-650 spectrophotometer (Japan) equipped with an ISV-722 Integrating Sphere, in the range 200-800 nm with a scan rate of 400 nm/min.

REFERENCES

1. L.K.C. de Souza, J.R. Zamian, G.N. da Rocha Filho, L.E.B. Soledade, I.M.G. dos Santos, A.G. Souza, Th. Scheller, *Dyes and Pigments*, **2009**, *81*, 187–192.
2. I. Mandru, D. Gingasu, G. Marinescu, L. Patron, *Spinelic structured oxidic nanomaterial design*, Ed. Matrix Rom, Bucuresti, **2009**, ISBN 978-973-755-437-6.
3. G.L. Pashkov, S.V. Saikova, M.V. Panteleeva, E.V. Linok, A.S. Samoilo, and G.N. Bondarenko Translated from *Steklo i Keramika*, **2013**, *6*, 28–31.
4. M. Gaudonn, L.C. Robertson, E. Lataste, M. Duttine, M. Ménétrier, A. Demourgues, *Ceramics International*, **2014**, *40*, 5201–5207.
5. I. Lazau, S. Borcanescu, C. Pacurariu, R. Lazau, I. Corovita, *Romanian Journal of Materials*, **2010**, *40*, 28-40.
6. E. Popovici, E. Dvininov, *Nanostructured materials - nanoparticles*, Ed. Demiurg Iasi, **2009**, ISBN 978-973-152-001-8.
7. I. Lazau, C. Pacurariu, Z. Ecedi, R. Ianos, *Unconventional Methods Used for Oxide Compounds Synthesis*, Ed. Politehnica, Timisoara, **2008**.
8. C. Suci, A.C. Hoffman, A. Vik, F. Goga, *Studia UBB Chemia*, **2007**, *LII(2)*, 3-12.
9. C. Suci, A. Vik, F. Goga, E. Dorolti, R. Teteanu, A.C. Hoffman, *Studia UBB Chemia*, **2009**, *LIV(4)*, 262-272.
10. C. Suci, A.C. Hoffman, A. Vik, F. Goga, *Chemical Engineering Journal*, **2008**, *138*, 608.
11. I. Lazau, C. Corcoveanu, C. Pacurariu, R.I. Lazau, *Romanian Journal of Materials*, **2013**, *43*, 425-437
12. A.B.P. Lever, *Inorganic Electronic Spectroscopy*, Elsevier Pub. Comp. Amsterdam, London, New York, **1968**.
13. G. Lorenzi, G. Baldi, F.D. Benedetto, V. Faso, *Journal of European Ceramic Society*, **2006**, *26*, 317.
14. F. Iova, A. Trutia, *Optical Materials*, **2000**, *13*, 455.

***Dedicated to Professor Luminița Silaghi-Dumitrescu
on the occasion of her 65th anniversary***

ANTIMICROBIAL ACTIVITY OF CERAMIC DISKS LOADED WITH SILVER IONS AND NITROXOLINE

**ANCUTA DANISTEAN^a, MARIA GOREA^a, ALEXANDRA AVRAM^a,
SORIN RAPUNTEAN^b, GHEORGHE TOMOAIAC^c, AURORA MOCANU^a,
CORINA GARBO^a, OSSY HOROVITZ^a, MARIA TOMOAIAC-COTISEL^{a*}**

ABSTRACT. Ceramic porous disks made of hydroxyapatite, HAP, loaded with silver ions and nitroxoline (5-nitro-8-hydroxyquinoline, NHQ) are used in vitro against pathogens, such as *Staphylococcus aureus*. HAP powder was synthesized by a wet chemical method, and its phase purity and nanocrystalline structure were assessed by X-ray diffraction (XRD), transmission electron microscopy (TEM) and atomic force microscopy (AFM). Disk samples of HAP were prepared and impregnated with Ag⁺ ions and NHQ solutions. A strong antimicrobial activity of all samples was assessed by the diffusion assay in vitro against *Staphylococcus aureus*. Through the development of the optimal composition of these biomaterials, this approach might hold potential applications for antimicrobial coating, bone tissue engineering scaffolds and biomedical devices.

Keywords: *ceramics, hydroxyapatite, silver ions, 5-nitro-8-hydroxyquinoline, antimicrobial effect*

INTRODUCTION

Ceramics, such as nano crystalline hydroxyapatite, HAP, has been widely used as bone cement due to its structural similarity to inorganic component of natural bone and to its bone conductive properties. The HAP

^a Babeş-Bolyai University, Faculty of Chemistry and Chemical Engineering, 11 Arany Janos Str., RO-400028, Cluj-Napoca, Romania

^b University of Agricultural Sciences and Veterinary Medicine of Cluj-Napoca, 3-5, Mănăstur Str., RO-400372, Cluj-Napoca, Romania

^c Orthopedy and Traumatology Department, Iuliu Hatieganu University of Medicine and Pharmacy, 47 Traian Mosoiu Str., RO-400132 Cluj-Napoca, Romania

* Corresponding author: mcotisel@gmail.com

coatings of orthopedic implants are also used, particularly in hip surgery, to enhance the implant osseointegration. Although the estimated risk is rather low (about 5%), the post-operative infections are still a major cause of bone tissue damage and might lead to the removal of implants and consequently, to an increased cost of treatment. To reduce the implant-derived infections, the localized delivery of antimicrobial compounds using HAP as a support is the best choice for the prevention of bone infections [1-4]. Due to increased antibiotic resistance, the alternative use of Ag^+ or silver nanoparticles, alone or in combination with antibiotics, is recommended [5-13]. 5-Nitro-8-hydroxyquinoline (nitroxoline: NHQ) [14] is a broad-spectrum antimicrobial agent, used as a urinary antibiotic [15]. It is practically insoluble in water, at room temperature, but soluble in organic solvents [16]. At 298 K, the mole fraction, x , of NHQ in its saturated solution in ethanol is $x = 0.0018$ [16], which corresponds to a 0.02 M solution (3.8 g NHQ/L).

This investigation is focused on the antimicrobial effect of nitroxoline and of silver nitrate, and on the possible interaction of Ag^+ and NHQ leading to supramolecular associations, which could modulate their biological activity. They are adsorbed on HAP disks, which possess an enhanced adsorptive ability both for Ag^+ and for biomolecules, such as nitroxoline. Their antimicrobial effectiveness is assessed by Kirby-Bauer diffusion assay [17] on agar plates, against *Staphylococcus aureus* microbial strain.

RESULTS AND DISCUSSION

Characterization of HAP powders. Two synthesized HAP powders are used, namely HAP1 calcined at 450 °C and HAP2 further calcined at 850 °C. The XRD patterns are similar for HAP1 and HAP2 and show only the characteristic peaks for pure HAP indicating a unique phase of stoichiometric HAP of high phase purity. As an example XRD patterns for HAP2 are given in Fig. 1. The average crystallite size estimated by the Debye-Scherrer method is about 49.6 nm (HAP1) and 60.3 nm (HAP2), while the crystallinity degree for HAP1 is about 64.8% and for HAP2 is rather high, around 78.5 %.

TEM images for HAP2 are given in Fig. 2, together with the histogram obtained by measuring the diameters of a large number of particles. The average diameter of HAP2 particles is of 65.1 ± 17.0 nm.

A representative example of AFM images is given in Fig. 3 and confirms this size of HAP2 particles, about 67 ± 5 nm.

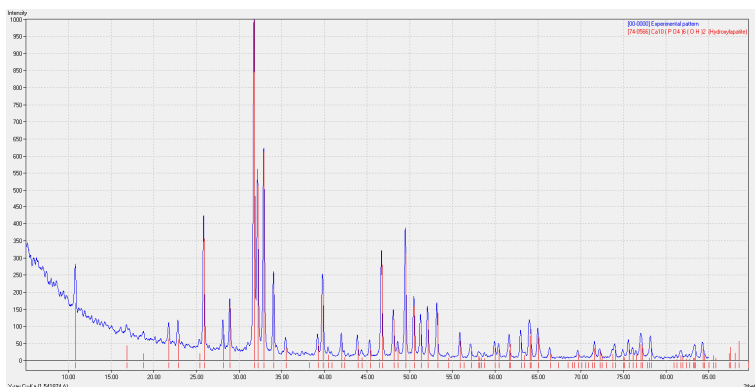


Figure 1. XRD patterns for the synthesized HAP2 powder compared with PDF 74-0566 for stoichiometric hydroxyapatite

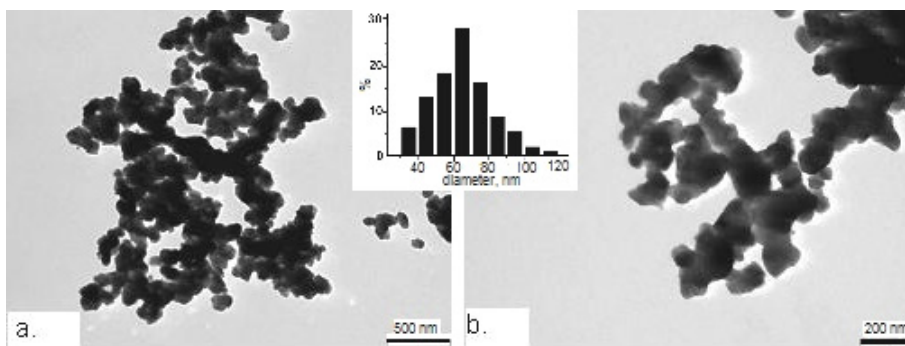


Figure 2. TEM images for HAP2 particles and histogram of their size distribution. The bars in the TEM images are 500 nm (a), and 200 nm (b).

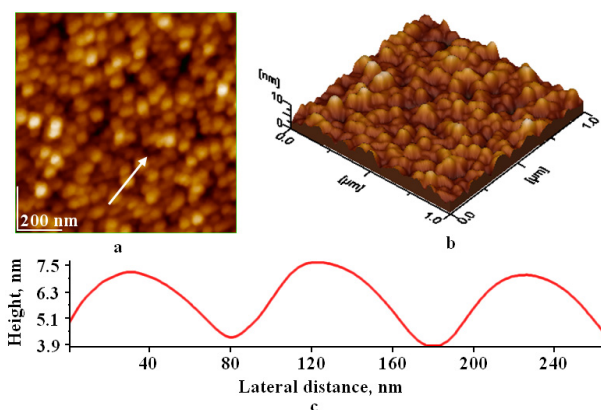


Figure 3. AFM images for HAP2 adsorbed on glass for 10 s from aqueous dispersion: (a) 2D-topographical image; (b) 3D-topographical image; (c) cross section profile along the arrow in panel (a); scanned area: 1 μm x 1 μm

Characterization of ceramic disks. Compactness characteristics of the sintered disk ceramics were determined using air and water weight method. Apparent density, ρ_a , water absorption, a_m , and apparent porosity, P_a , were determined (Table 1). The apparent porosity of ceramic disks is high. This property allows various solutions to penetrate within porous disks, and give an optimal choice for disk adsorption of the components from solutions. Consequently, active silver ions and NHQ biomolecules, impregnated into HAP disks, can be released into microbial medium.

Antimicrobial activity. In Fig. 4 are presented representative images of the agar plates with *Staphylococcus aureus* cultures after incubation at 37°C for 24 hours, with ceramic disks (Fig. 4a) and with the initial solutions in which the disks had been immersed (Fig. 4b). The diameters of the inhibition zones, in mm, are given in Table 2.

Table 1. Characteristics of the ceramic disks

Ceramic disks	Sample No	Apparent density, ρ_a [%]	Water absorption, a_m [%]	Apparent porosity, P_a [%]
HAP1	1	1.24	38.27	47.67
	2	1.36	34.41	47.01
	3	1.46	37.31	54.73
HAP2	1	1.57	29.44	46.39
	2	1.31	36.70	48.12
	3	1.21	36.63	44.56

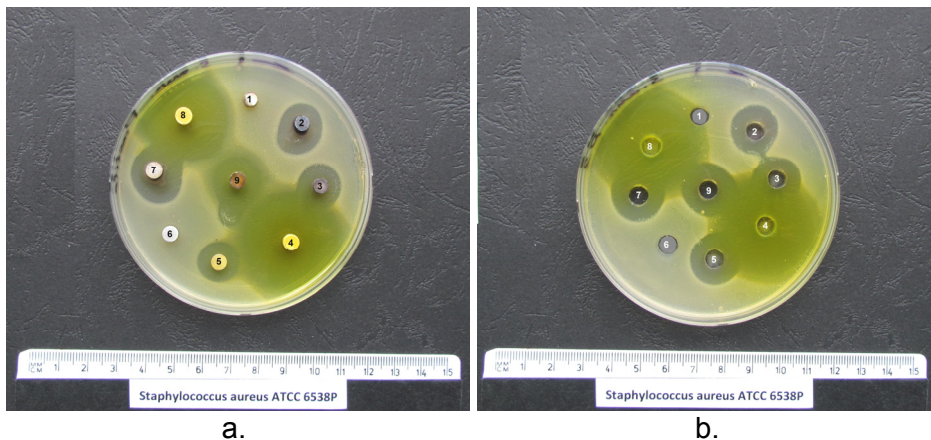


Figure 4. Inhibition zones for *Staphylococcus aureus* in presence of ceramic disks loaded with antimicrobial solutions (a), or in presence of antimicrobial solutions in wells (b). Samples are numbered as follows: 1 for HAP1/water and 6: HAP2/water, each as control; 2 and 3: HAP1/AgNO₃; 7: HAP2 /AgNO₃; 4: HAP1/NHQ; 8: HAP2/NHQ; 5: HAP2/NHQ + AgNO₃; 9: HAP1/NHQ + AgNO₃.

Table 2. Inhibition zones for the samples presented in Fig. 4; the labels are the same as in Fig. 4

Samples	Inhibition zones (mm)								
	1	2	3	4	5	6	7	8	9
Disks	-	15	15	>30	14	-	17	>30	18
Solutions	-	18	18	>30	17	-	18	>30	18

The control disks, samples 1 and 6 (HAP1, HAP2, in pure water) did not produce any inhibition zone. The largest effect is observed for disks loaded with NHQ, sample 4 (HAP1) and sample 8 (HAP2) (Fig. 4a), and for their corresponding NHQ solutions, which remained after removing the disks (at about 24h from preparation) for antimicrobial evaluation (Fig. 4b). The antimicrobial effect of the NHQ impregnated HAP1 disk (sample 4) was very strong (> 30 mm) and comparable with that of the sample 8, HAP2/NHQ. It is clear evidence that NHQ adsorbed and incorporated into ceramic disks has a strong effect on *S. aureus*. The antimicrobial effect of ceramic disks loaded with NHQ is also comparable with that of NHQ solutions (samples 4 and 8, in Fig. 4b) showing that *S. aureus* is highly susceptible in vitro to NHQ. The Ag⁺ ions loaded disks (Fig. 4a) and their corresponding AgNO₃ solutions (Fig. 4b), namely samples 2, 3 and 7 also show distinct inhibition zones. The antimicrobial effect of Ag⁺ loaded HAP1 disk (samples 2 and 3, Fig. 4a) is smaller than that corresponding to the Ag⁺ solutions (Fig. 4b). The cause might be the interaction of Ag⁺ with the surface of ceramic nanoparticles within the disk leading to a retard delivery of Ag⁺. However, the inhibition zone is almost the same (Table 2) for HAP2 disk loaded with Ag⁺ (sample 7, Fig. 4a) and for Ag⁺ in solution (sample 7, Fig. 4b). This shows that characteristics of HAP disks are also important.

The antimicrobial effect (Table 2) for HAP1 disk (sample 9) previously immersed in the initial NHQ solution for 30 min, is higher than that of HAP2 disk immersed for 15 min (sample 5), both immersed after removing from NHQ, in 5 mL 10⁻² M AgNO₃ solution each. The effect of the disk sample 5 (14 mm) is lower than that for its corresponding solution, sample 5 in Fig. 4b (17 mm, Table 2). On the other hand, the antimicrobial effect of the disk sample 9 is the same as that of its corresponding solution (Table 2), showing the importance of adsorption time of biomolecules on ceramic disks to reach adsorption equilibrium. This situation is more complex and shows also the importance of the self-assemblies of NHQ and Ag⁺, adsorbed on ceramic disks as well as their role in antimicrobial activity. Specifically, the antimicrobial effects of AgNO₃ solutions, samples 5 and 9, are almost the same as those for samples 2, 3 and 7, showing in fact the effect of pure AgNO₃ solution, since this was the final solution around ceramics disks impregnated with NHQ (samples 5 and 9).

The results are in substantial agreement with earlier results [17] showing discrete inhibitory effects characteristic for an investigated system.

CONCLUSIONS

This investigation demonstrates the antimicrobial effect of nitroxoline (NHQ), Ag⁺ and their self-assemblies or clusters against *Staphylococcus aureus* in vitro, under given experimental conditions. Results demonstrate for the first time the ability of NHQ and of Ag⁺ to diffuse from ceramic disks and to exert their antimicrobial effect. This technique of self-assembly on ceramic disks uses as a driving force for surface adsorption, electrostatic and van der Waals interaction, as well as hydrogen bonding and hydrophobic interaction [24, 25]. It offers another approach to depositing antimicrobial agents, such as NHQ and silver ions, within ceramics disks for their local retard delivery with potential applications to prevent or to treat infections. Further studies are needed to evaluate the efficacy of NHQ and silver ions impregnated ceramic disks against *S. aureus*. This investigation can be extended to various pathogens to explore the possible applications of NHQ and Ag⁺ incorporated in ceramic disks to address the susceptibility of microbial biofilms.

EXPERIMENTAL SECTION

Preparation of HAP powders. A chemical precipitation method was applied [17-23]. A 0.25 M calcium nitrate solution was obtained from Ca(NO₃)₂·4H₂O (pure p.a., Poch S.A., Gliwice, Poland) dissolved in ultrapure water, with 25% ammonia solution, pH value 8.5, and o-toluidine p.a. (Merck) as template. A second solution was a 0.15 M diammonium hydrogen phosphate ((NH₄)₂HPO₄ pure p.a., SC Nordic Invest SRL, Romania) solution in ultrapure water, with 25% NH₃ solution, pH 11 and ethylene diamine (EDA, from Merck) as template. Equal volumes of the two solutions, at 22°C, were quickly mixed using a peristaltic pump (Masterflex L/S Digital Drive, 600 RPM, 115/230 VAC, EW-07523-80) and an impact reactor type Y for the two fluid streams, with the reactants in stoichiometric molar ratio Ca/P = 1.67. A maturation treatment was applied to the obtained suspension (70°C, 24 h). To avoid agglomeration of particles during further processing, they were coated with urea-formaldehyde (UF) resin prepared *in situ* from an aqueous 30% CH₂O solution and urea in a 1.5 mole ratio, final pH 8.5. After maturation (85-95°C, 8 h) the precipitate was filtered (Filter Disks Munktell, grade: 382), washed with ultrapure water (until free of nitrate ions) and dried by

lyophilization. Thus obtained material was dispersed in a colloidal mill, for 2 h and calcined 4h at 450 °C, in order to burn the organic matter (HAP1 powder); and further for another 4 h at 850°C, for HAP2 powder, with increased crystallinity.

Physical characterization methods. X-ray diffraction (XRD) patterns were obtained using a DRON-3 diffractometer, in Bragg–Brentano geometry, having a X-ray tube with copper K_{α} radiation, wave-length 1.541874 Å). Phases were identified by comparing the peak positions with PDF (Powder Diffraction File) 74-0566 for stoichiometric hydroxyapatite. HAP aqueous dispersions needed for TEM and AFM imaging were prepared by ultra-sonication (Sonics Vibra-Cell, model VCX 750), for 5 min, at 22°C. TEM images obtained with TEM, JEOL – JEM 1010 equipment have been recorded with JEOL standard software. The AFM JEOL 4210 equipment was operated in tapping mode [26], using standard cantilevers with silicon nitride tips. The particles were adsorbed (vertical adsorption) from their aqueous dispersion for 10 s on glass. Different areas from 10 $\mu\text{m} \times 10 \mu\text{m}$ to 0.5 $\mu\text{m} \times 0.5 \mu\text{m}$ were scanned on the same HAP layer. The AFM images (2D- and 3D-topographies) and cross-section profiles for the adsorbed HAP layer, along a selected direction were processed by the standard AFM JEOL procedures.

Preparation of ceramic disks. The HAP powder was mixed with a 2 % polyvinyl alcohol solution as a binding material for granulating and obtaining a final powder humidity of 6%. The ceramic disks with 6 mm diameter and 3 mm in height were pressed at 1000 kgf/cm². The raw HAP disks were dried in a laboratory oven at 100 °C. Dried ceramic disks were sintered in air at 900 °C in a laboratory kiln using a 5 °C/min heating rate and a plateau at the maximum temperature of one hour.

Antimicrobial activity assessment. The HAP1 and HAP2 disks were treated by immersing each in 5 mL of the following solutions: ultrapure water (witness samples 1 (HAP1) and 6 (HAP2); 10⁻² M AgNO₃ (Merck, Germany) solution: samples 2 and 3 (HAP1), and 7 (HAP2); saturated NHQ (Sigma-Aldrich, Germany) solution in ethanol (sample 4: HAP1, and sample 8: HAP2); NHQ solution for 15 min (HAP2, sample 5), and for 30 min (HAP1, sample 9) and then moved in AgNO₃ solution. The tested microbial strain was *Staphylococcus aureus* 6538P ATCC. It was streaked on glucose medium (nutrient broth and agar) (TM MEDIA, TITAN BIOTECH, India). The inhibitory effect was determined by Kirby-Bauer technique [17] (agar diffusion test). The nutrient agar, after liquefaction by heating on a water bath, was poured in Petri dishes (diameter of 90 mm) in an amount of 25 ml to form a uniform layer with about 3 mm thick. Inoculation was done by flooding, using 1 ml suspension

of the test strain at a density of 0.5 (according to "McFarland Standards"). The agar surface was dried in the incubator for 20 min with the lid slightly open. After 24h, the disks were removed from the liquid using a tissue plier DeBakey, previously sterilized in open flame and cooled in sterile distilled water. Disks were radially placed on the agar plate. On another plate, wells ($\varnothing = 6$ mm) were cut in the agar gel, also by a radial pattern, and 20 μ L of the liquid in contact with the disks was put in each well. The plates were incubated at 37°C for 24 h, and then the presence or absence of *S. aureus* culture development around the disks or wells was assessed. In the case of an inhibitory effect, the diameter of the inhibition zones was measured. The plates were further maintained under observation for an extra 5 days.

ACKNOWLEDGMENTS

The authors acknowledge funding by the UEFISCDI through the grants no. 171 and 257.

REFERENCES

1. M. Vukomanović, I. Bračko, I. Poljanšek, D. Uskoković, S.D. Škapin, D. Suvorov, *Crystal Growth & Design*, **2011**, *11*, 3802.
2. L. Yang, X. Ning, Q. Xiao, K. Chen, H. Zhou, *Journal of Biomedical Materials Research, Part B*, **2007**, *81B*, 50.
3. B. Xiao, M. Karren, M.R. Christopher, A. Rabiei, *Acta Biomaterialia*, **2010**, *6*, 2264.
4. V. Stanic, D. Janackovic, S. Dimitrijevic, B.S. Tanaskovic, M. Mitric, S.M. Pavlovic, A. Krstic, D. Jovanovic, S. Raicevic, *Applied Surface Science*, **2011**, *257*, 4510.
5. P.N. Lim, L. Chang, E.S. Thian, *Nanomedicine*, **2015**, *11*, 1331.
6. W.K. Jung, H.C. Koo, K.W. Kim, S. Shin, S.H. Kim, Y.H. Park, *Applied and Environmental Microbiology*, **2008**, *74*, 2171.
7. Q.L. Feng, J. Wu, G.Q. Chen, F.Z. Cui, T.N. Kim, J.O. Kim, *Journal of Biomedical Materials Research*, **2000**, *52*, 662.
8. I. Chopra, *Journal of Antimicrobial Chemotherapy*, **2007**, *59*, 587.
9. S.H. Kim, H.S. Lee, D.S. Ryu, S.J. Choi, D.S. Lee, *Korean Journal of Microbiology and Biotechnology*, **2011**, *39*, 77.
10. A.R. Shahverdi, A. Fakhimi, H.R. Shahverdi, S.Minaian. *Nanomedicine: Nanotechnology, Biology, and Medicine*, **2007**, *3*, 168.
11. A.M. Fayaz, K. Balaji, M. Girilal, R. Yadav, P.T. Kalachelvan, R. Venketesan, *Nanomedicine: Nanotechnology, Biology, and Medicine*, **2010**, *6*, 103.
12. W. Suvannapruk, F. Thammarakcharoen, P. Phanpiriya, J. Suwanprateeb, *Journal of Nanomaterials*, **2013**. Article ID 542584, 9 pages
<http://dx.doi.org/10.1155/2013/542584>

13. J.R. Morones-Ramirez, J.A. Winkler, C.S. Spina, J.J. Collins, *Science Translational Medicine*, **2013**, *5*, 190ra81.
14. V.G. Voronin, I.D. Petrova, A.N. Leksin, B.V. Shemeryankin, *Pharmaceutical Chemistry Journal*, **1976**, *10*, 1215.
15. A. Sobke, M. Klinger, B. Hermann, S. Sachse, S. Nietzsche, O. Makarewicz, P.M. Keller, W. Pfister, E. Straube, *Antimicrobial Agents and Chemotherapy*, **2012**, *56*, 6021.
16. Y. Cong, J. Wang, C. Du, S. Han, L. Meng, H. Zhao, *The Journal of Chemical Thermodynamics*, **2016**, *100*, 60.
17. A. Mocanu, G. Furtos, S. Răpunțean, O. Horovitz, C. Flore, C. Garbo, A. Dănișteanu, G. Răpunțean, C. Prejemrean, M. Tomoaia-Cotisel, *Applied Surface Science*, **2014**, *298*, 225.
18. C. Garbo, M. Sindilaru, A. Carlea, Gh. Tomoaia, V. Almasan, I. Petean, A. Mocanu, O. Horovitz, M. Tomoaia-Cotisel, *Particulate Science and Technology*, **2015**, DOI:10.1080/02726351.2015.1121180.
19. Gh. Tomoaia, A. Mocanu, L.-D. Bobos, L.-B. Pop, O. Horovitz, M. Tomoaia-Cotisel, *Studia UBB Chemia*, **2015**, *60(3)*, 265.
20. Gh. Tomoaia, M. Tomoaia-Cotisel, L. B. Pop, A. Pop, O. Horovitz, A. Mocanu, N. Jumate, L.-D. Bobos, *Revue Roumaine de Chimie*, **2011**, *56*, 1039.
21. Gh. Tomoaia, L.B. Pop, I. Petean, M. Tomoaia-Cotisel, *Materiale Plastice*, *49* (1), 48-54 (2012).
22. Gh. Tomoaia, O. Soritau, M. Tomoaia-Cotisel, L.-B. Pop, A. Pop, A. Mocanu, O. Horovitz, L.-D. Bobos, *Powder Technology*, **2013**, *238*, 99.
23. Gh. Tomoaia, A. Mocanu, I. Vida-Simiti, N. Jumate, L. D. Bobos, O. Soritau, M. Tomoaia-Cotisel, *Materials Science and Engineering C*, **2014**, *37*, 37.
24. X. Wei, M. Luo, H. Liu, *Colloids and Surfaces B: Biointerfaces*, **2014**, *116*, 418.
25. B. Zhou, Y. Li, H. Deng, Y. Hu, B. Li, *Colloids and Surfaces B: Biointerfaces*, **2014**, *116*, 432.
26. O. Horovitz, Gh. Tomoaia, A. Mocanu, T. Yupsanis, M. Tomoaia-Cotisel, *Gold Bulletin*, **2007**, *40*, 295.

*Dedicated to Professor Luminița Silaghi-Dumitrescu
on the Occasion of Her 65th Anniversary*

THEORETICAL INVESTIGATION OF SYMMETRICAL THREE-TERMINAL JUNCTIONS

KATALIN NAGY^a, CSABA L. NAGY^{a*}, MIRCEA V. DIUDEA^a

ABSTRACT. In the present study atomistic models of three-terminal Y junctions with D_{3h} symmetry were built by the covalent assembly of single-walled armchair carbon nanotubes and the energetic properties were evaluated using quantum chemical methods at the PM6 level of theory. The theoretical study follows the influence of the relative position of the heptagonal ring defects on the structure and stability of the junction. The deformation of the attached nanotube branches is discussed in terms of the evaluated geometric parameters. Results indicate that the size of the junction and the diameter of the nanotube will determine the proper position of the defects corresponding to the energetically favourable cluster.

Keywords: *armchair carbon nanotubes, three-terminal junctions, PM6, POAV*

INTRODUCTION

Theoretical works predicted [1] and experimentally it was confirmed [2,3] that the electronic property of a single-walled carbon nanotube (SWCNT) strongly depends on the chiral vector – the direction along the graphene sheet is folded into the nanotube. Since carbon nanotubes can be both metals and semiconductors, this makes them promising candidates for miniaturizing electronics [4]. This would mean that silicon-based devices would be eventually replaced by all-carbon systems. The building blocks of such devices are the SWCNT junctions [5]. The unique electrical and mechanical properties of single nanotubes are reduced when they are joined electrostatically and share only a small contact area [6,7]. However the assembly of the quasi one-dimensional carbon nanotubes into an ordered covalent network remains a challenge in nanotechnology.

^a Babeş-Bolyai University, Faculty of Chemistry and Chemical Engineering, Arany Janos 11, RO-400028, Cluj-Napoca, Romania

* Corresponding author: nc35@chem.ubbcluj.ro

It is required that topological defects (non-hexagonal rings) to be introduced into the hexagonal lattice when assembling SWCNT junctions, so that the sp^2 electron configuration of each atom is retained. Experiments have demonstrated [8,9] that the creation of defects by damaging the material is necessary for nanotubes to be merged covalently. High-temperature electron beam irradiation [8] or the use of atomic welders [9] of crossing nanotubes during heat treatment have demonstrated to create the necessary instability to allow the joining of nanotubes. A recent review [7] summarizes all the progress and techniques made towards welding carbon nanotubes to obtain novel architectures. Related theoretical studies [10-15] have shown that pentagon-heptagon defects allow nanotubes to be joined in junctions with different morphology.

Soon after the discovery of multiwall carbon nanotubes the first symmetrical three-terminal SWCNT junction was theoretically proposed by Scuseria [16] and later they have been observed in electric arc experiments [17, 18]. Controlled growth of Y junctions has been achieved by template based synthesis using alumina with branching microchannels [19]. By the pyrolysis of methane over cobalt supported on magnesium oxide [20] Y junctions with straight branches and uniform diameters have been obtained, where the angles between the three arms are close to 120° .

'Super'-carbon nanostructures, including 'super' graphene-sheet [21] which is the rolled up to form 'super' single-walled nanotubes [21] and also topologically closed 'super'-fullerenes [22] have been proposed. Following the topology of a known carbon nanostructure the 'super' structures were constructed by replacing the sp^2 carbon atoms with Y-junctions and the carbon-carbon bonds with nanotubes resulting macromolecules with high-porosity. Their properties have been evaluated using tight-binding and density of states calculations and molecular dynamics simulations [21,22].

RESULTS AND DISCUSSION

The Y shaped nanotube junctions (Yj) studied in the present work are built by the covalent interconnection of three of the same finite length armchair single walled nanotubes which intersect each other at 120° , and are defined by (4,4), (6,6), (8,8) and (10,10) chiral vectors. The built structural models have D_{3h} symmetry and require six heptagonal rings as determined by the Euler polyhedral formula. The relative position of these defects located at the conjunction areas defines the morphology of the structure.

THEORETICAL INVESTIGATION OF SYMMETRICAL THREE-TERMINAL JUNCTIONS

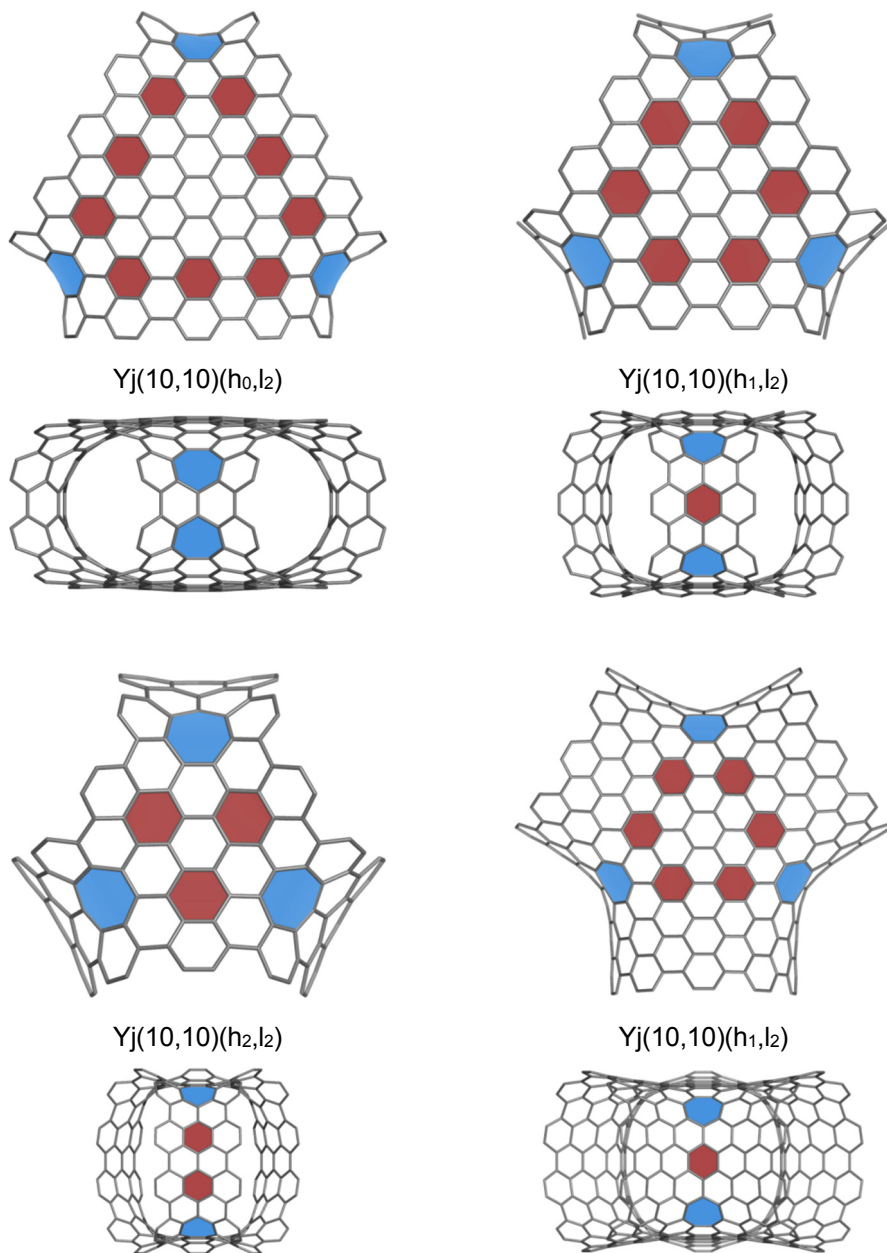


Figure 1. PM6 optimized geometries of the $Y_j(10,10)$ junctions viewed along the C_3 (top view) and C_2 axis (side view), respectively. Position of the heptagonal rings is highlighted in light blue, while the hexagons are shaded in dark red.

To the openings of the junction armchair carbon nanotubes are covalently attached (junction branches), resulting a seamless connection where all carbon atoms preserve the sp^2 hybridization state. Hydrogen atoms were used for saturating the dangling bonds located at the junction boundaries. From each Y_j a short-branch and a long-branch junction were derived by attaching a nanotube of length 2 and 5.

To label the structures the nanotube chirality, the location of heptagons and the branch length is given. Here h refers to the number of hexagonal rings between the two heptagons as viewed from the side of the structure, whereas l defines the number of layers of carbon atoms in the junction branch and equals to the length of the nanotube. Notice that when $l=2$ for armchair nanotubes it corresponds to the nanotube unit cell.

The relative position of the six heptagonal rings not only defines the morphology and electronic properties of the junction, but also alters the shape of the attached nanotube from a circular to an elliptic cross section. Figure 1 presents the optimized geometries of the $Y_j(10,10)$ junctions viewed from the top and the side of the structures. Heptagonal rings are shaded in light blue, while to make it easier to follow the hexagons located between the sevenfold rings are highlighted in dark red. When h equals zero, two heptagons located at the side of the junction are at one bond length distance from each other (see example $Y_j(10,10)(h_0,l_2)$ in Figure 1). As h increases the number of hexagons decrease as viewed from the top of the molecule.

It can be observed in Figure 1 (side view) that in the case of structures $Y_j(10,10)(h_0,l_2)$ and $Y_j(10,10)(h_2,l_2)$ the cross section of the nanotube branches is elliptical. On the other hand junction $Y_j(10,10)(h_1,l_2)$ has a close circular cross section, which transforms to a better circular shape when the attached nanotube is longer, as it can be seen in case of $Y_j(10,10)(h_1,l_2)$. This concludes that the length of the nanotube will have an influence on the morphology of the junction, where longer nanotubes rather than changing the cross sectional shape will force the junction opening to have a close to circular outline.

Notice that in the case of the (8,8) and (10,10) nanotubes it is possible to build the $Y_j(8,8)(h_2,l_2)$ and $Y_j(10,10)(h_3,l_2)$ junctions, respectively. However, during geometry optimization the junction becomes highly distorted, therefore these structures have been excluded from the study. We presume that as the diameter of the nanotube increases, it is more likely that the energetically favoured junction will have the heptagons located closer to the side of the structure.

During energy minimization by employing the PM6 method the symmetry of the structure has been preserved. To verify if global minimum is reached, deformed initial geometries have been also used and no symmetry constraints have been used during geometry optimization.

Table 1. Binding energies (BE/N_C in kcal/mol), gap energies (E_{gap} in eV), and total energies (E_{tot} in kcal/mol) obtained at the PM6 level of theory.

	Label	Formula	BE/N_C (kcal/mol)	E_{gap} (eV)	E_{tot} (kcal/mol)
1	Yj(4,4)(h ₀ ,l ₂)	C ₉₀ H ₂₄	220.988	5.865	764.212
2	Yj(4,4)(h ₀ ,l ₅)	C ₁₆₂ H ₂₄	214.363	5.013	1448.482
3	Yj(6,6)(h ₀ ,l ₂)	C ₁₅₀ H ₃₆	222.704	5.764	807.879
4	Yj(6,6)(h ₀ ,l ₅)	C ₂₅₈ H ₃₆	217.491	5.007	1384.013
5	Yj(6,6)(h ₁ ,l ₂)	C ₁₃₂ H ₃₆	223.446	5.998	838.068
6	Yj(6,6)(h ₁ ,l ₅)	C ₂₄₀ H ₃₆	216.387	4.923	1683.232
7	Yj(8,8)(h ₀ ,l ₂)	C ₂₂₂ H ₄₈	222.399	5.371	988.376
8	Yj(8,8)(h ₀ ,l ₅)	C ₃₆₆ H ₄₈	218.063	4.747	1594.005
9	Yj(8,8)(h ₁ ,l ₂)	C ₁₉₂ H ₄₈	223.751	5.844	933.147
10	Yj(8,8)(h ₁ ,l ₅)	C ₃₃₆ H ₄₈	218.279	5.047	1595.893
11	Yj(10,10)(h ₀ ,l ₂)	C ₃₀₆ H ₆₀	221.834	5.042	1214.064
12	Yj(10,10)(h ₀ ,l ₅)	C ₄₈₆ H ₆₀	218.133	4.510	1888.225
13	Yj(10,10)(h ₁ ,l ₂)	C ₂₆₄ H ₆₀	223.117	5.406	1137.863
14	Yj(10,10)(h ₁ ,l ₅)	C ₄₄₄ H ₆₀	218.546	4.784	1811.677
15	Yj(10,10)(h ₂ ,l ₂)	C ₂₃₄ H ₆₀	224.434	5.867	1055.472
16	Yj(10,10)(h ₂ ,l ₅)	C ₄₁₄ H ₆₀	218.706	5.018	1834.199

To evaluate the stability of the structures the binding energy (BE/N_C in kcal/mol) divided by the number of carbon atoms and the gap energy (E_{gap} in eV) have been followed as a measure of thermodynamic and kinetic stability. The results for the 16 studied junctions obtained at the PM6 level of theory are listed in Table 1.

When the HOMO-LUMO gap energies of the short- and long-branch nanotube junctions are compared, it can be observed in each case that the shorter junction has the higher gap. This property of a vanishing gap with the length of the nanotube has been previously published [23].

Among the studied junctions Yj(6,6)(h₁,l₂) is the most kinetically stable with a gap value of ~6 eV. This is followed closely by structures 15, 1, and 9 with gap values of 5.867, 5.865, and 5.844, respectively. All these structures are short-branched Y-junctions. It can be observed that this stability order is not affected by the size of the structure (number of carbon atoms). In each series of junctions having the same chirality, the gap energy increases with the value of h . This fact indicates that the junction is the most relaxed when the heptagons are located at the corresponding position. This observation could be compared with the preferential position of pentagonal rings in case of fullerene isomers.

The binding energy per atom values (Table 1) do not give the same stability ordering as in the case of the gap energy. Higher binding energy values indicate a larger stability of the cluster. Structure 15 has the largest binding energy (224.434 kcal/mol), followed by junctions 9, 5, and 13 in decreasing order (223.751, 223.446, and 223.117 kcal/mol, respectively). Once again the energy values cannot be associated with the cluster size.

Table 2. Average pyramidalization angles (θ_P) per carbon atom evaluated as defined by the POAV theory.

Label	Yj		Yj arm		Yj core	
	N_C	θ_P	N_C	θ_P	N_C	θ_P
Yj(4,4)(h ₀ ,l ₂)	90	4.107	48	4.119	42	4.093
Yj(4,4)(h ₀ ,l ₅)	162	5.755	120	6.117	42	4.719
Yj(6,6)(h ₀ ,l ₂)	150	2.490	72	2.755	78	2.246
Yj(6,6)(h ₀ ,l ₅)	258	3.550	180	3.934	78	2.662
Yj(6,6)(h ₁ ,l ₂)	132	2.502	72	2.663	60	2.308
Yj(6,6)(h ₁ ,l ₅)	240	3.910	180	3.898	60	3.947
Yj(8,8)(h ₀ ,l ₂)	222	1.707	96	1.994	126	1.489
Yj(8,8)(h ₀ ,l ₅)	366	2.477	240	2.814	126	1.834
Yj(8,8)(h ₁ ,l ₂)	192	1.528	96	1.964	96	1.091
Yj(8,8)(h ₁ ,l ₅)	336	2.555	240	2.797	96	1.951
Yj(10,10)(h ₀ ,l ₂)	306	1.271	120	1.564	186	1.081
Yj(10,10)(h ₀ ,l ₅)	486	1.888	300	2.157	186	1.454
Yj(10,10)(h ₁ ,l ₂)	264	1.071	120	1.492	144	0.720
Yj(10,10)(h ₁ ,l ₅)	444	1.917	300	2.119	144	1.495
Yj(10,10)(h ₂ ,l ₂)	234	1.274	120	1.544	114	0.990
Yj(10,10)(h ₂ ,l ₅)	414	1.841	300	2.158	114	1.008

To find a correlation between the energy of the Y junctions and the strain energy of the carbon atoms associated with the pyramidalization angles (θ_P), a POAV study was also performed. These values are presented in Table 2, and give a good estimate about the strain in the local geometry of carbon atoms. In Table 2 the average (per carbon atom) values are presented for the whole structure, and also for both the junction core and branches. The θ_P values of Yj arm can be compared with the one obtained for the single-walled nanotubes, and it is an indicator of the deformation from the perfect tubular shape. In case of armchair nanotubes (4,4), (6,6), (8,8) and (10,10) with five layers of carbon atoms the θ_P values are 4.187, 2.556, 1.786, and 1.355, respectively. It can be observed that in case of the junctions the attached nanotube is more strained having larger θ_P values.

The θ_P values listed for junctions Yj(10,10) can be easily compared with the optimized geometries from Figure 1. Notice that structure 13 has a less deformed attached nanotube than in the case of junctions 11 and 15. The junction core is also the most relaxed one in case of structure 13. The global θ_P value indicates that the least strained structure is Yj(10,10)(h₁,l₂), whereas the most strained short-branched junction is 1, which is in contrast with the gap value stability ordering.

To compare the local strain with the geometry of the structural fragments, the tubularity (T) of the nanotube branch, and the sphericity (S) of the junction core were computed. A quantitative measure of the attached nanotube tubularity defined by geometry can be expressed as:

$$T = \sqrt{\left(N_C \sum_{i=1}^{N_C} r_i^2 \right) \cdot \left(\sum_{i=1}^{N_C} r_i \right)^{-2}} - 1$$

where N_C represents the number of carbon atoms in one layer of the nanotube, whereas r_i is the distance of each carbon atom to the mass center of the given atom layer. It is based on finding the radius of a circle for each layer of carbon atoms, such that the sum of squares of the distance from each atom to this least-squares circle is minimal. In a similar way a measure of sphericity of the junction core can be defined [24].

In case of an armchair nanotube where all carbon atoms in a layer are arranged on a circle, the value of tubularity is zero. The larger the distortion of the nanotube the higher the values of T are.

Table 3 lists the sphericity and tubularity values obtained for the short-branched (10,10) Y-junctions. It can be observed that the shape of the tube cross-section is nearly circular in case of structure 13. Sphericity of the junction core increases with the decrease of the number of carbon atoms in the core section.

Table 3. Sphericity (S) of the junction core, tubularity (T) of the junction arm, the maximum (r_{\max}), minimum (r_{\min}), and average (r_{avg}) radius (in Å) of both structural fragments for Yj(10,10) short-branched junctions.

Label	Yj core				T	Yj arm		
	S	r_{avg}	r_{\max}	r_{\min}		r_{avg}	r_{\max}	r_{\min}
Yj(10,10)(h ₀ ,l ₂)	0.178	7.78	10.10	5.43	0.059	10.92	11.76	10.03
Yj(10,10)(h ₁ ,l ₂)	0.130	7.67	8.94	5.84	0.024	10.15	10.44	9.80
Yj(10,10)(h ₂ ,l ₂)	0.053	7.64	8.10	6.75	0.047	9.42	9.87	8.81

CONCLUSIONS

A set of 16 finite length single-walled armchair carbon nanotube Y junctions with D_{3h} symmetry has been investigated using quantum chemistry calculations employing the PM6 Hamiltonian. The present study adds valuable information about the influence on the structure and electronic properties of the relative position of the six heptagonal defects included at the conjunction of the nanotubes. Although the stability ordering by different parameters is not always pertinent, the obtained results indicate that structures are more relaxed if the non-hexagonal defects in case of Y junctions are located at the side of the structure. Shape of the junction core and the attached tubular branches are in good correlation with the structure stability as evaluated by various geometrical parameters.

COMPUTATIONAL DETAILS

The initial geometries have been fully optimized in the given symmetry using a tight SCF convergence criteria using the semiempirical parametrization method 6 (PM6) [25] as implemented in the Gaussian 09 program package [26]. The optimization of the open-ended structures has been carried out with the saturation of the dangling bonds with hydrogens, appearing at the outer layer of carbon atoms. Harmonic vibrational analysis confirms that they are local minima on the potential energy hypersurface.

On the optimized geometries the strain energy of the three-connected carbon atoms have been evaluated by computing the piramidalization angles (θ_p) according to the π -orbital axis vector (POAV) theory [27].

ACKNOWLEDGMENTS

The authors acknowledge the financial support offered by UEFISCDI under the project number PN-II-ID-PCE-2011-3-0346.

REFERENCES

1. R. Saito, M. Fujita, G. Dresselhaus, M.S. Dresselhaus, *Applied Physics Letters*, **1992**, 60, 2204.
2. T.W. Odom, J.L. Huang, P. Kim, C.M. Lieber, *Nature*, **1998**, 391, 62.

3. J.W. G. Wildöer, L.C. Venema, A.G. Rinzler, R.E. Smalley, C. Dekker, *Nature*, **1998**, 391, 59.
4. L. Chico, V.H. Crespi, L.X. Benedict, S.G. Louie, M.L. Cohen, *Physical Review Letters*, **1996**, 76, 971.
5. H.W.C. Postma, T. Teepen, Z. Yao, M. Grifoni, C. Dekker, *Science*, **2001**, 293, 76.
6. J.M. Romo-Herrera, M. Terrones, H. Terrones, S. Dag, V. Meunier, *Nano Letters*, **2007**, 7, 570.
7. G.S. Roberts, P. Singjai, *Nanoscale*, **2011**, 3, 4503.
8. M. Terrones, F. Banhart, N. Grobert, J.C. Charlier, H. Terrones, P.M. Ajayan, *Physical Review Letters*, **2002**, 89, 075505/1.
9. M. Endo, H. Muramatsu, T. Hayashi, Y.A. Kim, G. Van Lier, J.C. Charlier, H. Terrones, M. Terrones, M.S. Dresselhaus, *Nano Letters*, **2005**, 5, 1099.
10. A.N. Andriotis, M. Menon, D. Srivastava, L. Chernozatonskii, *Physical Review Letters*, **2001**, 87, 668021.
11. J.C. Charlier, T.W. Ebbesen, P. Lambin, *Physical Review B - Condensed Matter and Materials Physics*, **1996**, 53, 11108.
12. B. Gan, J. Ahn, Q. Zhang, Q.F. Huang, C. Kerlit, S.F. Yoon, Rusli, V.A. Ligachev, X.B. Zhang, W. Z. Li, *Materials Letters*, **2000**, 45, 315.
13. M. Menon, A.N. Andriotis, D. Srivastava, I. Ponomareva, L.A. Chernozatonskii, *Phys. Rev. Lett.*, **2003**, 91, 4.
14. M. Menon, D. Srivastava, *Physical Review Letters*, **1997**, 79, 4453.
15. R. Saito, G. Dresselhaus, M.S. Dresselhaus, *Physical Review B - Condensed Matter and Materials Physics*, **1996**, 53, 2044.
16. G.E. Scuseria, *Chemical Physics Letters*, **1992**, 195, 534.
17. L.A. Chernozatonskii, *Physics Letters A*, **1992**, 172, 173.
18. D. Zhou, S. Seraphin, *Chemical Physics Letters*, **1995**, 238, 286.
19. J. Li, C. Papadopoulos and J. Xu, *Nature*, **1999**, 402, 253.
20. W.Z. Li, J.G. Wen and Z.F. Ren, *Applied Physics Letters*, **2001**, 79, 1879.
21. V.R. Coluci, R.P.B. Dos Santos, D.S. Galvão, *Journal of Nanoscience and Nanotechnology*, **2010**, 10, 4378.
22. V.R. Coluci, D.S. Galvao, A. Jorio, *Nanotechnology*, **2006**, 17, 617.
23. K. Nagy, C.L. Nagy, "Hypergraphene from Armchair Nanotube Y Junctions", in: M.V. Diudea, C.L. Nagy, (Eds.), "Diamond and Related Nanostructures", Springer, Dordrecht, **2013**, chapter 11.
24. Y. Wang, M. Alcamí, F. Martin, "Stability of Charged Fullerenes", in: K.D. Sattler, (Ed.), "Handbook of Nanophysics: Clusters and Fullerenes", CRC Press, Boca Raton, **2010**, chapter 25.
25. J.J.P. Stewart, *Journal of Molecular Modeling*, **2007**, 13, 1173.

26. M.J. Frisch, G.W. Trucks, H.B. Schlegel, G.E. Scuseria, M.A. Robb, J.R. Cheeseman, G. Scalmani, V. Barone, B. Mennucci, G.A. Petersson, H. Nakatsuji, M. Caricato, X. Li, H.P. Hratchian, A.F. Izmaylov, J. Bloino, G. Zheng, J.L. Sonnenberg, M. Hada, M. Ehara, K. Toyota, R. Fukuda, J. Hasegawa, M. Ishida, T. Nakajima, Y. Honda, O. Kitao, H. Nakai, T. Vreven, J.A. Montgomery, Jr., J.E. Peralta, F. Ogliaro, M. Bearpark, J.J. Heyd, E. Brothers, K.N. Kudin, V.N. Staroverov, R. Kobayashi, J. Normand, K. Raghavachari, A. Rendell, J.C. Burant, S.S. Iyengar, J. Tomasi, M. Cossi, N. Rega, J.M. Millam, M. Klene, J.E. Knox, J.B. Cross, V. Bakken, C. Adamo, J. Jaramillo, R. Gomperts, R.E. Stratmann, O. Yazyev, A.J. Austin, R. Cammi, C. Pomelli, J.W. Ochterski, R.L. Martin, K. Morokuma, V.G. Zakrzewski, G.A. Voth, P. Salvador, J.J. Dannenberg, S. Dapprich, A.D. Daniels, Ö. Farkas, J.B. Foresman, J.V. Ortiz, J. Cioslowski, D.J. Fox, Gaussian 09, Revision A.02, Gaussian, Inc., Wallingford CT, 2009.
27. R.C. Haddon, K. Raghavachari, *Tetrahedron*, **1996**, 52, 5207.